

**THREE-DIMENSIONAL NONLINEAR FINITE ELEMENT  
MODEL FOR SINGLE AND MULTIPLE DOWEL-TYPE  
WOOD CONNECTIONS**

by

JUNG-PYO HONG

B.Sc., Seoul National University, 1994  
M.Sc., Seoul National University, 1999

A THESIS SUBMITTED IN PARTIAL FULFILMENT OF  
THE REQUIREMENTS FOR THE DEGREE OF

DOCTOR OF PHILOSOPHY

in

THE FACULTY OF GRADUATE STUDIES

(Forestry)

THE UNIVERSITY OF BRITISH COLUMBIA

December 2007

© Jung-Pyo Hong 2007

## ABSTRACT

A new three-dimensional finite solid element (3D FE) model for dowel-type wood connections was developed using the concept of a beam on a nonlinear wood foundation, which addresses the intricate wood crushing behaviour under the connector in a dowel type connection.

In order to implement the concept of wood foundation with solid elements, a 3D FE wood foundation model was defined within a prescribed foundation zone surrounding the dowel. Based on anisotropic plasticity material theory, the material model for the foundation zone was developed using effective foundation material constants that were defined from dowel-embedment test data.

New 3D FE single nail connection models were developed that incorporated the wood foundation model. The 3D wood foundation model was justified and validated using dowel-embedment test data with a range of dowel diameters, from a 2.5-mm nail to a 25.4-mm bolt. The connection models provided successful results in simulating the characteristics of load-slip behaviour that were experimentally observed.

Based on the success of the single nail connection models, several applications of the 3D FE connection models were investigated including statistical wood material models, bolted connection models and a multiple nail connection model. Throughout the application studies, discussion of the benefits and limitations of the new model approach using the 3D FE wood foundation are presented. Also, future areas of study are proposed in order to improve the 3D FE dowel-type wood connections models.

# TABLE OF CONTENTS

ABSTRACT.....	ii
TABLE OF CONTENTS.....	iii
LIST OF TABLES.....	vii
LIST OF FIGURES .....	viii
ACKNOWLEDGEMENTS.....	xvii
CHAPTER 1. INTRODUCTION.....	1
1.1 Motivation and statement of problem.....	1
1.2 Objective and Scope .....	4
CHAPTER 2. LITERATURE REVIEW.....	5
2.1 Constitutive model of wood.....	5
2.1.1 Elasticity-based model.....	6
2.1.2 Plasticity-based model .....	8
2.2 Finite element models of dowel-type wood connections .....	9
2.2.1 Three-dimensional finite element models of dowel-type wood connections	10
2.2.2 Two-dimensional finite element models of dowel-type wood connections .	12
CHAPTER 3. THREE-DIMENSIONAL MATERIAL MODEL FOR WOOD.....	16
3.1 Elasto-plastic, transversely isotropic material model for wood.....	16
3.2 Determination of wood material parameters .....	18
3.2.1 Modulus of elasticity and the yield stress.....	21
3.2.2 Elastic shear modulus and shear yield strain .....	23
3.2.3 Poisson's ratio.....	25
3.2.4 A spreadsheet tool for generating a code of wood material model .....	25
CHAPTER 4. COMPRESSION TEST AND MODEL VALIDATION .....	26
4.1 Compression test.....	26
4.1.1 Specimen preparation .....	26
4.1.2 Test methods.....	28

4.1.2.1 Parallel to grain compression.....	28
4.1.2.2 Perpendicular to grain compression.....	29
4.1.2.3 Definitions of compressive MOE and yield stress .....	30
4.1.3 Results and discussion: Material constants of Douglas-fir.....	31
4.2 Validation of FE material model .....	34
4.2.1 Wood material models.....	34
4.2.2 General description of the 3D FE model for wood compression .....	35
4.2.3 Simulation of the 1×1×4 parallel to grain compression .....	38
4.2.4 Simulation of the 1×1×4 perpendicular to grain compression .....	41
4.2.5 Simulation of the 2×2×6 perpendicular to grain compression .....	46
4.3 Conclusions for the wood material model .....	50
<b>CHAPTER 5. WOOD FOUNDATION MODEL .....</b>	<b>52</b>
5.1 Problem identification .....	52
5.2 Development of the wood foundation model .....	55
5.2.1 Rationale.....	55
5.2.2 Definitions of foundation modulus and foundation yield point .....	57
5.2.2.1 Nominal foundation properties.....	57
5.2.2.2 Effective foundation material constants .....	59
5.3 Validation of the wood foundation model.....	60
5.3.1 Dowel embedment test .....	61
5.3.2 Generalization of the wood foundation model .....	65
5.3.3 Model development .....	69
5.3.3.1 Wood foundation and calibration factors .....	69
5.3.3.2 Model for the dowel embedment test .....	72
5.3.4 Simulation results .....	76
5.3.4.1 Simulation of 3.3-mm nail-embedment test .....	77
5.3.4.2 Simulation of the 3.3-mm nail-embedment test in the 45-degree to grain direction.....	81
5.3.4.3 Model verification using Foschi's exponential models.....	84
5.3.4.4 Simulation of bolt embedment tests .....	89
5.3.5 Model application to other species .....	96
5.3.5.1 Model description .....	96
5.3.5.2 Simulation results .....	98
5.3.6 Calibration factors for intermediate sizes of wood foundation .....	103
5.3.6.1 Model description .....	103
5.3.6.2 Simulation results .....	104
5.3.6.3 Linear interpolation of calibration factors and size of wood foundation.....	107

CHAPTER 6. THREE-DIMENSIONAL FINITE ELEMENT MODEL OF NAIL CONNECTIONS..... 109

6.1 Lateral resistance test of the single nail connection ..... 109

6.2 Development of the single nail connection model ..... 114

    6.2.1 Model description ..... 114

    6.2.2 Steel material model and mechanical properties of the nail and steel plate 116

        6.2.2.1 Mechanical properties of nail ..... 117

        6.2.2.2 Mechanical properties of the CP-T steel plate..... 121

6.3 Test results and model validation ..... 122

    6.3.1 Experimental observations for load-slip behaviour of the nail connection 122

    6.3.2 Simulated results and model validation ..... 125

        6.3.2.1 Simulated deformation..... 125

        6.3.2.2 Load-deformation relationship ..... 129

        6.3.2.3 Effect of nail yield stress on the 3D FE connection model ..... 130

6.4 Feasibility study on the statistical 3D FE material model ..... 138

    6.4.1 Approximation of 95<sup>th</sup> and 5<sup>th</sup> percentile foundation material model ..... 138

    6.4.2 Simulation of the N<sup>th</sup> percentile lateral resistance of the single nail connection..... 143

CHAPTER 7. THREE-DIMENSIONAL FINITE ELEMENT MODEL OF BOLTED CONNECTIONS ..... 146

7.1 Preliminary knowledge..... 146

7.2 Model description ..... 149

7.3 Simulation of the  $l/d=2$  configuration: Full- vs. Half-hole embedment ..... 150

    7.3.1 The discrepancy and similarity of the full- and half-hole embedment tests 151

    7.3.2 Deformed shapes of the bolt embedment model ..... 153

7.4 Simulation bolted connection:  $l/d=5$  and  $l/d=7$  ..... 156

    7.4.1 Deformed shape of bolted connections..... 156

    7.4.2 Load-deformation relationship ..... 163

    7.4.3 Share of wood and bolt in total strain energy of the connection ..... 166

CHAPTER 8. MULTIPLE NAIL CONNECTION-JAPANESE CP-T JOINT ..... 169

8.1 Japanese CP-T nail connection model ..... 169

    8.1.1 Experimental reference work and model description ..... 169

    8.1.2 Square foundation meshing ..... 176

8.2 Simulation results depending on the loading schemes ..... 181

8.2.1 Deformed shapes of the CP-T connection model .....	181
8.2.1.1 Effect of loading method .....	181
8.2.1.2 Deformation of nail and CP-T connector .....	183
8.2.2 Load-deformation curve of the CP-T connection .....	188
8.2.3 Influence of the end-tearout of nail in the tenon on model prediction .....	190
8.2.3.1 Modification of the model .....	192
8.2.3.2 Simulation results of the modified model .....	192
8.2.4 Recommendations for the improvement of the 3D FE CP-T joint model ..	195
<b>CHAPTER 9. CONCLUSIONS AND RECOMMENDATION.....</b>	<b>196</b>
9.1 Summary of research .....	196
9.2 Scientific contribution of the research .....	197
9.3 Future research.....	197
9.3.1 Compressive perpendicular to grain MOE .....	198
9.3.2 Full bolted connection model .....	198
9.3.3 Failure analysis .....	199
9.3.4 Three-dimensional FE analysis for wood structure .....	199
<b>BIBLIOGRAPHY .....</b>	<b>200</b>
<b>APPENDIX A .....</b>	<b>205</b>
<b>APPENDIX B .....</b>	<b>209</b>
<b>APPENDIX C .....</b>	<b>210</b>

## LIST OF TABLES

Table 3.1	Procedures for determining the material constants of the 3D FE model for wood and wood foundation.....	21
Table 4.1	Basic mechanical properties of Douglas-fir lumber. ....	27
Table 4.2	Compressive MOEs and yield stresses from the 25×25×100 mm (1×1×4 in.) test and the conventional standard 50×50×150 mm (2×2×6 in.) perpendicular to grain test for Douglas-fir. ....	33
Table 4.3	Material constants of 3D FE material model for Douglas-fir.....	35
Table 5.1	Summary of specimen preparation for the dowel embedment test. ....	62
Table 5.2	Nominal foundation properties according to dowel diameter. ....	66
Table 5.3	Generalized calibration factors for the prescribed foundations.....	70
Table 5.4	Material constants for the generalized wood foundation models of Douglas-fir.....	71
Table 5.5	Individual calibration factors for the 1.8×bolt diameter wood foundation model. ....	90
Table 5.6	Material properties for linear elastic orthotropic wood material. ....	97
Table 5.7	Material constants of wood foundation model for Sugi, Yellow Cedar and Western Hemlock. ....	98
Table 5.8	Optimized calibration factors of intermediate wood foundations for a 12.7-mm bolt with Douglas-fir. ....	104
Table 6.1	Material specifications of the single nail connection.....	110
Table 6.2	Material specification and reference mechanical properties of nail and steel plate.....	117
Table 6.3	Steel material constant inputs for 3D FEA of ZN65 nail bending.....	119
Table 6.4	Lateral resistances of the single nail connections.....	123
Table 6.5	Comparison of the lateral resistance of nail connection.....	132
Table 6.6	Fifth percentile and 95 <sup>th</sup> percentile foundation material model for 3.3-mm diameter nail connection with Douglas-fir. ....	143

## LIST OF FIGURES

Figure 1.1	Three-dimensional microstructure of wood.....	2
Figure 2.1	Planes related to modeling: a plane parallel to the length of the dowel (left), a plane normal to the length of the dowel (right). ....	13
Figure 3.1	Three principal directions and sections in wood. ....	18
Figure 3.2	Bilinear normal stress-strain relationships in the anisotropic plasticity model. ....	19
Figure 3.3	An example of a bilinear stress-strain curve fitting to an experimental curve; the yield point should be defined at the break point. ....	22
Figure 4.1	Douglas-fir specimens for the 25×25×100 mm (1×1×4 in.) compression tests in longitudinal, radial and tangential direction (from left). ....	28
Figure 4.2	Compression test setup for the 25×25×100 mm (1×1×4 in.) prismatic specimen. ....	29
Figure 4.3	The conventional ASTM D 143 perpendicular to grain compression test. ..	31
Figure 4.4	Three-dimensional FE model for the 1×1×4 compression test.....	37
Figure 4.5	Three-dimensional FE model for the 2×2×6 compression perpendicular to grain test.....	38
Figure 4.6	Simulated load-deformation curves of parallel to grain compression. ....	39
Figure 4.7	Simulated longitudinal plastic strain contour of the 1×1×4 parallel to grain compression using the WOOD11 model. ....	40
Figure 4.8	Simulated longitudinal plastic strain contour of the 1×1×4 parallel to grain compression using the WOOD22 model. The upper steel block was omitted. ....	40
Figure 4.9	Compressive failure of the 1×1×4 parallel to grain specimen. For visibility, excessive load was also applied to the failed specimen.....	41
Figure 4.10	Simulated load-deformation curves of the 1×1×4 perpendicular to grain compression. ....	43
Figure 4.11	Simulated longitudinal plastic strain contour of the 1×1×4 perpendicular to grain compression at 4 mm-displacement load level using the WOOD11 model. ....	44

Figure 4.12 Simulated longitudinal plastic strain contour of the 1×1×4 perpendicular to grain compression at 4 mm-displacement load level using the WOOD22 model. ....	44
Figure 4.13 Progress of longitudinal plastic strain contour under the perpendicular to grain compression, simulated using the WOOD11 material model. ....	45
Figure 4.14 Actual deformed shapes of the 1×1×4 radial specimen and the 1×1×4 tangential specimen overloaded. ....	46
Figure 4.15 Simulated load-deformation curves of the 2×2×6 perpendicular to grain compression. ....	48
Figure 4.16 Crushed surface of the 2×2×6 perpendicular to grain compression specimen. ....	48
Figure 4.17 Simulated Y-directional stress contour of the 2×2×6 perpendicular to grain compression test at 2.54 mm-displacement-load level using the WOOD11 model. ....	49
Figure 4.18 Simulated Y-directional stress contour of the 2×2×6 perpendicular to grain compression test at 2.54 mm-displacement-load level using the WOOD22 model. ....	49
Figure 4.19 End split failure of the 2×2×6 perpendicular to grain compression specimen. ....	50
Figure 5.1 Three-dimensional finite element analysis for a parallel to grain nail embedment into Douglas-fir block: Y-directional stress. ....	54
Figure 5.2 Comparison of experimental and predicted load-embedment curves based on the WOOD11 material model. ....	54
Figure 5.3 A load-embedment curve can be converted to a bilinear stress-strain curve, in order to obtain the material constants for the wood foundation model. ...	56
Figure 5.4 Key points in a bilinear load per unit length-embedment plot from the dowel-embedment test. ....	58
Figure 5.5 Test specimen and setup for the nail-embedment test. ....	63
Figure 5.6 Test specimen and setup for the bolt-embedment test. ....	64
Figure 5.7 Relationship between the nominal foundation modulus and the dowel diameter in the parallel to grain direction. ....	67
Figure 5.8 Relationship between the nominal foundation modulus and the dowel diameter in the perpendicular to grain direction. ....	67

Figure 5.9	Relationship between the nominal foundation yield strain and the dowel diameter in the parallel to grain direction. ....	68
Figure 5.10	Relationship between the nominal foundation yield strain and the dowel diameter in the perpendicular to grain direction. ....	68
Figure 5.11	Three-dimensional finite element model for the nail-embedment test. (Radius of the wood foundation = $4.5 \times d$ ). ....	74
Figure 5.12	Three-dimensional finite element model for the bolt-embedment test. (Radius of the wood foundation = $1.8 \times d$ ). ....	75
Figure 5.13	Simulated parallel to grain load-embedment curve of 3.3-mm nail-embedment in Douglas-fir. ....	79
Figure 5.14	Simulated perpendicular to grain load-embedment curve of 3.3-mm nail-embedment in Douglas-fir. ....	79
Figure 5.15	Simulated Y-directional plastic strain contour of 3.3-mm nail-embedment in Douglas-fir in the parallel to grain direction. Half of the wood elements are shown. ....	80
Figure 5.16	Simulated Y-directional plastic strain contour of 3.3-mm nail-embedment in Douglas-fir in the perpendicular to grain direction. Half of the wood elements are shown. ....	80
Figure 5.17	Simulated Y-directional plastic strain contour of 3.3-mm nail-embedment in Douglas-fir in the parallel to grain direction using the WOOD11 model only. Half of the wood elements only are shown. ....	81
Figure 5.18	Grain angle of 45-degree embedment specimen. ....	82
Figure 5.19	Schematic unbalanced foundation in 45-degree grain angle embedment test. ....	83
Figure 5.20	Simulated Y-directional plastic strain contour of 45-degree to grain embedment; the force-controlled case (left) showed the tilted embedment of the nail compared to the uniform embedment of the displacement-controlled case (right). ....	83
Figure 5.21	Simulated 45-degree to grain load-embedment curve of 3.3-mm nail-embedment in Douglas-fir. Force-controlled method showed better prediction. ....	84
Figure 5.22	Simulated parallel to grain load-embedment curve of Foschi's nail embedment in Douglas-fir. ....	87

Figure 5.23 Simulated perpendicular to grain load-embedment curve of Foschi’s nail embedment in Douglas-fir. ....	87
Figure 5.24 Simulated Y-directional strain contours for nail embedment in Douglas-fir with 2.5-, 4.1- and 6.4-mm nails in parallel/perpendicular to grain directions. Half models are shown. ....	88
Figure 5.25 Simulated parallel to grain load-embedment curve of 12.7-mm bolt embedment in Douglas-fir. ....	91
Figure 5.26 Simulated perpendicular to grain load-embedment curve of 12.7-mm bolt embedment in Douglas-fir. ....	91
Figure 5.27 Simulated parallel to grain load-embedment curve of 19.1-mm bolt embedment in Douglas-fir. ....	92
Figure 5.28 Simulated perpendicular to grain load-embedment curve of 19.1-mm bolt embedment in Douglas-fir. ....	92
Figure 5.29 Simulated parallel to grain load-embedment curve of 25.4-mm bolt embedment in Douglas-fir. ....	93
Figure 5.30 Simulated perpendicular to grain load-embedment curve of 25.4-mm bolt embedment in Douglas-fir. ....	93
Figure 5.31 Simulated Y-directional plastic strain contours for bolt embedment in Douglas-fir with 12.7-, 19.1- and 25.4-mm bolts in parallel/perpendicular to grain directions. ....	94
Figure 5.32 Comparison of wood crushing shape for 25.4-mm bolt parallel to grain embedment test. The simulated Y-directional plastic strain contour is shown (bottom). ....	95
Figure 5.33 Simulated parallel to grain load-embedment curve of 3.8-mm nail embedment in Sugi. ....	100
Figure 5.34 Simulated perpendicular to grain load-embedment curve of 3.8-mm nail embedment in Sugi. ....	100
Figure 5.35 Simulated parallel to grain load-embedment curve of 3.8-mm nail embedment in Yellow Cedar. ....	101
Figure 5.36 Simulated perpendicular to grain load-embedment curve of 3.8-mm nail embedment in Yellow Cedar. ....	101
Figure 5.37 Simulated parallel to grain load-embedment curve of 3.8-mm nail embedment in Western Hemlock. ....	102

Figure 5.38	Simulated perpendicular to grain load-embedment curve of 3.8-mm nail embedment in Western Hemlock.....	102
Figure 5.39	Simulated Y-directional plastic strain contours for 12.7-mm ( $d$ ) bolt embedment in Douglas-fir in parallel/perpendicular to grain directions, using the intermediate sized wood foundations.....	105
Figure 5.40	Comparison of the parallel to grain load-embedment curves, predicted using the intermediate sized wood foundations.....	106
Figure 5.41	Comparison of the perpendicular to grain load-embedment curves, predicted the intermediate sized wood foundations.....	106
Figure 5.42	Assumed linear relationships between the radius multiplier and the calibration factors. ....	107
Figure 6.1	Specification of Japanese CP-T connector (units: mm).....	111
Figure 6.2	Lateral resistance test of single nail connection in parallel to grain direction and the corresponding three-dimensional FE model (units: mm).....	112
Figure 6.3	Lateral resistance test of the single nail connection in the perpendicular to grain direction and the corresponding three-dimensional FE model (units: mm).....	113
Figure 6.4	Sectioned single nail connection FE model.....	115
Figure 6.5	Surface-to-surface contact elements of the single nail connection model..	115
Figure 6.6	Three-point nail bending test setup (top) and simulated bending of ZN65 nail with the yield stress of 517 MPa (bottom).....	120
Figure 6.7	Load-deflection curve of three-point ZN65 nail bending and trace of 3D FE analysis for the yield stress. ....	121
Figure 6.8	Localized wood crushing failure in the parallel to grain direction: nail on the tangential surface-PAT (left), and nail on the radial surface-PAR (right)..	124
Figure 6.9	Localized wood crushing failure in the perpendicular to grain direction: nail on the tangential surface-PET (left), and nail on the radial surface-PER (right). ....	124
Figure 6.10	Slip behaviour in the parallel to grain direction: experiment (top) vs. simulation (bottom) for the PA test. ....	126
Figure 6.11	Simulated deformation of the nail connection was superimposed on the best fit photo image from the real deformation (the PAT specimen).....	127

Figure 6.12 Simulated Y-directional plastic strain contour of the steel plate in the PA test. Wood-to-steel plate contact surface view including transparent nail elements. ....	127
Figure 6.13 Simulated wood crushing shapes. Y-directional plastic strain contour plots; PA simulation (top), PE simulation (bottom). ....	128
Figure 6.14 Simulated load-deformation curve of the single nail connection in the parallel to grain direction. ....	131
Figure 6.15 Simulated load-deformation curve of the single nail connection in the perpendicular to grain direction. ....	131
Figure 6.16 Comparison of the simulated nail-slip curve to the average test data at intervals of the 1.5 mm slip for the parallel to grain nail connection test (PA test). ....	133
Figure 6.17 Comparison of the simulated nail-slip curve to the average test data at intervals of the 1.5 mm slip for the perpendicular to grain nail connection test (PE test). ....	133
Figure 6.18 Deformation progress at each interval slip for the parallel to grain connection test. Y-directional plastic strain (PA simulation). ....	134
Figure 6.19 Deformation progress at each interval slip for the perpendicular to grain connection test. Y-directional plastic strain (PE simulation). ....	135
Figure 6.20 Progress of Z-directional plastic strain for the PA connection model with a nail yield stress of a 310 MPa. ....	136
Figure 6.21 Progress of Z-directional plastic strain for the PE connection model with a nail yield stress of 310 MPa. ....	137
Figure 6.22 Two-parametric Weibull distribution fit to the parallel to grain nominal foundation modulus. ....	141
Figure 6.23 Linear relationship between the parallel to grain foundation nominal modulus and the perpendicular to grain nominal foundation modulus. ....	141
Figure 6.24 Linear relationship between the parallel to grain nominal foundation modulus and the parallel to grain nominal yield strain. ....	142
Figure 6.25 Linear relationship between the perpendicular to grain nominal foundation modulus and the perpendicular nominal yield strain. ....	142
Figure 6.26 Approximations of the 5th percentile limit and the 95th percentile curves in the parallel to grain lateral resistance of the single nail connection. ....	145

Figure 6.27	Approximations of the 5th percentile limit and the 95th percentile curves in the perpendicular to grain lateral resistance of the single nail connection.	145
Figure 7.1	Configuration and parameters of the compression loaded bolted connection test analogous to the full-hole embedment test. The $l/d=2$ , $e/d=7$ and $w/d=4$ configuration is shown.	148
Figure 7.2	Bi-sectioned bolted connection model with and without the wood foundation. The $l/d=7$ , $e/d=7$ and $w/d=4$ configuration is shown.	150
Figure 7.3	Comparison of the simulated load-embedment curves between the full-hole FEA and the half-hole FEA, using the wood foundation-based model, for the $l/d = 2$ , $e/d = 7$ configuration.	152
Figure 7.4	Comparison of the simulated load-embedment curves between the full-hole FEA and the half-hole FEA, using the conventional model (wood material only), for the $l/d = 2$ , $e/d = 7$ configuration.	152
Figure 7.5	Progress of the Z-directional plastic strain contour for the $l/d=2$ , $e/d=7$ half-hole embedment test: the wood foundation-based model (top) and the conventional model (bottom).	154
Figure 7.6	Progress of the Z-directional plastic strain contour for the $l/d=2$ , $e/d=7$ full-hole embedment test: the wood foundation-based model (top) and the conventional model (bottom).	155
Figure 7.7	Comparison of the apparent deformed shapes of the $l/d=5$ bolted connection: the wood foundation-based model (left) and the wood material model only (right).	158
Figure 7.8	Progress of the Z-directional plastic strain contour for the $l/d=5$ , $e/d=7$ bolted connection: the wood foundation-based model (top) and the conventional model (bottom).	159
Figure 7.9	Progress of the Z-directional plastic strain contour for the $l/d=7$ , $e/d=7$ bolted connection: the wood foundation-based model (top) and the conventional model (bottom).	160
Figure 7.10	Distribution of contact pressure over the wood-to-bolt interface at a deformation of 2.5 mm for the $l/d=5$ bolted connection: the wood foundation-based model (top) and the conventional model (bottom). Contact element-CONTA174.	161
Figure 7.11	Distribution of contact pressure over the wood-to-bolt interface at a deformation of 0.5 mm for the $l/d=7$ bolted connection: the wood foundation-based model (top) and the conventional model (bottom). Contact element-CONTA174.	162

Figure 7.12 Comparison of the predicted load-deformation curves of 12.7-mm bolted connection with aspect ratios of $l/d = 2, 5$ and $7$ , and the predicted half-hole load-embedment curve obtained by the wood foundation-based model simulation.....	165
Figure 7.13 Comparison of the predicted load-deformation curves of 12.7-mm bolted connection with aspect ratios of $l/d = 2, 5$ and $7$ , and the predicted half-hole load-embedment curve obtained by the conventional model simulation. ..	165
Figure 7.14 Change of material sharing in the total strain energy for the $l/d=2$ connection. ....	167
Figure 7.15 Change of material sharing in the total strain energy for the $l/d=5$ connection. ....	168
Figure 7.16 Changes of material sharing in the total strain energy for the $l/d=7$ connection. ....	168
Figure 8.1 The reference test setup by Stefanescu (2000) and the corresponding 3D FE CP-T connection model (units: mm). ....	172
Figure 8.2 A tilted CP-T connection under loading. $\Theta$ was the tilting angle. (photo by Stefanescu 2000).....	173
Figure 8.3 Failure mode; perpendicular to grain tension splitting (photo by Stefanescu 2000). ....	173
Figure 8.4 Failure modes; nail pull-out (left) and CP-T connector in shear (right) (photo by Stefanescu 2000). ....	174
Figure 8.5 Illustration of the meshed model of the Japanese CP-T joint. ....	175
Figure 8.6 Square wood foundation model overlapped (colored portions).....	177
Figure 8.7 Wood foundation models: Square foundation model (left) and cylindrical foundation model (right). ....	178
Figure 8.8 Comparison of the simulated parallel to grain load-embedment curves between the square foundation and cylindrical foundation models. 3.3-mm diameter nail in Douglas-fir. ....	179
Figure 8.9 Comparison of the simulated perpendicular to grain load-embedment curves between the square foundation and cylindrical foundation models. 3.3-mm diameter nail on Douglas-fir. ....	179
Figure 8.10 Definitions of the contact elements and the coefficients of friction. ....	180

Figure 8.11 Simulated deformations by the two different loading schemes: $\Theta$ -tilting angle, ① and ②- points for displacement measurement.....	182
Figure 8.12 The Y-directional plastic strain contour for the nails: displacement-controlled loading (top) and force-controlled loading (bottom).....	184
Figure 8.13 The Y-directional plastic strain contour for the CP-T connector: displacement-controlled loading (top) and force-controlled loading (bottom). .....	185
Figure 8.14 Progress of the simulated deformation by the displacement-controlled loading scheme. Sectioned views. ....	186
Figure 8.15 Progress of the simulated deformation by the force-controlled loading scheme. Sectioned views. ....	187
Figure 8.16 Simulated load-deformation curve of the displacement-controlled loading method, superimposed on Stefanescu's experimental curves.....	189
Figure 8.17 Simulated load-deformation curve of the force (pressure)-controlled loading method, superimposed on Stefanescu's experimental curves.....	189
Figure 8.18 Typical failure types of the three nails penetrating the tenon: nail edge splitting (off) in the side nails and nail end-tearout in the centre nail. ....	191
Figure 8.19 Simulated deformed shape of the three nail connections in the tenon. The model could not reproduce the edge wood splitting and the nail end-tearout. .....	191
Figure 8.20 Deformed shaped of the CP-T model modified with the initial edge split of the side nail connections. ....	194
Figure 8.21 Simulated load-deformation curve of the modified CP-T model. ....	194

## ACKNOWLEDGEMENTS

I wish first to express my deep appreciation to my supervisor, Dr. J. David Barrett, not only for his thoughtful guidance, encouragement and financial support, but also for showing me a good model of scholarly dignity.

I would like to thank my advisory committee members, Drs. Frank Lam and Ricardo. O. Foschi, for sharing their ideas related to my research, and giving me valuable suggestions. Without them, my doubts about the success of the research would never have ended. Indeed, I had originally thought the development of a 3D FE nail connection model was out of the question. At this point, I also thank former committee member, Dr. Helmut G. L. Prion, for his encouragement in my research proposal. Also, I extend special thanks to Dr. J. J. Lee for his encouragement.

My thanks are extended to my colleagues and fellow graduate students for their assistance and for all the activities I enjoyed with them.

I would like to express my deepest gratitude to my wife, Jiyoung, my son, Sean, and my daughter, Sooah. Jiyoung is given special thanks for all of her love, support and understanding. Also, I thank my parents-in-law for their encouragement and support.

In closing, I dedicate this thesis to my parents, Soonuk and Jungja, who have given me their endless love, encouragement and support.

## CHAPTER 1. INTRODUCTION

### 1.1 Motivation and statement of problem

Dowel-type wood connections are widely used in timber construction. This connection often leads to premature failure due to unpredictable brittleness that can occur if the critical stress that evolves in the connection is poorly estimated. Due to the anisotropic strength properties of wood, it has always been a challenge for designers to identify the critical stress and the mode of failure.

Currently, the main method for minimizing this catastrophic failure is to adopt design specifications that prescribe minimum edge distance, end distance, connector spacing and member size in the connection. These empirical design specifications have been established mostly through experimental investigations in uniaxial loading tests. However, since output from uniaxial loading tests represents a global load-deformation response, these tests do not provide the fundamental knowledge needed for stress-strain analysis of wood connections. Thus, it has been proposed that the wood connection should be analyzed to determine the three-dimensional stress-strain behaviour.

To this end, many attempts have been made to utilize the three-dimensional finite element (3D FE) method in analysis of wood connections. In fact, only 3D FE analysis can produce the entire stress-strain response for the connections. However, as shown in Figure 1.1, the anisotropic, porous and defective material characteristics of wood makes it difficult to construct a wood material model that is suitable for the 3D FE connection model (Patton-Mallory 1996, Moses 2000).

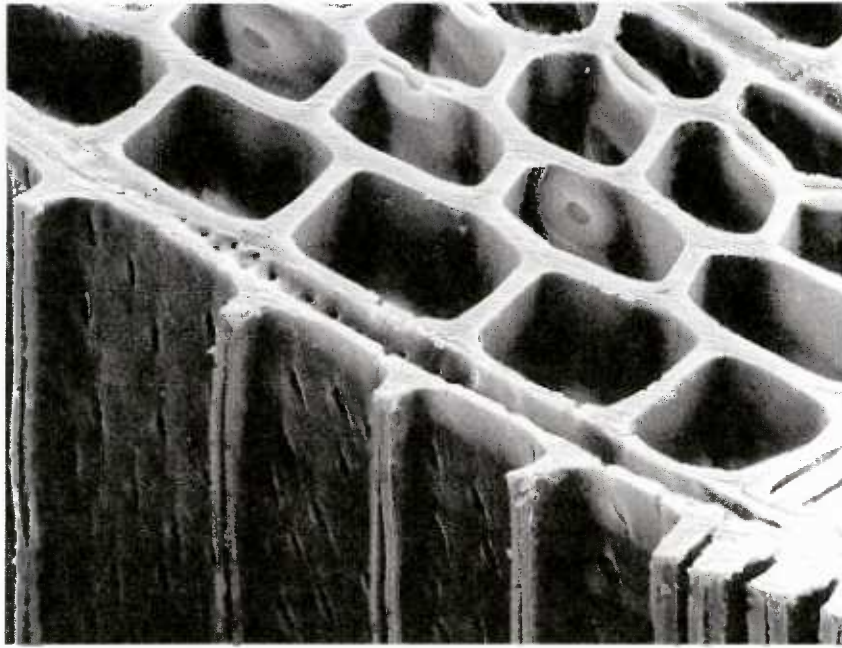


Figure 1.1 Three-dimensional microstructure of wood.

The greatest difficulty in simulating wood behaviour in connections is due to localized wood crushing failure at a contact area between the wood and connector. The crushing behaviour cannot be simulated by simply using general material mechanics based on standard uniaxial loading test-based material properties that represent macroscopic compression behaviour of wood<sup>1</sup> (Foschi 1974, 1977 and 2000, McLain et al. 1983). When a dowel contacts to wood surface under compression the interaction at the contact surface is governed by the wood fibre behaviour rather than by the gross wood behaviour. In this case, the difference of fibre density between earlywood and latewood is also influential in the wood crushing behaviour depending on the direction of loading. This explains why the European yield connection model adopts dowel embedding strengths

---

<sup>1</sup> In this study, the standard uniaxial test-based material properties refer mainly to the modulus of elasticity and yield stress, as determined with the ASTM standard test methods.

rather than the standard modulus of elasticity or wood compression strengths for the connection design. The difference between the wood compressive behaviour in general compression and in dowel embedding is a major challenge in the development of a 3D FE constitutive model for wood.

The conventional 3D FE modeling approach for wood has been to use the orthotropic material model with the standard uniaxial loading test-based elastic constants. When the nonlinear behaviour of wood is considered, the nonlinear stress-strain relationships for the 3D FE material model have been defined using bilinear or multilinear models (Patton-Mallory 1996, Moses 2000). However, due to the characteristics of wood embedment behaviour, the conventional 3D FE models investigated to date have not provided successful simulations of the behaviour of a range of dowel-type connections.

Generally, the discrepancy between the predicted and actual behaviour becomes larger as the diameter of a dowel decreases, due to increasing stress concentrations. This explains why many studies using solid finite elements have focused only on bolted connections with a relatively large diameter. Whereas, a solid element model of a small dowel connection, such as a nail connection, have never been attempted, although many one- or two-dimensional finite element models have been developed.

The challenge in this study was, therefore, the development of a wood material model that is able to account for dowel-embedment behaviour, in order to model a dowel-type wood connection properly. Since this challenge was the main obstacle to using the 3D FE method as a general analysis tool for dowel-type wood connections, this study was initiated by the goal of overcoming this obstacle and making the 3D FE method a regular tool for studying the behaviour of connections used in timber structures.

## 1.2 Objective and Scope

The main objective of this study was the development of a three-dimensional nonlinear finite element (3D FE) model for predicting the behaviour of dowel-type wood connections, including nail and bolted connections, under static loading.

Generally, the success of a 3D FE model is governed by the material model. Therefore, the main efforts in this study were directed at developing a wood material model that was able to represent the localized wood crushing behaviour of the wood surrounding a dowel connection. To this end, the following sub-objectives were studied:

- a) Development of a three-dimensional plasticity-based empirical model for wood.
- b) Development of a method to model the localized wood crushing behaviour in three dimensions.
- c) Development of nonlinear 3D FE models of dowel-type wood connections with dowel sizes ranging from nails to bolts.
- d) Applications of the 3D FE model for selected wood connections.

## CHAPTER 2. LITERATURE REVIEW

Although the finite element method has been recognized as the most powerful numerical tool in structural analysis, it has seldom been used for analysis of wood connections, due to the lack of an acceptable wood material model that adequately represents the 3D behaviour of wood. The FE studies of dowel-type connections in literature were mainly limited to bolted connections and, even then, only a few studies using 3D FE models have been reported.

In this chapter, the relevant literature is reviewed with a focus on limitations and problems encountered in the FE modeling of wood connections.

### 2.1 Constitutive model of wood

To date, orthotropic material theory has been widely used as the best mathematical description of wood on a 3D macroscopic level (Bodig et al. 1982, Dinwoodie 2000). The orthotropic model includes the assumption that wood is a continuum, regardless of the differences between earlywood and latewood, fibre porosity, and inherent discontinuities, such as knots, pith and ray. The orthotropic model only considers the difference of stress-strain relations according to the longitudinal, radial and tangential directions. The constitutive relationships in the three directions can be determined using the standard uniaxial loading tests. Some appropriate tests are given in the ASTM Standards (ASTM 2003).

The linear elastic orthotropic model has been proven to work properly for FE analysis for wood when wood behaves within an elastic range. However, wood material exhibits nonlinear behaviour, for instance, in parallel and perpendicular to grain compression,

although wood under tension or shear behaves in a more linearly brittle manner. The compressive nonlinear behaviour must be considered when modeling dowel-type connections that show highly nonlinear load-deformation behaviour. The most influential component of this nonlinearity comes from the dowel embedment into the wood in parallel and/or perpendicular to grain compression.

In most previous studies, the wood material constants of the orthotropic model have been determined from uniaxial compressive stress-strain relationships. Thus, based on the assumption of the orthotropy, a more realistic model could be made by incorporating nonlinear stress-strain relationships. In terms of the constitutive model for wood, the nonlinear stress-strain curve could be represented as a linear, bilinear or multilinear curve model. Also, in relation to energy conservation, elasticity-based models and plasticity-based models could be considered.

### **2.1.1 Elasticity-based model**

In the 3D FE modeling of wood, the simplest model reported was the linear elastic transversely isotropic model in which the assumption of plane symmetry was added to the orthotropic model. For wood behaviour within the proportional limit, this model produces acceptable results.

Teofil (1998) used the transversely isotropic model for wood to study the performance of various mortise and tenon joints using a 3D FE model. Since the main objective of his study was to optimize the geometry of the mortise and tenon joints through a 3D FE parametric study, simulated results within the linear elastic range of the connections were sufficient. However, no consideration of the crushing behaviour for wood-to-wood

contact resulted in the prediction of stiffer results than were observed in the experimental results.

Guan and Rodd (2000 and 2001) developed a 3D FE model for a hollow dowel connection in glued-laminated timber that was locally reinforced by densified veneer wood (DVW). In this connection, the deformation of the timber member could be assumed to remain within the elastic range, because the timber member was sandwiched between the DVW reinforcements and a tube-type dowel connector was used to induce the failure at the connector itself in a ductile manner. This study showed that, if a given connection did not involve too much local nonlinear compression failure, use of the linear orthotropic elastic model for wood may be suitable for a 3D FE connection model.

For a general dowel-type connection, however, the nonlinear behaviour of the wood should be taken into account for predicting the full load-deformation response. For these cases, Patton-Mallory (1996) proposed a 3D FE nonlinear material model for wood. Based on the elastic orthotropic model, tri-linear constitutive relations were fitted to parallel to grain compressive stress-strain curves and shear stress-strain curves, which were incorporated into the transversely isotropic elastic material model for modeling bolted connections. The major shortcoming of this tri-linear model was that it needed a process for finding the fictitious material parameters, including Poisson's ratio and break points in the tri-linear curves. If the parameters were not defined properly, negative stiffness coefficients could occur on the diagonal terms of the stiffness matrix, creating a problem in solution convergence. However, it is an interesting model, because it was the first 3D finite solid element nonlinear material model for wood connections.

In order to trace the nonlinear stress-strain relationship more accurately, function-based methods were devised, rather than piecewise linearization methods. Davalos-Sotelo et al. (1992) investigated a two-dimensional incremental-iterative secant stiffness approach. Tabiei et al. (2000) expanded this approach to a 3D nonlinear orthotropic finite element material model for wood. Using power functions of a ratio between incremental-iterative stresses, they developed a model to update the change in modulus of elasticity in order to track the nonlinearity of the stress-strain curve. The model showed good simulations of the uniaxial load-deformation curves in shear and compression, because the nonlinear parameters of the power function were determined from the experimental shear and compression data for the given species. However, with this model, no attempts were made to predict the behaviour of a wood connection, which usually includes a very complex stress state. Also, it is questionable whether this model was free from the occurrence of negative stiffness coefficients that were experienced by Patton-Mallory.

Basically, the elasticity-based model is limited in that it can only predict reversible strains. The results of the elasticity-based models can only be justified within the elastic response of the wood. However, in reality, the nonlinear response of wood comes mainly from the permanent deformation of wood fibres, which is a non-conservative and path-dependent phenomenon. Therefore, to overcome the limitation of the elastic model, the development of a plasticity theory-based model was initiated.

### **2.1.2 Plasticity-based model**

The most plausible plastic theory applicable for a 3D wood material model is the anisotropic plastic theory. Using this plastic material model, Moses (2000) reproduced Patton-Mallory's 3D FE models of the bolted connections. The material model assumed

bilinear stress-strain relationships of compression, tension and shear in transverse isotropy. The associative flow rule and work hardening were also assumed. This appears to be the first plasticity-based three-dimensional material model for wood. Kharouf (2001) developed a two-dimensional model, similar to the Moses model, for prediction of the behaviour of bolted connections.

These material models used Hill's yield criterion. Theoretically, this yield criterion can be modified to account for differences in yield strength in tension and compression. However, Moses reported that considering these differences made it difficult to satisfy the requirements of the yield criterion, especially for highly orthotropic material like wood (see section 3.1). Thus, by setting tension equal to compression in the stress-strain relationship, only the compression-based plastic model has been implemented in the models of Moses and Kharouf.

An ideal plasticity-based model for wood should account for the differences of yield strength and stiffness in tension and compression; however, currently, such a material theory has not yet been explored. The development of a new material theory for wood was not considered in this study.

## **2.2 Finite element models of dowel-type wood connections**

Finite element models of dowel-type wood connections can be categorized into one-, two- and three-dimensional models. In terms of the modeling process, the approach to one-dimensional models is quite different from other two because the one-dimensional model does not necessarily need an independent process of constitutive modeling for the wood itself, as should be studied in two- and three-dimensional models. That is, in a one-dimensional model, wood behaviour under a dowel is generally described by a load-

dowel embedment equation; while in two- and three-dimensional models, the wood material model itself should be capable of predicting the wood behaviour under a dowel.

To date, a number of one-dimensional models have been proposed. The salient load-dowel embedment equations can be found in Foschi's exponential model (Foschi 1974), McLain's logarithmic model (McLain 1983) and Hirai's stress-embedment model (Hirai 1991). However, this one-dimensional equation approach is not suitable for inclusion in the solid element model of the connection, because a solid element requires its own 3D material model. The review on FE models of the connections was, therefore, done with the focus on wood material model approaches.

### **2.2.1 Three-dimensional finite element models of dowel-type wood connections**

Using 8-node brick elements and a tri-linear material model, Patton-Mallory (1996) developed a 3D FE model of single bolted connections with a 12.7 mm (0.5 in.)-diameter bolt. The connection geometries studied had aspect ratios ( $l/d$  = member thickness/bolt diameter) of 2, 5 and 7, and end distance ratios ( $e/d$  = end distance/bolt diameter) of 2, 4, and 7.

The configuration of the test was actually more like a full-hole bolt-embedment test rather than a single bolted connection test. The model did not include the slip behaviour from the side members, because these members were not considered. In respect to the complexity of modeling, this model had a simple load-transfer path, where loads applied directly at the end of the pin element were transferred to the wood element via contact elements. On this point, Patton-Mallory's model was insufficient to be regarded as a full 3D connection model. However, the analysis gave fairly good agreement between the

measured and predicted load-deformation curves, although the predicted load-deformation curves were always stiffer than the experimental curves.

Based on the Patton-Mallory's bolted connection model, Moses (2000) re-analyzed the same bolted connections using an anisotropic plasticity material model for wood. Moses' model showed improvement in the prediction of the load-deformation curve in the post-elastic region.

The models of Patton-Mallory and Moses appear to be the only 3D FE models for wood connection using a nonlinear 3D FE material model for the wood. However, it was found that these connection models could not be used for general application to a broader class of bolted or dowel connections. The wood material models, which they constructed with the standard uniaxial loading test-based material properties, did not work for small dowel connections involving highly localized crushing failure, (for example, failure found in the slip process of a nailed connection).

In terms of reality of 3D FE models, as they excluded modeling of side members, the effect of existence of side members on the results could not be assessed. Also, their analyses on the predictions for the load-deformation curves were not based on realistic deformed shapes. Their predicted deformations were different from the observed deformations in the real tests. The evidence was that the predicted deformed shape showed plastic bending of the bolt in the  $l/d = 2$  bolted connection, which should not occur in the connection with the ratio of  $l/d = 2$  as observed in the Patton-Mallory's experimental test (more details on this are given in section 7.3).

A full 3D FE connection model including the side members could be found in many composite laminated connection models (Guan et al. 2000 and 2001, Tserpes et al. 2001,

McCarthy et al. 2005). A full 3D FE model for wood connections, however, does not appear to have been developed yet.

Guan and Rodd's hollow-dowel connection model (Guan et al. 2000 and 2001) included solid wood members in their DVW reinforced composite laminates. This connection was a special case for 3D FE modeling, in that the linear elastic orthotropic model worked successfully, because the contribution of the wood members to the total deformation of the connection was relatively small. The special features of this connection design were that DVW resisted most of the dowel-embedding load and that the dowel was hollowed to increase ductility of the connection.

From this standpoint, the development of a full 3D nonlinear finite element model for a dowel-type wood connection was still needed for general applications. In particular, the analysis of nailed connections using a full 3D FE models has remained unexplored since the conventional approach to wood material models reviewed did not work for the 3D FE nailed connection model (Hong and Barrett 2006a, 2006b). The major reason for this was that the predicted stiffness behaviour was too high for the dowel-embedding behaviour. More explanations for this are provided in the following section, which reviews 2D FE connection models.

### **2.2.2 Two-dimensional finite element models of dowel-type wood connections**

There are two different approaches to two-dimensional finite element models of dowel-type wood connections, depending on the plane concerned (Figure 2.1). One type of model uses a plane parallel to the length of the dowel. This model should predict the lateral slip, the lateral resistance and the withdrawal behaviour in the connection. Previously, most mechanics-based models and FE models for dowel-type wood

connections were made in this plane, where the behaviour normal to the plane was ignored.

The other approach is to develop a model in a plane normal to the length of the dowel, with the assumption of uniform stress across the thickness of wood member when either very thin or very thick wood members can justify neglecting dowel bending. This 2D model has been used to predict the load-deformation behaviour, the effects of a pre-drilled hole, the stress distribution around a dowel, and dowel-embedding behaviour (Tsujimoto et al. 1986, Lessard et al. 1995, Kharouf 2001, Chen et al. 2003). Most of the models in this plane were developed for analysis of the bolted connection.

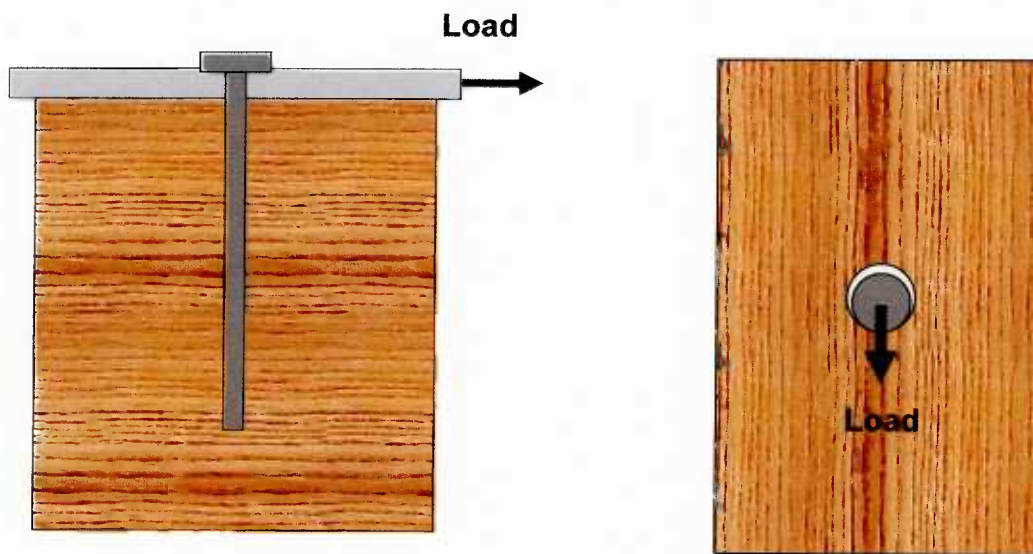


Figure 2.1 Planes related to modeling: a plane parallel to the length of the dowel (left), a plane normal to the length of the dowel (right).

The plane-dependent limitation to the modeling was that the predicted behaviour on the selected plane did not include any influences from the response in the other plane. This explains why the 3D FE model is needed for the dowel-type connection. Only the 3D model can overcome this limitation.

For nailed connections, the FE model has been developed only in a plane parallel to dowel length. Most of the 2D nailed connection models employed one-dimensional finite element approximations with the assumption of a beam on nonlinear foundation (Foschi 1974, Erki 1991, Ni 1997, He 2002). Basically, these models were nonlinear spring-based models. A pure 2D FE model, which would use plane elements and an explicitly defined material model, has not yet been developed for nailed connections.

The pure 2D FE model has only been studied for bolted connections in a plane normal to dowel length. Chen et al. (2003) did a plane stress analysis for a 16 mm-diameter dowel wood connection, with or without fiberglass reinforcement. This 2D model used two-dimensional tri-node elements and a linear elastic model for the wood. The uniqueness of the model was that they introduced a soft zone for the bolt-embedding area, in order to account for localized wood crushing behaviour. The soft zone was modeled by reducing the original elastic moduli of wood by a factor of 0.5. Although dimensions of the soft zone and the reduction factor of 0.5 were not clearly explained, the general approach took into account dowel-embedment behaviour in the FE model.

Using similar model geometry, a 2D FE model with a plasticity-based wood material model was developed by Kharouf (2001). This model can be regarded as a two-dimensional version of Moses' 3D FE model with the assumption of uniform stress along the member thickness. The major criticism of this model is that it gave an unacceptably high initial stiffness for the load-deformation curve. The high stiffness prediction was attributed to the standard uniaxial loading test-based modulus of elasticity (MOE) of wood, which was used for modeling the dowel-embedding region where the model of Chen et al. used the  $0.5 \times$  MOE for the soft zone.

Returning to the 3D FE models of Patton-Mallory and Moses, the predicted load-deformation curve showed relatively good agreement when compared with Kharouf's 2D FE model predictions, although the 3D FE models used the same standard uniaxial loading test-based MOE values. The reason for this may be found in unrealistic bolt bending in the 3D FE models. Erroneous energy dissipation due to unrealistic bolt bending compensated for the wood crushing behaviour under the dowel, thereby contributing to the matching of the predicted and observed load-deformation curves. However, Kharouf's 2D FE model, did not consider wood crushing behaviour, as Chen et al. (2003) did. Consequently, it is obvious that a prospective FE model of dowel-type connections should take into account localized wood crushing behaviour under the dowel.

## **CHAPTER 3. THREE-DIMENSIONAL MATERIAL MODEL FOR WOOD**

The finite element model chosen for this study uses solid elements to construct the actual shape of a dowel-type wood connection. The key challenge in implementing the model was the development of an appropriate wood material model to represent the complex nonlinear stress-strain behaviour of wood in the region surrounding a dowel-type connector.

Since there was no generally accepted 3D FE material model that described the complete nonlinear behaviour of wood, the primary focus of this study was to develop and validate the suitability of a wood material model that could be used to predict the behaviour of dowel-type connections.

An “anisotropic plasticity material model” was chosen, and the suitability of the previous models that have been reported in the literature was discussed.

### **3.1 Elasto-plastic, transversely isotropic material model for wood**

By accounting for permanent deformation and energy dissipation, the anisotropic plasticity material model has proven to be effective in 3D FE modeling of wood material (Moses, 2000). Bilinear stress-strain relationships were assumed in the three orthogonal directions of compression, tension and shear respectively. Based on each directional compressive constitutive relationship, the same bilinear stress-strain relationships were assumed in tension (Patton-Mallory 1996, Moses 2000, Kharouf 2001, Chen et al. 2003).

Although introducing the different yield stresses in tension is theoretically possible, it is usually abandoned because it causes a high chance of failing two criteria; the consistency equation and the closed yield surface requirement. Equation [3.1] defines the consistency equation of the anisotropic plasticity model that must be satisfied, due to the requirement of plastic incompressibility.

The yield strengths must also be satisfied, in order to maintain the elliptical cross section of the yield surface. Equation [3.2] provides the condition when an elliptical yield surface is defined (ANSYS, Inc. 2006). Details on the anisotropic plasticity model adopted in this study are presented in Appendix A.

Basically, the uniaxial yield strengths are interrelated by these the two aforementioned criteria, in theory. This means that all experimental yield strengths are not guaranteed for model application. Ideally, in order to apply the anisotropic plasticity theory for wood, the tensile and compressive yield stresses in the three principal directions should be determined using uniaxial loading tests. For most structural timber, especially, highly orthotropic species such as Hemlock, it cannot be assumed that these raw experimental yield strengths will always meet the criteria throughout the loading history.

To overcome this restriction, transverse isotropy was assumed and compressive-based stress-strain relationships were adopted for both tension and compression. These assumptions reduce the number of input parameters from six to two yield stresses for the three principal directions. This assumption also provided practical benefits, in terms of the cost of developing experimental data.

$$\frac{\sigma_{+1} - \sigma_{-1}}{\sigma_{+1}\sigma_{-1}} + \frac{\sigma_{+2} - \sigma_{-2}}{\sigma_{+2}\sigma_{-2}} + \frac{\sigma_{+3} - \sigma_{-3}}{\sigma_{+3}\sigma_{-3}} = 0 \quad [3.1]$$

$$A_{11}^2 + A_{22}^2 + A_{33}^2 - 2(A_{11}A_{22} + A_{22}A_{33} + A_{11}A_{33}) < 0 \quad [3.2]$$

$$A_{ii} = \frac{K}{\sigma_{+i}\sigma_{-i}}, \quad (i = 1, 2, 3) \quad [3.3]$$

Where,

$\sigma_{+i}$  and  $\sigma_{-i}$  = yield stresses in tension (+) and compression (-), respectively

K = material parameter

### 3.2 Determination of wood material parameters

Figure 3.1 defines the directions and sections in wood that are used to describe wood as an orthotropic material. A bilinear normal stress-strain curve and the relevant material constants in the three principal directions are shown in Figure 3.2.

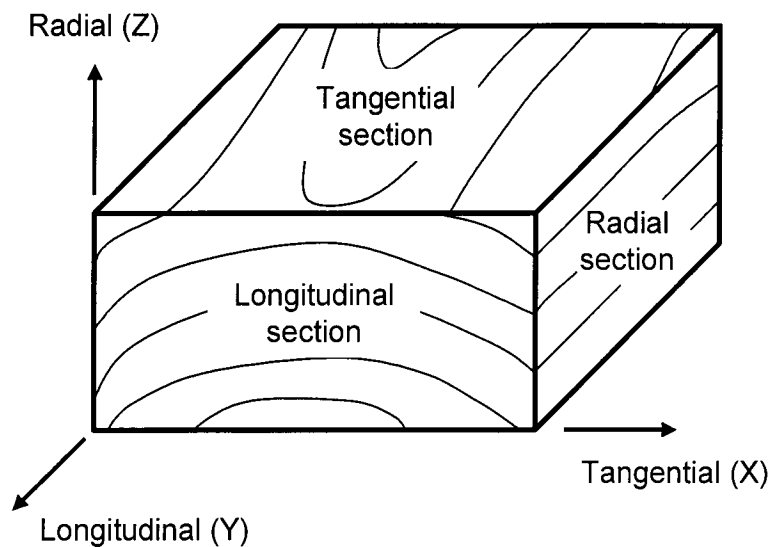


Figure 3.1 Three principal directions and sections in wood.

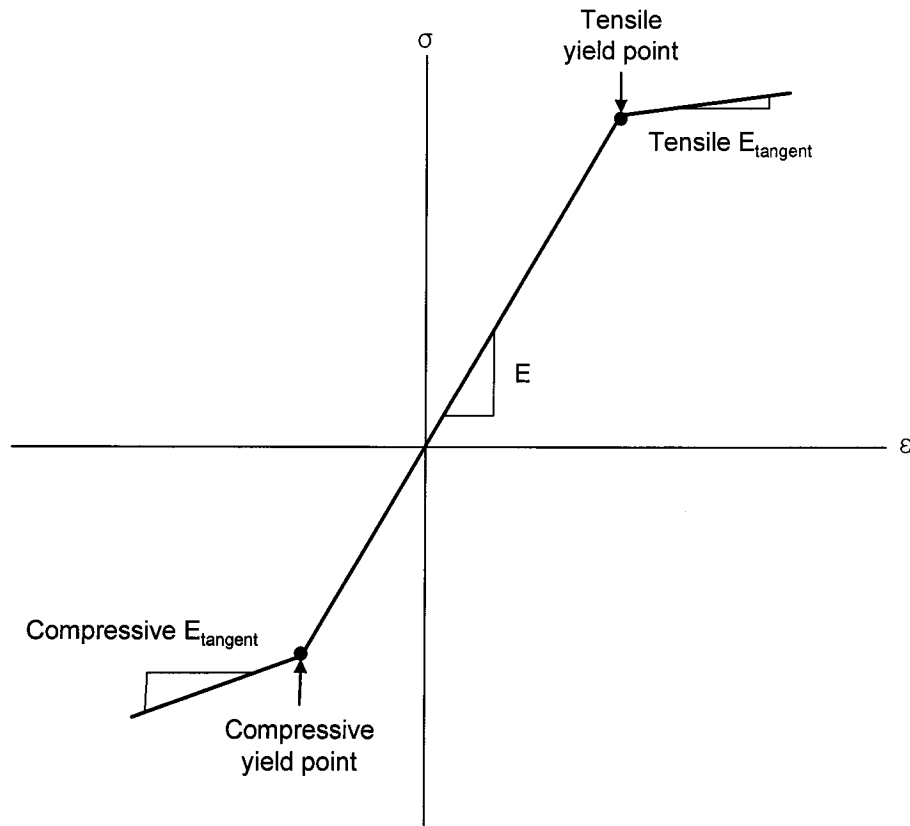


Figure 3.2 Bilinear normal stress-strain relationships in the anisotropic plasticity model.

A generalized 3D FE anisotropic plasticity material model with bilinear stress-strain relationships requires the following 27 material constants:

- Elastic moduli in X-, Y- and Z-directions.
- Tensile tangent moduli in X-, Y- and Z-directions.
- Compressive tangent moduli in X-, Y- and Z-directions.
- Tensile yield stresses in X-, Y- and Z-directions.
- Compressive yield stresses in X-, Y- and Z-directions.
- Shear elastic moduli in XY-, YZ- and XZ-directions.
- Tangent shear moduli in XY-, YZ- and XZ-directions.
- Shear yield stresses in XY-, YZ- and XZ-directions.
- Poisson's ratios in XY-, YZ- and XZ-directions.

In the wood material model developed here, the assumptions of transverse isotropy and compressive-based stress-strain relationships reduced the number of material constants from 27 to 14. The average values of the tangential and radial material constants were used to represent the perpendicular to grain material constants. The tension material constants were set equal to the compressive constants. The shear material constants were determined theoretically using the functions of the parallel and perpendicular to grain material constants, instead of using purely experimental values. The tangent moduli of compression and shear were calculated by applying the multiplier of 0.01 to the elastic modulus to include work-hardening behaviour.

Eventually, this process for determining the material constants required four independent material constants, excluding the Poisson's ratios. The four material constants were the elastic MOE and yield stress in both the parallel and perpendicular to grain directions, respectively. More details on the procedures for determining each material constant are presented in the following sections and summarized in Table 3.1.

Table 3.1 Procedures for determining the material constants of the 3D FE model for wood and wood foundation.

Requisite constant	Direction <sup>1</sup>	Method of determination
Elastic modulus	X, Y, Z	Compression test or dowel embedment test
Elastic shear modulus	XY, YZ, XZ	Coupled bilinear constitutive model <sup>2</sup>
Poisson's ratio	XY, YZ, XZ	Average values from the Wood Handbook
Tensile yield stress	X, Y, Z	Equal to compressive properties
Tensile tangent modulus	X, Y, Z	Equal to compressive properties
Compressive yield stress	X, Y, Z	Compression test or dowel embedment test
Compressive tangent modulus	X, Y, Z	0.01 × elastic modulus
Shear yield stress	XY, YZ, XZ	Coupled bilinear constitutive model <sup>2</sup>
Shear tangent modulus	XY, YZ, XZ	0.01 × elastic shear modulus

<sup>1</sup> Y=parallel to grain and X=Z=perpendicular to grain.

<sup>2</sup> Calculated values by theoretical relationships with the normal material constants. see section 3.2.2 for details.

### 3.2.1 Modulus of elasticity and the yield stress

The connection model developed in this study employed two different sets of wood material constants; one for original wood and the other for a wood foundation that accounts for wood crushing behaviour under a dowel. Accordingly, two different test methods were required to define the MOEs for the corresponding material model.

For the original wood material model, ASTM D 143 parallel and perpendicular to grain compression tests were used to determine the conventional MOEs and the associated yield stresses. The moduli for wood foundation material were determined from dowel-embedment tests that conformed to ASTM D 5764 in parallel and perpendicular to grain directions. Both tests provided load-deformation (embedment) curves. In order to determine the modulus and the yield stress, bilinear curve fitting was

then applied to the experimental stress-strain curves, which was converted from the load-deformation (embedment) curve (Figure 3.3).

The tangent modulus was taken as 0.01 times the initial modulus, and the break point of the bilinear curve was chosen as a yield point. The assumption of  $0.01 \times$  initial modulus for tangent modulus may not be reasonable in perpendicular to grain direction since the actual tangent modulus was usually higher than  $0.01 \times$  initial modulus (see Figure 4.15). However, it was found empirically that the use of the same fixed fraction of initial modulus for the parallel, and perpendicular to grain tangent modulus provided good solution convergence beyond the elastic behaviour. Otherwise, the chance of obtaining a solution in an incremental step became very low.

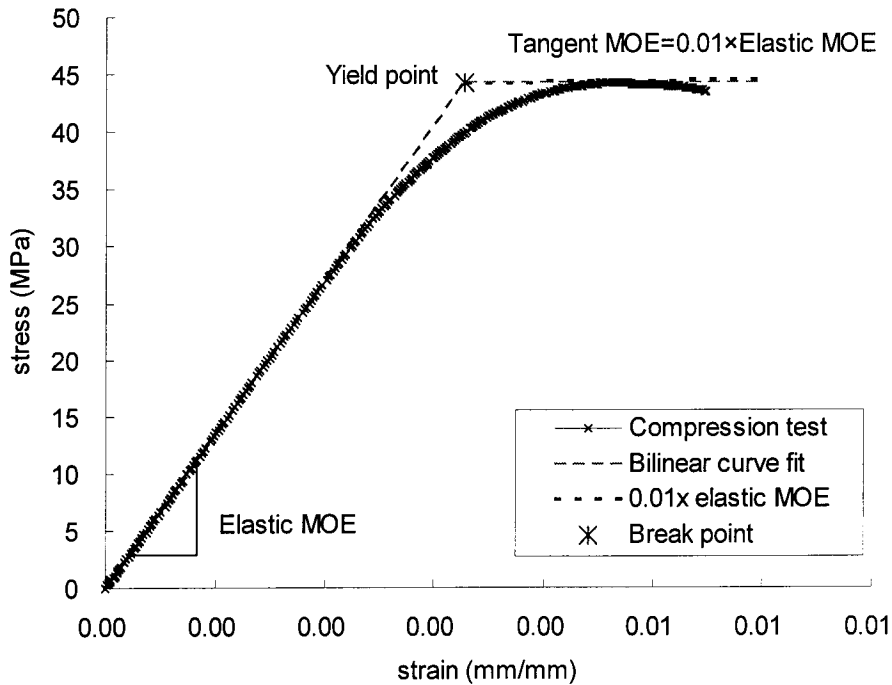


Figure 3.3 An example of a bilinear stress-strain curve fitting to an experimental curve; the yield point should be defined at the break point.

### **3.2.2 Elastic shear modulus and shear yield strain**

Saliklis et al. (2003) developed a theoretical model to estimate the bilinear shear stress-strain curve using known axial material properties. This model can easily be implemented in finite element applications.

In the current study, this theoretical estimation of shear constants was used to determine the elastic shear modulus and the shear yield strain for the wood and wood foundation material models. Introduction of the theoretical shear constants to the wood foundation material model was necessary since there was no method to evaluate the wood foundation shear constants under the dowel-embedment testing. Based on Saliklis et al.'s work (2003), the following equations were employed to calculate the theoretical shear constants.

- Initial shear modulus

$$G_{TL}, G_{LT} = \frac{\sqrt{E_L \cdot E_T}}{2 \cdot (1 + \sqrt{\nu_{TL} \cdot \nu_{LT}})} \quad [3.4]$$

$$G_{TT} = \frac{\sqrt{E_T \cdot E_T}}{2 \cdot (1 + \sqrt{\nu_{TT} \cdot \nu_{TT}})} = \frac{E_T}{2 \cdot (1 + \nu_{TT})} \quad [3.5]$$

- Shear strain

$$(\gamma_y)_{TL}, (\gamma_y)_{LT} = \frac{(\sigma_0)_T}{2 \cdot (E_T - (E_t)_T)} \cdot \sqrt{\frac{E_T}{G_{TL}}} \quad [3.6]$$

$$(\gamma_y)_{TT} = \frac{(\sigma_0)_T}{2 \cdot (E_T - (E_t)_T)} \cdot \sqrt{\frac{E_T}{G_{TT}}} \quad [3.7]$$

Where,

$L$  = (subscript) parallel to grain direction (or longitudinal)

$T$  = (subscript) perpendicular to grain direction (or transverse)

$E$  = Initial modulus; compressive MOE or foundation modulus [MPa]

$E_t$  = Tangent modulus ( $0.01 \times E$ ) [MPa]

$G$  = shear modulus [MPa]

$\nu$  = Poisson's ratio

$\gamma_y$  = shear yield strain in bilinear shear stress-strain curve [mm/mm]

$\sigma_0$  = stress intercept in bilinear normal stress-strain curve [MPa]

### 3.2.3 Poisson's ratio

Owing to the assumption of transverse isotropy, two independent Poisson's ratios ( $\nu_{LT}$  and  $\nu_{TT}$ ) and one calculated Poisson's ratio ( $\nu_{TL}$ ) were required for the wood material model. The independent ratios,  $\nu_{LT}$  and  $\nu_{TT}$ , averaged for transverse plane were taken from the Wood Handbook (Forest Products Laboratory 1999).

Using the known  $\nu_{LT}$ , the Poisson's ratio of  $\nu_{TL}$  was determined using Equation [3.8], in order to meet the symmetry requirement for the stiffness matrix. The same Poisson's ratios were used for the wood foundation model. These ratios were assumed to remain constant, regardless of the plastic response.

$$\nu_{TL} = \nu_{LT} \cdot (E_T / E_L) \quad [3.8]$$

#### 3.2.4A spreadsheet tool for generating a code of wood material model

With the six independent wood material constants of MOEs ( $E_L$ ,  $E_T$ ), yield stresses ( $(\sigma_L)_y$ ,  $(\sigma_T)_y$ ) and Poisson's ratios ( $\nu_{LT}$  and  $\nu_{TT}$ ), all other dependent material constants could be obtained using the procedures shown in Table 3.1.

In order to facilitate preparation of the code of the FE material models, a tool was developed using an EXCEL<sup>®</sup> spreadsheet. Having received user input for the six independent constants, the spreadsheet was programmed to check the two criteria (Equations [3.1] and [3.2]) up to 50% plastic strain and, then, generate the dependent constants. Finally, the ANSYS material input code was produced for the ANSYS input file. The interface of the spreadsheet is shown in Appendix B.

## CHAPTER 4. COMPRESSION TEST AND MODEL VALIDATION

Compression tests were conducted to obtain compressive MOE and compressive yield stress for the empirical wood material model developed in this study. This chapter describes the experimental compression tests and the model suitability. Emphasis was placed on the effect of the test methods on the determination of the material constants and on the choice of the appropriate material constants for the subsequent FE modeling.

### 4.1 Compression test

#### 4.1.1 Specimen preparation

Three pieces of 105 mm (width)  $\times$  105 mm (depth)  $\times$  4000 mm (length) dry Douglas-fir (*Pseudotsuga menziesii*) with average moisture content of 14.5%, were used as the source for compression test specimens (Table 4.1). These lumber specimens were carefully selected to have flat growth rings that were parallel to one of the faces of the specimen.

To match sampling for other test programs, including the nail embedment test and the single nail connection test, the same number of compression test specimens were cut from each lumber specimen. The remnants of each sample piece were numbered and saved for other test programs. A typical cutting pattern is illustrated in Appendix C.

ASTM D 143 provides primary and secondary methods for determining compression parallel to grain strength properties. The specimen for the secondary method had the dimensions of 25 $\times$ 25 $\times$ 100 mm (1 $\times$ 1 $\times$ 4 in.), whereas the specimen for the primary

method was 50×50×200 mm (2×2×8 in). In this study, using the secondary method, the 50×50×200 mm (1×1×4 in.) compression specimens were prepared for longitudinal, radial and tangential direction tests (Figure 4.1). Herein, this specimen was called “1×1×4” specimen.

For perpendicular to grain compression, conventional ASTM D 143, 50×50×150 mm (2×2×6 in.) test specimens (called “2×2×6” specimen) were also prepared (Figure 4.3). The summary of test specimens is presented in Table 4.2.

Table 4.1 Basic mechanical properties of Douglas-fir lumber.

Lumber sample number	Moisture content* [%]	Specific Gravity** [ ]	Bending MOE** [GPa]
1	14.4	0.481	10.5
2	14.3	0.538	13.1
3	14.5	0.585	14.7
Mean	14.4	0.535	12.8

\* Measured by the Delmhorst® 2-pin moisture meter.

\*\* Measured by the Metriguard® 340 E transverse vibration system.



Figure 4.1 Douglas-fir specimens for the 25×25×100 mm (1×1×4 in.) compression tests in longitudinal, radial and tangential direction (from left).

#### 4.1.2 Test methods

##### 4.1.2.1 Parallel to grain compression

ASTM D 143 parallel to grain uniaxial compression tests were conducted with the 25×25×100 mm (1×1×4 in.) prismatic specimen. Deformation measurements were made using a jig with a direct current differential transformer (DCDT) (Figure 4.2).

Deformation was measured over a gauge length of 50 mm. A SINTECH test system was used to apply continuous compression loading at the rate of 0.6 mm/min. on a full cross section of the specimen, so that it induced uniform compressive stress over the specimen.

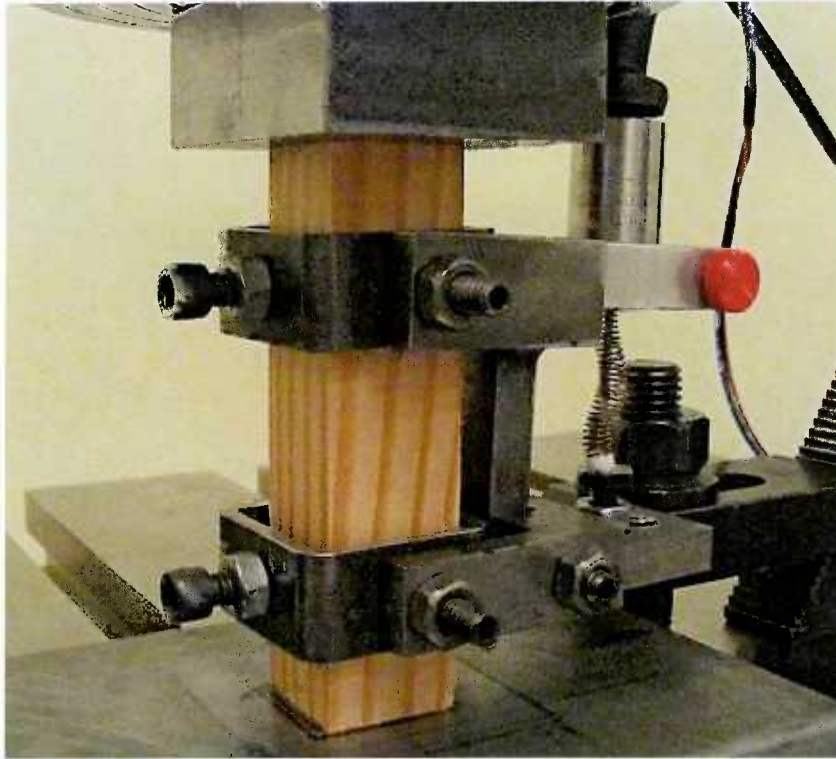


Figure 4.2 Compression test setup for the 25×25×100 mm (1×1×4 in.) prismatic specimen.

#### 4.1.2.2 Perpendicular to grain compression

Perpendicular to grain compression tests were conducted using a 25×25×100 mm (1×1×4 in.) specimen in radial and tangential directions. The conventional ASTM D 143, perpendicular to grain compression test was also conducted on a 50×50×150 mm (2×2×6 in.) specimen.

For the conventional perpendicular to grain compression test, the load was applied through a 50.0 mm (width) × 63.5 mm (depth) × 50.0 mm (height) (2 × 2.5 × 2 in.) steel bearing block, which provided a loading contact area of 50×50 mm, (4 in.<sup>2</sup>) placed at the centre of the specimen (Figure 4.3). The test jig for obtaining deformation included a pivoting rod connected to two perpendicular arms interacting with brackets on opposite

sides of the steel bearing block. At the far end of one of these arms, a single DCDT was used to obtain average compression deformation.

A SINTECH test system applied the load at a rate of 0.6 mm/min. It should be noted that the conventional perpendicular to grain compression test used a partial contact loading area, which caused non-uniform stress in the specimen and a combined crushing and shear failure at the edges of the steel bearing block.

#### 4.1.2.3 Definitions of compressive MOE and yield stress

The load-deformation curve obtained from the experiment was converted to a stress-strain curve for obtaining the MOE and yield stress. The stress and strain were calculated according to Equation [4.1] and Equation [4.2], respectively. A bilinear curve was fitted to the stress-strain curve. The initial slope of the bilinear curve was taken as the compressive MOE, and the stress at the breaking point of the bilinear curve was designated as a yield point (see Figure 3.3).

- Stress = applied load / loading contact area [4.1]

- Strain =  $\frac{\text{DCDT displacement reading}}{\text{original (gauge) length along the center line of loading}}$  [4.2]

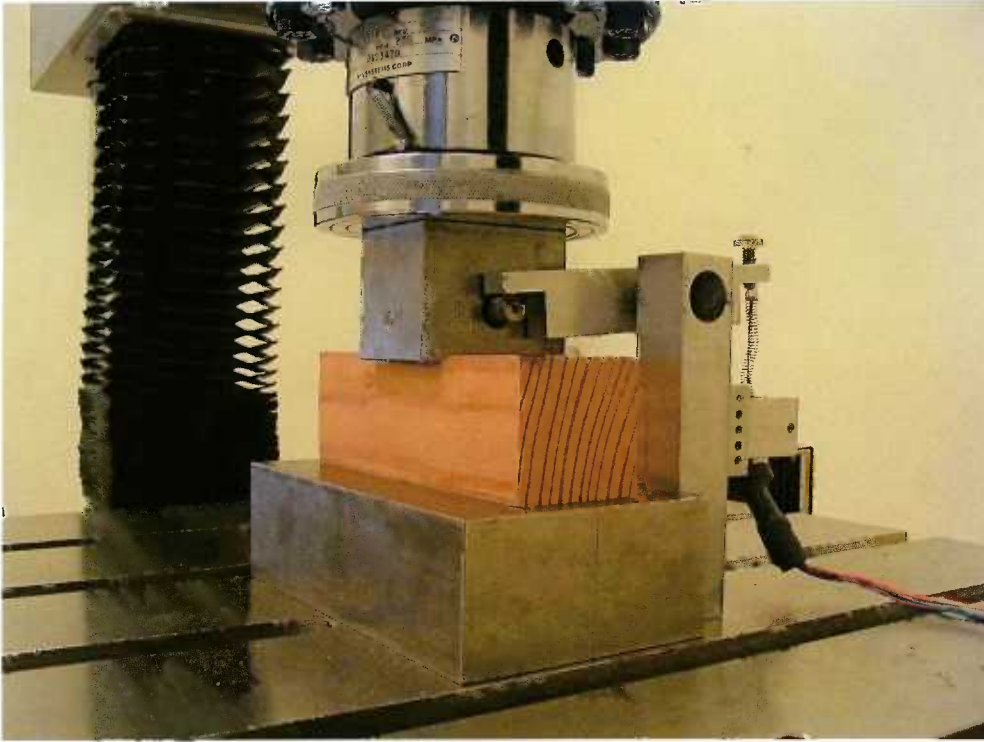


Figure 4.3 The conventional ASTM D 143 perpendicular to grain compression test.

#### 4.1.3 Results and discussion: Material constants of Douglas-fir<sup>2</sup>

Table 4.2 summarizes the MOE values and yield stresses obtained from the compression tests for the Douglas-fir specimens. For parallel to grain material constants, the average MOE of 16,900 MPa and average yield stress of 44.2 MPa were obtained from the  $1 \times 1 \times 4$  compression tests.

Compared with the  $1 \times 1 \times 4$  tangential compression results, the conventional perpendicular to grain compression test ( $2 \times 2 \times 6$  test) results showed significantly higher MOE and yield stress. The yield stress of the  $2 \times 2 \times 6$  specimen (10.3 MPa) was 114% higher than that of the  $1 \times 1 \times 4$  specimen (4.81 MPa). If, for comparison, averages of the

---

<sup>2</sup>  $1 \times 1 \times 4$  tests and  $2 \times 2 \times 6$  test represent the compression tests using  $25 \times 25 \times 100$  mm specimen and  $50 \times 50 \times 150$  mm specimen, respectively.

radial and tangential data from the  $1 \times 1 \times 4$  compression tests were used as the perpendicular to grain material constants, the two different test methods made little difference in MOE (average 832 MPa for the  $1 \times 1 \times 4$  perpendicular to grain MOE versus 835 MPa for the  $2 \times 2 \times 6$  perpendicular to grain MOE). However, there was still a large difference in the yield stress, depending on the test method (average 4.45 MPa for the  $1 \times 1 \times 4$  perpendicular to grain yield stress versus 10.3 MPa for the  $2 \times 2 \times 6$  perpendicular to grain yield stress).

Currently, there is no specific ASTM procedure for determining MOE and yield stress in the perpendicular to grain direction. The conventional  $2 \times 2 \times 6$  ASTM D 143 perpendicular to grain compression test was originally devised for determining standardized compression strength rather than material properties, such as MOE and yield stress.

The validity of this test method for determining material properties has, therefore, been challenged due to the non-uniform stress distribution induced by partial contact loading (Korin 1990, Leicester et al. 1998, Madsen 2000, Blass et al. 2004). The major difference between the two test methods arises because of the local crushing and shear failure at the edges of the load bearing block, which always happens in compression test with a partial loading contact area, in the  $2 \times 2 \times 6$  test.

The MOE and yield stress determined from the  $1 \times 1 \times 4$  uniformly stressed test specimens produced more valid wood material constants. However, data from the conventional ASTM perpendicular to grain test standard, which has a philosophy that the test method should simulate in-service use as closely as possible, may be more effective for practical applications. It is important to note that the previous nonlinear wood

material models developed by others (Patton-Mallory 1996, Moses 2000, Kharouf 2001) used the 2×2×6 specimens for perpendicular to grain compression to develop the material properties for their models.

For comparison purposes, two material models for wood that employed the two different compression perpendicular to grain test data sets were used in this study. Validation studies were then conducted, in order to assess the influence of the choice of material properties on predicted load-deformation behaviour.

Table 4.2 Compressive MOEs and yield stresses from the 25×25×100 mm (1×1×4 in.) test and the conventional standard 50×50×150 mm (2×2×6 in.) perpendicular to grain test for Douglas-fir.

Test program	Dimension of specimen [mm]	Loading direction	Repetition*	Compressive MOE (cov) [MPa]	Yield stress (cov) [MPa]	Wood Handbook MOE /Strength [MPa]
Parallel to grain compression	25×25×100	Longitudinal	45	16,900 (11.6%)	44.30 (11.4%)	14,900 /50.0
		Radial	45	923 (44.0%)	4.08 (22.7%)	
Perpendicular to grain compression	25×25×100	Tangential	45	740 (43.2%)	4.81 (28.5%)	883
		mean	-	832 (45.1%)	4.45 (27.5%)	/6.0
	50×50×150	Tangential	12	835 (39.3%)	10.30 (31.0%)	

\* Fifteen 25×25×100 mm samples and four 50×50×150 mm samples per each lumber specimen.

## 4.2 Validation of FE material model

Three-dimensional finite element models for the compression tests were developed using the finite element analysis (FEA) software package, ANSYS ver.8.0. The compressive behaviour of wood observed in the tests was simulated using the wood material model containing the material properties developed in the experimental program.

### 4.2.1 Wood material models

Using two sets of the perpendicular to grain material constants from the 1×1×4 test and the 2×2×6 tests, two wood material models, called “WOOD11” and “WOOD22”, respectively, were coded for ANSYS material model inputs<sup>3</sup>. Table 4.3 shows the material constants for the two wood material models, which were established through the process in Table 3.1. Note that the computed shear constants and the computed Poisson’s ratio,  $\nu_{TL}$ , should also be changed according to the perpendicular to grain MOE selected.

---

<sup>3</sup>Note: WOOD11 properties were developed from the 1×1×4 specimen only. However, WOOD22 properties included the 2×2×6 perpendicular to grain compression test data.

Table 4.3 Material constants of 3D FE material model for Douglas-fir.

Material constant*	WOOD11	WOOD22
Elastic MOE: L [MPa]	16,900	16,900
Elastic MOE: R / T [MPa]	832 / 832	835 / 835
Elastic shear modulus: RL / LT [MPa]	1,740 / 1,740	1,550 / 1,550
Elastic shear modulus: RT [MPa]	301	302
Poisson's ratio: RL	0.018	0.023
Poisson's ratio: LT	0.37	0.37
Poisson's ratio: RT	0.38	0.38
Compressive, tensile yield stress: R / L / T [MPa]	4.5 / 44.3 / 4.5	10.3 / 44.3 / 10.3
Compressive, tensile tangent modulus: R / L / T [MPa]	8.3 / 169 / 8.3	8.4 / 169 / 8.4
Shear yield stress: RL / LT / RT [MPa]	3.2 / 3.2 / 1.3	7.0 / 7.0 / 3.1
Shear tangent modulus: RL / LT / RT [MPa]	17.4 / 17.4 / 3.0	15.5 / 15.5 / 3.0

\* L= longitudinal, R= radial and T= tangential.

#### 4.2.2 General description of the 3D FE model for wood compression

SOLID45 (from ANSYS, Inc.) is a three-dimensional eight-noded, quadrilateral isoparametric brick element that has three degrees of freedom at each node; and, these elements were used for creating the prismatic wood specimen model and the steel bearing block model. The shape function used for the solid element is given in Equation [4.3].

$$\text{shape functions, } N_i = \frac{1}{8}(1 \pm \xi)(1 \pm \eta)(1 \pm \zeta) \quad [4.3]$$

Where,

$i$  = node number, 1,2,3,4,5,6,7 and 8

$\xi$ ,  $\eta$ , and  $\zeta$  = natural coordinate

In order to simulate real test conditions as closely as possible, the wood compression model included a steel bearing block, and the displacement-controlled loading was defined at the top surface (Figure 4.4, Figure 4.5). This approach was chosen to investigate the capability of the model to simulate the local crushing failure at the steel-to-wood contact zone. Thus, all the contact surfaces between the steel block and wood specimen were modeled with surface-to-surface contact elements (CONTA174 and TARGE170 from ANSYS, Inc.). The coefficient of friction for the contact interface was assigned a value of 0.7, which was generally reported for FE implementation in wood applications (Smith 1983).

For the steel material model, elastic-perfectly plastic behaviour was assumed with an MOE of 200 GPa, yield stress of 250 MPa and Poisson's ratio of 0.3. Mesh convergence was identified for all the compression models by checking the convergence of the simulated load-deformation curves through the process of mesh enrichment (or the  $h$ -refinement process) (Zienkiewicz et al. 1991).

The nodes on the bottom surface of the model were fixed for the boundary condition. Initially, the restraint of the nodes had been applied only in the loading direction (Y-direction). However, it caused rotation of the entire model. Thus, zero-displacements in X- and Z-directions were also set for specific nodes. The additional restraint did not influence the final results. (Note that, herein X-, Y-, and Z-directions are the coordinates of the global coordinate system).

For construction of the simulated load-deformation curve, the Y-directional reaction at the boundary nodes was summed; and, the deformation was obtained from the specified Y-directional nodal displacement. For the  $1 \times 1 \times 4$  specimen model, the two nodes at the

ends of the 50-mm gauge were selected to calculate the contraction within the gauge length. For the  $2 \times 2 \times 6$  specimen model, the displacement of the centre node on the top surface of the wood specimen was chosen for deformation analysis.

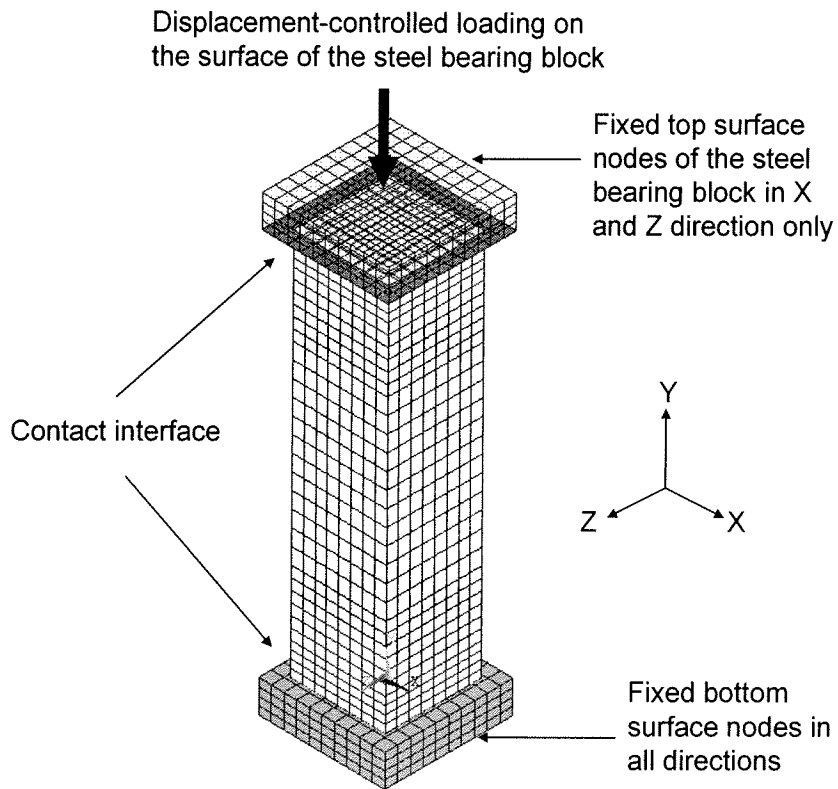


Figure 4.4 Three-dimensional FE model for the  $1 \times 1 \times 4$  compression test.

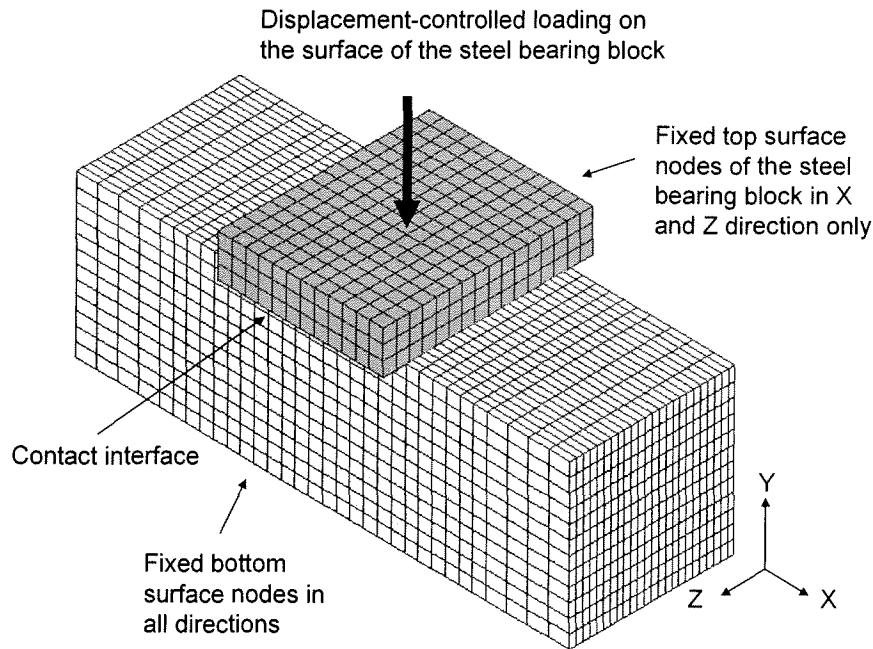


Figure 4.5 Three-dimensional FE model for the  $2 \times 2 \times 6$  compression perpendicular to grain test.

### 4.2.3 Simulation of the $1 \times 1 \times 4$ parallel to grain compression

For the parallel to grain compressive load-deformation curve, both material models showed very good agreement with the experimental average bilinear curve (Figure 4.6). However, as expected, the simulated curves showed acute elastic-plastic transition compared to the more gradual experimental transition. As long as the assumption of a bilinear stress-strain relationship was adopted, the acute transition was inevitable.

Overall, the deformed shape of the model agreed with the observed deformation. Figure 4.7 and Figure 4.8 show the non-uniform plastic strain contours in the longitudinal direction, including zones with an orientation of 45 degrees from the middle

of the specimen. This is a notable finding, because it agreed well with the fact that most of the test specimens failed with a 45-degree failure line (Figure 4.9).

In terms of model reality, the boundary condition used in this simulation was “as-is”, in that the inclusion of the steel bearing blocks provided the real loading condition for the wood component of the model. The issue of the loading condition has been controversial, because the analysis results vary depending on the assumed boundary conditions in 2D and 3D FE implementation (Tsujiimoto et al. 1986, Chen et al. 2003). The as-is condition used here eliminates this kind of issue.

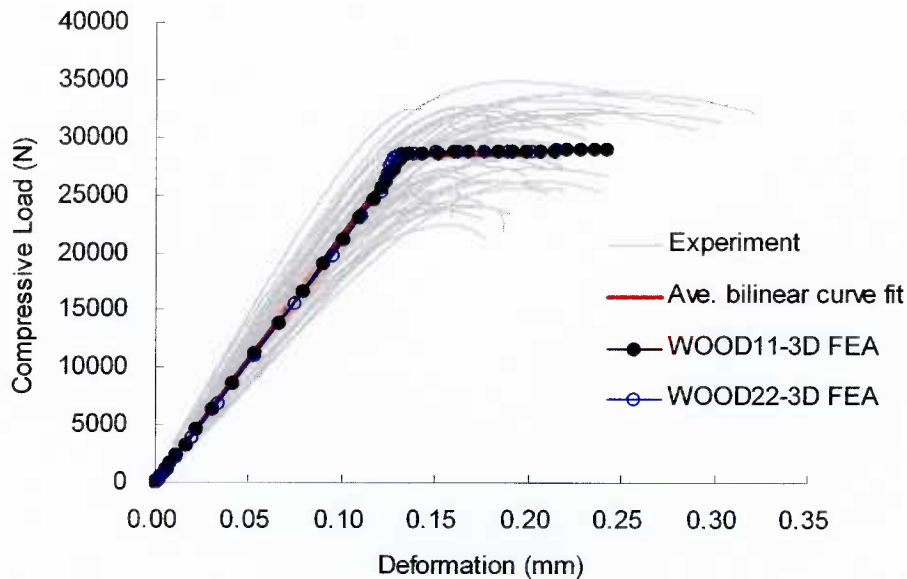


Figure 4.6 Simulated load-deformation curves of parallel to grain compression.

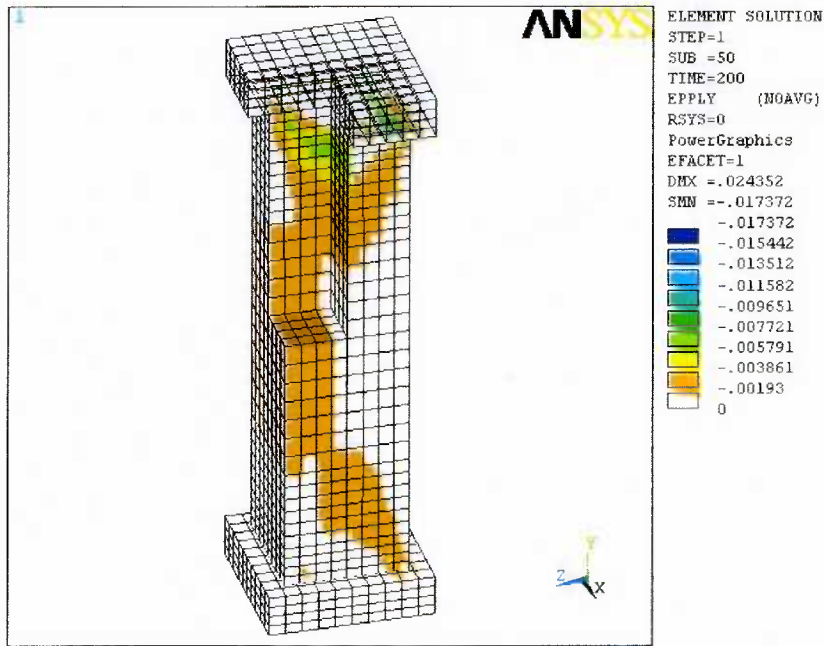


Figure 4.7 Simulated longitudinal plastic strain contour of the  $1 \times 1 \times 4$  parallel to grain compression using the WOOD11 model.

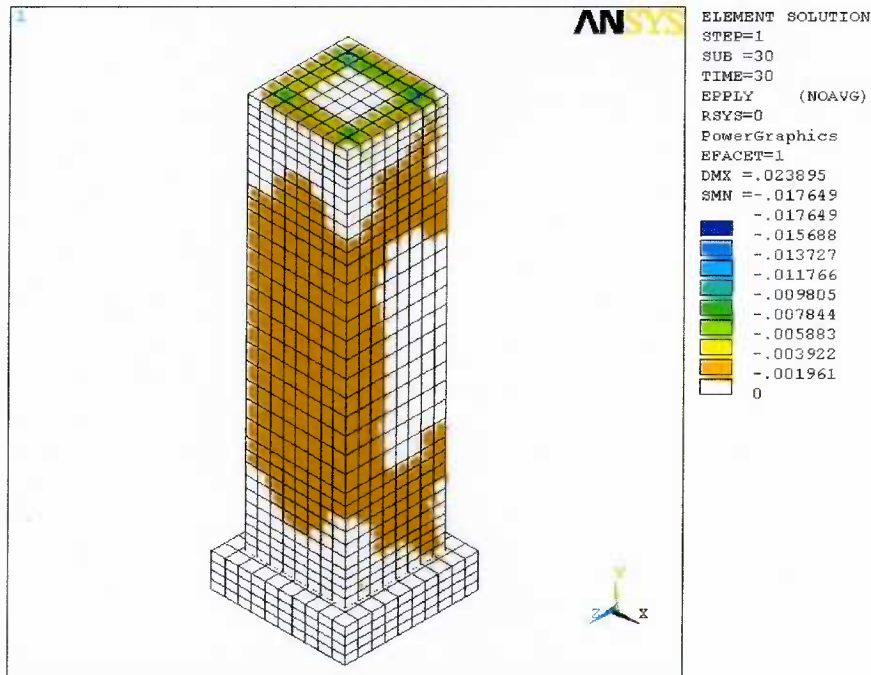


Figure 4.8 Simulated longitudinal plastic strain contour of the  $1 \times 1 \times 4$  parallel to grain compression using the WOOD22 model. The upper steel block was omitted.

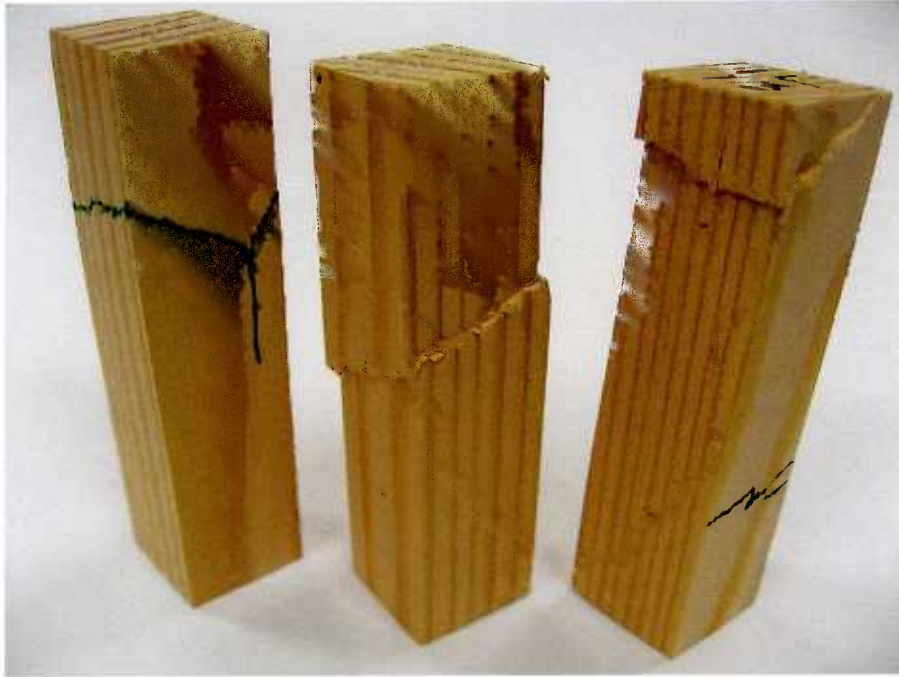


Figure 4.9 Compressive failure of the  $1 \times 1 \times 4$  parallel to grain specimen. For visibility, excessive load was also applied to the failed specimen.

#### 4.2.4 Simulation of the $1 \times 1 \times 4$ perpendicular to grain compression

The simulated load-deformation curve using the WOOD11 material properties showed good agreement with the perpendicular to grain experimental data (Figure 4.10). The model with the WOOD22 material properties gave good agreement only in the initial stiffness response.

The simulated yield load using WOOD22 was too high (6,640 N) compared to the experimental yield load (2,950 N). The different input of the perpendicular to grain yield stress for WOOD11 and WOOD22 (4.5 MPa and 10.3 MPa, respectively) was directly reflected in the difference of the simulated yield load.

The difference of the yield stress influenced the deformation pattern. As shown in Figure 4.11 and Figure 4.12, compared to the WOOD22 deformation of 4 mm, the WOOD11 deformation revealed severe contraction and a slight bulge in the middle of the

specimen. The deformation based on the WOOD22 material properties tended to buckle rather than bulge out. In fact, the contour of the WOOD22 case, shown in Figure 4.12, could also be found in the WOOD11 contour when the WOOD11 specimen was partially plasticized at a low displacement-load sub-step. Figure 4.13 shows the progress of the plastic contour of the model using the WOOD11 material properties.

The higher yield stress input for WOOD22 created the tendency for the specimen to buckle. The WOOD22 deformation seemed to agree with the phenomenological deformation of the real specimen, since most of the test specimens showed the buckling behaviour illustrated in Figure 4.14. However, it was thought that the buckling was due to a crooked grain in the real test specimen, which was not considered in the model specimen. For the tangential test specimen especially, the buckling direction was guided by the arc of the grain along the length of the specimen. This buckling behaviour also explains why the experimental curves of the  $1 \times 1 \times 4$  perpendicular to grain compression showed inconsistent tails in the post-elastic region with high variability (Figure 4.10). Indeed, the effect of the grain slope has been one of the difficulties in the FE macroscopic modeling of wood.

Assuming that, ideally, the grain in the real specimen was straight, the WOOD11 deformation would be a more realistic pattern than the WOOD22 deformation, because the fully plastic behaviour in the middle of the specimen conformed to a band of crushing wood cells, which is usually observed in wood under uniform compression in the perpendicular to grain direction.

Use of the WOOD22 material properties was abandoned in subsequent studies, because the high yield stress input turned out to be invalid in the simulated perpendicular to grain load-deformation curve (Figure 4.10).

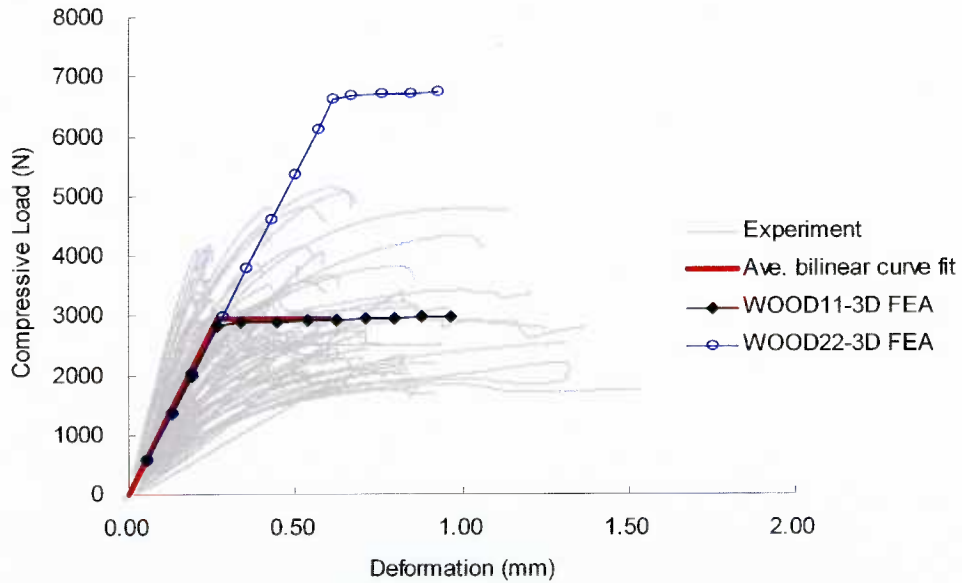


Figure 4.10 Simulated load-deformation curves of the 1x1x4 perpendicular to grain compression.

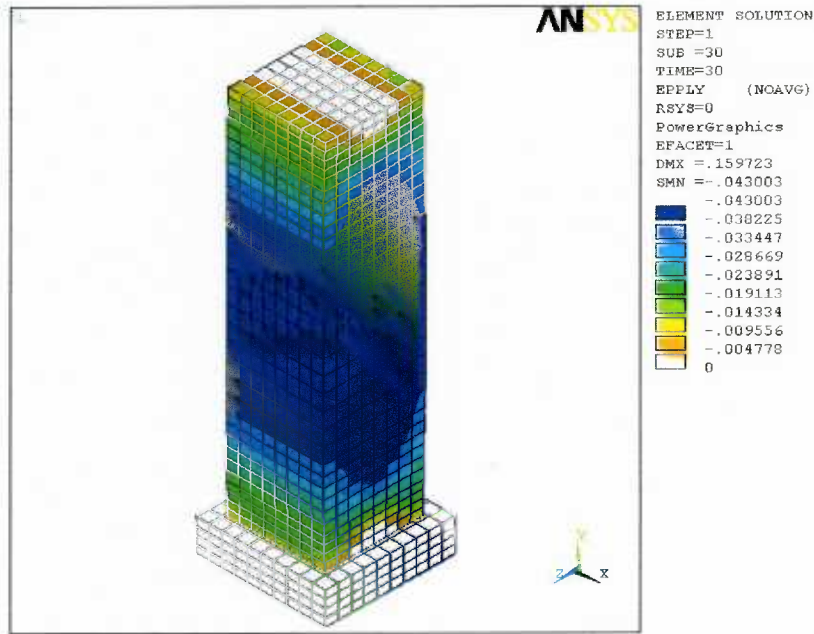


Figure 4.11 Simulated longitudinal plastic strain contour of the  $1 \times 1 \times 4$  perpendicular to grain compression at 4 mm-displacement load level using the WOOD11 model.

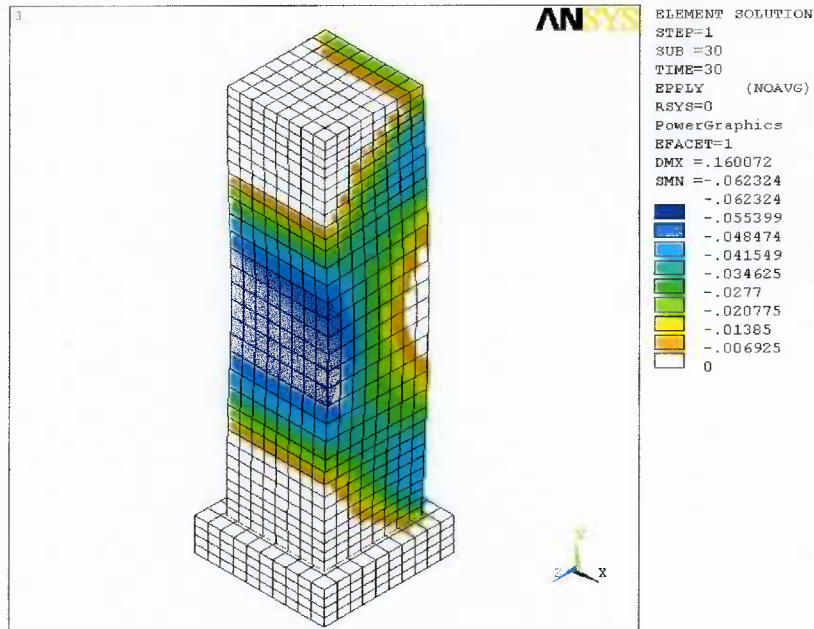


Figure 4.12 Simulated longitudinal plastic strain contour of the  $1 \times 1 \times 4$  perpendicular to grain compression at 4 mm-displacement load level using the WOOD22 model.

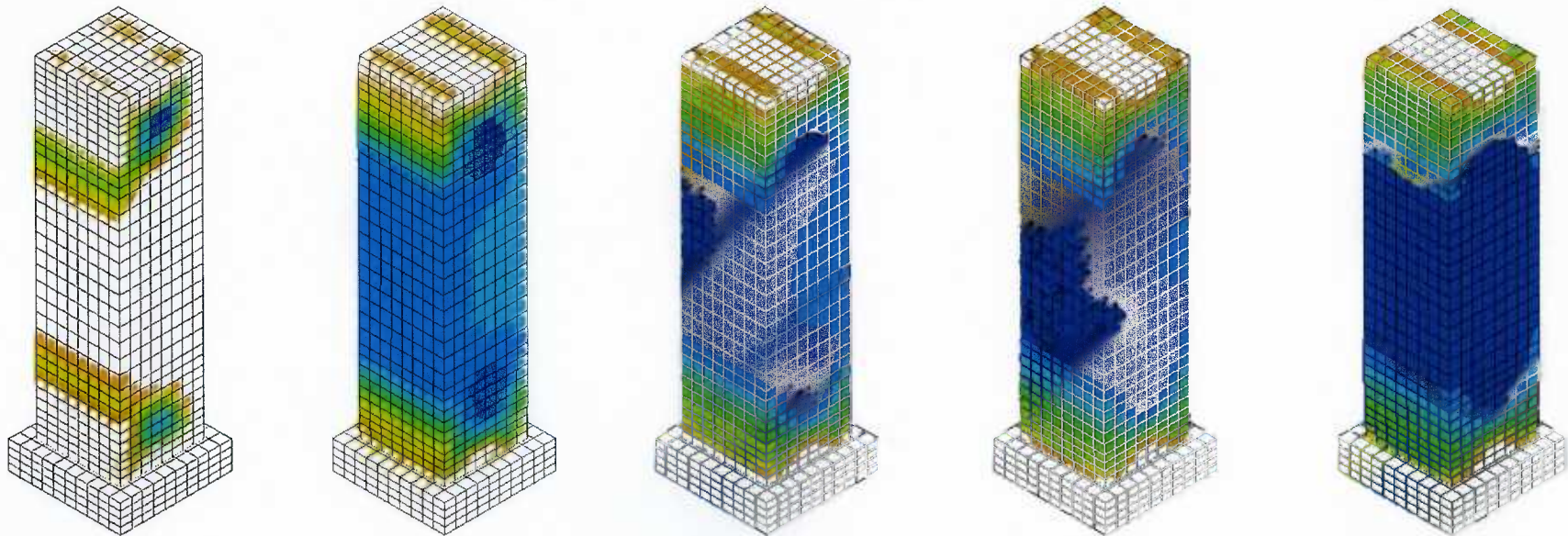


Figure 4.13 Progress of longitudinal plastic strain contour under the perpendicular to grain compression, simulated using the WOOD11 material model.

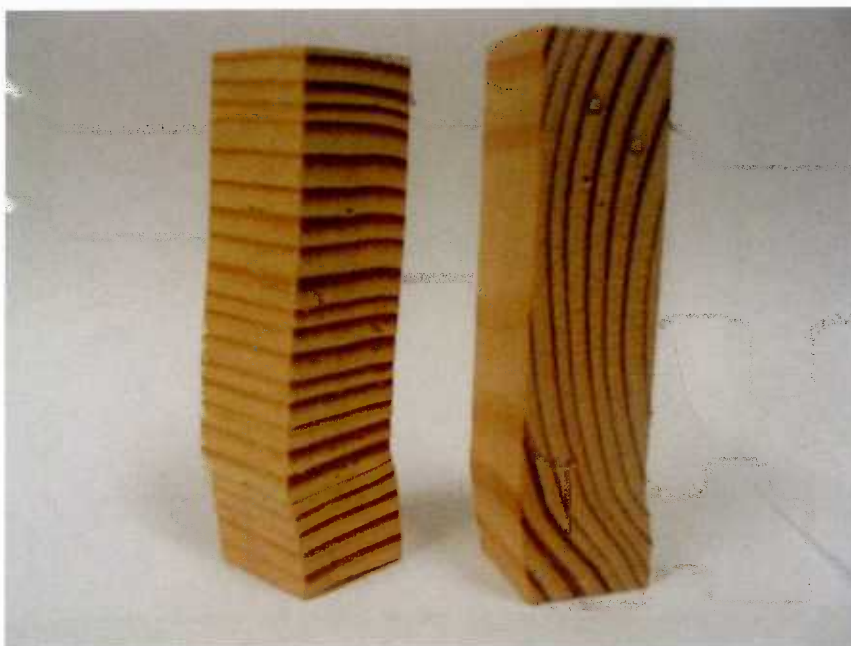


Figure 4.14 Actual deformed shapes of the  $1 \times 1 \times 4$  radial specimen and the  $1 \times 1 \times 4$  tangential specimen overloaded.

#### 4.2.5 Simulation of the $2 \times 2 \times 6$ perpendicular to grain compression

The key focus of this simulation was to model the local crushing failure at the edge of the steel bearing block. Unfortunately, as shown Figure 4.15, both material models did not give desirable load-deformation predictions. The simulated initial stiffness was slightly higher than the tested one. The WOOD11 and WOOD 22 models produced lower yield points that were lower and higher, respectively, than the average bilinear yield point derived from the experimental data. Although the simulated load-deformation curve of WOOD11 could be judged acceptable, the accuracy of the simulation became much less acceptable when compared with the cases of the  $1 \times 1 \times 4$  compression test, which employed uniform stress loading.

It is thought that one of the causes for the poor results may be attributed to the details of the fibre crushing and shear failure process at the edges of the steel bearing block.

Also, the disagreement in the yield point could not be clearly explained. It was assumed that the correct yield stress for this simulation should have been between 4.5 MPa (used for WOOD11 input) and 10.3 MPa (used for WOOD22 input). Therefore, it was concluded that both yield stress inputs for the material models were not appropriate for simulations where wood was subjected to crushing (or bearing) due to partial loading on the wood surface.

It has been reported that the apparent perpendicular to grain bearing strength increases as the length of the contact edge of the bearing block on the wood specimen increases (Madsen 2000, Blass et al. 2004). For the FE modeling of the dowel connection, this response must be understood and resolved, because the slip behaviour of the dowel connection always includes this kind of local crushing failure.

For deformed shape, the WOOD11 simulation showed quite acceptable results, showing a strong indication of the end split that was observed in a few test specimens (Figure 4.16, Figure 4.17 and Figure 4.19). As in the case of the  $1 \times 1 \times 4$  perpendicular to grain compression, the stress contour of WOOD22 in Figure 4.18 showed only the previous contour that the WOOD11 experienced at a low displacement-load sub-step.

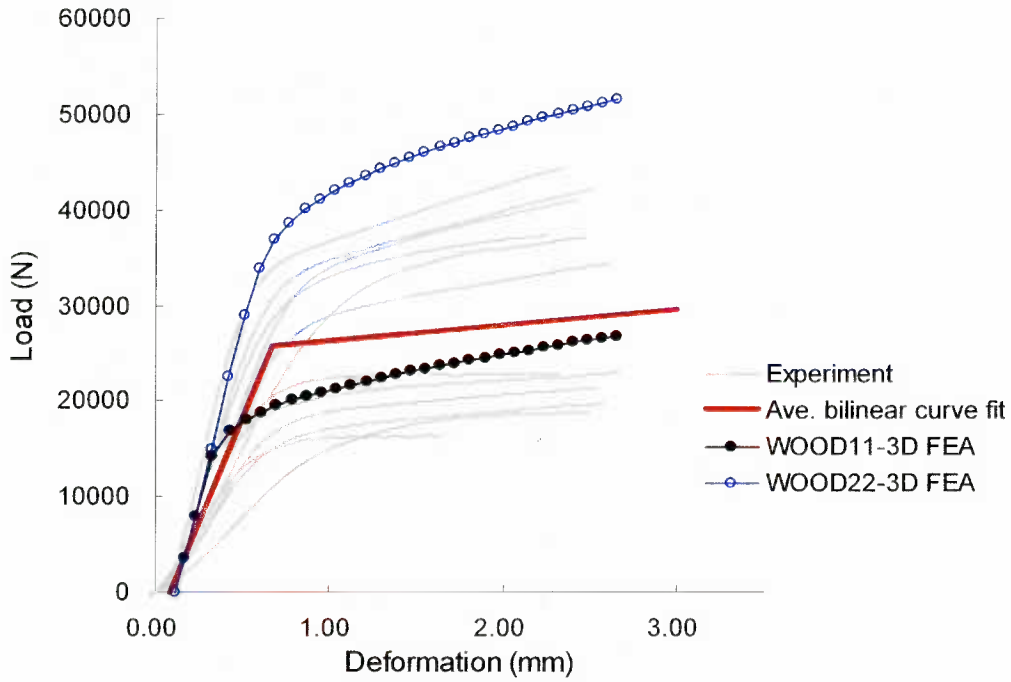


Figure 4.15 Simulated load-deformation curves of the 2x2x6 perpendicular to grain compression.



Figure 4.16 Crushed surface of the 2x2x6 perpendicular to grain compression specimen.

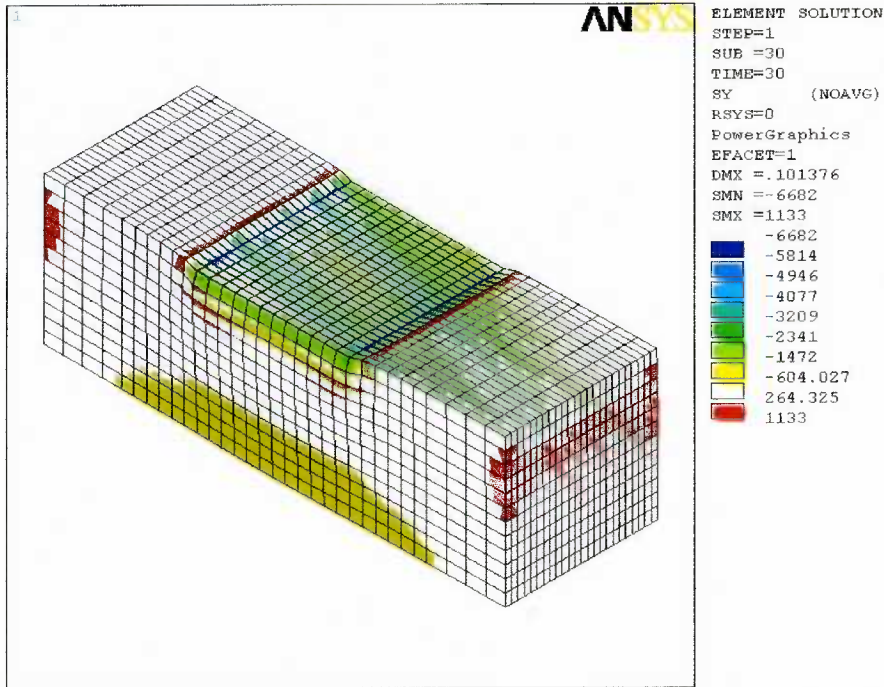


Figure 4.17 Simulated Y-directional stress contour of the 2×2×6 perpendicular to grain compression test at 2.54 mm-displacement-load level using the WOOD11 model.

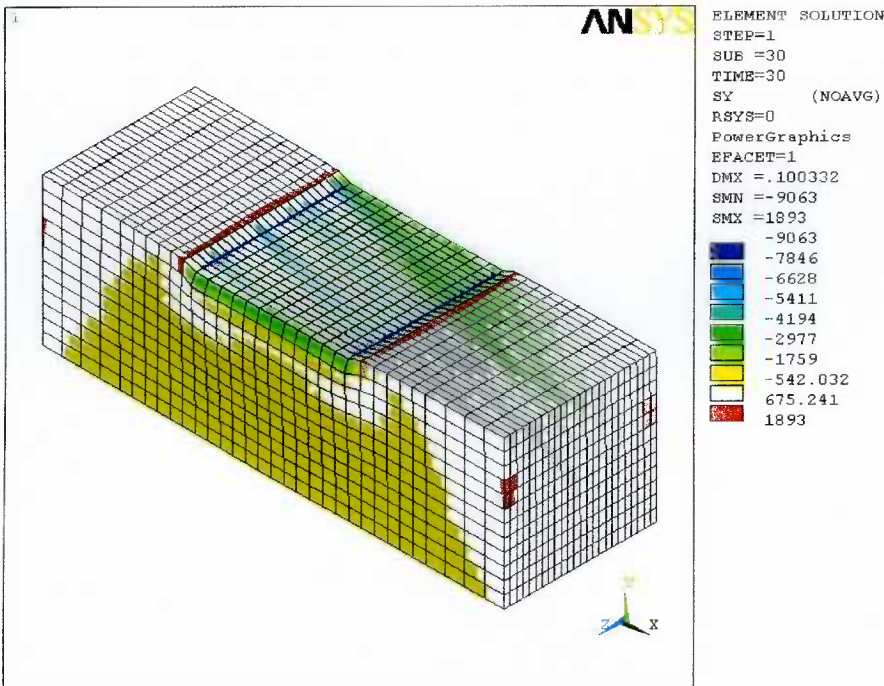


Figure 4.18 Simulated Y-directional stress contour of the 2×2×6 perpendicular to grain compression test at 2.54 mm-displacement-load level using the WOOD22 model.



Figure 4.19 End split failure of the 2×2×6 perpendicular to grain compression specimen.

### 4.3 Conclusions for the wood material model

A plasticity-based compressive wood material model for solid finite elements was devised and validated. The procedure for writing the code of the material model used the minimum independent number of material constants. Comparisons of the two candidate models revealed that the material constants should be determined by a uniform stress-based test, such as the 1×1×4 compression test. The ASTM D 143, 2×2×6 perpendicular to grain compression test was not appropriate for determination of the yield point.

For Douglas-fir, both perpendicular to grain compression tests produced almost the same MOE. Thus, where only linear elastic behaviour is concerned and the yield stresses are unnecessary, both tests provide acceptable results. In cases where wood was

subjected to a bearing load on a partial surface, it was found that the wood material model developed here could not properly simulate the local crushing behaviour. Consequently, this remained a major challenge that needed to be resolved in order to advance the 3D FE analysis of dowel-type wood connections.

## CHAPTER 5. WOOD FOUNDATION MODEL

Results in the last chapter showed that the three-dimensional wood material model employing the ASTM standard compression test-based material constants (WOOD11 and WOOD22) did not successfully simulate the local crushing behaviour of wood under a partial bearing load. For modeling a dowel-type wood connection, this limitation must be overcome because deformation of the connection is always accompanied by local wood crushing around the dowel.

In this chapter, a wood foundation model is introduced that addresses the local crushing around the dowel connector. This wood foundation model was a useful technique for developing a three-dimensional finite element model of dowel-type connections that is applicable for a broad range of connectors, from nails to bolts.

The model development started with a nailed connection, due to its importance in structural applications and the complexities of its load-deformation behaviour. The study was then extended to the 3D FE analysis of bolted connections and other applications.

### 5.1 Problem identification

For many designs of dowel-type connectors, the dowel-embedment strength is a critical characteristic governing the connection design. Therefore, if a 3D FE model for the connection behaviour is to be successful, an acceptable material model must be able to simulate dowel-embedment. However, as determined in the previous chapter, the wood material model with the standard test-based material constants does not have the ability to model the local bearing behaviour.

In order to study the effect of the material model on the predicted embedment, a 3D FE analysis of nail-embedment parallel to grain behaviour was illustrated. As shown in Figure 5.1, a 3D FE model of the actual nail embedment test was developed (more details on the model development are given in section 5.3.3.2). The test consisted of a 65 mm-length, 3.3 mm-diameter wire nail and a 50 mm (height)  $\times$  50 mm (width)  $\times$  38 mm (length) Douglas-fir specimen.

The WOOD 11 material model was used to predict the load-deformation response. The predicted response overestimated the experimental load-embedment results derived in this study (Figure 5.2). This implies that the WOOD11 material model was too stiff, and the poor prediction can be attributed to the fact that the material model was not appropriate in the region surrounding the dowel connector (further discussion is given in section 5.3.4.1). To address these inconsistencies, a modified material model was employed that used material constants derived from the dowel-to-wood interaction. This special wood material model is called the “wood foundation (material) model”.

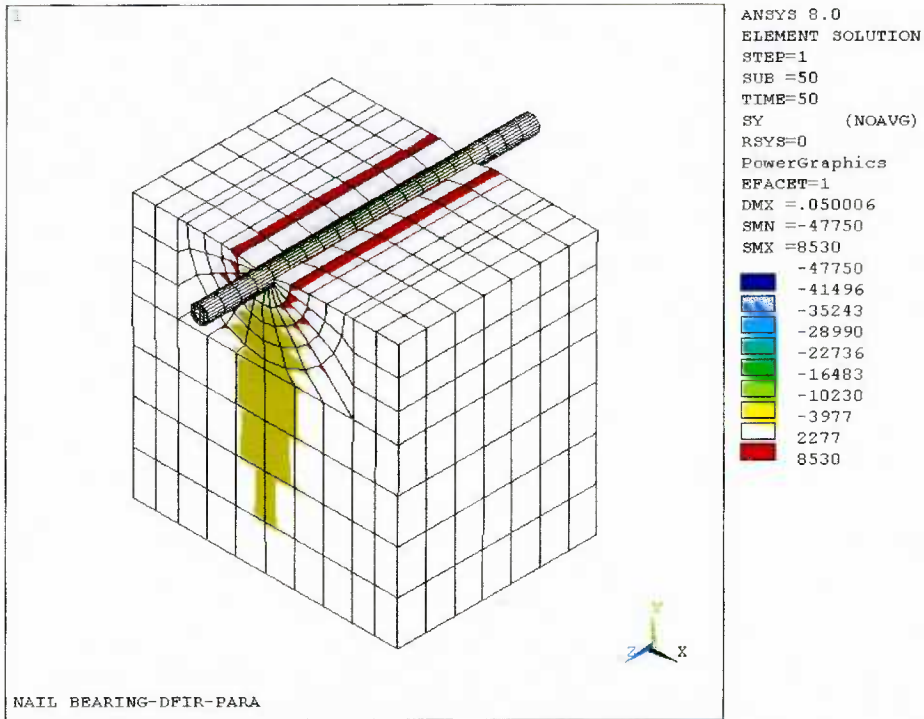


Figure 5.1 Three-dimensional finite element analysis for a parallel to grain nail embedment into Douglas-fir block: Y-directional stress.

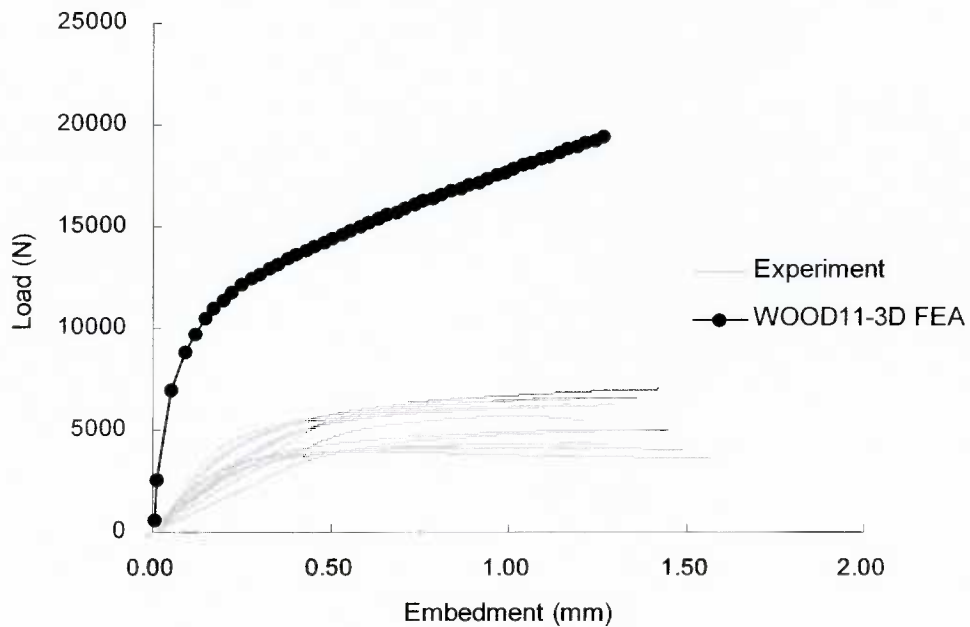


Figure 5.2 Comparison of experimental and predicted load-embedment curves based on the WOOD11 material model.

## 5.2 Development of the wood foundation model

### 5.2.1 Rationale

To model the load-slip behaviour of nailed connections, Foschi (1974) treated the wood under the nail as a nonlinear foundation. The load-deformation response of the wood was expressed by an exponential function (Equation [5.1]) fit to experimental data that was derived from nail-embedment tests.

Basically, the exponential function contains the backbone of a bilinear relationship (Figure 5.3). This implies that, if the backbone load-embedment relationships in the three directions are converted to the corresponding bilinear stress-strain relationships, a material model accounting for the embedment behaviour can be defined using the material model properties provided in Table 3.1. Then, a zone around the nail shank can be defined as the 3D wood foundation. This approach allows the zone around the shank to be modeled as a bilinear wood foundation material model. A three-dimensional conceptual illustration for the wood foundation model is shown in Figure 5. By adopting this approach, a method was devised for determining the requisite material constants for the wood foundation model, including the foundation modulus and foundation yield point.

$$p = (p_0 + p_1 w) \left( 1 - e^{-\frac{Kw}{p_0}} \right) \quad [5.1]$$

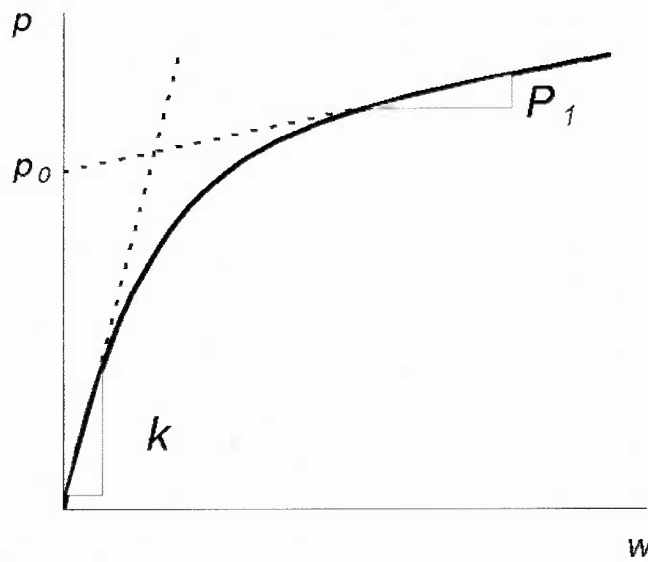


Figure 5.3 A load-embedment curve can be converted to a bilinear stress-strain curve, in order to obtain the material constants for the wood foundation model.

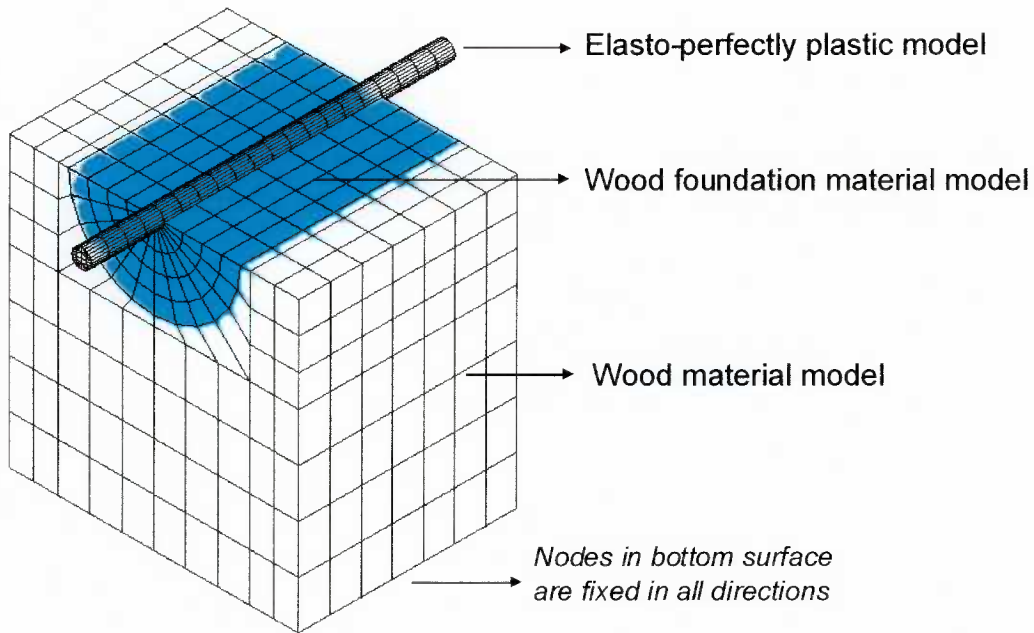


Figure 5. Conceptual illustration for the wood foundation model in the 3D FE nail-embedment model.

## 5.2.2 Definitions of foundation modulus and foundation yield point

### 5.2.2.1 Nominal foundation properties

The foundation modulus and foundation yield point were defined based on the load-embedment curve from dowel-embedment tests. Firstly, the load-embedment plot was converted to a bilinear load per unit length-embedment curve (Figure 5.4). From this curve, an initial slope and break point between two linear regions were identified. The nominal foundation modulus and nominal yield point were then calculated using Equations [5.2], [5.3] and [5.4]. The equation for the nominal yield stress (Equation [5.2]) is identical to the calculation of dowel-embedment strength in ASTM D 5764.

For the nominal yield strain, the units of the yield deformation should be converted to dimensionless units. The diameter of the dowel, which was presumed to be the most important non-material factor governing the local wood crushing behaviour (Equation [5.3]), was chosen to normalize the dimensions of variables involved.

Once the yield stress and yield strain were defined, the nominal foundation modulus could be obtained (Equation [5.4]). Then, these nominal properties should be calibrated to the effective foundation material constants, depending on a prescribed volume of the foundation.

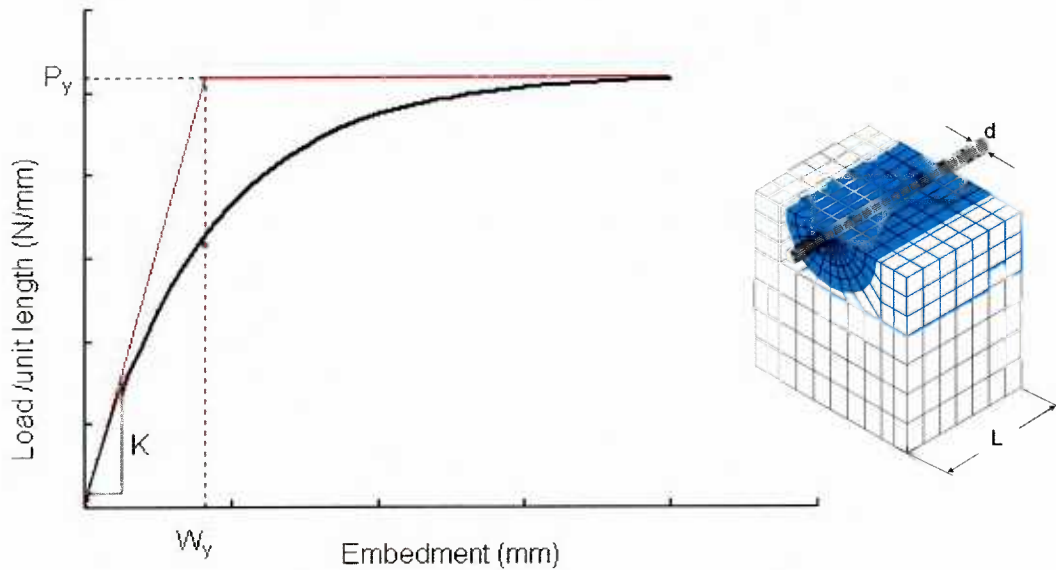


Figure 5.4 Key points in a bilinear load per unit length-embedment plot from the dowel-embedment test.

- Nominal yield stress of wood foundation,  $\sigma_y$

$$\sigma_y = \frac{(P_y/L)}{d} = \frac{p_y}{d} \quad (MPa) \quad [5.2]$$

- Nominal yield strain of wood foundation,  $\varepsilon_y$

$$\varepsilon_y = \frac{w_y}{d} \quad (mm/mm) \quad [5.3]$$

- Nominal foundation modulus,  $S$

$$S = K = \frac{P_y}{w_y} = \frac{\sigma_y}{\varepsilon_y} \quad (MPa) \quad [5.4]$$

Where,

$d$  = diameter of the nail shank

$L$  = length of the wood block

$P_y$  = applied load at the breaking point in the load-embedment curve

$p_y = \frac{P_y}{L}$  = yield load in the load/unit length-embedment curve

$w_y$  = yield deformation in the load/unit length-embedment curve

$\varepsilon_y$  = yield strain of the wood foundation

### 5.2.2.2 Effective foundation material constants

The calibrated foundation properties are called the “effective foundation material constants”. To convert the nominal foundation properties to the effective foundation material constants, dimensionless calibration factors were introduced into the nominal modulus and nominal yield strain, as shown in Equations [5.5] and [5.6].

Factors denoted by  $\alpha_i$  ( $i$  = parallel to grain, //, or perpendicular to grain,  $\perp$ ) were used for calibrating the nominal modulus in the parallel to grain and perpendicular to grain directions, respectively. After calibrating the nominal foundation moduli, a factor,  $\beta_i$ , was introduced as a locator to find the effective yield point by calibration of the nominal yield strain in each direction.

Before these factors could be determined, the size and shape of the foundation must be prescribed. Judgment and trial and error methods were used to determine the appropriate size and shape of the foundation. Based on the prescribed foundation, the factors were determined by iterative runs of the dowel-embedment FE simulation.

Starting with the nominal foundation material constants as seed input for the wood foundation material model (factors  $\alpha_i$  and  $\beta_i$ , were set equal to one), an updating technique was used in the simulation of the load-embedment curves until the predicted curve agreed with the average bilinear experimental curves in parallel to grain and perpendicular to grain directions simultaneously. The optimized factors produced by this process were selected as the final calibration factors.

- Effective foundation modulus,  $(S_{FE})_i$

$$(S_{FE})_i = \alpha_i \cdot K_i \quad [5.5]$$

- Effective foundation yield strain,  $(\varepsilon_{FE})_i$

$$(\varepsilon_{FE})_i = \frac{(w_y)_i}{\beta_i \cdot d} = \frac{1}{\beta_i} \cdot (\varepsilon_y)_i \quad [5.6]$$

Where,

$i$  = parallel to grain direction ( $//$ ) or perpendicular to grain ( $\perp$ ) direction

$\alpha_i$  = calibration factor for the foundation modulus

$\beta_i$  = calibration factor for the foundation yield strain

### 5.3 Validation of the wood foundation model

Originally, the wood foundation model was developed for nail connections. In order to generalize the foundation model, the 3D FE dowel-embedment model was applied to the embedment tests with a wide range of dowel sizes. A database on the embedment test with the range of dowel sizes was created, combining new test data with existing experimental data taken from the literature. This made it possible to validate the model for a range of dowel diameters from 2.5 mm (0.1 in.) diameter nails to 25.4 mm (1.0 in.) diameter bolts, based on embedment tests with Douglas-fir (*Pseudotsuga menziesii*).

New data in this thesis was derived from dowel-embedment tests conducted for 3.3 mm (0.13 in.) diameter nails and 12.7 mm (0.50 in.), 19.1 mm (0.75 in.) and 25.4 mm (1.00 in.) diameter bolts. The existing data were taken from Foschi (1977). The database also contains test data for other species, including Sugi (*Cryptomeria japonica*), Yellow Cedar (*Chamaecyparis nootkatensis*) and Western Hemlock (*Tsuga heterophylla*),

developed by the UBC Wood Mechanics Group (Lam et al. 2004). The 3D FE embedment models for these species were also tested.

### 5.3.1 Dowel embedment test

As shown in Figure 5.5, the wood blocks for the nail-embedment tests were prepared for longitudinal, radial and tangential directions using specimens cut from the lumber described in section 4.1.1. Additionally, wood embedment blocks with a 45-degree ring orientation were prepared to investigate the model's ability of prediction in a non-principal direction. Extension to the bolt-embedment test required additional lumber. A piece of lumber with similar properties (specific gravity (SG) = 0.54, bending MOE = 12.2 GPa and moisture content (MC) = 14.7%) to the three pieces previously used was selected and cut into the specimens for the bolt-embedment tests. Details of the test specimen are listed in Table 5.1.

The ASTM D 5764 half-hole embedment test method was selected, because the full-hole test method is not appropriate for nails due to the high likelihood of nail bending. A perfectly fitting half-hole was drilled for the nail on the loaded surface of the wood block, in order to remove any influences of pre-stresses that may have been produced by a smaller half-hole. The dowels were placed on the wood blocks. The test setups are shown in Figure 5.5 and Figure 5.6.

For bolts, the diameter of the half hole was 1.6 mm (1/16 in.) larger than the bolt diameter, according to ASTM D 5764. The load was applied through a steel bearing block to the specimen with the loading rate of 0.1 mm/sec. using a SINTECH test system.

Table 5.1 Summary of specimen preparation for the dowel embedment test.

Dowel diameter [mm]	Species	Repetitions* [parallel/perpendicular]	Size of wood block [W×H×D (mm)]**
3.3-nail	Douglas-fir	14(L), 14(R), 15(T),	50×50×38 (L, R, T)
		15(45-degree)	50×33×33 (45-degree)
12.7-bolt	Douglas-fir	14/15	100×50×38
19.1-bolt	Douglas-fir	16/12	100×76×38
25.4-bolt	Douglas-fir	20/12	100×50×38

\* L = longitudinal, R = radial and T = Tangential

\*\* W×H×D = width × height × depth

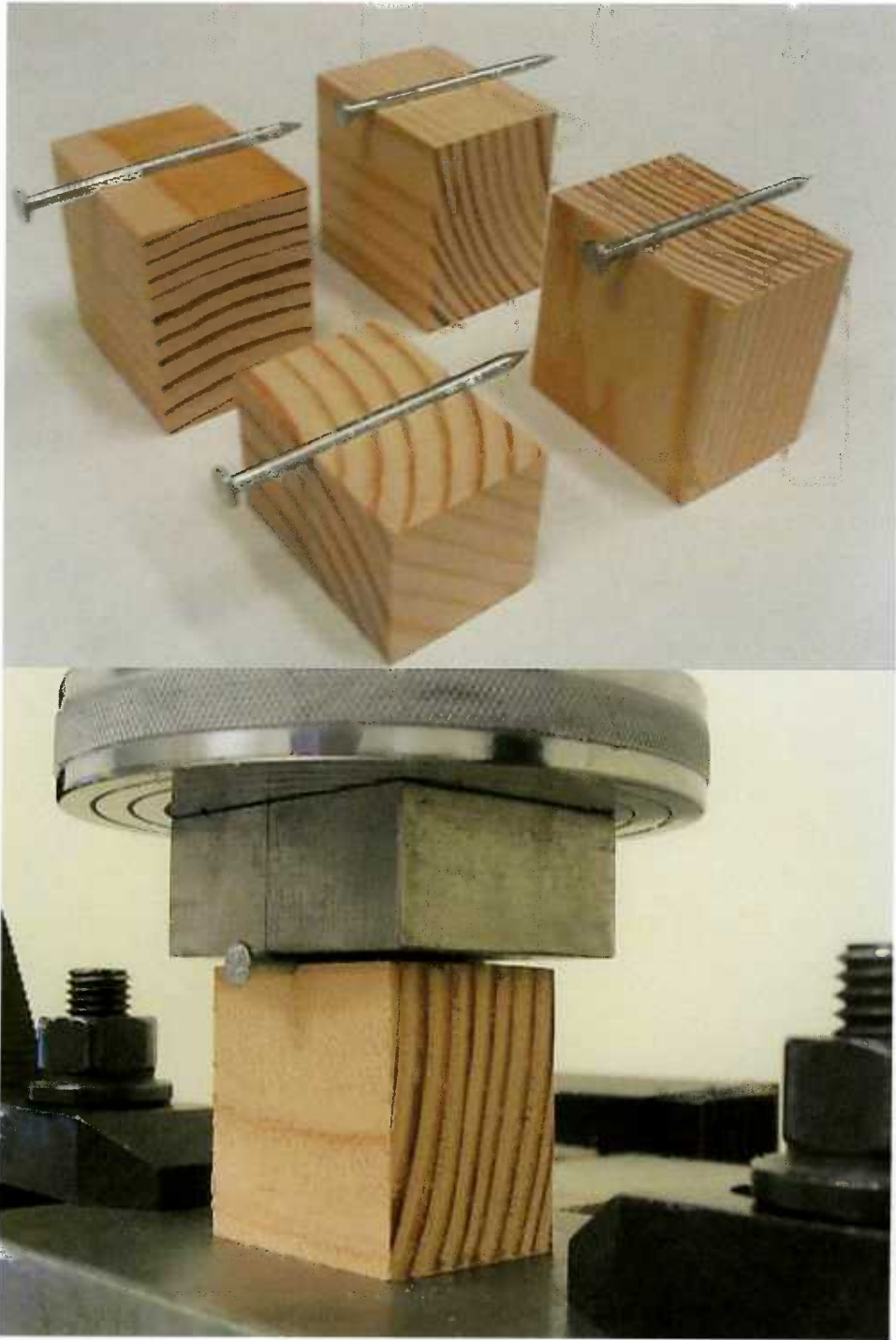


Figure 5.5 Test specimen and setup for the nail-embedment test.

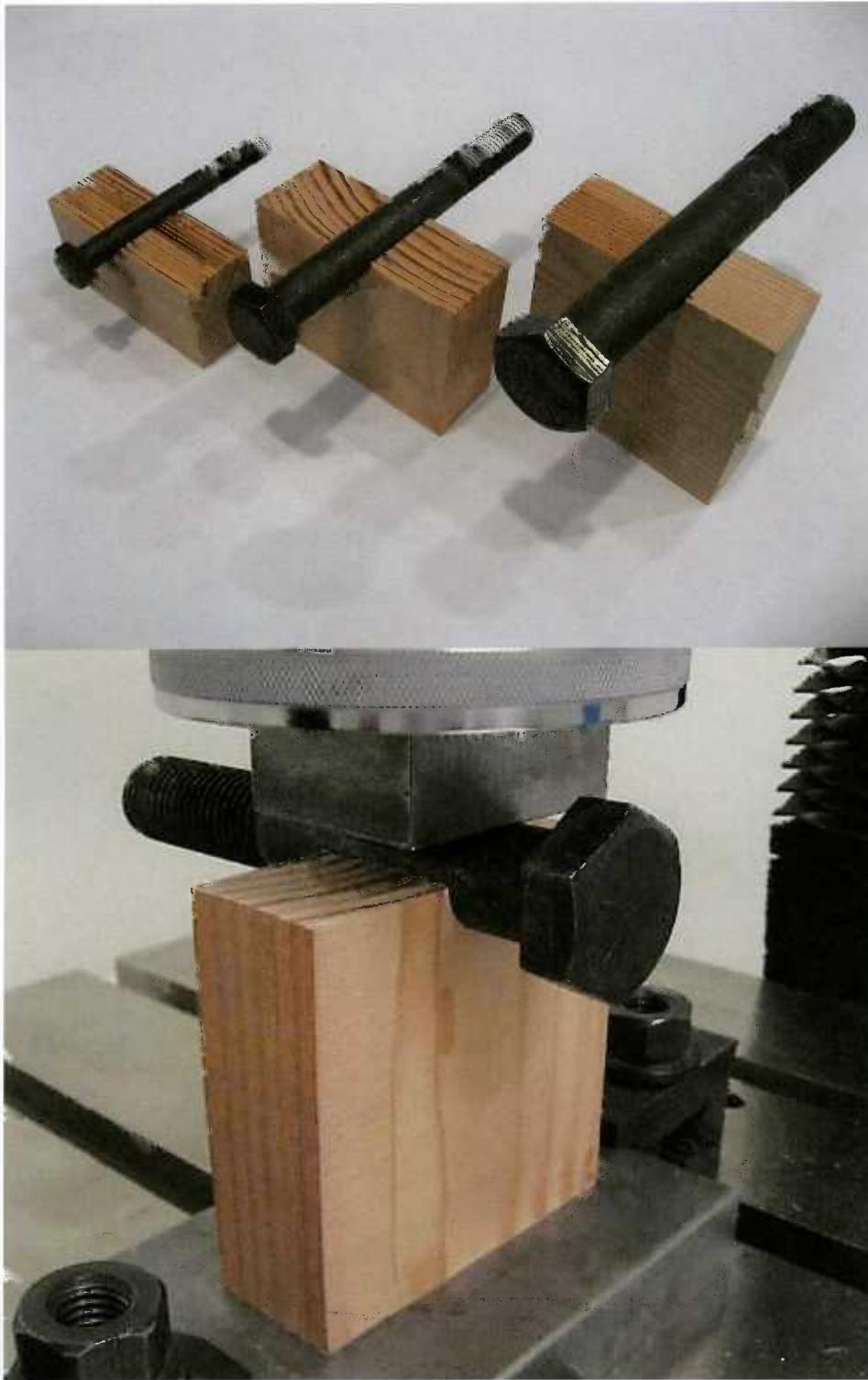


Figure 5.6 Test specimen and setup for the bolt-embedment test.

### 5.3.2 Generalization of the wood foundation model

To investigate relationships between dowel diameter and the foundation material properties, a database for dowel embedment into Douglas-fir was developed for dowel diameters ranging from 2.5 mm to 25.4 mm. The dowel-embedment results included data from Foschi (1977) (Table 5.2). The goal was to generalize the foundation material model by establishing relationships between the dowel diameter and the foundation material properties.

For the nominal foundation modulus, a linear relationship with the diameter was found in the parallel to grain direction (Figure 5.7). In the perpendicular to grain direction, the foundation modulus was taken to be a constant of 150 MPa, regardless of the dowel diameter (Figure 5.8). The foundation moduli showed a consistent trend with the dowel diameter, suggesting that the calibration modulus factors ( $\alpha_i$ ) may be constant over the range of the dowel size.

The relationships between the nominal yield strain and the diameter were nonlinear in both directions. However, the relationship in the parallel to grain direction was assumed to be linear since its nonlinearity is mild (Figure 5.9). In the perpendicular to grain direction, it was found that the nominal yield strain became almost constant with diameters of 6.4 mm and larger (Figure 5.10). In fact, for the perpendicular to grain embedment curve, it was hard to define a yield point, because the load-embedment response showed so much nonlinearity in a ductile manner that the linear part in the curve was obscured (see dowel-embedment experimental curves in section 5.3.4). Based on this investigation, the possibility for generalization of the wood foundation model was assured. It is confirmed in the next section.

Table 5.2 Nominal foundation properties according to dowel diameter.

Shank Diameter [mm]	Nominal foundation modulus (//)* [MPa]	Nominal foundation modulus ( $\perp$ ) [MPa]	Nominal foundation yield strain (//) [mm/mm]	Nominal foundation yield strain ( $\perp$ ) [mm/mm]	Data source
2.5	390	160	0.123	0.144	Foschi
3.3	430	160	0.098	0.136	Test
4.1	430	150	0.103	0.117	Foschi
6.4	520	150	0.085	0.085	Foschi
12.7	500	160	0.063	0.071	Test
19.1	770	140	0.042	0.079	Test
25.4	990	140	0.031	0.061	Test

\* // = parallel to grain direction,  $\perp$  = perpendicular to grain direction

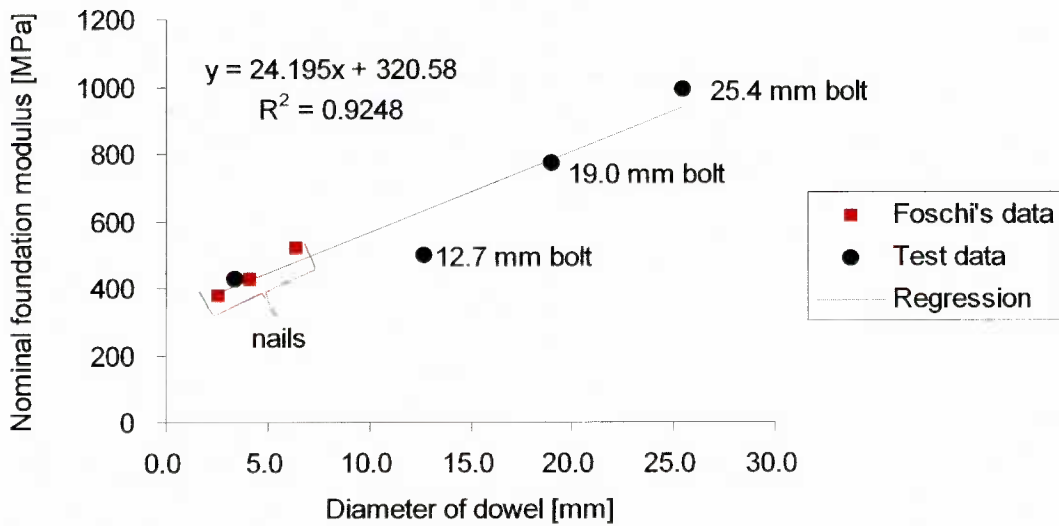


Figure 5.7 Relationship between the nominal foundation modulus and the dowel diameter in the parallel to grain direction.

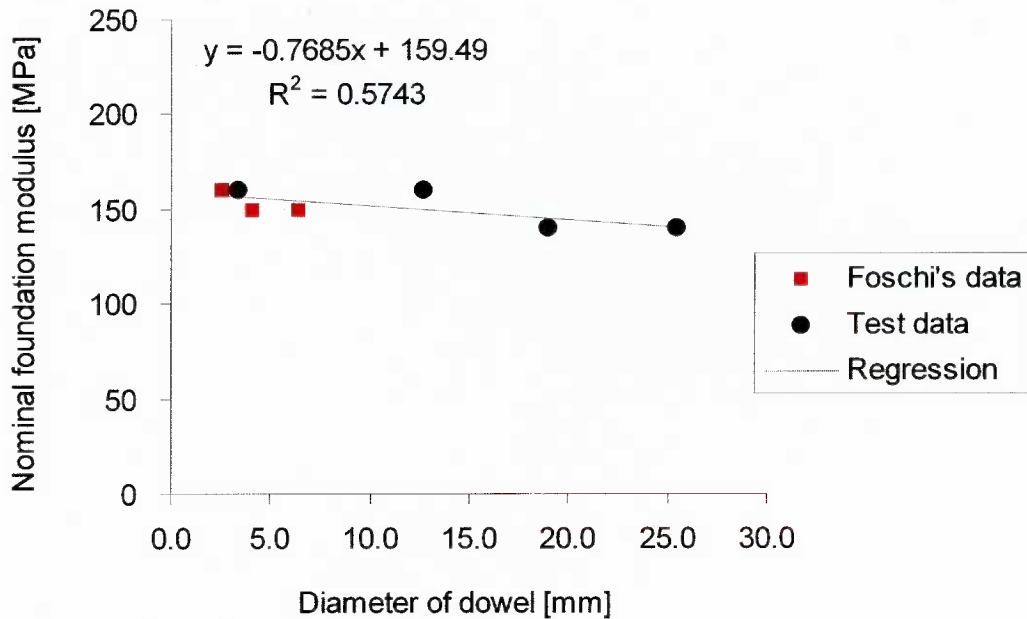


Figure 5.8 Relationship between the nominal foundation modulus and the dowel diameter in the perpendicular to grain direction.

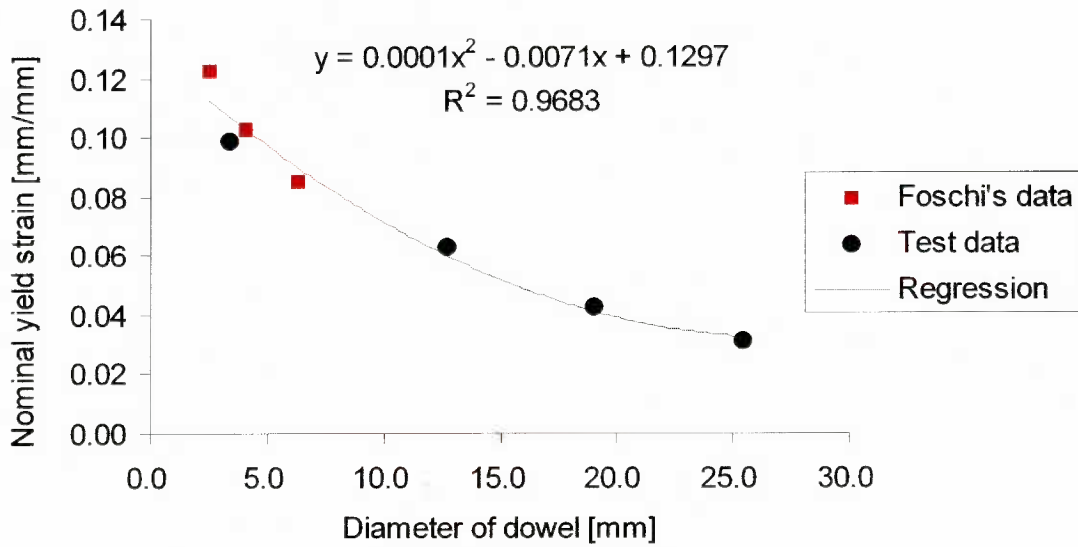


Figure 5.9 Relationship between the nominal foundation yield strain and the dowel diameter in the parallel to grain direction.

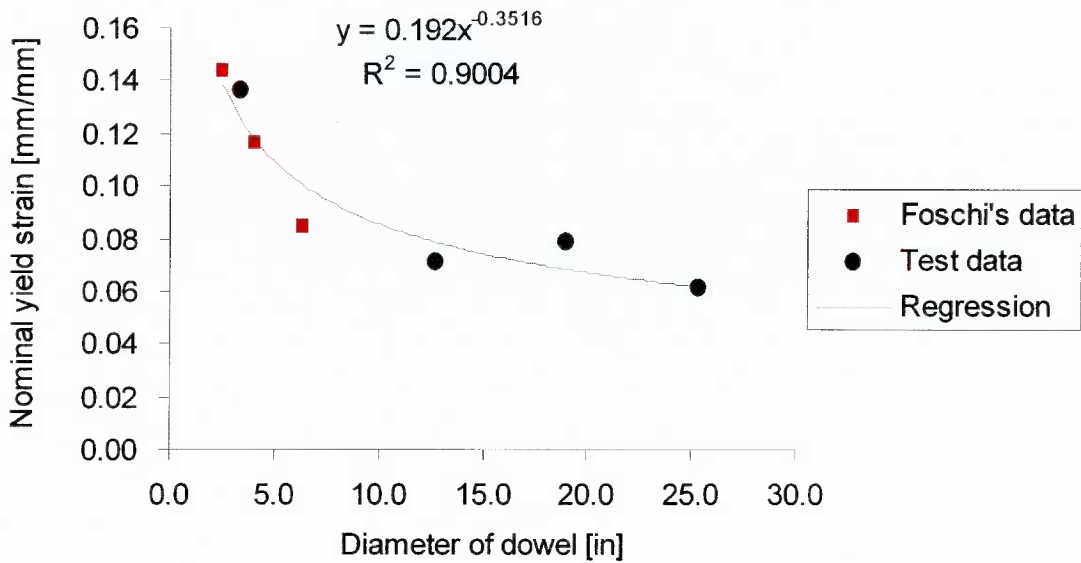


Figure 5.10 Relationship between the nominal foundation yield strain and the dowel diameter in the perpendicular to grain direction.

### 5.3.3 Model development

#### 5.3.3.1 Wood foundation and calibration factors

The geometry of the wood foundation was defined as a half-cylinder along the length of a dowel. The radius of the half-cylinder was chosen as a multiple of the dowel diameter ( $d$ ). In this study, the multipliers were selected empirically to be 4.5 for nails and 1.8 for bolts that provided foundation zones enough to accommodate the localized wood crushing failure around a dowel. The corresponding calibration factors were determined using the iterative method introduced in section 5.2.2.2.

By calculating the effective foundation properties and applying the procedures in Table 3.1, the full set of the material constants for the wood foundation model was established.

For the nail-embedment test, the only data available was for the 3.3 mm-diameter nail. Therefore, using the  $4.5 \times d$  foundation, the calibration factors were first identified as  $\alpha_{//}=1.7$ ,  $\alpha_{\perp}=0.9$ ,  $\beta_{//}=4.2$  and  $\beta_{\perp}=2.8$  for 3.3-mm nail embedment in Douglas-fir. It was then confirmed, with simulation, that these factors were appropriate for the 2.5-, 4.1-, and 6.4-mm nail embedment.

The factors for 12.7-, 19.1-, and 25.4-mm diameter bolt-embedment test data were determined individually. Then, averages of three sets of the factors were used as the generalized factors for the  $1.8 \times d$  wood foundation model. It resulted in  $\alpha_{//}=1.50$ ,  $\alpha_{\perp}=0.73$ ,  $\beta_{//}=1.70$  and  $\beta_{\perp}=1.63$ . The individual factors that were determined are described in section 5.3.4.4. Table 5.3 shows the list of the generalized factors determined for the prescribed volume of the foundations.

Table 5.3 Generalized calibration factors for the prescribed foundations.

Calibration factors	Direction	For nails [4.5× <i>d</i> ]	For bolts [1.8× <i>d</i> ]
Foundation modulus factor, $\alpha_i$	Parallel to grain, $\alpha_{//}$	1.7	1.50
	Perpendicular to grain, $\alpha_{\perp}$	0.9	0.73
Foundation yield strain factor, $\beta_i$	Parallel to grain, $\beta_{//}$	4.2	1.70
	Perpendicular to grain, $\beta_{\perp}$	2.8	1.63

Table 5.4 Material constants for the generalized wood foundation models of Douglas-fir.

Constants	Wood foundation material						
	Size of prescribed foundation	4.5 × shank diameter				1.8 × shank diameter	
Shank diameter [mm]	2.5	3.3	4.1	6.4	12.7	19.1	25.4
Elastic MOE: L [MPa]	660	740	740	890	760	1160	1460
Elastic MOE: R=T [MPa]	140	140	140	130	110	100	100
Elastic shear modulus: RL= LT [MPa]	130	140	140	150	130	160	180
Elastic shear modulus: RT [MPa]	52	51	50	48	41	38	38
Poisson's ratio: RL	0.08	0.07	0.07	0.06	0.05	0.03	0.03
Poisson's ratio: LT	0.37	0.37	0.37	0.37	0.37	0.37	0.37
Poisson's ratio: RT	0.38	0.38	0.38	0.38	0.38	0.38	0.38
Compressive, tensile yield stress:							
: R (=T) [MPa]	4.9	6.5	5.7	4.0	5.0	5.1	5.1
: L [MPa]	79.2	16.0	18.1	18.0	27.9	28.9	28.9
Compressive, tensile tangent modulus							
: R (=T) [MPa]	1.4	1.4	1.4	1.3	1.1	1.0	1.0
: L [MPa]	6.6	7.4	7.4	8.9	7.6	11.6	11.6
Shear yield stress							
: RL (=LT) [MPa]	2.3	3.2	2.9	2.1	2.7	3.1	3.1
: RL [MPa]	1.5	3.2	1.7	1.2	1.5	1.5	1.5
Shear tangent modulus							
: RL (=LT) [MPa]	1.3	1.4	1.4	1.5	1.3	1.6	1.6
: RL [MPa]	0.5	0.5	0.5	0.5	0.4	0.4	0.4

### 5.3.3.2 Model for the dowel embedment test

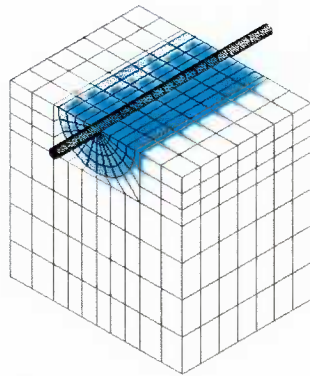
Technically, the creation, boundary condition and analysis method of the 3D FE dowel-embedment model followed the same procedure as used for the wood compression model (see section 4.2.2), except for the inclusion of the wood foundation. Brick element (SOLID45) was used to create the dowel and the wood block. Surface contact elements (CONTA174 and TARGE170) with the coefficient of friction of 0.7 (Smith, 1983) were used for the wood-to-dowel contact interface.

The radius of the wood foundation zone was a multiple of the dowel diameter. Figure 5.11 and Figure 5.12 show the dowel-embedment models with the wood foundation geometry. The wood foundation material model was assigned to the solid elements within the foundation. The WOOD11 material model and the steel material model ( $MOE = 200$  GPa,  $\sigma_y = 250$  MPa and  $\nu = 0.3$ ) were used for the wood and dowel elements, respectively.

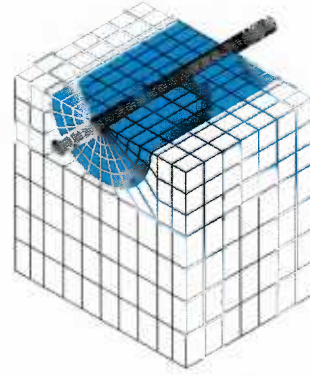
For Foschi's 2.5- and 4.1-mm nail-embedment data, it was assumed that the dimensions of the wood block were 50 mm (width)  $\times$  50 mm (height)  $\times$  38 mm (depth), because the exact dimensions of the wood block were not available. For the 6.4 mm nail-embedment data, a 76 mm (width)  $\times$  76 mm (height)  $\times$  38 mm (depth) wood block was assumed, so that the block was able to accommodate the  $4.5 \times d$  foundation geometry (resulted in the half cylinder diameter of 57.2 mm). Generally, if the size of the wood block exceeds the minimum requirements addressed in ASTM D 5764, it is assumed that the size of the block does not affect the results of the dowel-embedment test. The assumed size of the block model in this study met the minimum requirements.

For the bolt-embedment model, the geometry of the real-test specimen was used with the  $1.8 \times d$  foundation incorporated. In fact, the reason for choosing the multiplier of 1.8 was to accommodate the foundation model within the size of the bolt-embedment wood block.

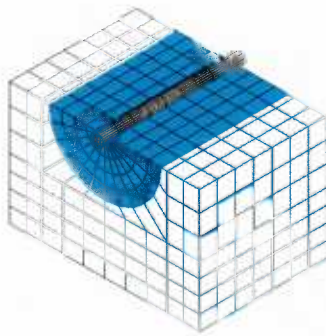
Using parametric modeling, all FE models were re-created from a prototype model (3.3-mm nail-embedment model) by changing the size parameters of the dowel and the wood block geometry.



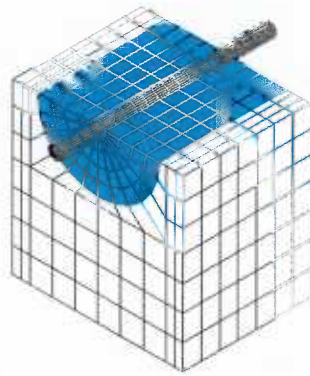
2.5-mm nail



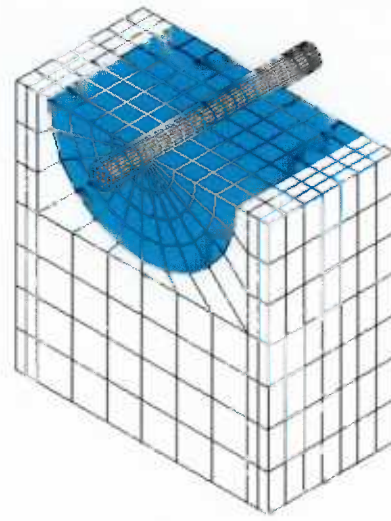
3.3-mm nail



3.3-mm nail: 45-degree to grain

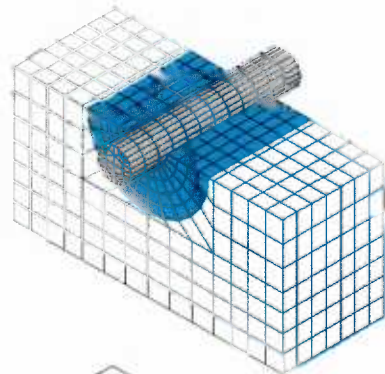


4.1-mm nail

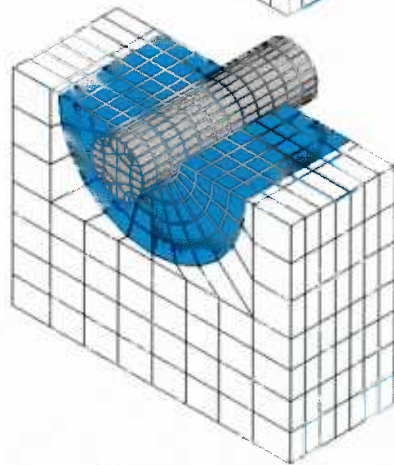


6.4-mm nail

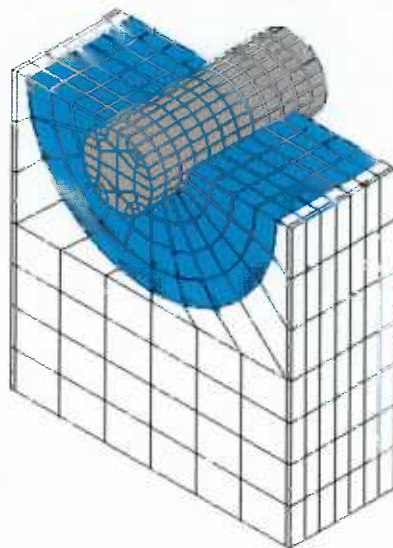
Figure 5.11 Three-dimensional finite element model for the nail-embedment test.  
(Radius of the wood foundation =  $4.5 \times d$ ).



12.7-mm bolt



19.1-mm bolt



25.4-mm bolt

Figure 5.12 Three-dimensional finite element model for the bolt-embedment test.  
(Radius of the wood foundation =  $1.8 \times d$ ).

### 5.3.4 Simulation results

Three-dimensional finite element simulations for selected dowel-embedment behaviour are presented in the following sequence. The simulated load-embedment curves superimposed on the experimental curves and the three-dimensional deformed shapes will be illustrated.

- Dowel embedment in Douglas-fir
  - a) 3.3-mm diameter nail (parallel/perpendicular to grain)
  - b) 3.3-mm diameter nail (45-degree-to grain)
  - c) 2.5-, 4.1- and 6.4-mm diameter nail using Foschi's exponential model (parallel/perpendicular to grain)
  - d) 12.7-mm diameter bolt (parallel/perpendicular to grain)
  - e) 19.1-mm diameter bolt (parallel/perpendicular to grain)
  - f) 25.4-mm diameter bolt (parallel/perpendicular to grain)
  
- Nail embedment in on Sugi (Japanese Cedar) and Yellow Cedar
  - g) 3.8-mm diameter nail on Sugi (parallel/perpendicular to grain)
  - h) 3.8-mm diameter nail on Yellow Cedar (parallel/perpendicular to grain)
  - i) 3.8-mm diameter nail on Western Hemlock (parallel/perpendicular to grain)

#### 5.3.4.1 Simulation of 3.3-mm nail-embedment test

For 3.3-mm nail-embedment simulation, good matching of the experimental and simulated curves in the parallel to grain and perpendicular to grain directions was anticipated, because the process for determining the calibration factors was based on matching these curves as closely as possible (Figure 5.13 and Figure 5.14).

For these tests, Foschi's exponential model (Foschi et al. 1977) was used for comparisons. The embedment parameters of the exponential model corresponding to 3.3-mm nail in Douglas-fir were obtained by interpolation between the parameters for the 2.5- and 4.1-mm nails, as instructed in their paper. Equations [5.7] and [5.8] provided the exponential models for 3.3-mm nail embedment on Douglas-fir in the parallel to grain and perpendicular to grain directions. The exponential curves were superimposed on the experimental curves. Good agreement between the Foschi's model and the 3D FE model implied that the same rationale of the Foschi's nail-slip model (Foschi et al. 1977), which used the exponential model for wood foundation, was valid for the three-dimensional finite element model of the dowel-type connection.

Simulated deformed shapes also showed good results in the parallel to grain and perpendicular to grain directions. For the real tests, the indentation of the wood by the 3.3-mm diameter nail was not discernable in both directions. As shown in Figure 5.15 and Figure 5.16, the models also predicted plastic strain contour only within a small region.

The plastic strain contour simulated by a model without the wood foundation (only WOOD11 material model was applied to whole wood elements) is presented for comparison purposes in Figure 5.17. The apparent contour showed no significant

difference from that of the model with wood foundation; but, it gave an invalid load-embedment curve (see Figure 5.2). This justified the use of the wood foundation model in modeling of wood crushing behaviour under a dowel.

- Foschi's exponential models for 3.3-mm nail-embedment in Douglas-fir  
( $L = 38$  mm)

$$\text{Parallel to grain (N): } p = [153.10 \times (1 - e^{\frac{-411.85w}{153.10}})] \times L \quad [5.7]$$

$$\text{Perpendicular to grain (N): } p = [(37.14 + 67.21w) \times (1 - e^{\frac{-155.41w}{37.14}})] \times L \quad [5.8]$$

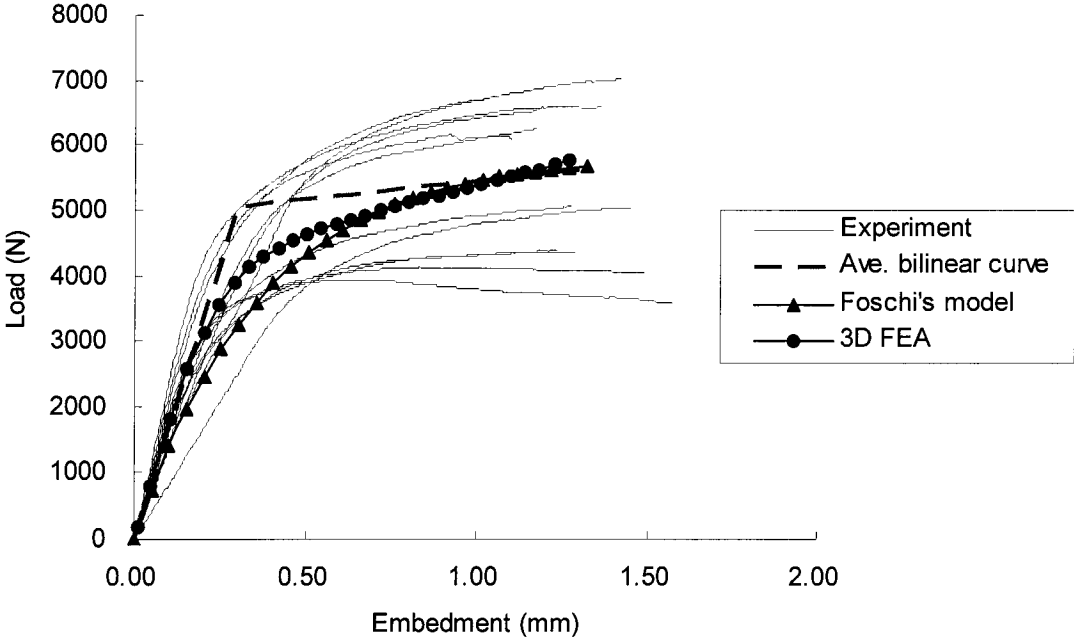


Figure 5.13 Simulated parallel to grain load-embedment curve of 3.3-mm nail-embedment in Douglas-fir.

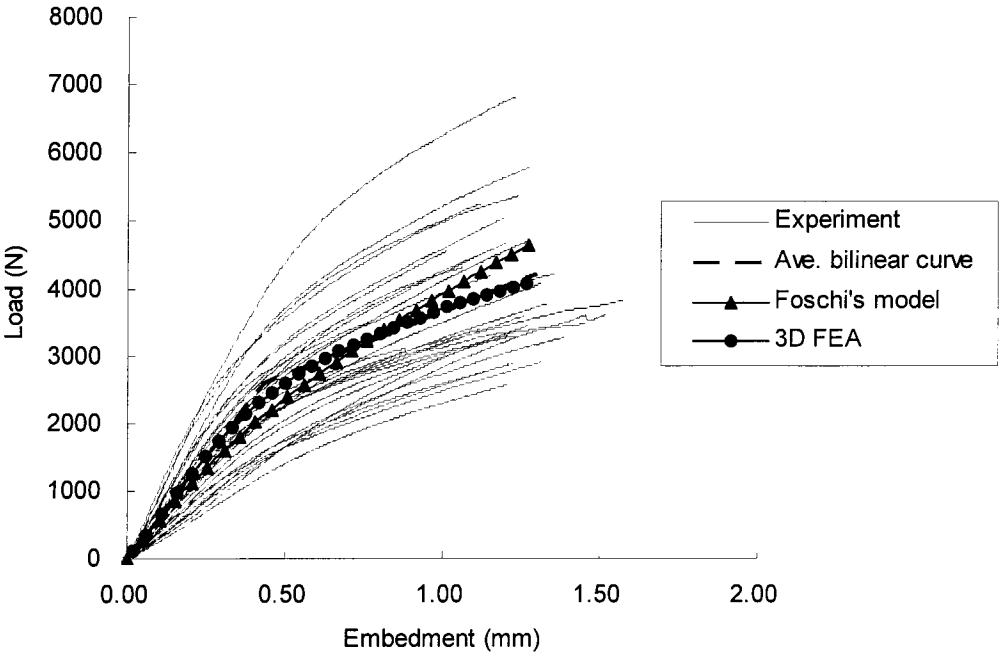


Figure 5.14 Simulated perpendicular to grain load-embedment curve of 3.3-mm nail-embedment in Douglas-fir.

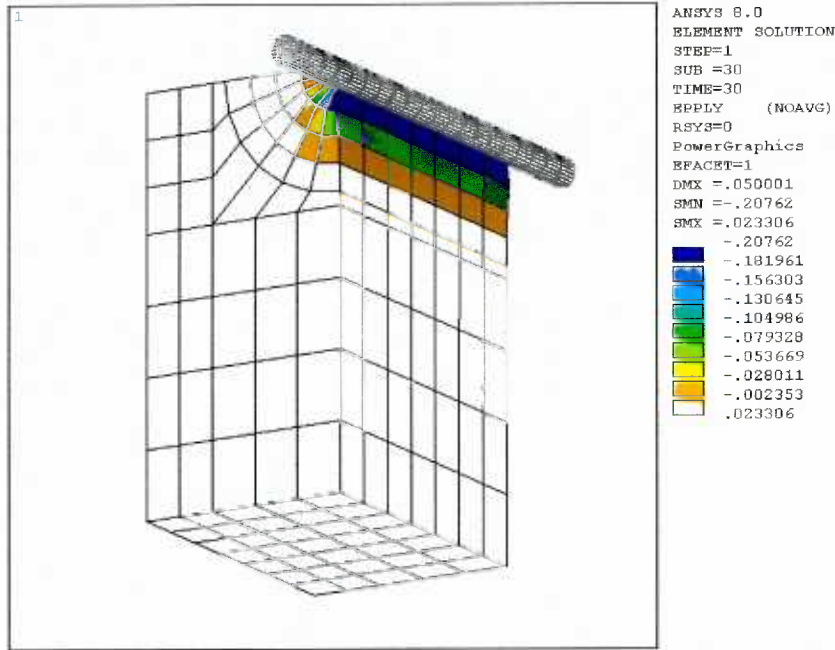


Figure 5.15 Simulated Y-directional plastic strain contour of 3.3-mm nail-embedment in Douglas-fir in the parallel to grain direction. Half of the wood elements are shown.

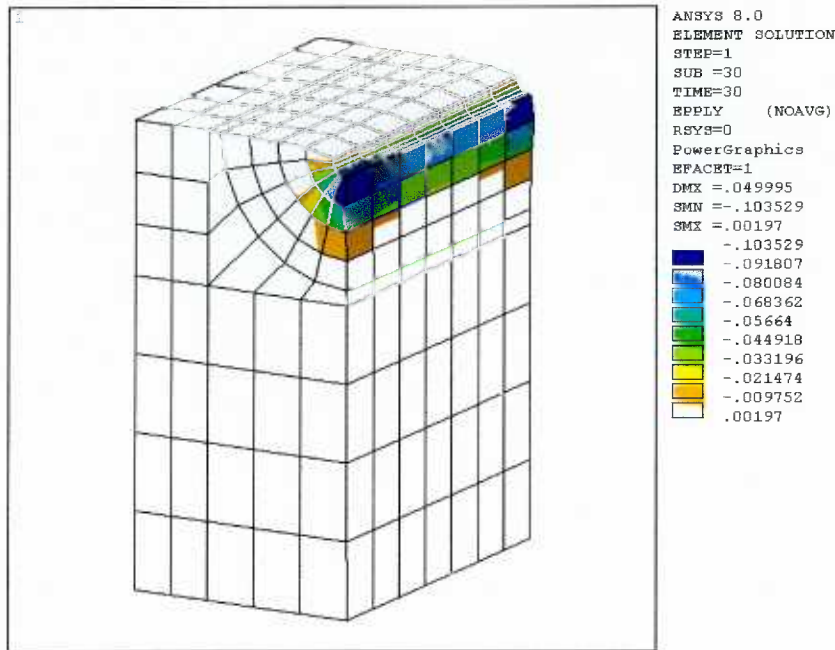


Figure 5.16 Simulated Y-directional plastic strain contour of 3.3-mm nail-embedment in Douglas-fir in the perpendicular to grain direction. Half of the wood elements are shown.

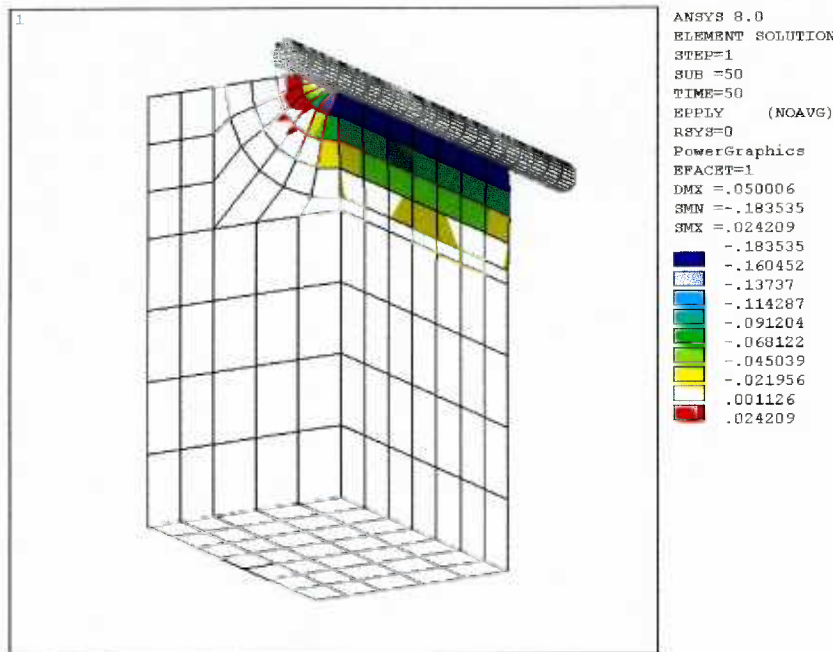


Figure 5.17 Simulated Y-directional plastic strain contour of 3.3-mm nail-embedment in Douglas-fir in the parallel to grain direction using the WOOD11 model only. Half of the wood elements only are shown.

#### 5.3.4.2 Simulation of the 3.3-mm nail-embedment test in the 45-degree to grain direction

The fibre direction and grain angle in the 45-degree embedment-test specimen are shown in Figure 5.18. The grain angle of 45 degrees to the embedding direction involved an unbalanced wood foundation support, due to the directional differences in wood strength properties, as shown in Figure 5.19. This unbalanced support caused the nail embedment to progress in a tilting manner (left in Figure 5.20). In the real test, a spherical bearing in the crosshead was used to accommodate for the tilting behaviour. Thus, for the tested specimens, it was observed that wood crushing failure at the lower end of the tilted nail was always more severe than at the higher end.

This tilting behaviour could not be simulated correctly by a displacement-controlled loading method, because it employed uniformly incremental displacement along the nail

shank. In order to model the tilting behaviour properly, a model run under force (pressure)-controlled loading was required. Figure 5.20 shows the difference in the deformed shapes between the force-controlled loading model and the displacement-controlled model. Only the force-controlled model produced the tilting behaviour properly.

The simulated load-embedment curves for the two loading methods, however, were almost identical (Figure 5.21). For the force-controlled case, the displacement data was collected by averaging the two nodal displacements at the tilted ends in the wood elements. For the displacement-controlled case, the centre node in the wood contacting the nail shank was selected to determine the displacement data. The predicted load-embedment curves were judged acceptable, although overall stiffness of the curves was slightly higher than that of the average bilinear experimental curve.

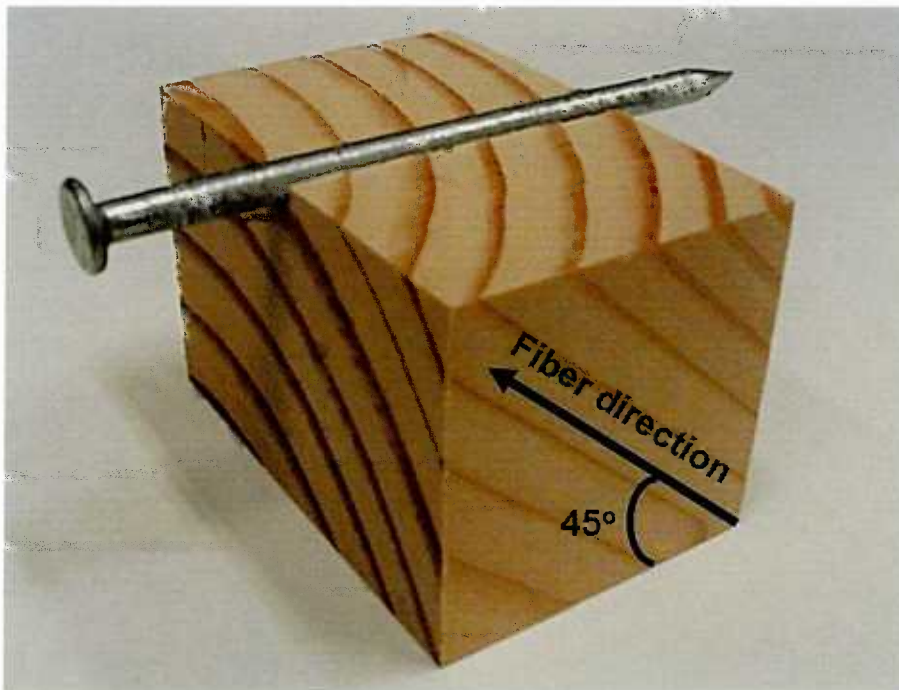


Figure 5.18 Grain angle of 45-degree embedment specimen.

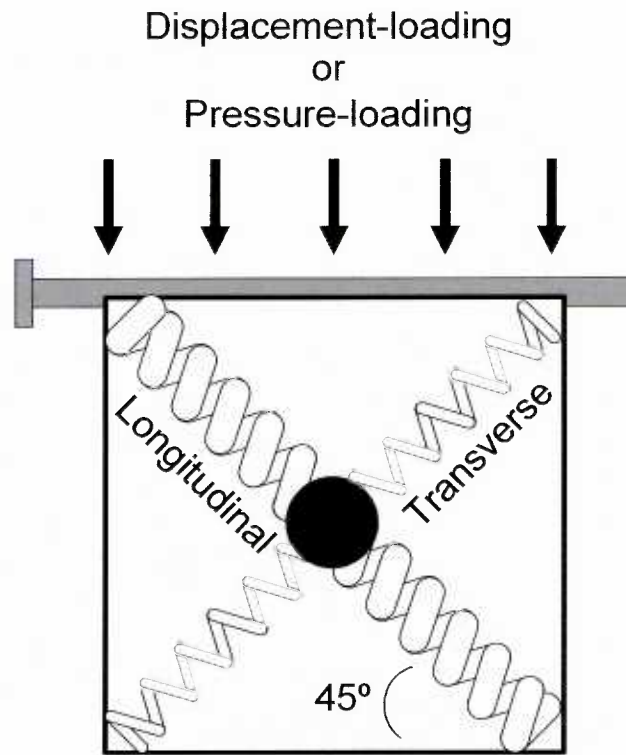


Figure 5.19 Schematic unbalanced foundation in 45-degree grain angle embedment test.

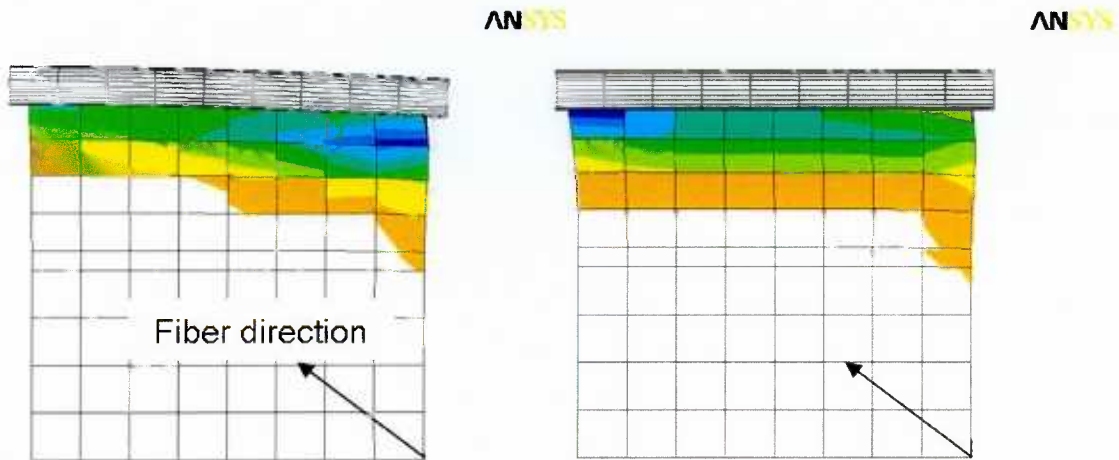


Figure 5.20 Simulated Y-directional plastic strain contour of 45-degree to grain embedment; the force-controlled case (left) showed the tilted embedment of the nail compared to the uniform embedment of the displacement-controlled case (right).

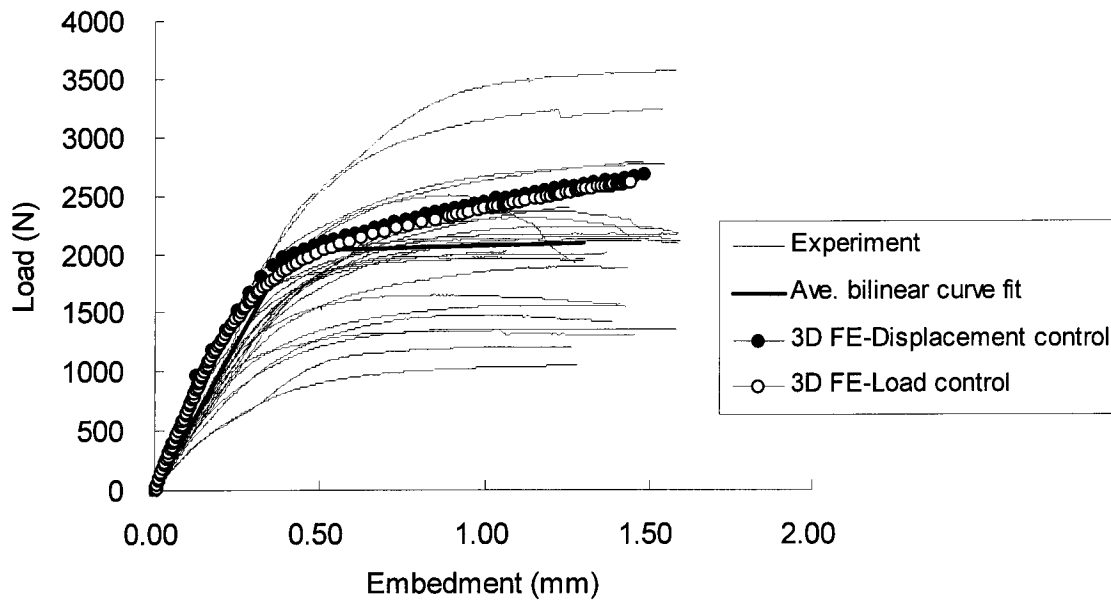


Figure 5.21 Simulated 45-degree to grain load-embedment curve of 3.3-mm nail-embedment in Douglas-fir. Force-controlled method showed better prediction.

### 5.3.4.3 Model verification using Foschi's exponential models

Foschi's exponential models (1977) for nail embedment in Douglas-fir were reproduced using the 3D FE nail-embedment model. As shown in Table 5.2, the material constants adopted for the 3D FE model could be derived from the embedment parameters of the exponential model published. The exponential models for 2.5-, 4.1- and 6.4-mm nail embedment in Douglas-fir are presented in Equations [5.9] to [5.14].

The 3D FE load-embedment curves superimposed on the exponential curves showed good agreement for the parallel to grain direction models (Figure 5.22). For the perpendicular to grain direction, the 3D FE model showed good agreement in the initial stiffness. However, the post-yield stiffness of the exponential model was always higher than those of the 3D FE model (Figure 5.23).

The exponential perpendicular to grain model tended to over-predict post-yield embedment behaviour. It is generally thought that the ultimate strength of the parallel to grain embedment is much higher than that of the perpendicular to grain embedment. However, the exponential model produced similar ultimate strengths in both directions. For example, the 4.1-mm diameter nail-embedment exponential model produced ultimate strengths at a 2-mm embedment (half-diameter embedment) of 180 N/mm in the parallel to grain direction and 178 N/mm. in the perpendicular to grain direction.

The perpendicular to grain embedment curves from the 3D FE models predicted the trend of the post-yield behaviour observed in the embedment experimental data quite accurately. Therefore, the discrepancy in perpendicular to grain post-yield behaviour between the exponential model and the 3D FE model was ignored.

In Figure 5.24, simulated Y-directional total strain contours for the nail embedment were presented.

- **2.5-mm diameter nail embedment**

$$\text{Parallel to grain (N/mm): } p = 120 \times \left(1 - e^{\frac{-386w}{120}}\right) \quad [5.9]$$

$$\text{Perpendicular to grain (N/mm): } p = (34 \times 66w) \times \left(1 - e^{\frac{-159w}{34}}\right) \quad [5.10]$$

- **4.1-mm diameter nail embedment**

$$\text{Parallel to grain (N/mm): } p = 182 \times \left(1 - e^{\frac{-434w}{182}}\right) \quad [5.11]$$

$$\text{Perpendicular to grain (N/mm): } p = (40 \times 68w) \times \left(1 - e^{\frac{-152w}{40}}\right) \quad [5.12]$$

- **6.4-mm diameter nail embedment**

$$\text{Parallel to grain (N/mm): } p = 282 \times \left(1 - e^{\frac{-524w}{282}}\right) \quad [5.13]$$

$$\text{Perpendicular to grain (N/mm): } p = (42 \times 70w) \times \left(1 - e^{\frac{-148w}{42}}\right) \quad [5.14]$$

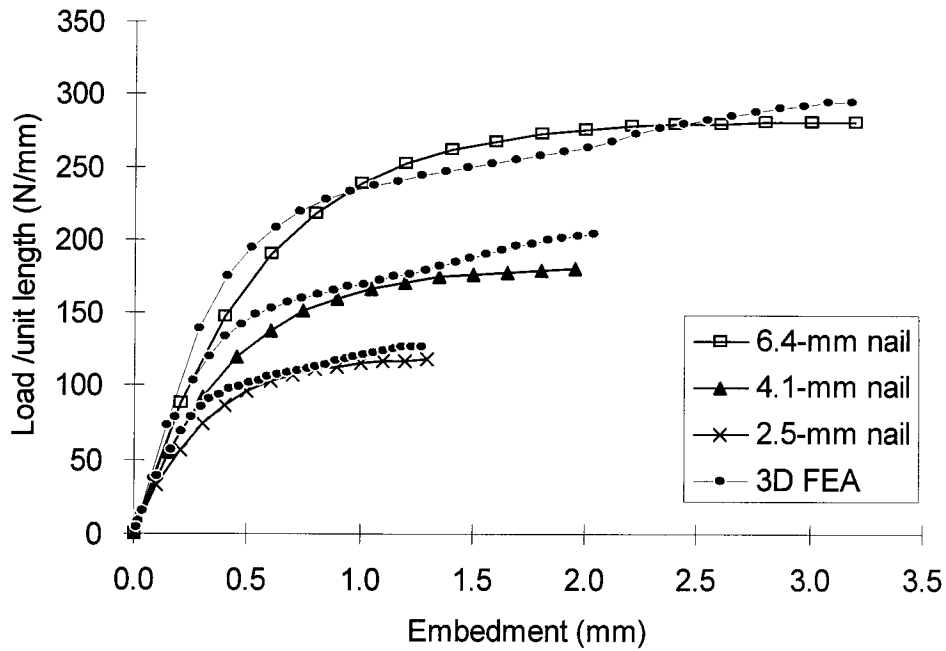


Figure 5.22 Simulated parallel to grain load-embedment curve of Foschi's nail embedment in Douglas-fir.

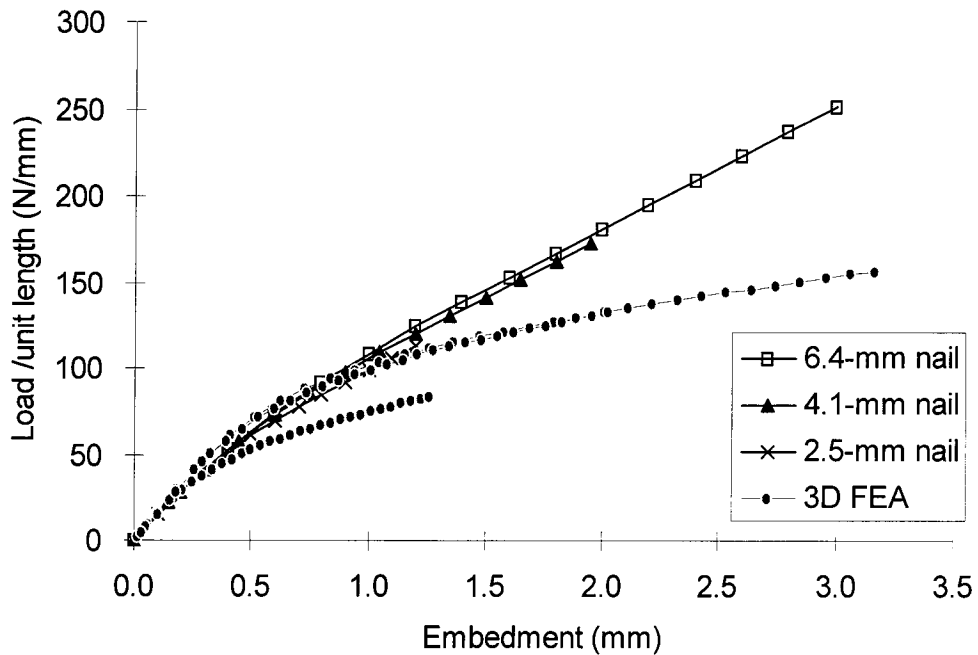


Figure 5.23 Simulated perpendicular to grain load-embedment curve of Foschi's nail embedment in Douglas-fir.

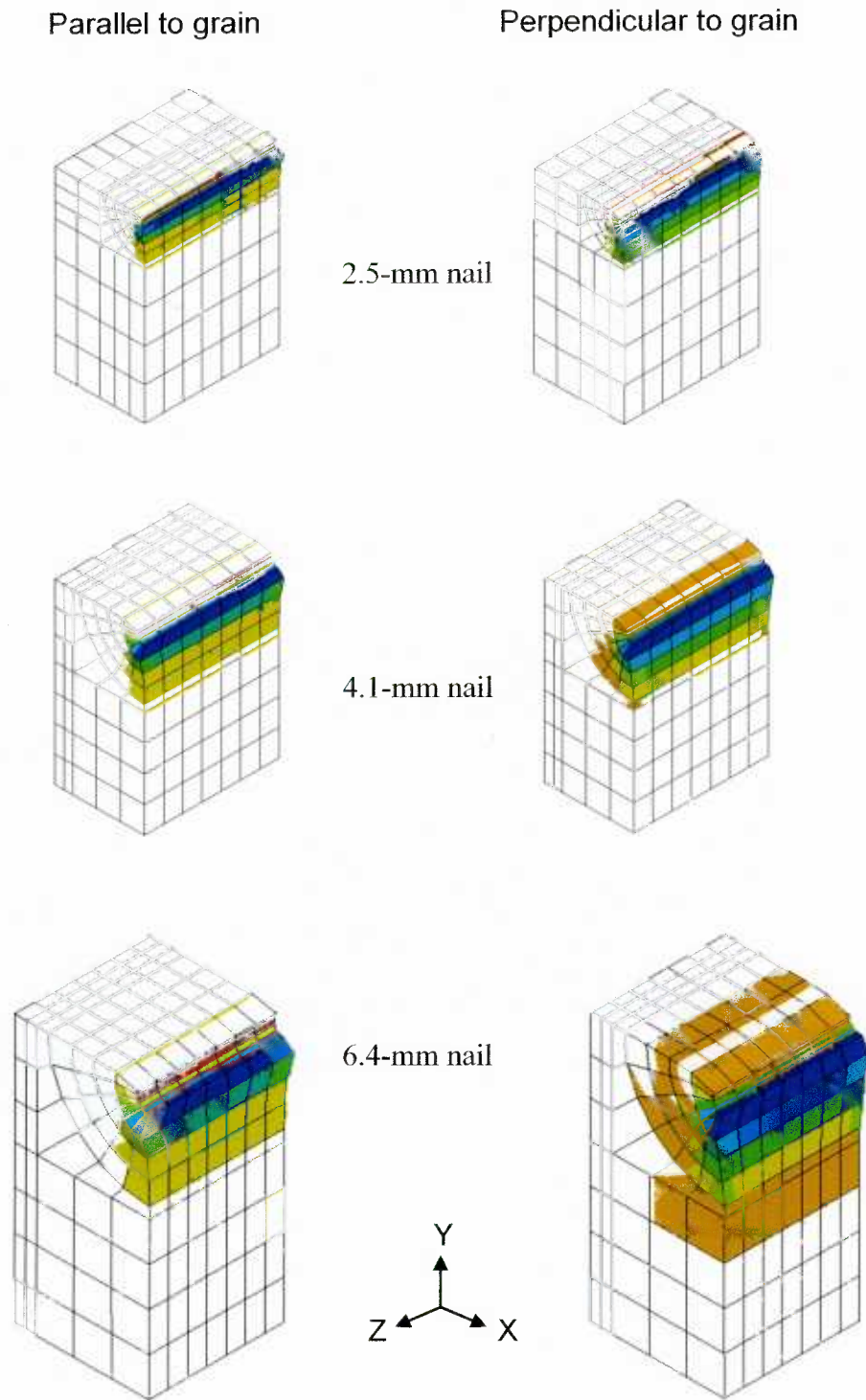


Figure 5.24 Simulated Y-directional strain contours for nail embedment in Douglas-fir with 2.5-, 4.1- and 6.4-mm nails in parallel/perpendicular to grain directions. Half models are shown.

#### 5.3.4.4 Simulation of bolt embedment tests

As mentioned in section 5.3.2, the individual iterative runs identified the best calibration factors for the 12.7-, 19.1- and 25.4-mm diameter bolt wood foundation models. These factors were listed in Table 5.5. Although the set of the factors listed in the table provided optimized results for the corresponding bolt-embedment simulation, the averages of the three sets of the factors were used for the foundation models because of the generalization of the factors for application to an intermediate diameter of bolt.

Simulation results using the generalized factors only are presented here. Overall, the 3D FE model predicted acceptable load-embedment curves in parallel to grain and perpendicular to grain directions. Comparisons of the simulated load-embedment curves with the experimental curves are presented in Figure 5.25 to Figure 5.30.

Figure 5.31 shows the Y-directional plastic strain contour of the bolt-embedment tests. Reasonable deformed shapes and strain contours were obtained. The tendency for the wood around the bolt to sink toward the bolt hole in the real test was simulated effectively, particularly for perpendicular to grain embedment.

Figure 5.32 shows the comparison of wood crushing deformation for the 25.4-mm bolt parallel to grain embedment and tells how the solid element can simulate the crushing progress.

Table 5.5 Individual calibration factors for the 1.8×bolt diameter wood foundation model.

Calibration factors	Direction	Diameter of bolt [mm]			Mean calibration factors
		12.7	19.1	25.4	
Foundation modulus factor, $\alpha_i$	Parallel to grain, $\alpha_{//}$	1.50	1.50	1.50	1.50
	Perpendicular to grain, $\alpha_{\perp}$	0.75	0.70	0.75	0.73
Foundation yield strain factor, $\beta_i$	Parallel to grain, $\beta_{//}$	1.70	1.70	1.70	1.70
	Perpendicular to grain, $\beta_{\perp}$	1.50	1.70	1.70	1.63

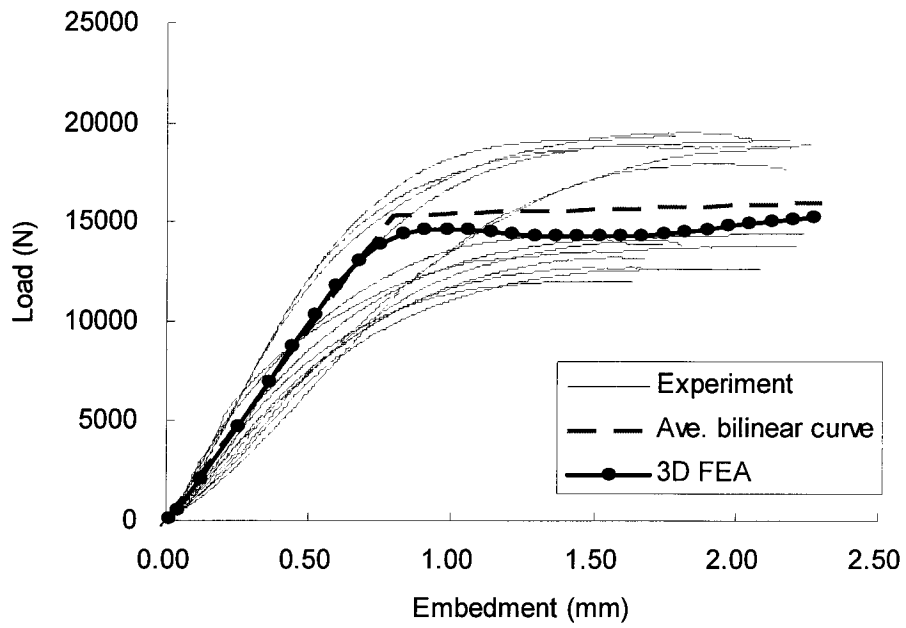


Figure 5.25 Simulated parallel to grain load-embedment curve of 12.7-mm bolt embedment in Douglas-fir.

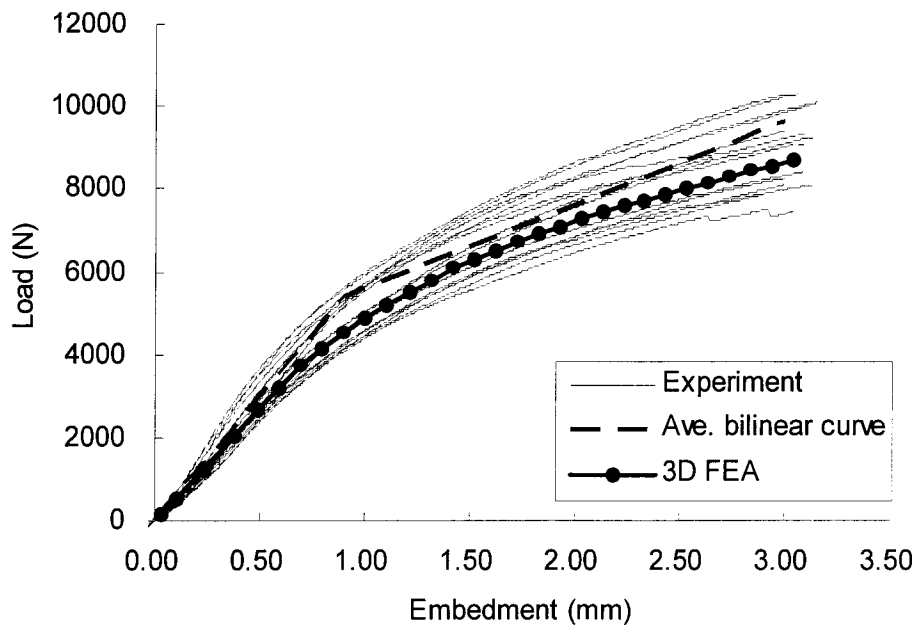


Figure 5.26 Simulated perpendicular to grain load-embedment curve of 12.7-mm bolt embedment in Douglas-fir.

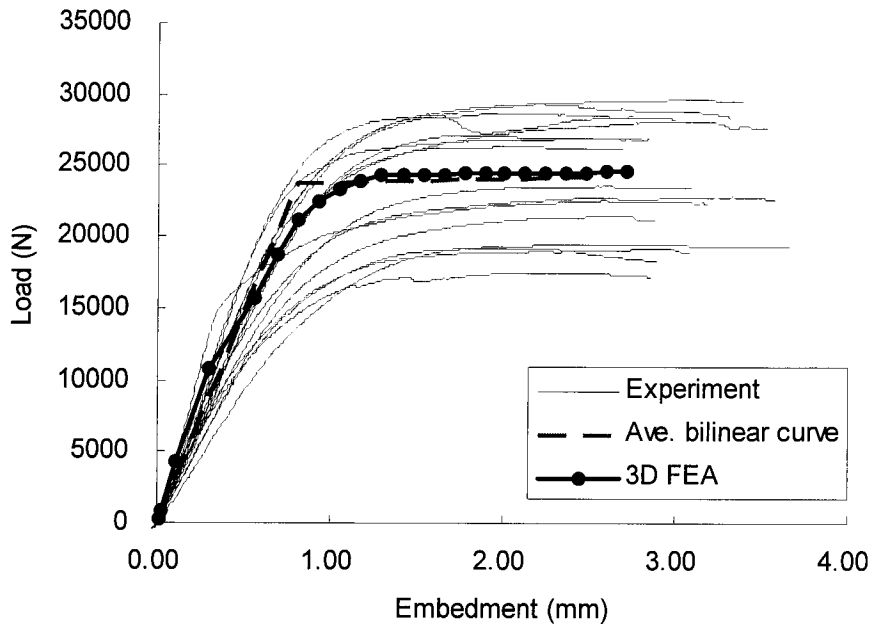


Figure 5.27 Simulated parallel to grain load-embedment curve of 19.1-mm bolt embedment in Douglas-fir.

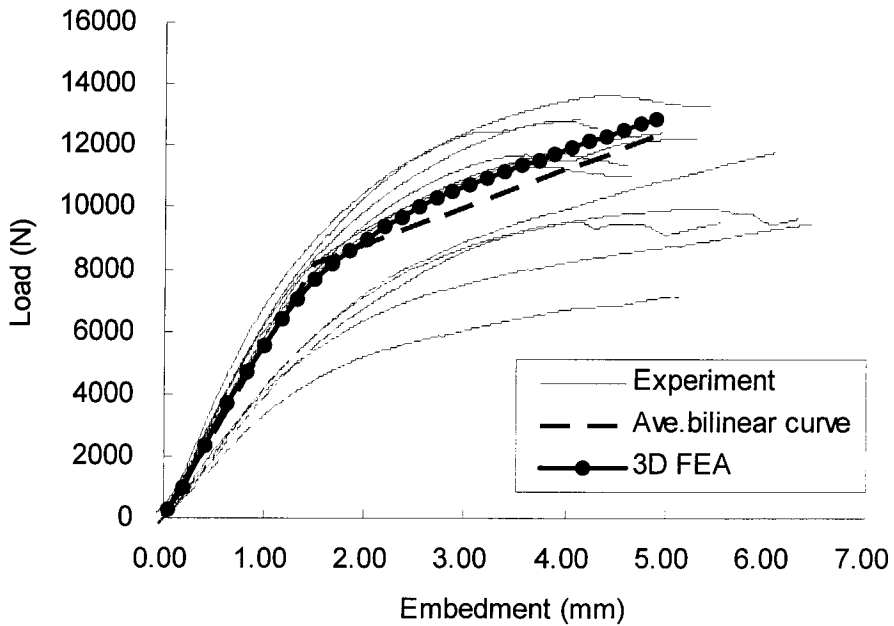


Figure 5.28 Simulated perpendicular to grain load-embedment curve of 19.1-mm bolt embedment in Douglas-fir.

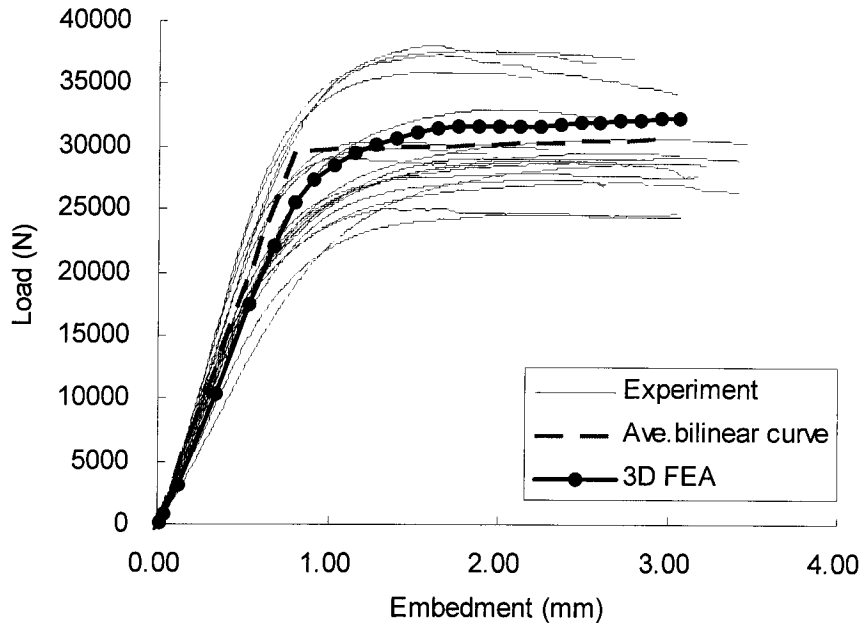


Figure 5.29 Simulated parallel to grain load-embedment curve of 25.4-mm bolt embedment in Douglas-fir.

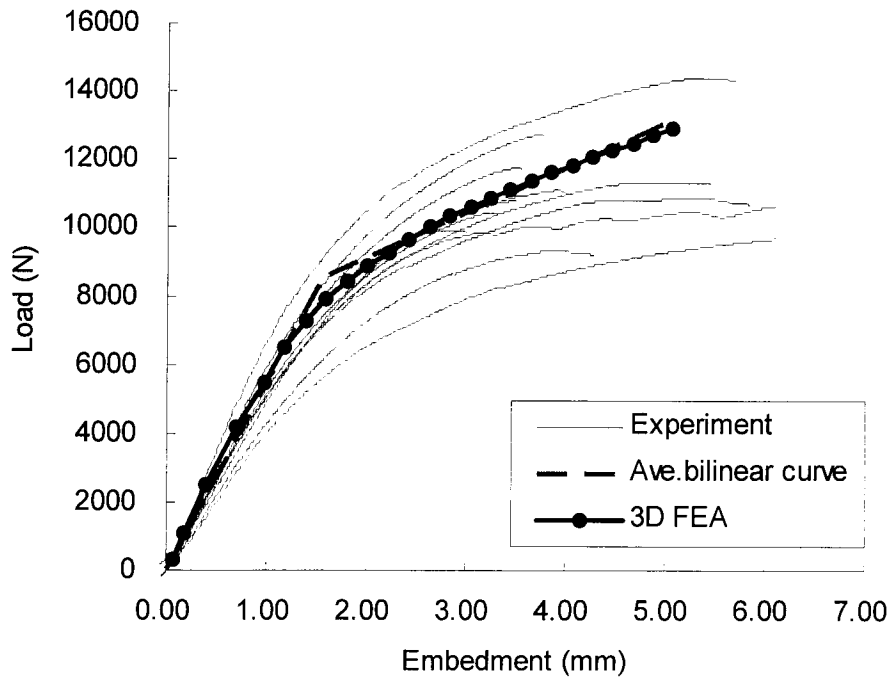


Figure 5.30 Simulated perpendicular to grain load-embedment curve of 25.4-mm bolt embedment in Douglas-fir.

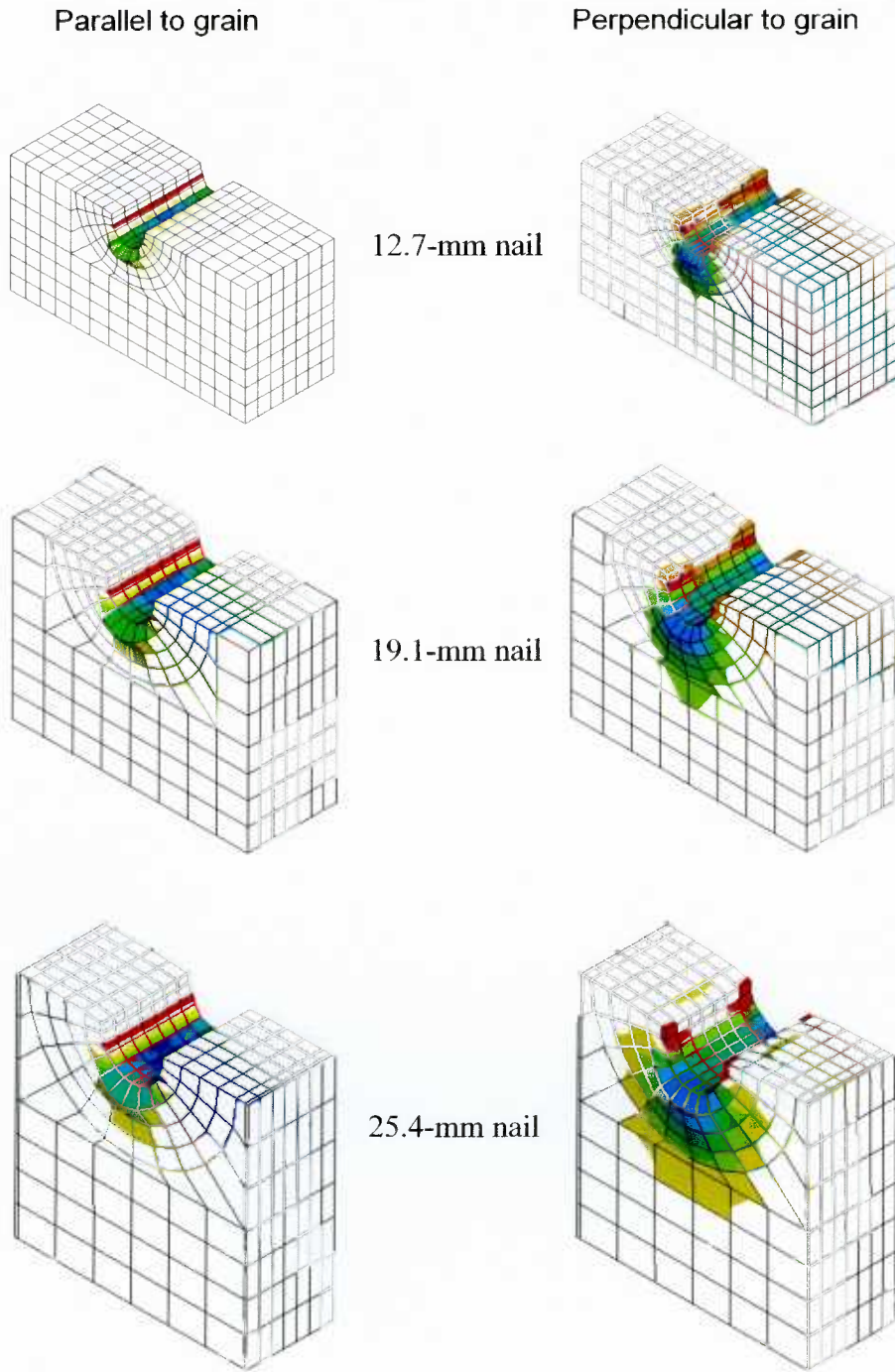


Figure 5.31 Simulated Y-directional plastic strain contours for bolt embedment in Douglas-fir with 12.7-, 19.1- and 25.4-mm bolts in parallel/perpendicular to grain directions.

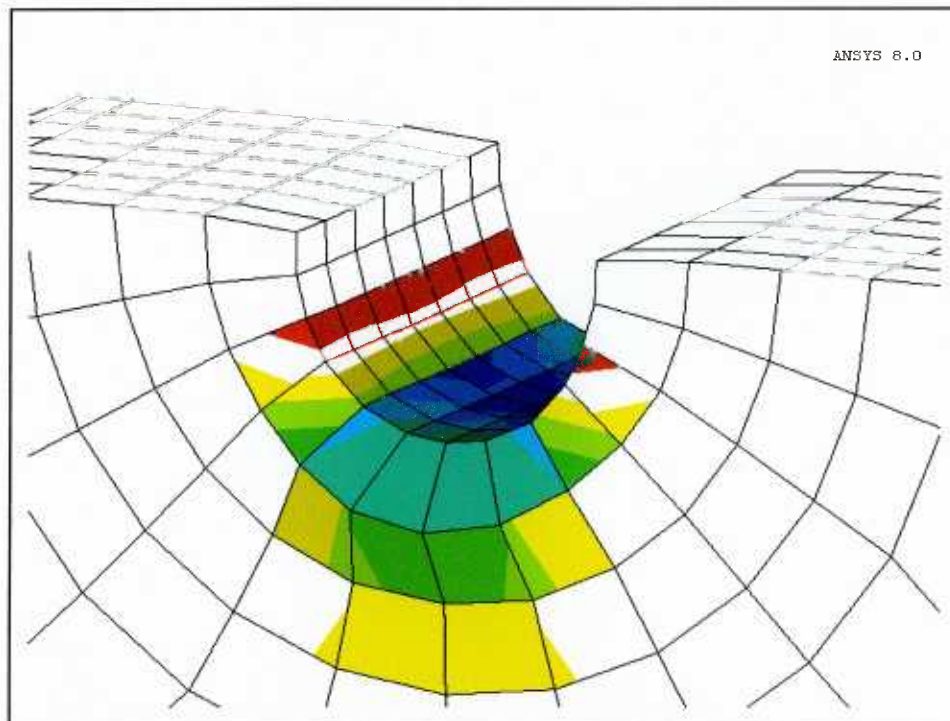
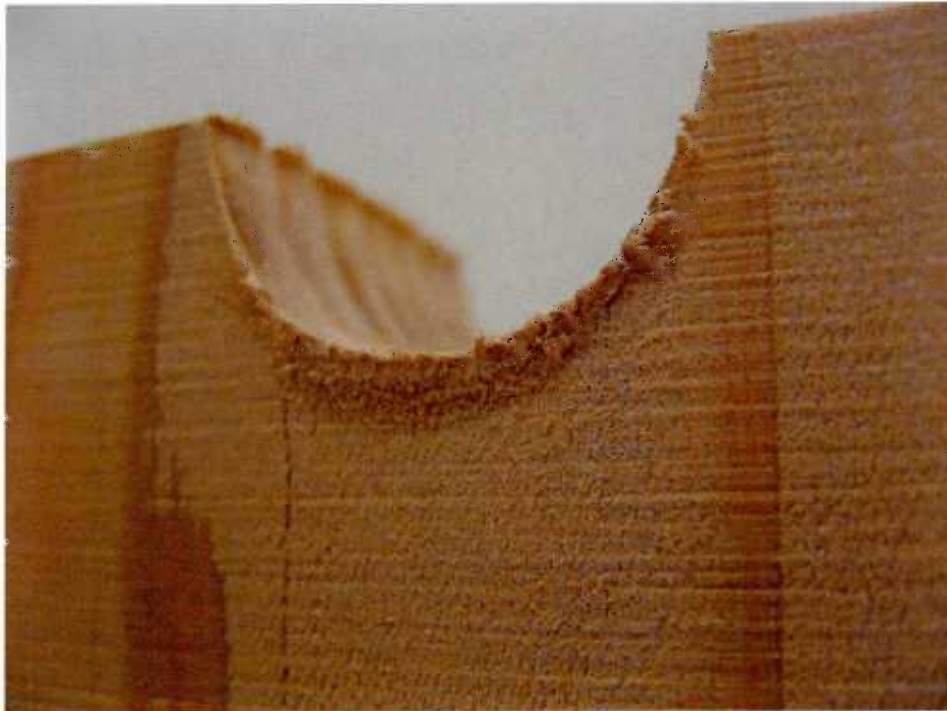


Figure 5.32 Comparison of wood crushing shape for 25.4-mm bolt parallel to grain embedment test. The simulated Y-directional plastic strain contour is shown (bottom).

### 5.3.5 Model application to other species

The application of the nail-embedment test model to other species was investigated using the generalized calibration factors. The test data for 3.8-mm diameter nail embedment on Sugi, Yellow Cedar and Western Hemlock were selected for simulation (Lam et al. 2004).

#### 5.3.5.1 Model description

The test procedure and the 50 mm (width)  $\times$  50 mm (height)  $\times$  38 mm (depth) wood block with a half hole were same as those used in the study by Lam et al. (2004). However, they used a 3.3-mm diameter hole, which is smaller than the 3.8-mm nail diameter in this study. Therefore, the experimental load-embedment curve contained the effects of initial stresses due to the smaller hole. For the 3D FE embedment model, the effect of the smaller hole was not considered. The model was created to have a perfect fit nail hole.

For every species, the material constants were not fully available, especially for yield stress. Thus, the linear elastic model for the wood was assumed. Indeed, it is justifiable because, as found in section 5.3.4.3, plastic deformation outside the wood foundation never occurred in the nail embedment model.

Basic material properties for Sugi and Poisson's ratios of Yellow Cedar were not available. Alternatively, since Western Red Cedar ( $SG = 0.32$ ) has similar mechanical properties to Sugi ( $SG = 0.38$ , own data), the mechanical properties of Western Red Cedar from the Wood Handbook were used for the wood material model. Poisson's ratios of Western Red Cedar were assumed for those of Yellow Cedar. Material properties for the linear elastic models of Yellow Cedar and Western Hemlock were obtained from the

Wood Handbook. The material constants used for the wood material model and wood foundation material model are summarized in Table 5.6 and Table 5.7, respectively.

Except for nail diameter, the generalized calibration factors for the  $4.5 \times d$  foundation, as well as the same model geometry, used for the previous model were applied for these simulations. Note that the generalized calibration factors were developed from the dowel-embedment test data for Douglas-fir.

Table 5.6 Material properties for linear elastic orthotropic wood material.

	Sugi**	Yellow Cedar	W. Hemlock
MOE: L [MPa]	9,240	10,800	13,600
MOE: R=T [MPa]	570	590	550
Shear modulus*: RL=LT [MPa]	1,060	1,170	1,250
Shear modulus*: RT [MPa]	200	210	190
Poisson's ratio: RL	0.02	0.02	0.02
Poisson's ratio: LT	0.34	0.34**	0.45
Poisson's ratio: RT	0.44	0.44**	0.41

\* Computed modulus

\*\* Not available, properties of Western Red Cedar were used alternatively

Table 5.7 Material constants of wood foundation model for Sugi, Yellow Cedar and Western Hemlock.

	Sugi	Yellow Cedar	W. Hemlock
Foundation modulus: L [MPa]	405	440	490
Foundation modulus: R = T [MPa]	67	120	88
Shear modulus: RL=LT [MPa]	72	97	87
Shear modulus: RT [MPa]	23	41	31
Poisson's ratio: RL	0.06	0.09	0.08
Poisson's ratio: LT	0.34	0.34	0.45
Poisson's ratio: RT	0.44	0.44	0.41
Com., ten. yield stress			
: R (=T) [MPa]	5.60	8.50	5.90
: L [MPa]	13.70	16.13	16.90
Com., ten. tangent modulus			
: R (=T) [MPa]	0.66	1.18	0.88
: L [MPa]	4.05	4.42	4.92
Shear yield stress			
: RL (=LT) [MPa]	2.90	3.80	2.74
: RL [MPa]	1.65	2.48	1.75
Shear tangent modulus			
: RL (=LT) [MPa]	0.72	0.97	0.87
: RL [MPa]	0.23	0.41	0.30

### 5.3.5.2 Simulation results

Simulated load-embedment curves superimposed on the experimental curves are presented in Figure 5.33 to Figure 5.38. Although the simulated curves using the generalized calibration factors seemed acceptable overall, it was thought that specific calibration factors optimized for individual species may improve the results. Investigation of the specific calibration factors for each species was not conducted.

For Sugi, the initial and post-yield slopes of the perpendicular to grain curve were simulated slightly high. This may be due to the fact that the foundation modulus factor,  $\alpha_{\perp}$ , of 0.9 and the yield strain factor,  $\beta_{\perp}$ , of 2.8 may be too high for Sugi.

Overall, for all species examined in this section, the model analysis showed stiffer parallel to grain post-yield slopes than the experimental slopes. The differences between the experimental and simulated curves may be attributed to the inappropriateness of the calibration factors for the species, and to the fact that the load-embedment test data included the effect of the initially stressed wood around a nail. Related to 3D FE modeling for nail connections, the initially stressed dowel-embedment test, that is, the “in-service condition test”, may be regarded more reasonable. At the beginning of this study, it was thought that this initial stress state should be simulated by a model; however, it could not be included in the foundation material model. For this reason, the hole was made to fit perfectly to the diameter of nail in the tests. The issue of the initial stress condition test calls for further study.

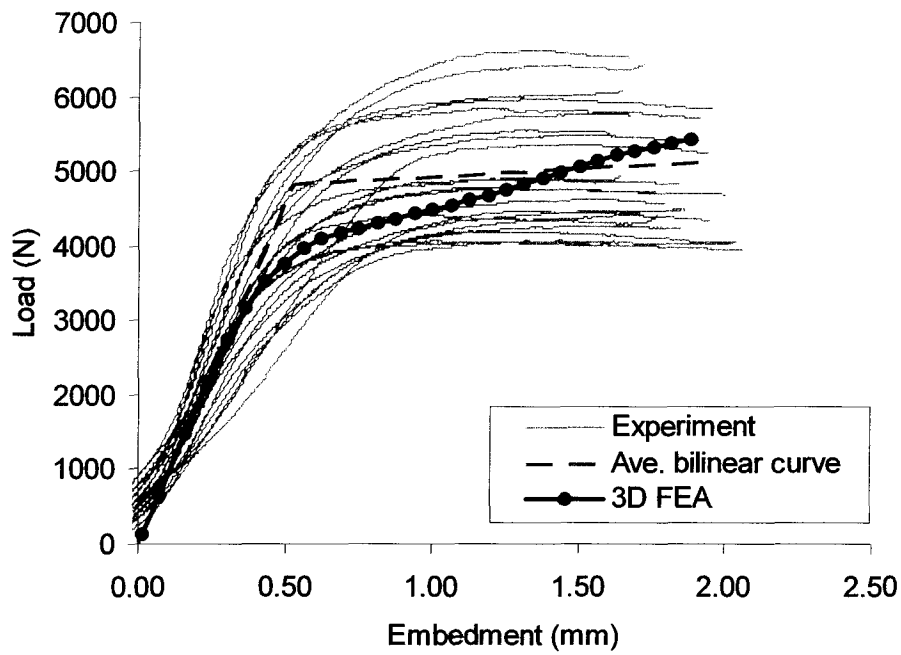


Figure 5.33 Simulated parallel to grain load-embedment curve of 3.8-mm nail embedment in Sugi.

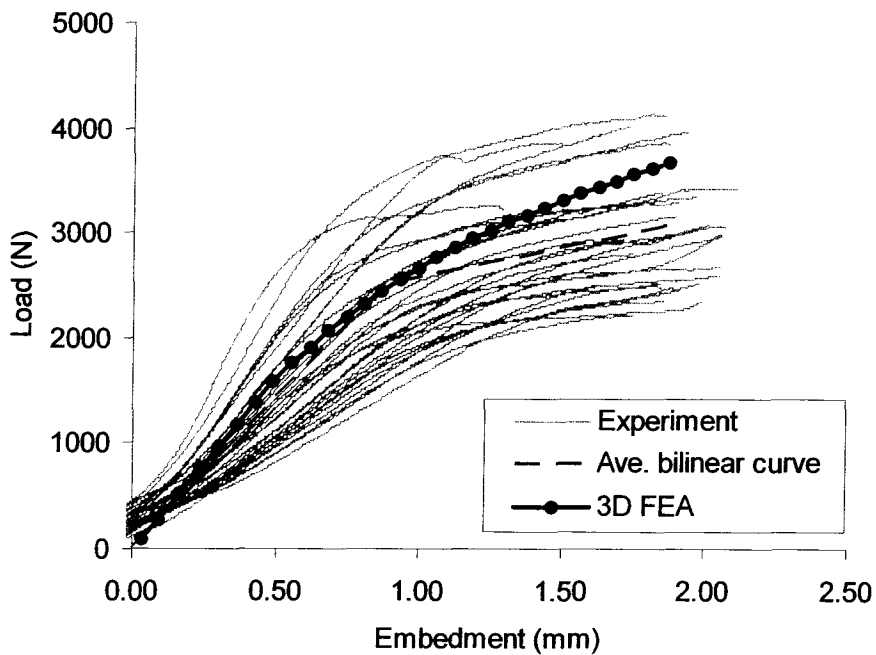


Figure 5.34 Simulated perpendicular to grain load-embedment curve of 3.8-mm nail embedment in Sugi.

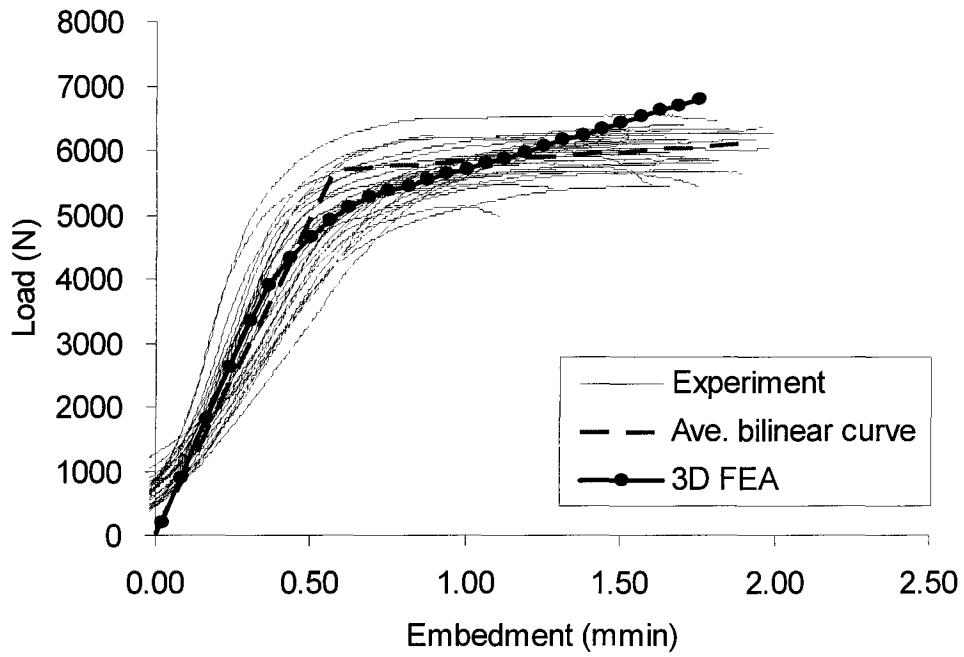


Figure 5.35 Simulated parallel to grain load-embedment curve of 3.8-mm nail embedment in Yellow Cedar.

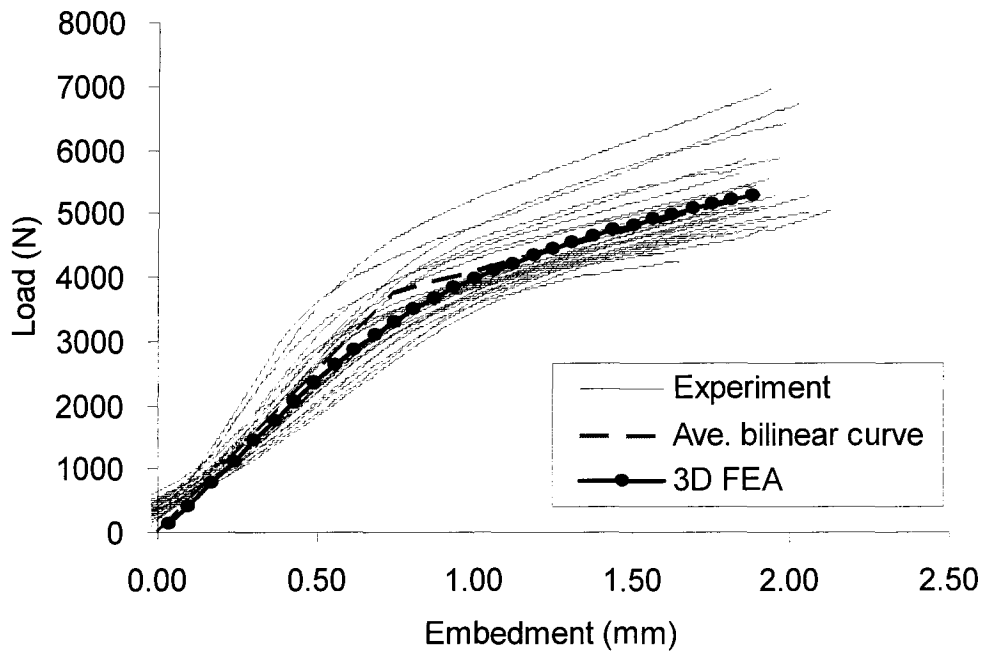


Figure 5.36 Simulated perpendicular to grain load-embedment curve of 3.8-mm nail embedment in Yellow Cedar.

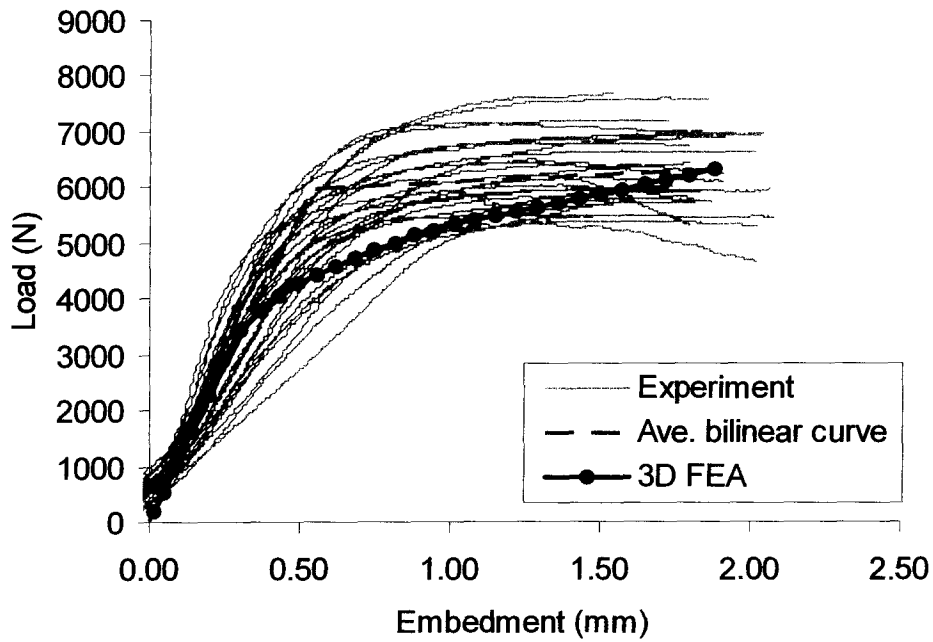


Figure 5.37 Simulated parallel to grain load-embedment curve of 3.8-mm nail embedment in Western Hemlock.

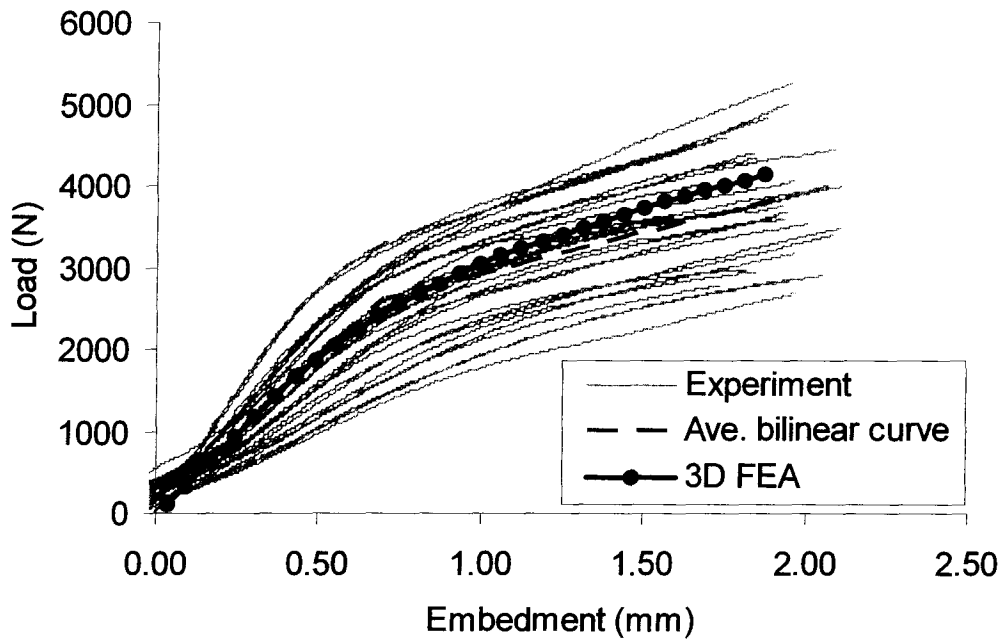


Figure 5.38 Simulated perpendicular to grain load-embedment curve of 3.8-mm nail embedment in Western Hemlock.

### 5.3.6 Calibration factors for intermediate sizes of wood foundation

Determining appropriate size of the wood foundation zone and the corresponding wood foundation material properties was one of the major technical challenges of this work. Relationships between the calibration factors and the size of wood foundation were investigated in detail in order to generalize the wood foundation model with respect to the size of the wood foundation.

Wood foundation zones with diameter multipliers ( $M$ ) of 2.5, 3.0 and 3.5 times diameter of the dowel were selected to construct intermediate wood foundations that had a cylindrical shape. The cylindrical shape provides the simplest shape that would permit modeling of connection deformation in the transverse direction in the wood member (the material properties were assumed to be transversely isotropic). The individual calibration factors ( $\alpha_{//}$ ,  $\alpha_{\perp}$ ,  $\beta_{//}$  and  $\beta_{\perp}$ ) determined for the intermediate foundation were then plotted with the diameter multipliers  $M$ , in order to find the relationships between them.

#### 5.3.6.1 Model description

A 12.7-mm diameter bolt, which was the middle size of dowel in this study, was selected for the dowel-embedment model. In order to incorporate the largest wood foundation ( $4.5 \times d$ ) into the wood block, the wood block model was created with dimensions of 152 mm (width)  $\times$  38 mm (depth)  $\times$  76 mm (height). The other details of the model were the same as those described in the previous dowel-embedment models (see section 5.3.3.2).

Applying the procedures described in section 5.2.2.2, the individual calibration factors for the intermediate foundation were determined. Table 5.8 shows the final individual calibration factors.

Table 5.8 Optimized calibration factors of intermediate wood foundations for a 12.7-mm bolt with Douglas-fir.

Calibration factors	Radius of wood foundation				
	$1.8 \times d^*$	$2.5 \times d$	$3.0 \times d$	$3.5 \times d$	$4.5 \times d$
$\alpha_{//}$	1.50	1.50	1.58	1.65	1.75
$\alpha_{\perp}$	0.75	0.75	0.80	0.80	0.85
$\beta_{//}$	1.70	2.50	2.85	3.15	3.90
$\beta_{\perp}$	1.50	1.60	1.80	1.85	2.10

\*  $d$  is a diameter of the dowel. The factors for the  $1.8 \times d$  wood foundation were taken from the values for the 12.7-mm bolt wood foundation listed in Table 5.5.

### 5.3.6.2 Simulation results

Simulated Y-directional plastic strain contours and load-deformation curves from the respective intermediate wood foundations are shown in Figure 5.39, Figure 5.40 and Figure 5.41. Compared with the results from the  $1.8 \times d$  wood foundation model (shown in Figure 5.31), each and all simulation results showed good agreement without any noticeable differences.

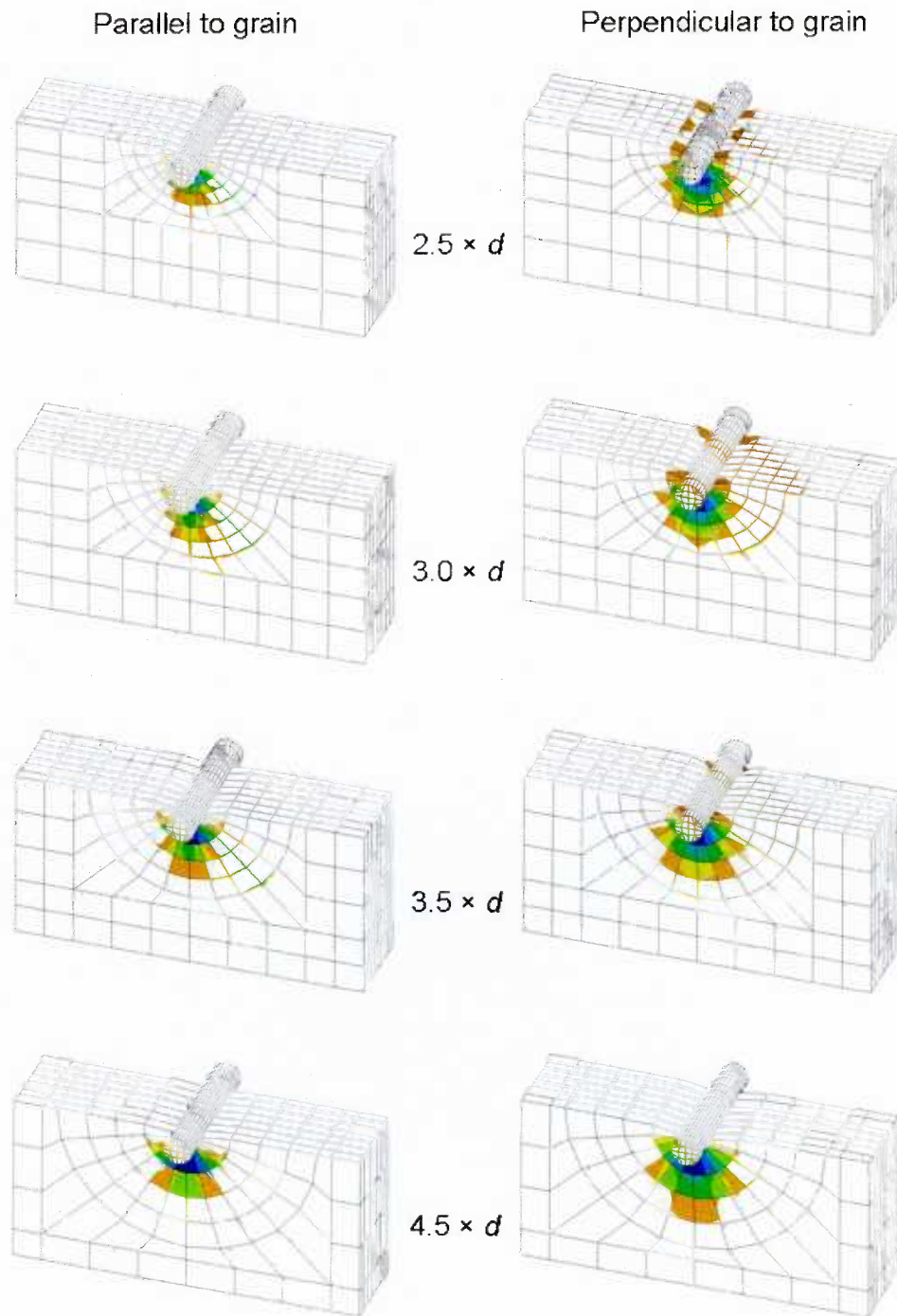


Figure 5.39 Simulated Y-directional plastic strain contours for 12.7-mm ( $d$ ) bolt embedding in Douglas-fir in parallel/perpendicular to grain directions, using the intermediate sized wood foundations.

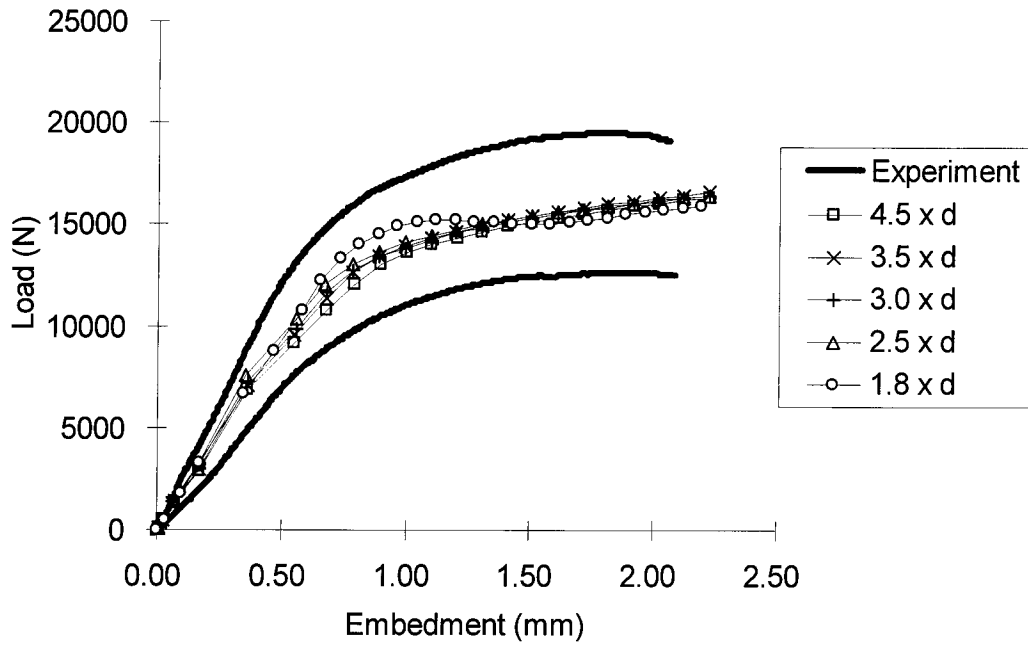


Figure 5.40 Comparison of the parallel to grain load-embedment curves, predicted using the intermediate sized wood foundations.

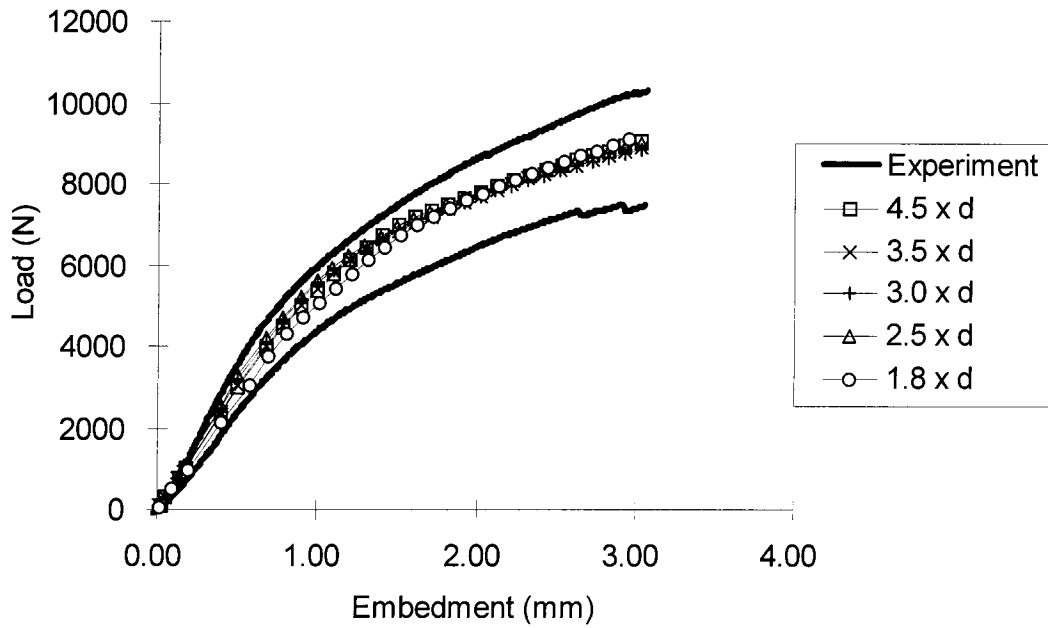


Figure 5.41 Comparison of the perpendicular to grain load-embedment curves, predicted the intermediate sized wood foundations.

### 5.3.6.3 Linear interpolation of calibration factors and size of wood foundation

Using the values in Table 5.8, the individual calibration factors ( $\alpha_{\parallel}$ ,  $\alpha_{\perp}$ ,  $\beta_{\parallel}$  and  $\beta_{\perp}$ ) were plotted with the diameter multipliers ( $M$ ). The relationships between the individual calibration factors and the multipliers showed almost linear. A linear regression model for each calibration factor is provided in Figure 5.42.

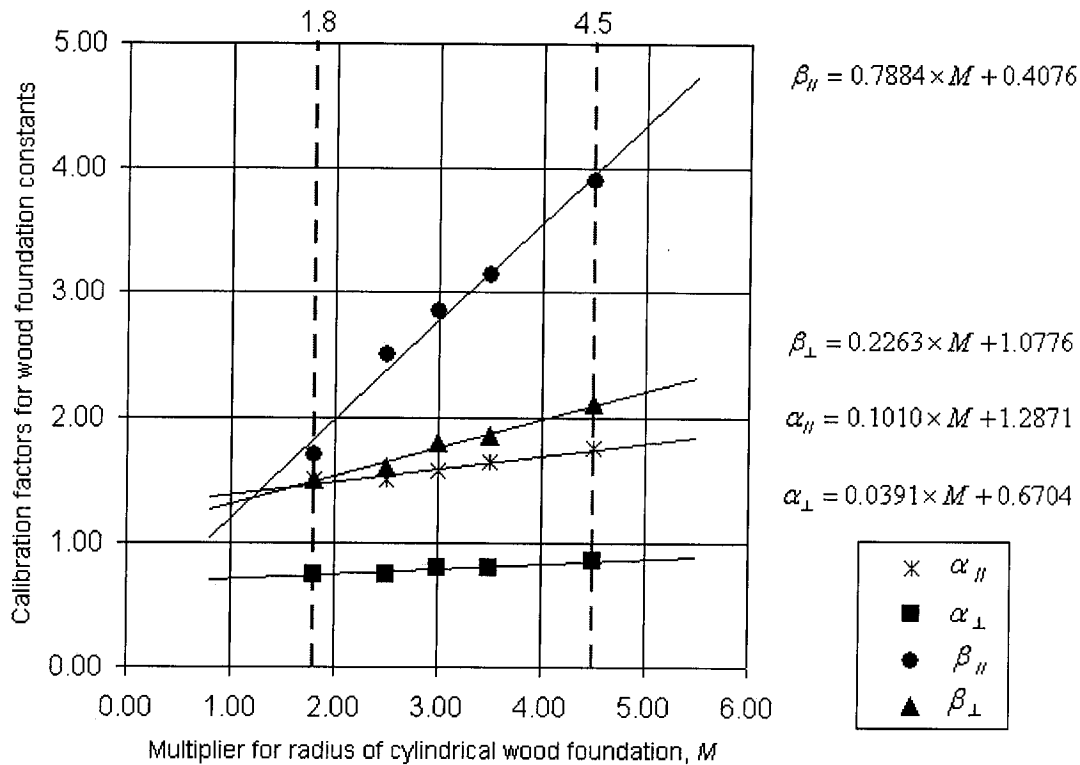


Figure 5.42 Assumed linear relationships between the radius multiplier and the calibration factors.

Under a cylindrical wood foundation, the regression models imply that the stiffness of wood foundation increases and the yield strain decreases in a linear manner with increases in the radius of the wood foundation.

Compared with the calibration factors optimized for nails with a  $4.5 \times d$  wood foundation, the calibration factors optimized for the bolt with the  $4.5 \times d$  wood

foundation showed differences (for nails,  $\alpha_{//} = 1.70$ ,  $\alpha_{\perp} = 0.90$ ,  $\beta_{//} = 4.2$  and  $\beta_{\perp} = 2.8$ ; and, for the 12.7-mm bolt,  $\alpha_{//} = 1.75$ ,  $\alpha_{\perp} = 0.85$ ,  $\beta_{//} = 3.90$  and  $\beta_{\perp} = 2.10$ ). Although the use of the calibration factors optimized for nails produced acceptable results for the bolt-embedment simulation with a  $4.5 \times d$  wood foundation, the accuracy of the results became less than with the use of the factors optimized for the bolt. This confirmed the finding in section 5.3.4.4 that the calibration factors were influenced by the size of dowel diameter.

Provided that extensive experiments and simulations were conducted to determine the relationships among the calibration factors, the diameter size of the dowel and the size of wood foundation, more integrative generalization of the calibration factors could be achieved. This may be a good area for future.

## CHAPTER 6. THREE-DIMENSIONAL FINITE ELEMENT MODEL OF NAIL CONNECTIONS

The lateral resistance behaviour of a single nail connection with a steel side plate was simulated using the 3D FE model incorporating the wood foundation concept. The ability of the FE model to simulate the load-slip characteristics of the connection was verified by comparing the simulated results to the experimental findings. To demonstrate the model characteristics, a study was also conducted to assess the ability of the model to predict the statistical variation of the load-slip data for nailed connections.

### 6.1 Lateral resistance test of the single nail connection

For model validation, six lateral resistance tests of a single nail connection with a steel plate were conducted in parallel to grain and perpendicular to grain loading directions. Depending on the loading direction, the test specimen was denoted as PA for the parallel to grain direction and PE for the perpendicular to grain direction. The specimens, PA and PE, were tested with nails driven into the radial surface (R) and the tangential surface (T). Suffixes of “R” and “T” have been used to denote the different cases.

The test specimen consisted of a galvanized wire nail hand-driven into a 105 mm (width)  $\times$  105 mm (depth)  $\times$  250 mm (length) Douglas-fir block with a 2.2 mm-thick T-shaped steel plate. The nail used was the Japanese standard ZN65 nail, and the T-shaped steel plate was the standard Japanese steel nail plate with ten pre-bored nail holes, called a CP-T connector. Figure 6.1 shows details of the plate. The CP-T connector with ten ZN65 nails driven in form the traditional Japanese post and beam standard connection. Specifications of the materials used are summarized in Table 6.1.

The configurations of the lateral resistance tests are illustrated in Figure 6.2 and Figure 6.3 for each direction. For a single nail connection, one test nail was driven into the wood specimen through a pre-bored hole located at the bottom centre of the connector and, in order to link the connector to the moveable crosshead, five nails were driven to wooden spacers through the upper five pre-bored holes. The wooden spacers were used to position the shear plane of the connection to the centre line of the crosshead. The speed of loading was set to 0.1 mm/sec, and one DCDT (direct current differential transformer) was installed on the nail-driven face for the measurement of deformation.

Table 6.1 Material specifications of the single nail connection.

Component	Material specifications
Wood medium	Dry Douglas-fir Specific gravity : 0.535 Dimensions: 105 mm (width) × 105 mm (depth) × 250 mm (length)
Nail	Japanese standard ZN65 Length : 65 mm Shank diameter : 3.3 mm Nail head diameter : 7.20 mm Nail head thickness : 1.68 mm
Steel plate	Japanese standard CP-T connector Thickness : 2.2 mm

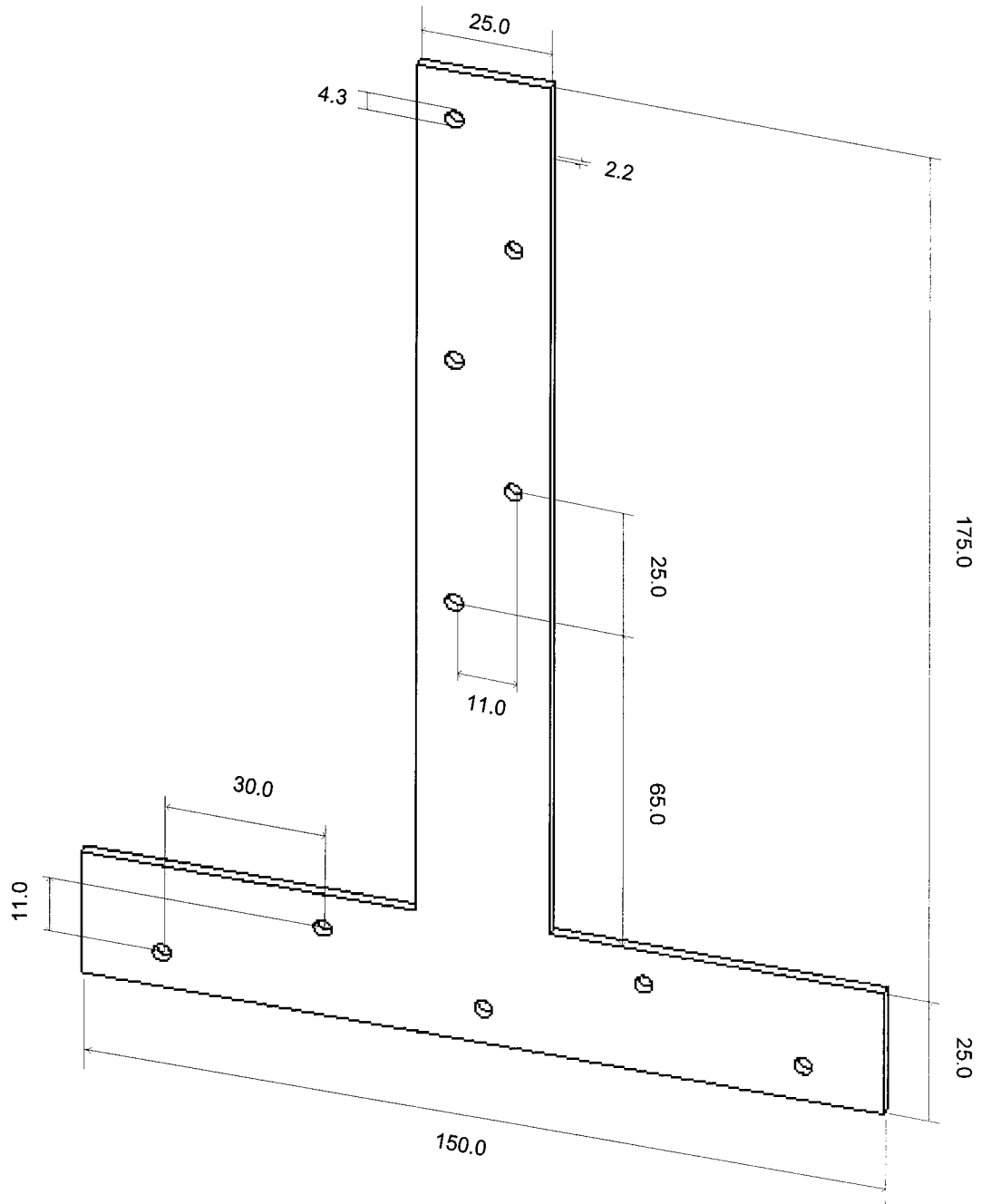


Figure 6.1 Specification of Japanese CP-T connector (units: mm).

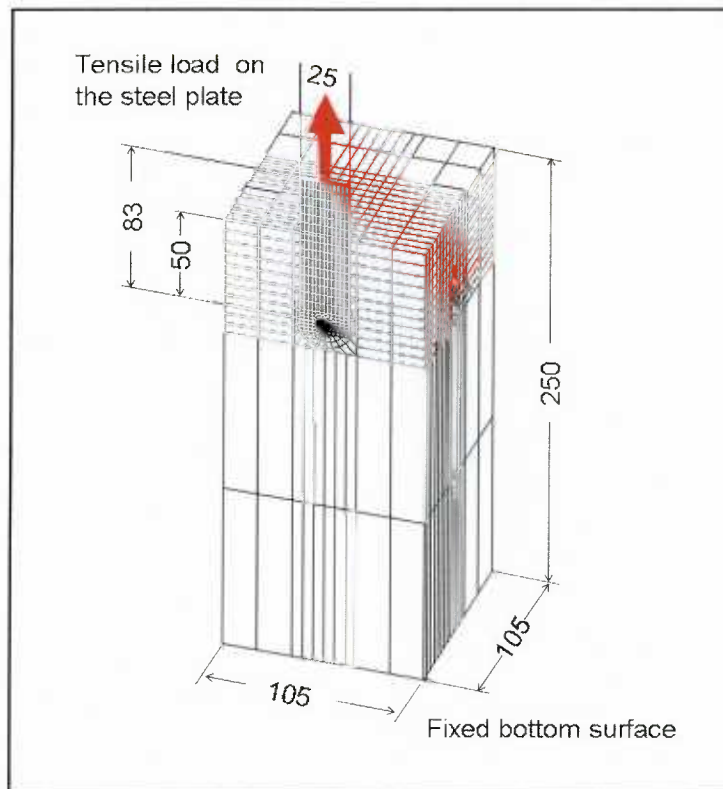


Figure 6.2 Lateral resistance test of single nail connection in parallel to grain direction and the corresponding three-dimensional FE model (units: mm).

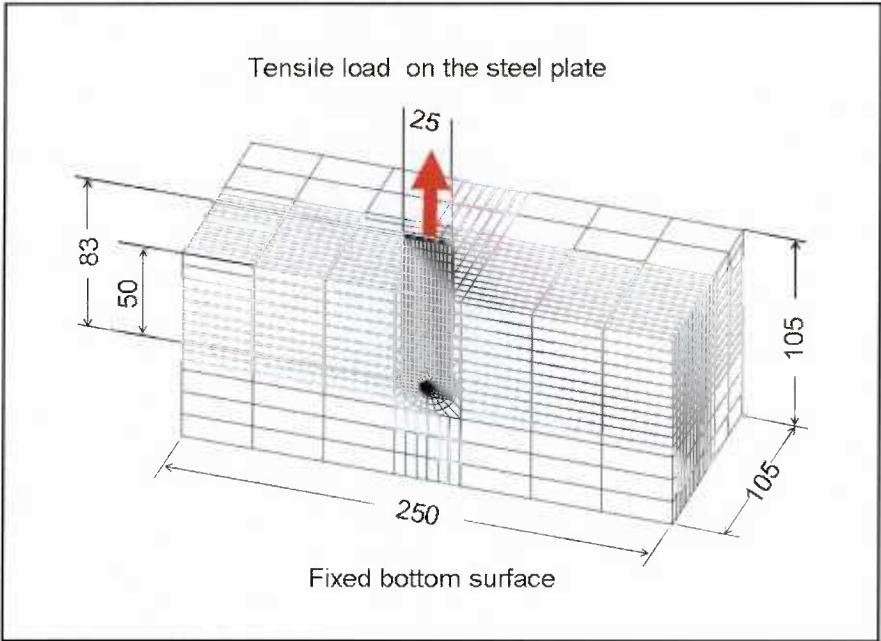
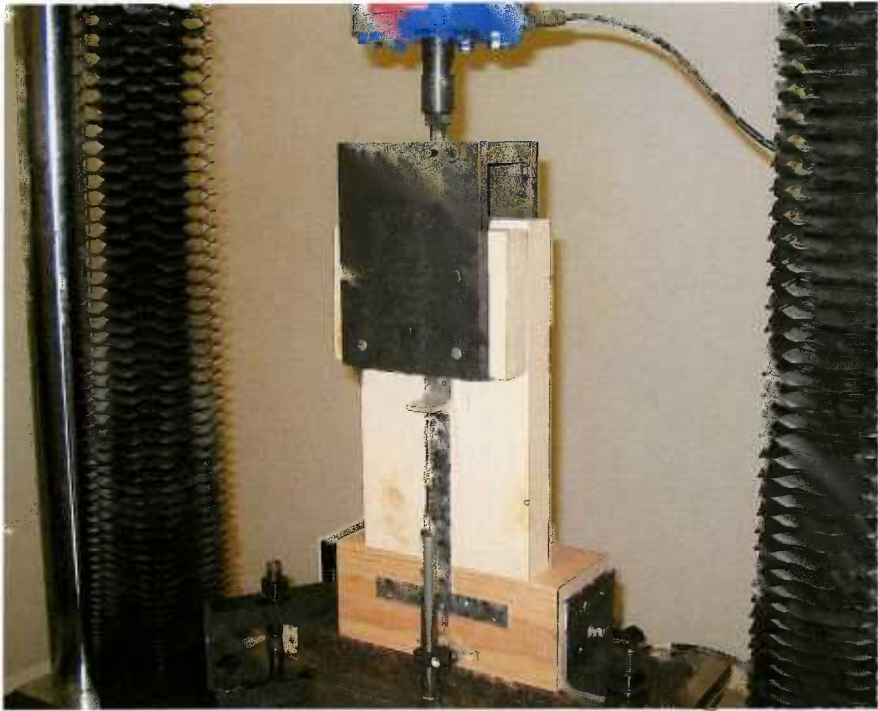


Figure 6.3 Lateral resistance test of the single nail connection in the perpendicular to grain direction and the corresponding three-dimensional FE model (units: mm).

## 6.2 Development of the single nail connection model

### 6.2.1 Model description

Figure 6.2 and Figure 6.3 show the three-dimensional finite element models for the single nail connections in the parallel to grain and perpendicular to grain directions. The model consists of three separate parts including the wood, a nail and a steel plate, all of which were generated with solid elements (SOLID45). As the wood foundation model was incorporated into the wood member, the wood elements contained one of two different material attributes. The wood foundation material properties, derived from the 3.3-mm nail-embedment model, were assigned to the  $4.5 \times d$  cylindrical foundation zone. Wood material properties (WOOD11) were assigned to the remaining wood elements.

Figure 6.4 shows the mesh of the 3D FE single nail connection model. The mesh scheme used for the nail-embedment model was adopted for the connection model. All contact surfaces between the nail, steel plate and wood volumes were modeled by surface-to-surface contact elements (CONTA174 and TARGE170), as shown in Figure 6.5. The coefficients of friction were 0.7 and 0.3 for the wood-to-steel contact interfaces and the nail-to-plate contact interfaces, respectively.

The bottom surface of the wood member was fixed for the boundary condition. A tensile load was applied to the end surface of the steel plate. Owing to parametric modeling, the perpendicular to grain model could be easily changed to the parallel to grain model just by modifying the parameters of the member dimension and element coordinate.

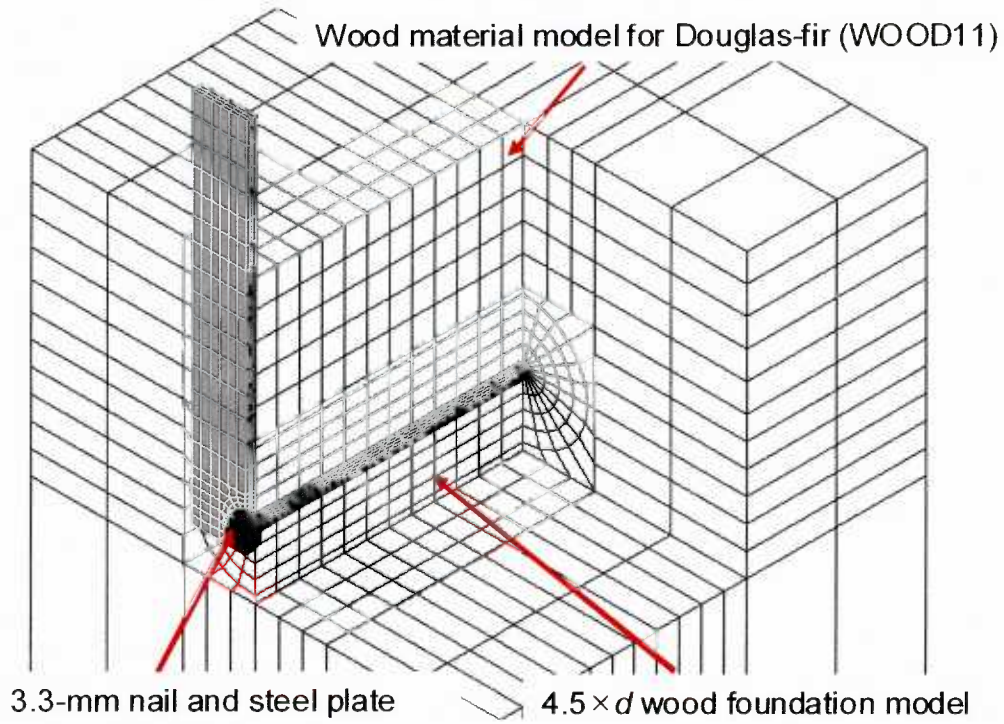


Figure 6.4 Sectioned single nail connection FE model.

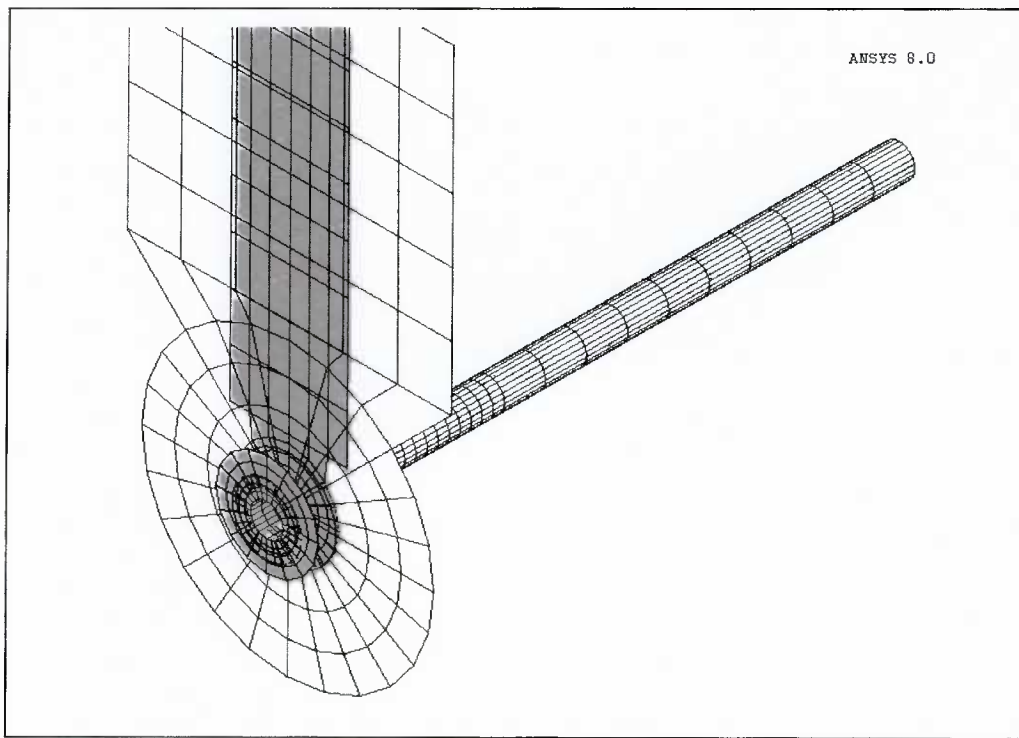


Figure 6.5 Surface-to-surface contact elements of the single nail connection model.

### **6.2.2 Steel material model and mechanical properties of the nail and steel plate**

An elasto-perfectly plastic material model was used for the steel materials, which included the nail and steel plate. As the load-slip behaviour of the connection always created highly plastic bending deformation in the nail, accurate mechanical properties were necessary for the steel material model.

For nail, the mechanical properties including yield stress ( $\sigma_{yt}$ ) and Young's modulus (MOE) should be determined through a tensile test (Foschi et al. 1977, Chui et al. 1998). The material properties obtained from a three-point nail bending test would be erroneous, due to non-uniform stress distribution, test machine deformation and partial yielding in the circular cross section of the nail (Chui et al. 1998).

Generally, the nail tensile test would be conducted with raw steel wire, which provides sufficient grip length. Unfortunately, a tensile test for the ZN65 nail could not be conducted, because the length of the nail (65 mm) was too short to provide adequate gripping power to create tension failure.

Alternatively, the mechanical properties of the nail and the steel plate could be estimated, based on the material specifications and existing values in literature. However, the estimation for the yield stress of the nail was complicated by the fact that data from the literature provided a wide range of yield stresses, which are listed in Table 6.2. Also, the data available from the manufacturer were general specifications of mild steel wire (JIS G 3532, SWM-N). Since the specification could not be relied upon to give an accurate yield stress of the ZN65 nail, a method to determine the yield stress using 3D

FE analysis (FEA) for nail bending was devised. Determination of the steel properties is detailed in the next section.

Table 6.2 Material specification and reference mechanical properties of nail and steel plate.

Material	Data source	Material specifications			
Nail	ZN65 Kaneshin company	-Manufacturer: Kaneshin Co. Ltd. (in Japan)			
		-3.3 mm-diameter zinc-coated (galvanized), low carbon steel wire for nail			
	-JIS G 3532, SWM-N				
	- Common nail				
	Foschi et al., 1977* Foschi, 2000**	Diameter [mm]	MOE [GPa]	$\sigma_{yt}$ [MPa]	
		3.50**	200	250 MPa	
			4.06*	200	
			622 MPa		
	Common steel wire for nail				
			Diameter [mm]	MOE [GPa]	$\sigma_{yt}$ [MPa]
Chui et al., 1998			2.78	194	810
			3.17	194	761
			3.69	193	711
			4.08	193	680
			Average	193	741
Steel plate	CP-T plate Kaneshin company	-Manufacturer: Kaneshin Co. Ltd. (in Japan)			
	-2.2 mm-thick hot-dip zinc-coated steel sheet				
		-JIS G 3302, SGHC-Z27			
		-3 mm-thick steel plate for Japanese post and beam connector			
Finckenstein, 1999		-MOE = 197 GPa			
		- $\sigma_{yt}$ = 276 MPa			

### 6.2.2.1 Mechanical properties of nail

The yield stress of the ZN65 nail was determined using 3D FE analysis for three-point nail bending. As shown in Figure 6.6, fifteen ZN65 nails were tested according to ASTM F 1575–Standard test method for determining bending yield strength for nails. Then, the average load-deflection curve from the bending test was obtained for comparison with the 3D FE analysis. Table 6.3 shows the list of some candidate material constants used

for simulation of three-point ZN65 nail bending. An MOE of 200 GPa was adopted for the analysis.

For comparison, a reference yield load of 360 N was used, which was the load at the breaking point of the average bilinear curve fitted to the experimental curves. A yield stress of 517 MPa was identified as the yield stress that produced the best fit to the reference yield load.

Figure 6.7 shows all the simulated load-deflection curves using the candidate yield stress inputs. It should be noted that as Chui et al. (1998) mentioned, machine deformation caused discrepancy of the initial stiffness, due to the different displacement-measurements obtained from the crosshead and transducer readings. The load data was recorded only by the load cell. They corrected this discrepancy. Therefore, if the correction was also applied to the bending test data, it was assumed that the experimental initial bending stiffness would match the simulated stiffness.

Finally, based on this determination, the elasto-perfectly plastic material model for the ZN65 nail was constructed with a yield stress of 517 MPa, MOE of 200 GPa and Poisson's ratio of 0.3. Also, in order to investigate the effect of yield stress input for the nail material model, simulations with the yield stress of 310 MPa were conducted.

Table 6.3 Steel material constant inputs for 3D FEA of ZN65 nail bending.

	Data input for FEA: Yield stress /MOE	Predicted bending yield load	Experimental yield load
Foschi's data (2000)	250 MPa / 200 GPa	180 N	
Estimated value (final)	517 MPa / 200 GPa	360 N	360 N
Foschi et al.'s data (1977)	622 MPa / 200 GPa	440 N	
Chui et al.'s data (1998)	741 MPa / 200 GPa	510 N	

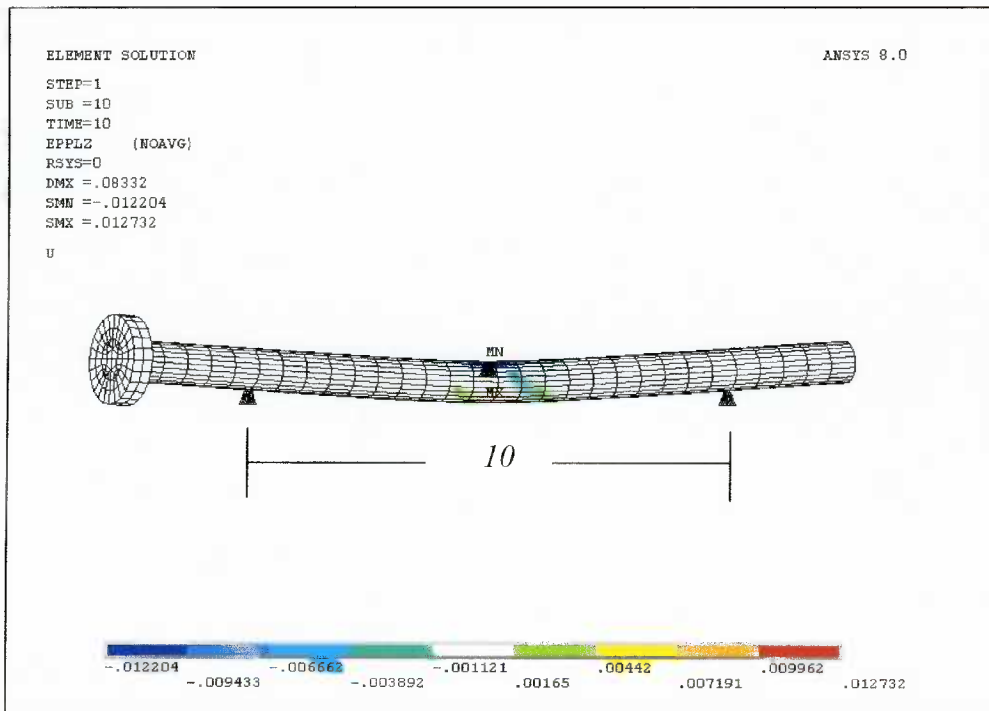


Figure 6.6 Three-point nail bending test setup (top) and simulated bending of ZN65 nail with the yield stress of 517 MPa (bottom).

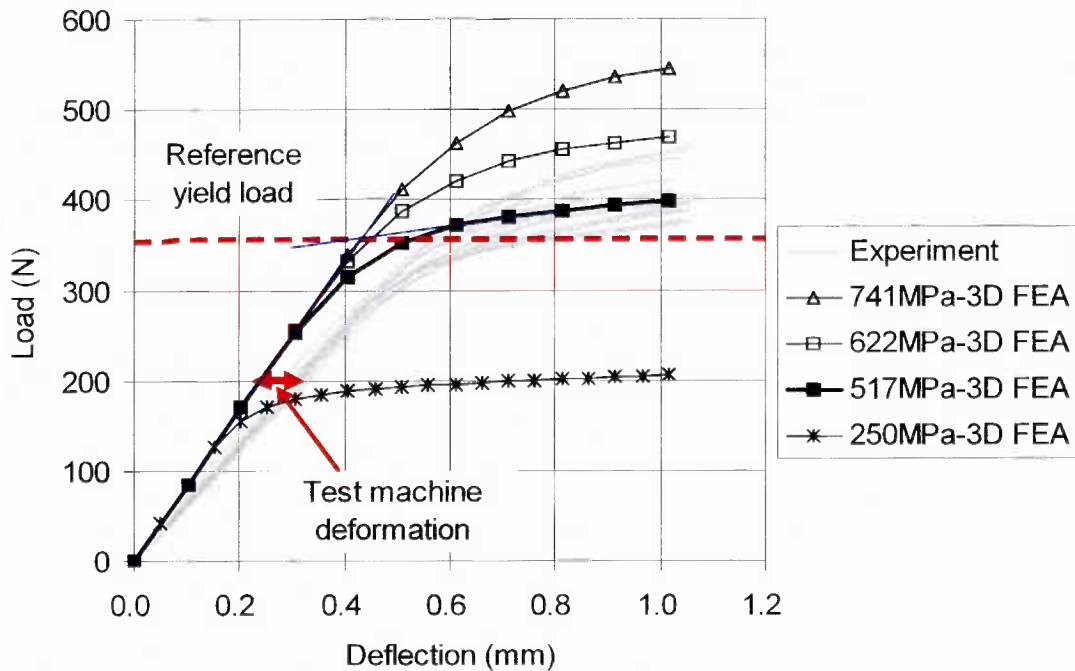


Figure 6.7 Load-deflection curve of three-point ZN65 nail bending and trace of 3D FE analysis for the yield stress.

### 6.2.2.2 Mechanical properties of the CP-T steel plate

The CP-T plate was made of hot-dipped zinc-coated steel sheet for common use (JIS G 3302, SGHC-Z27). The sheet steel material had a yield stress of 250 MPa and an MOE of 200 GPa (Steel and tube 2000). Also, Finckenstein's (1999) tensile coupon test for the Japanese post and beam connector (the material specifications were unknown) revealed a yield stress of 276 MPa and MOE of 197 GPa. Thus, the CP-T connector was assumed to have a yield stress of 250 MPa, MOE of 200 GPa and Poisson's ratio of 0.3.

## 6.3 Test results and model validation

### 6.3.1 Experimental observations for load-slip behaviour of the nail connection

All lateral resistance tests of the single nail connection exhibited an abrupt failure by nail-head shear-off. The ultimate resistance,  $F_{\max}$ , and the slip at  $F_{\max}$  are summarized in Table 6.4.

Photo images of typical wood crushing failure under the nail are presented in Figure 6.8 and Figure 6.9. The crushing pattern under the nail differed, depending on the surface that was loaded. Noticeably, the slip behaviour of the PAR specimen showed a strong tendency for the nail to crush wood along a layer of earlywood. This phenomenon resulted in a very ductile failure (Figure 6.14) and relatively low ultimate resistance (average PAR;  $F_{\max} = 3590$  N at 22.1 mm vs. average PAT;  $F_{\max} = 4100$  N at 11.1 mm).

For the CP-T connector, relatively little permanent deformation was observed around the nail hole. The 2.2 mm thickness of the steel plate was sufficient to shear off the nail-head in all tests without severe permanent deformation of itself. These experimental observations were used as comparison points to validate the FE model.

Table 6.4 Lateral resistances of the single nail connections.

Loading direction	Nail-driven surface	Specimen number	Ultimate resistance $F_{\max}$ [N]	Slip at $F_{\max}$ [mm]
Parallel to grain	Tangential	1PAT	3810	11.1
		2PAT	3720	12.8
		3PAT	4780	9.4
		Average	4100	11.1
	Radial	1PAR	3230	33.1
		2PAR	3290	19.3
		3PAR	4250	14.1
		Average	3590	22.1
		<b>Total average</b>	<b>3850</b>	<b>16.6</b>
		Perpendicular to grain	Tangential	1PET
2PET	4230			9.4
3PET	4500			9.6
Average	4160			11.4
Radial	1PER		3700	19.0
	2PER		3950	19.7
	3PER		4770	9.1
	Average		4140	15.9
	<b>Total average</b>		<b>4150</b>	<b>13.7</b>

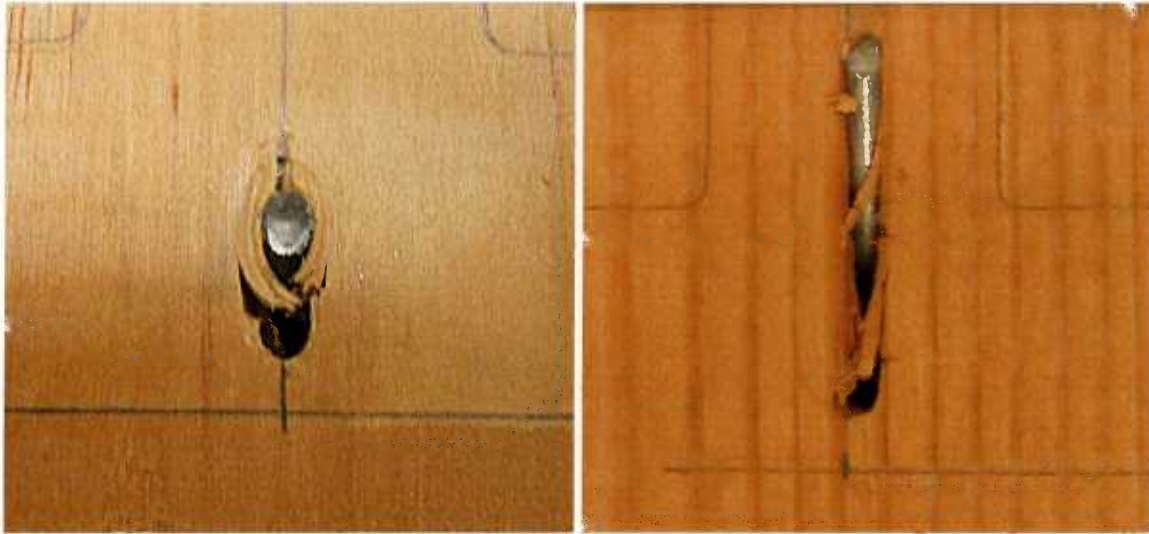


Figure 6.8 Localized wood crushing failure in the parallel to grain direction: nail on the tangential surface-PAT (left), and nail on the radial surface-PAR (right).



Figure 6.9 Localized wood crushing failure in the perpendicular to grain direction: nail on the tangential surface-PET (left), and nail on the radial surface-PER (right).

## 6.3.2 Simulated results and model validation

### 6.3.2.1 Simulated deformation

Although the macroscopic FE model could not simulate the detailed fibre crushing failures, especially those influenced by earlywood, the overall simulated deformation of the nail connection showed good agreement with the experimental observation (Figure 6.10).

In Figure 6.11, the simulated deformed shape of the nail was superimposed on a photo image of the sectioned wood specimen. Although the nail-head shear-off was not predicted by the plasticity-based FE model, the simulated deformed shape of the nail fitted well to the observed embedded wood.

The model showed very little permanent deformation around the nail hole of the steel plate. The predicted permanent deformation of the steel plate is presented by the plastic contour plot in Figure 6.12.

Simulation of the permanent wood deformation around the nail is shown in Figure 6.13. Compared to the real behaviour shown in Figure 6.8 and Figure 6.9, it was found that the model predicted the wood fibre failures, in terms of plastic deformation of the wood foundation.

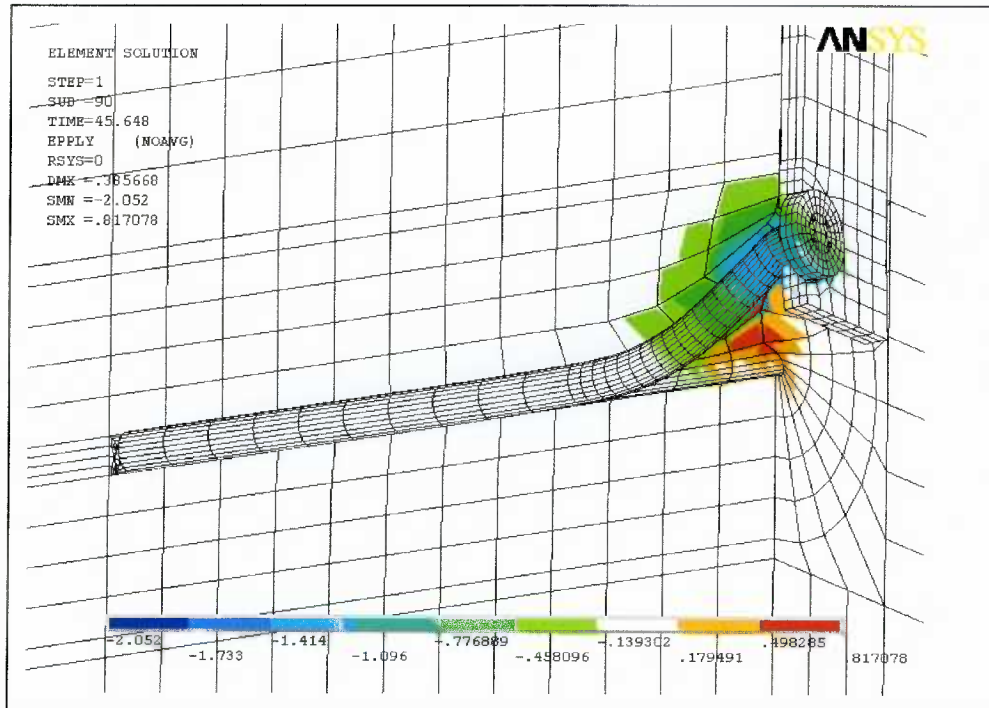


Figure 6.10 Slip behaviour in the parallel to grain direction: experiment (top) vs. simulation (bottom) for the PA test.

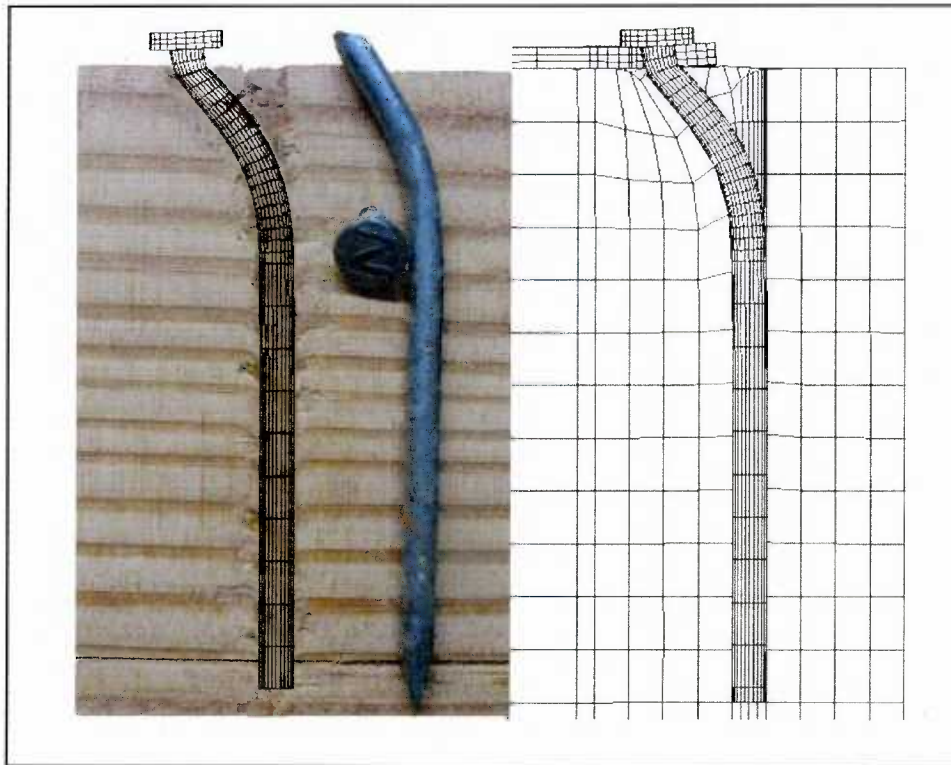


Figure 6.11 Simulated deformation of the nail connection was superimposed on the best fit photo image from the real deformation (the PAT specimen).

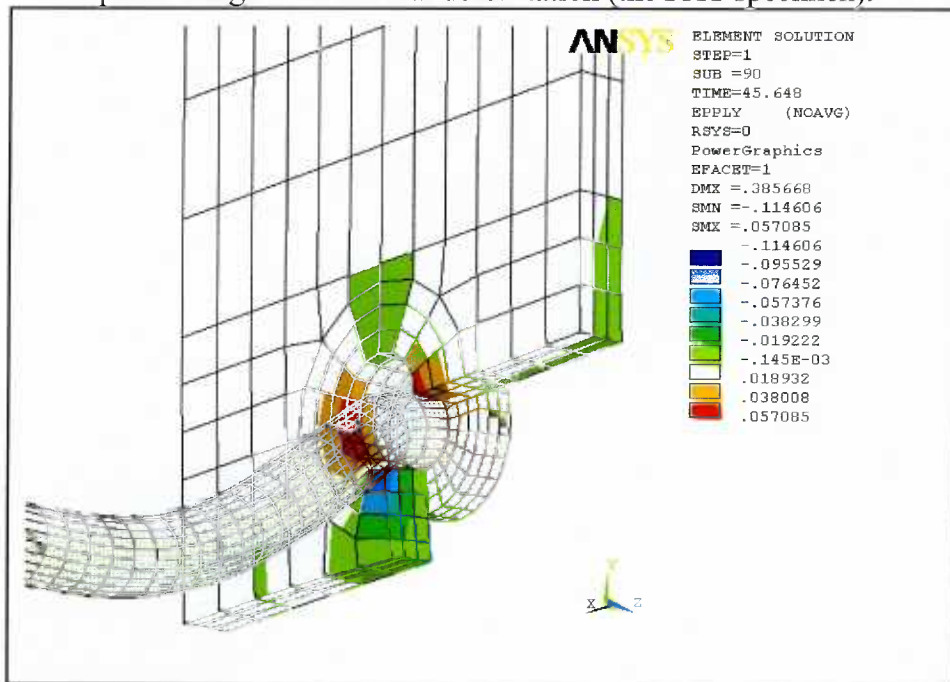


Figure 6.12 Simulated Y-directional plastic strain contour of the steel plate in the PA test. Wood-to-steel plate contact surface view including transparent nail elements.

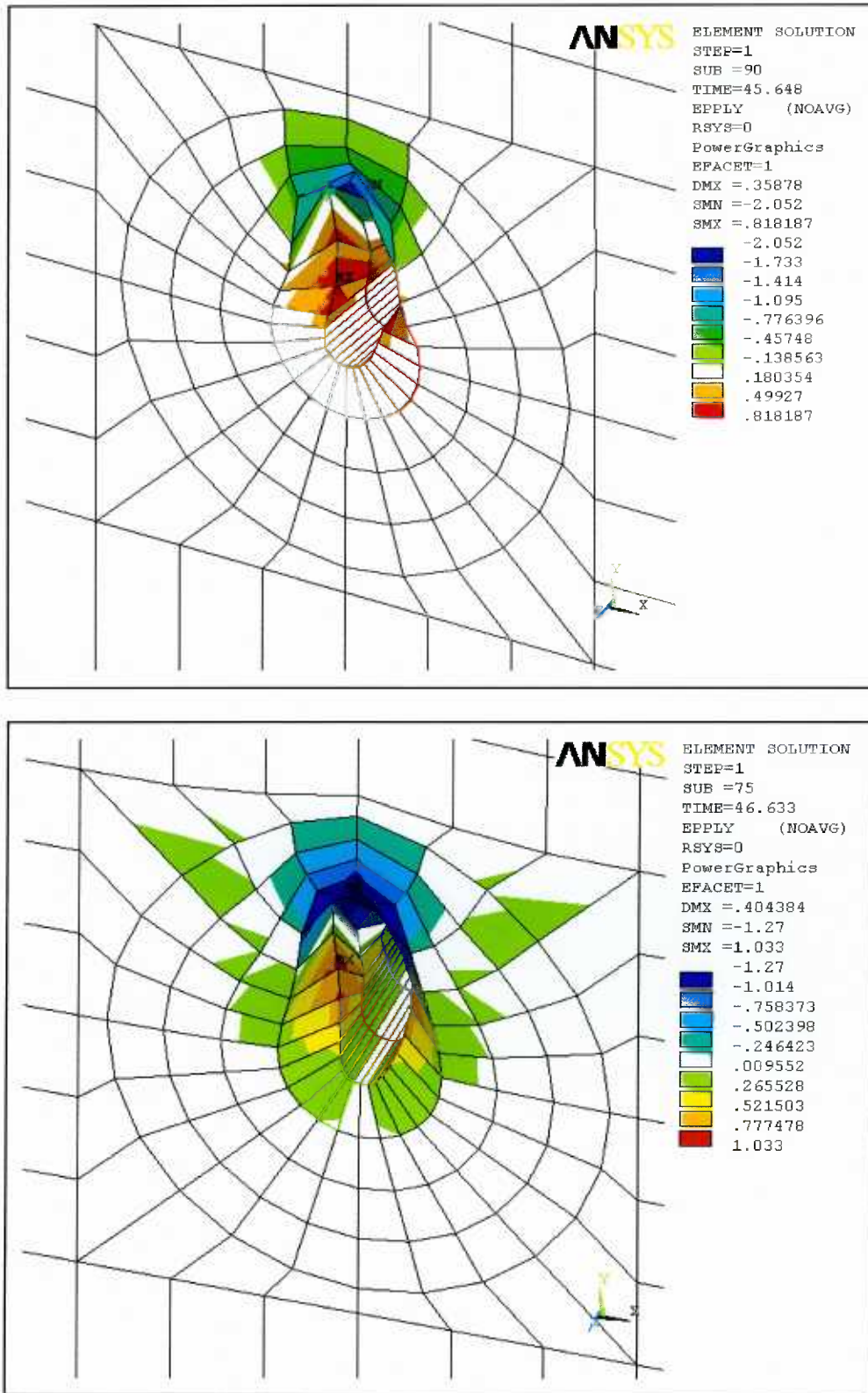


Figure 6.13 Simulated wood crushing shapes. Y-directional plastic strain contour plots; PA simulation (top), PE simulation (bottom).

### 6.3.2.2 Load-deformation relationship

The simulated load-deformation curves with the nail yield stress of 517 MPa for the connection are superimposed on the experimental curves in Figure 6.14 and Figure 6.15. The simulation with the nail yield stress of 310 MPa was also included. The simulated curves showed good agreement with the average experimental curve overall for both directions of loading, although a large variation of experimental curves was observed.

In fact, the average material constants-based model could predict only one average load-deformation curve. Prediction for this variation of curves could not be expected from one material model. However, it was suggested that if a statistical approach was applied to the material modeling, the variation would be partly simulated (a feasibility study of statistical material modeling is presented in section 6.4).

The model showed limits to the length of the predicted slip. Over these limits, excessive distortion of certain brick elements was assumed to cause termination of the analysis. However, the predicted load-deformation curves were suitable for analysis or design purposes.

Table 6.5 shows a comparison of the simulated lateral resistance to the average experimental results at the slip interval of 1.5 mm. It was intended to verify the model's capability for simulating the slip process. Using the data in Table 6.5, the lateral resistance-slip relationships were plotted, as shown in Figure 6.16 and Figure 6.17. In the early stages of slip, the simulated resistances agreed well with the experimental data in both directions. Then, the curves became more or less 10% higher than the experiments around the slip of 3 mm. The progress of the deformed shape in each direction is illustrated in Figure 6.18 and Figure 6.19.

### 6.3.2.3 Effect of nail yield stress on the 3D FE connection model

Adopting a nail yield stress of 310 MPa reduced the connection resistance. The simulation results confirmed that the nail yield stress had a significant effect on the connection resistance.

The simulated load-deformation curves with the nail yield stress of 310 MPa revealed the peak loads as 3,150 N at a slip of 7.3 mm for the PA case and 3,260 N at a slip of 7.8 mm for the PE case. The curves then started to drop down. Indeed, it was quite interesting to find that, as shown in Figure 6.20 and Figure 6.21, excessive plastic elongation of the nail elements occurred at the shear plane. This was a rare case and did not happen in other analyses. It was assumed that a state of uncontained plastic flow was occurring, and the plastic flow in the yielded elements was not resisted by any elastic strains (Chen et al. 1988). This was a potential indicator of nail-head shear off.

Compared to the experimental curves, the simulations using the yield stress of 310 MPa showed premature nail yielding in both directions. It justified the finding that the yield stress of the ZN65 nail should be over 310 MPa, which has been generally used as the common yield stress of mild steel for numerical analysis.

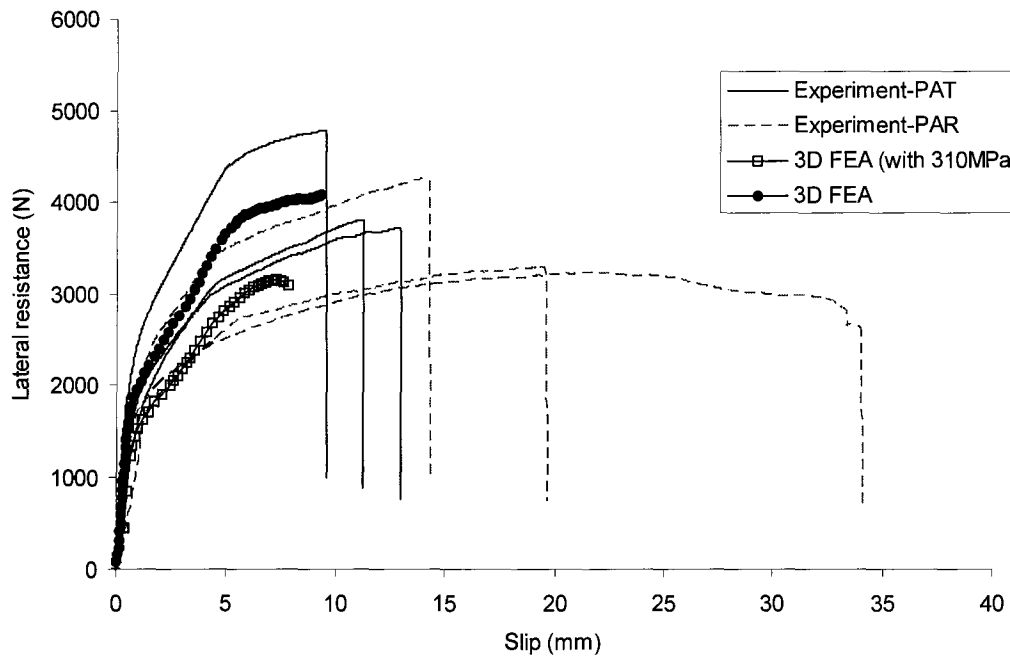


Figure 6.14 Simulated load-deformation curve of the single nail connection in the parallel to grain direction.

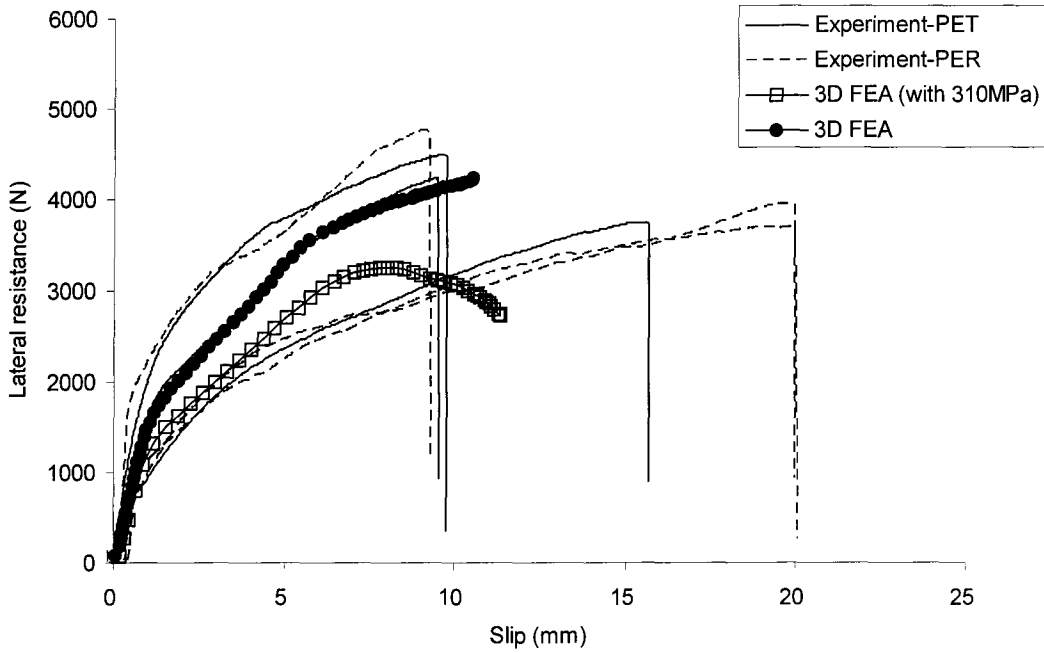


Figure 6.15 Simulated load-deformation curve of the single nail connection in the perpendicular to grain direction.

Table 6.5 Comparison of the lateral resistance of nail connection at a slip interval of 1.5 mm.

Test specimen	Data	Slip (mm)						
		0.50**	1.50	3.00	4.50	6.00	7.50	9.00
PA	Test average (N)	1310	2240	2780	3240	3490	3620	3730
	3D FEA (N)	1510	2240	2840	3500	3880	3990	4050
	Ratio**	0.87	1.00	0.98	0.93	0.90	0.91	0.92
PE	Test average (N)	875	1810	2440	2850	3190	3480	3700
	3D FEA (N)	790	1870	2480	3070	3610	3890	4060
	Ratio**	1.11	0.97	0.99	0.93	0.88	0.89	0.91

\* Initial slip point, comparable.

\*\* Ratio= Test average/3D FEA.

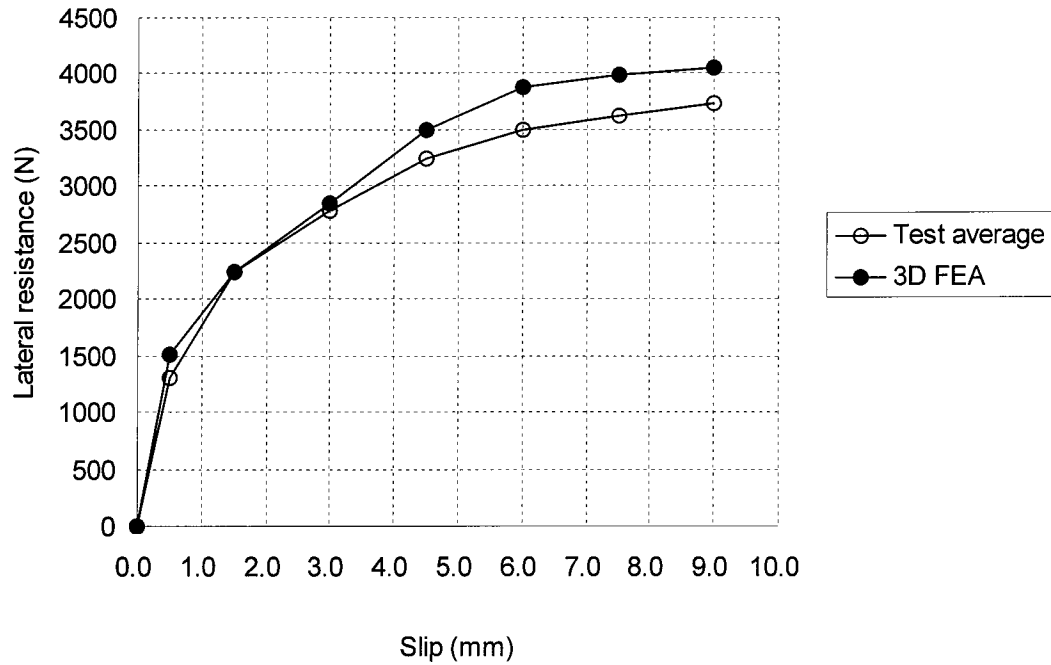


Figure 6.16 Comparison of the simulated nail-slip curve to the average test data at intervals of the 1.5 mm slip for the parallel to grain nail connection test (PA test).

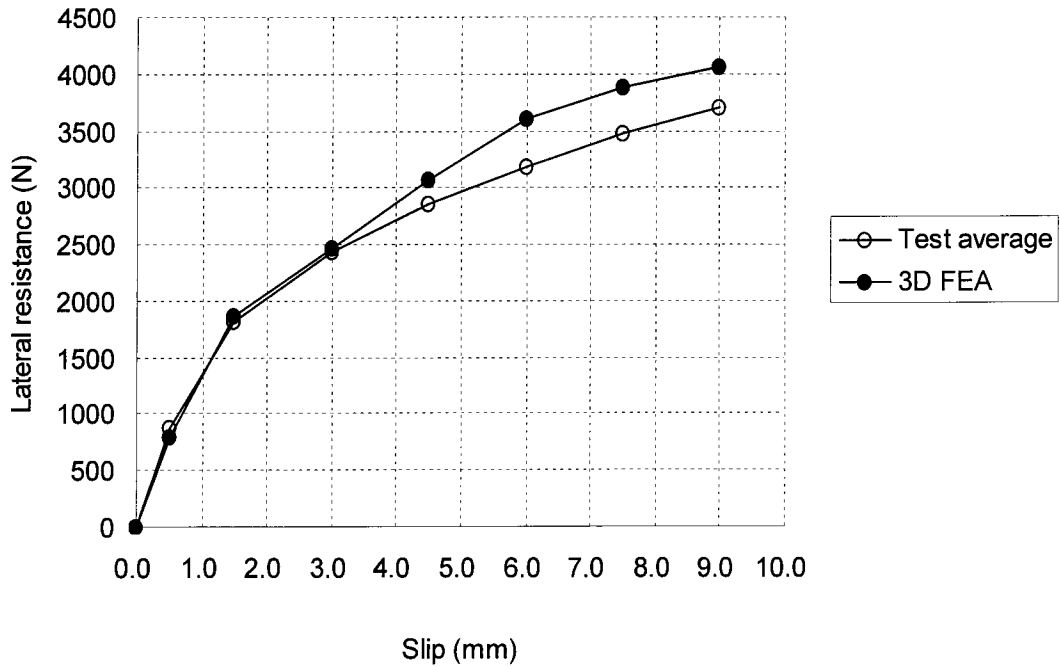


Figure 6.17 Comparison of the simulated nail-slip curve to the average test data at intervals of the 1.5 mm slip for the perpendicular to grain nail connection test (PE test).

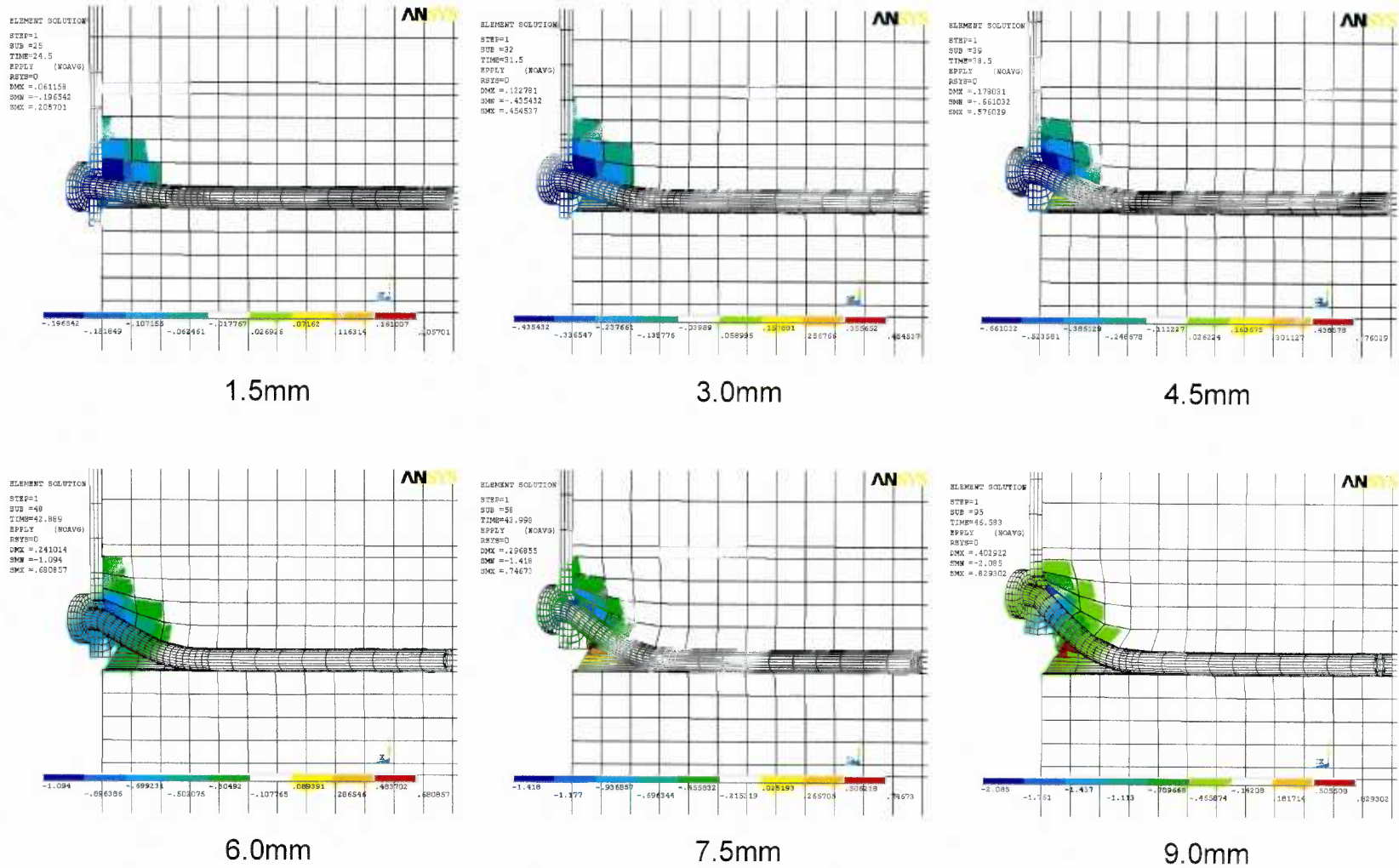


Figure 6.18 Deformation progress at each interval slip for the parallel to grain connection test. Y-directional plastic strain (PA simulation).

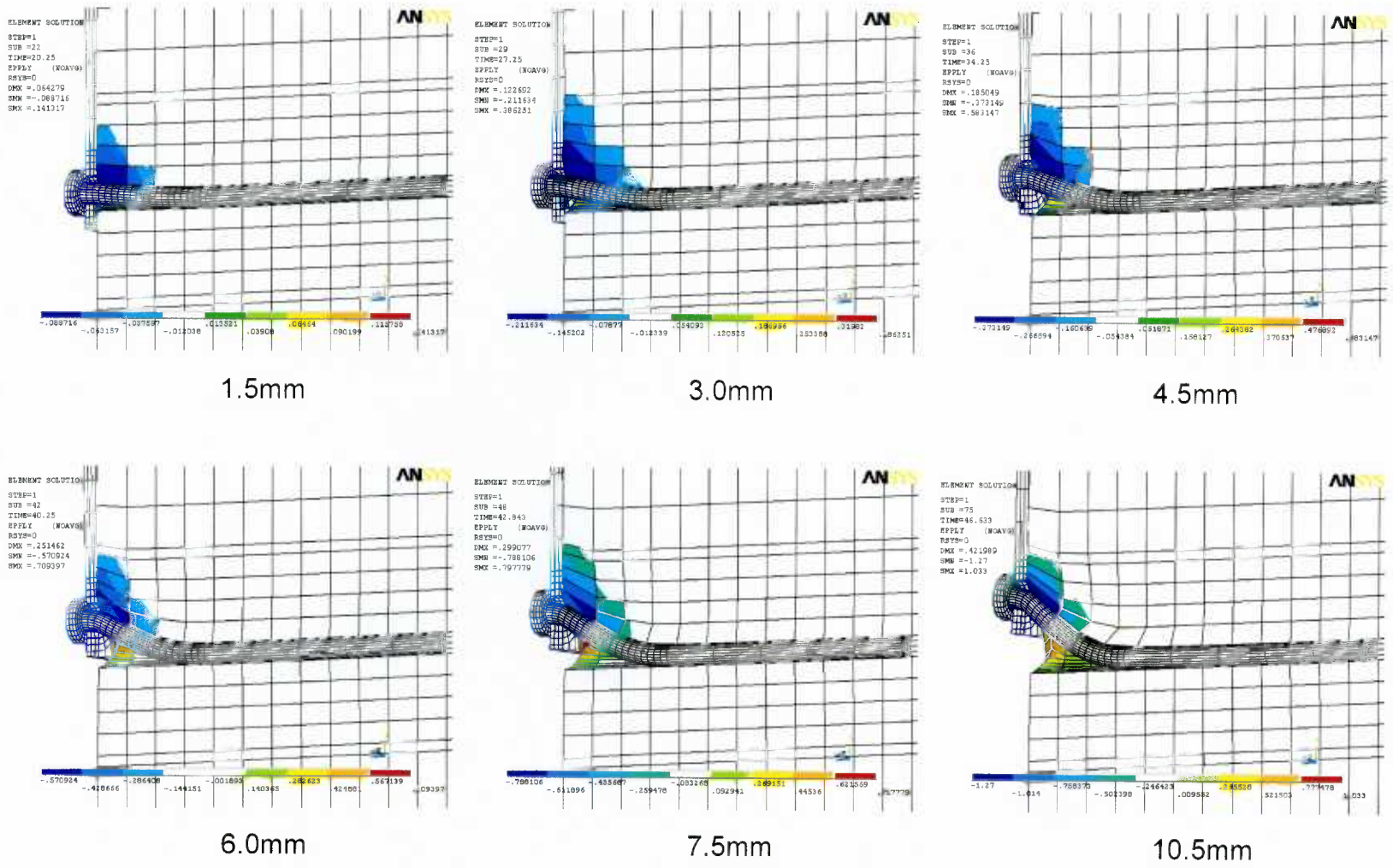


Figure 6.19 Deformation progress at each interval slip for the perpendicular to grain connection test. Y-directional plastic strain (PE simulation).

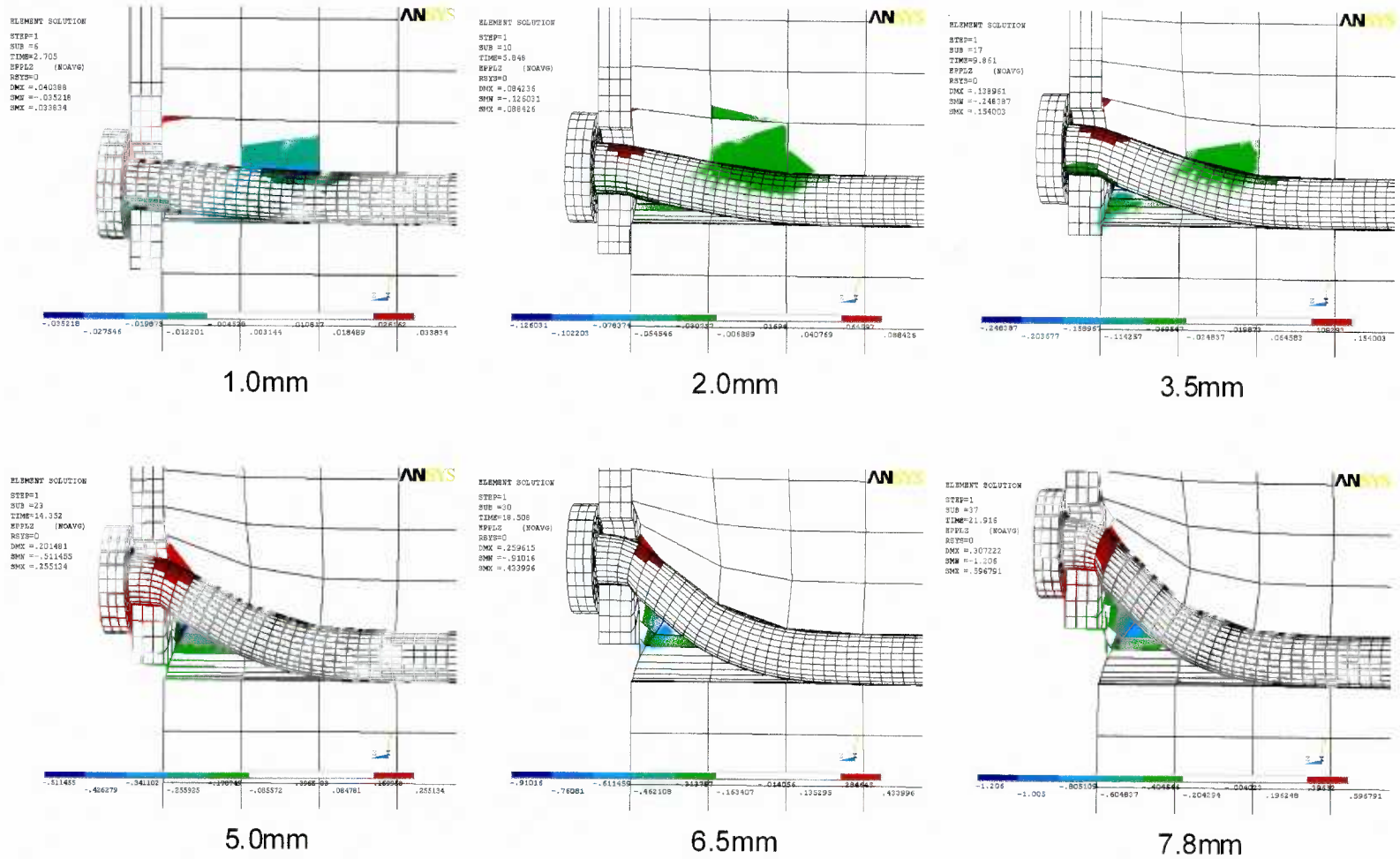


Figure 6.20 Progress of Z-directional plastic strain for the PA connection model with a nail yield stress of a 310 MPa.

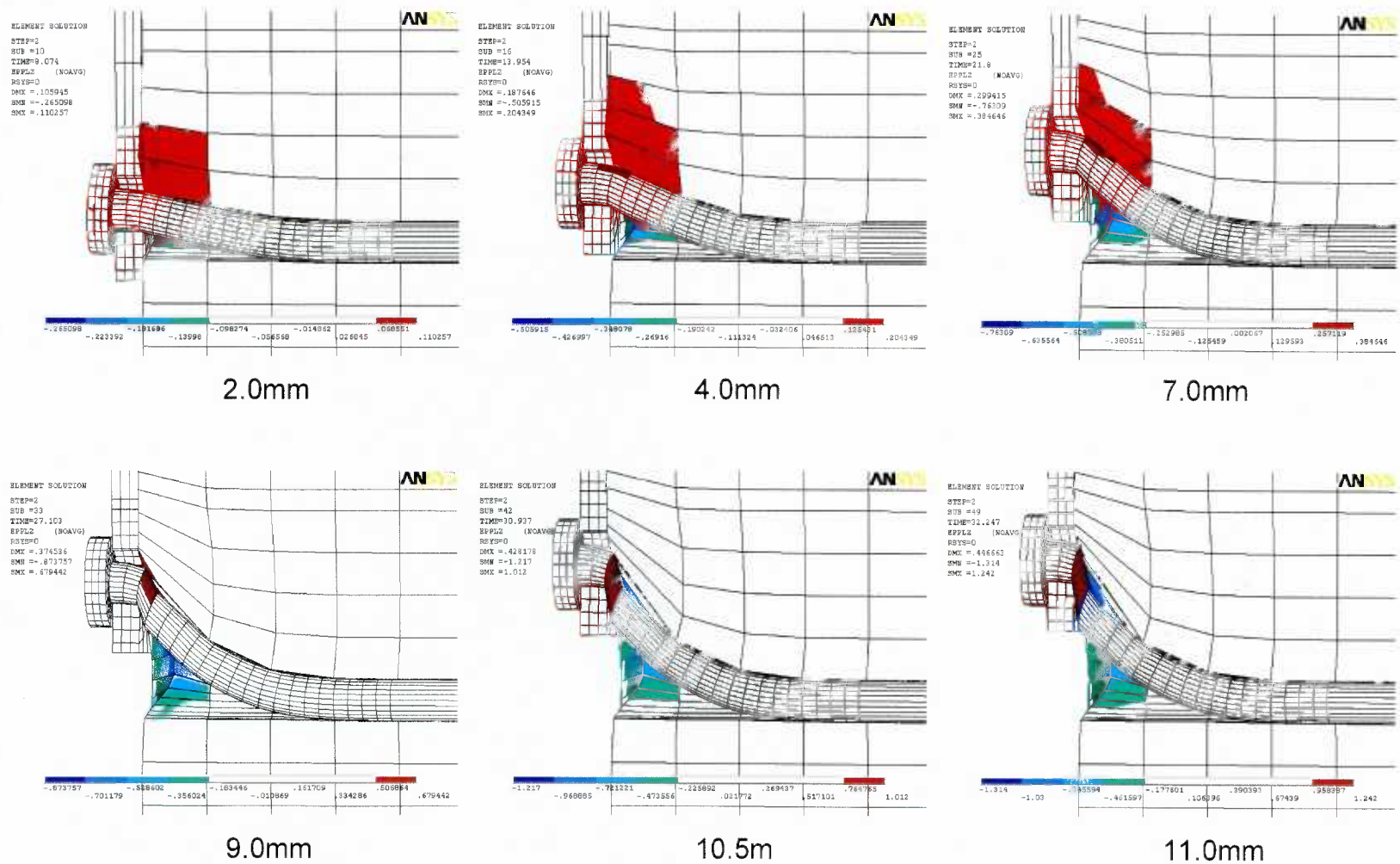


Figure 6.21 Progress of Z-directional plastic strain for the PE connection model with a nail yield stress of 310 MPa.

## **6.4 Feasibility study on the statistical 3D FE material model**

Generally, the material constants used for the 3D FE nail connection model are the major factors determining the simulation response. If the material constants were treated as random variables, the random variation in the lateral resistance of the nail connection could be predicted using the 3D FE nail connection model. The method of correlated random variable generation could be used to predict the variation of the material properties. By applying this method to determine the independent material constants, including MOE and yield stress, a random 3D wood material model or a random 3D foundation material model could be constructed. This method required, however, a long time to run the 3D FE models that needed to obtain statistical results on a common personal computer. Instead, using linear relationships among the independent variables, a feasibility study on the statistical analysis for lateral resistance of the nail connection was conducted.

### **6.4.1 Approximation of 95<sup>th</sup> and 5<sup>th</sup> percentile foundation material model**

Using a linear regression method, linear relationships among the foundation moduli and the yield stresses were established from the nail-embedment test data. Then, by selecting the  $N^{\text{th}}$  percentile parallel to grain modulus from the 2-P Weibull distribution fit, the required dependent material constants were determined using the linear relationships and the selected modulus. Finally, using the procedures for calculating the material constants (Table 3.1), the  $N^{\text{th}}$  percentile foundation material model was established.

Using this linear regression material model, the 5<sup>th</sup> and 95<sup>th</sup> percentile lateral resistances of the single nail connection were estimated through the 3D FE nail connection model.

A 2-parameter Weibull distribution was fitted to the test data for the nominal parallel to grain foundation modulus (Figure 6.22). From this distribution, the 5<sup>th</sup> and 95<sup>th</sup> percentile nominal moduli were identified as 232 MPa and 619 MPa, respectively. Then, the linear regression model (Equation [6.1]) relating the parallel to grain nominal foundation modulus and the perpendicular to grain nominal foundation modulus was used to determine the corresponding perpendicular to grain nominal foundation modulus (Figure 6.23).

The computed perpendicular to grain nominal foundation moduli determined were 82 MPa for the 5<sup>th</sup> percentile and 218 MPa for the 95<sup>th</sup> percentile. Nominal yield strains in each direction were also estimated by the linear regression models established between the nominal foundation modulus and the nominal yield strain: parallel to grain  $\varepsilon_{y_{5th}} = 0.142$  and  $\varepsilon_{y_{95th}} = 0.026$  by Equation [6.2]; and, perpendicular to grain  $\varepsilon_{y_{5th}} = 0.163$  and  $\varepsilon_{y_{95th}} = 0.122$  by Equation [6.3]. These linear relationships are shown in Figure 6.24 and Figure 6.25.

$$S_{\perp} = 0.3529 \times S_{//} \quad [6.1]$$

$$\varepsilon_{y//} = -0.0003 \times S_{//} + 0.2115 \quad [6.2]$$

$$\varepsilon_{y\perp} = -0.0003 \times S_{\perp} + 0.1878 \quad [6.3]$$

Where,

$S_i$  = Nominal foundation modulus [MPa]

$\varepsilon_{yi}$  = Nominal yield strain

$i$  = Parallel to grain ( $//$ ) or perpendicular to grain ( $\perp$ )

Applying the generalized calibration factors of the 3.3-mm diameter nail to these four nominal material constants, the effective foundation constants were determined. Then, the corresponding wood foundation material model was derived by the procedures of Table 3.1. The full set of constants for the 5<sup>th</sup> and 95<sup>th</sup> percentile material models is summarized in Table 6.6.

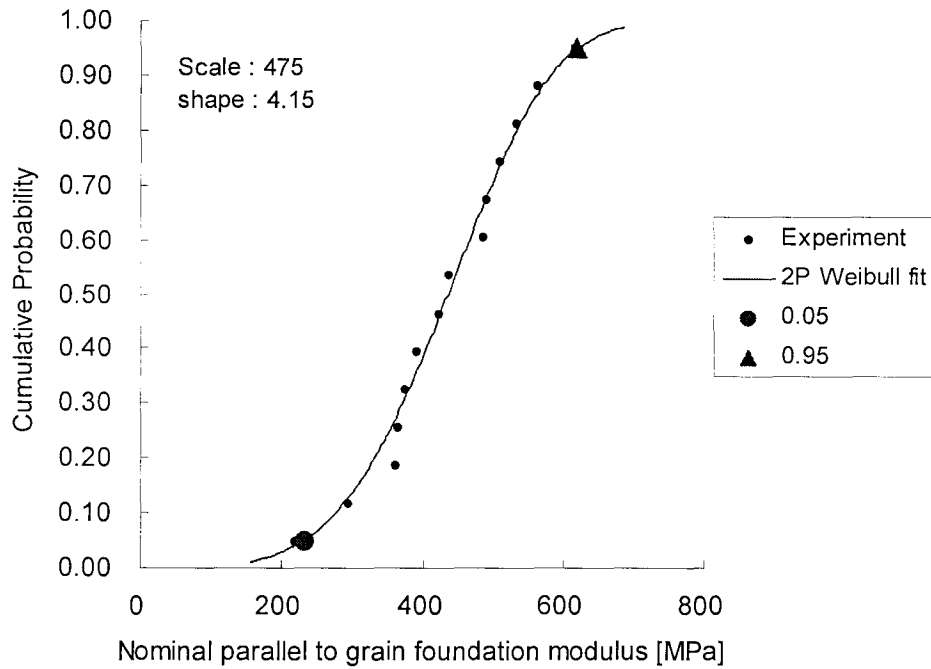


Figure 6.22 Two-parametric Weibull distribution fit to the parallel to grain nominal foundation modulus.

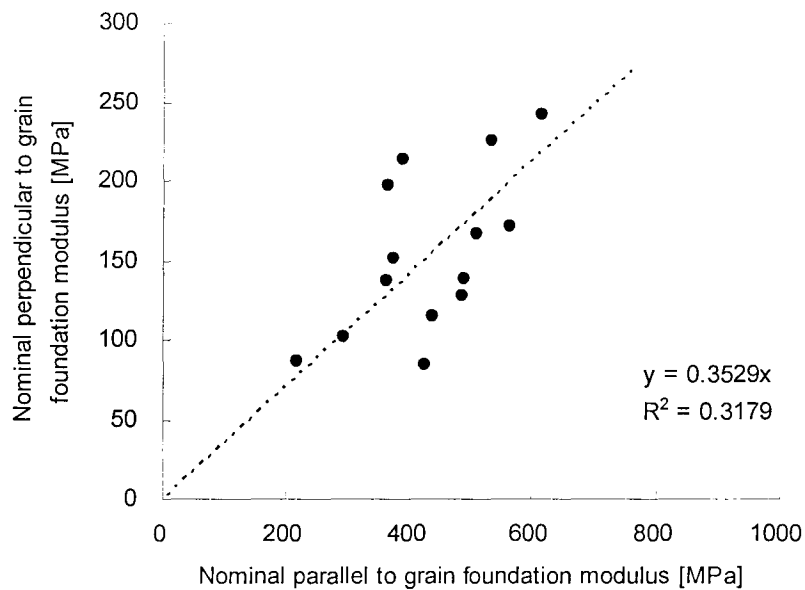


Figure 6.23 Linear relationship between the parallel to grain foundation nominal modulus and the perpendicular to grain nominal foundation modulus.

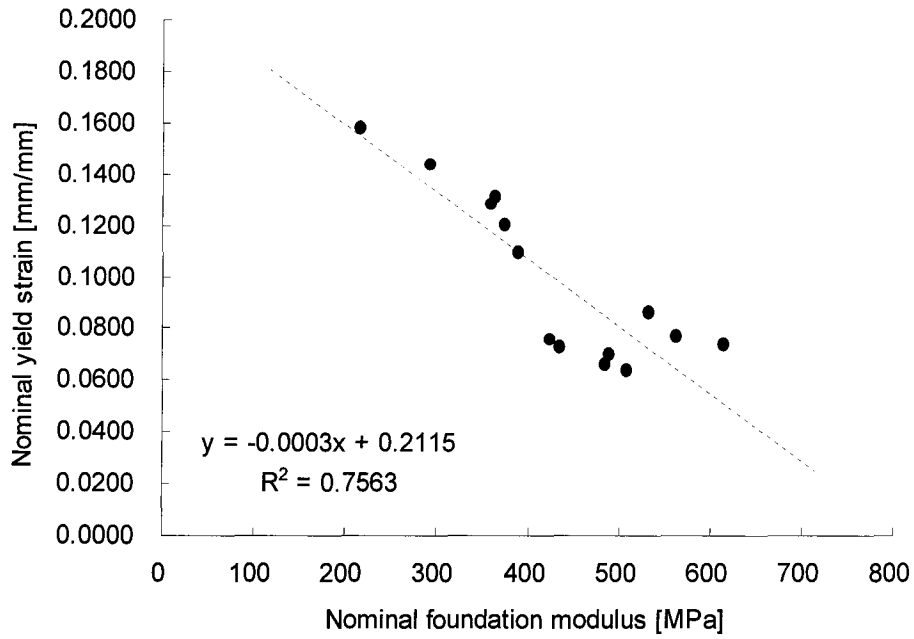


Figure 6.24 Linear relationship between the parallel to grain nominal foundation modulus and the parallel to grain nominal yield strain.

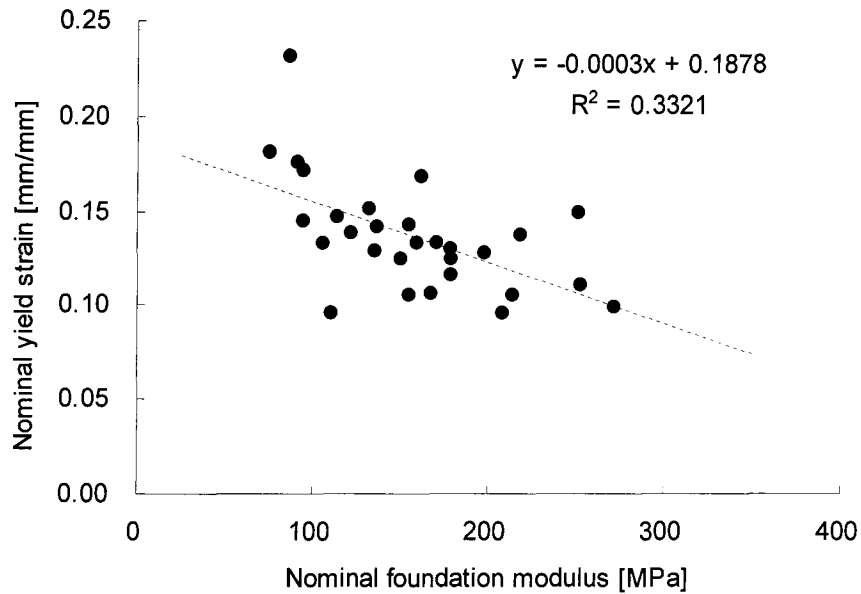


Figure 6.25 Linear relationship between the perpendicular to grain nominal foundation modulus and the perpendicular nominal yield strain.

Table 6.6 Fifth percentile and 95<sup>th</sup> percentile foundation material model for 3.3-mm diameter nail connection with Douglas-fir.

Material constant	5 <sup>th</sup> percentile foundation model	95 <sup>th</sup> percentile foundation model
Elastic modulus: L [MPa]	395	1050
Elastic modulus: R = T [MPa]	74	197
Elastic shear modulus: RL = LT [MPa]	74	196
Elastic shear modulus: RT [MPa]	26	71
Poisson's ratio: RL	0.069	0.069
Poisson's ratio: LT	0.37	0.37
Poisson's ratio: RT	0.38	0.38
Compressive, tensile yield stress : R (=T) [MPa]	4.3	8.58
: L [MPa]	13.3	6.46
Compressive, tensile tangent modulus : R (=T) [MPa]	0.73	1.96
: L [MPa]	3.95	10.52
Shear yield stress : RL (=LT) [MPa]	2.14	4.28
: RL [MPa]	1.29	2.58
Shear tangent modulus : RL (=LT) [MPa]	0.73	1.96
: RL [MPa]	0.26	0.71

#### 6.4.2 Simulation of the N<sup>th</sup> percentile lateral resistance of the single nail connection

Based on the 3D FE nail connection model developed in section 6.2.1, the average constants-based foundation material model was replaced by the N<sup>th</sup> percentile foundation material model. For the wood material model, the WOOD11 model was used without any changes. Then, the nail connection model was executed to obtain the 5<sup>th</sup> and 95<sup>th</sup> percentile resistances of nailed connections.

The simulated percentile load-slip curves are superimposed on the experimental curves in Figure 6.26 and Figure 6. Although the simulation for the 5<sup>th</sup> percentile resistance of the PA was terminated at a deformation of 4.8 mm, the percentile curves could predict the range of the variation reasonably well in each direction.

The linear regression foundation material model had the shortcoming that, since it involved only the deviation of the parallel to grain nominal foundation modulus, variations of other material constants, such as the perpendicular to grain modulus and the yield strains, could not be reflected accurately into the material model. However, the predictions using the linear regression model provided quite acceptable results.

The feasibility study concluded that, if the requisite statistical representations of the test data were provided and the dependent material constants were generated by a more sophisticated technique involving correlations amongst the multiple variables, the full range of variation of the resistance of the nail connection may be obtained.

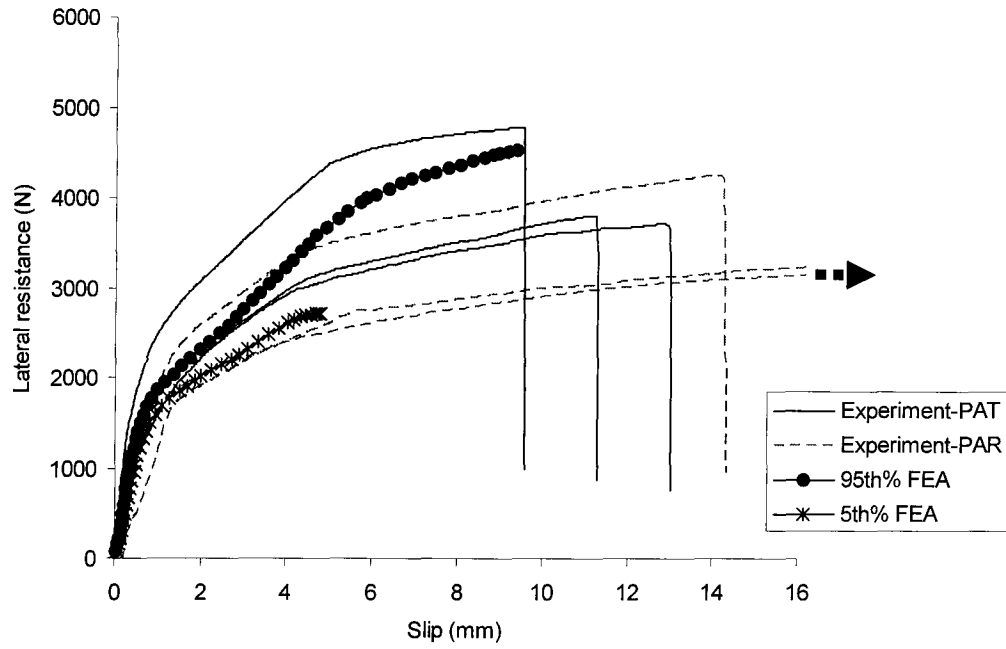


Figure 6.26 Approximations of the 5th percentile limit and the 95th percentile curves in the parallel to grain lateral resistance of the single nail connection.

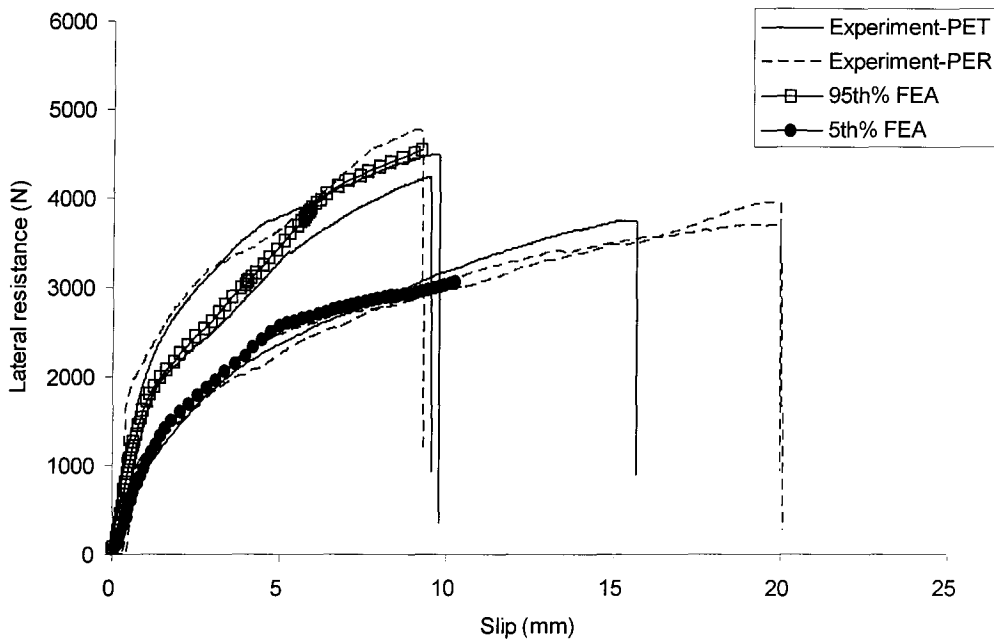


Figure 6.27 Approximations of the 5th percentile limit and the 95th percentile curves in the perpendicular to grain lateral resistance of the single nail connection.

## CHAPTER 7. THREE-DIMENSIONAL FINITE ELEMENT MODEL OF BOLTED CONNECTIONS

For bolted connections, many studies based on FE models have been conducted. The 3D FE studies by Patton-Mallory (1996) and Moses (2000) were considered the most relevant to this study; therefore, these models were used as references for the development and verification of the bolted connection model, which has been created with the wood foundation model in this work.

The referenced conventional models used only the standard uniaxial loading test-based wood material properties for the 3D FE wood material model. In this chapter, the simulated response of bolted connections from the wood foundation-based model and conventional models are compared and discussed.

### 7.1 Preliminary knowledge

Patton-Mallory (1996) developed a 3D FE bolted connection model to evaluate the interaction of the connection end distance (end distance/bolt diameter,  $e/d$ ) and the aspect ratio (thickness/bolt diameter,  $l/d$ ) with a 12.7-mm (0.5 in.) diameter bolt in Douglas-fir. The definition of geometric parameters and the configuration of the bolted connection test are reproduced in Figure 7.1. Later, Moses (2000) extended Patton-Mallory's bolted connection model by introducing an anisotropic plasticity material model. The Moses model showed an almost identical load-deformation prediction to Patton-Mallory's results but with improvement in the predicted post-yield behaviour.

Patton-Mallory's simplified bolted connection test had an analogous configuration of the standard test method for full-hole dowel-embedment strength given in the EN 383

(European Standards) or ASTM D 5764-97a full-hole test method. These standard test methods specify the dimensions of the wood block, so that the bending deformation of the dowel should be minimized during the testing. Patton-Mallory's test configuration with  $l/d = 2$  and  $e/d = 7$  corresponded to the full-hole embedment test, except for the width of  $3 \times d$  ( $w/d = 3$ ). For the  $l/d = 2$  and  $e/d = 7$  test, she reported that no significant permanent bending of the pin was observed, and the load-deformation curve from the tension/compression-loaded bolted connection test was slightly stiffer than the curve from the half-hole embedment test.

This slight difference between the full- and half-hole tests was also observed by Pope et al. (1995), who compared the bolt embedding strengths obtained from the EN 383 full-hole test and the ASTM half-hole test. For 12 mm (0.47 in.) diameter bolt embedment on European Whitewood/Redwood and Iroko, they reported the full-hole test produced a parallel to grain embedding strength that was an average of 4% higher than that obtained from the ASTM half-hole test.

In the current study, therefore, based on the 12.7-mm bolt half-hole embedment test data (see section 5.3.4.4), the ability of the model to represent the difference in the embedding strengths for the two different test procedures was used as the main criterion for the validation of the bolted connection model.

Three geometries of the 12.7-mm bolt full-hole embedment models with  $l/d = 2, 5$  and  $7$  and a constant ratio of  $e/d = 7$  were studied using the wood foundation model; and, the corresponding  $l/d = 2$  half-hole embedment model was created. Additionally, a model without the wood foundation, which was analogous to the conventional bolted

connection model that employed only the standard test-based material properties, was included in this study for comparison purposes.

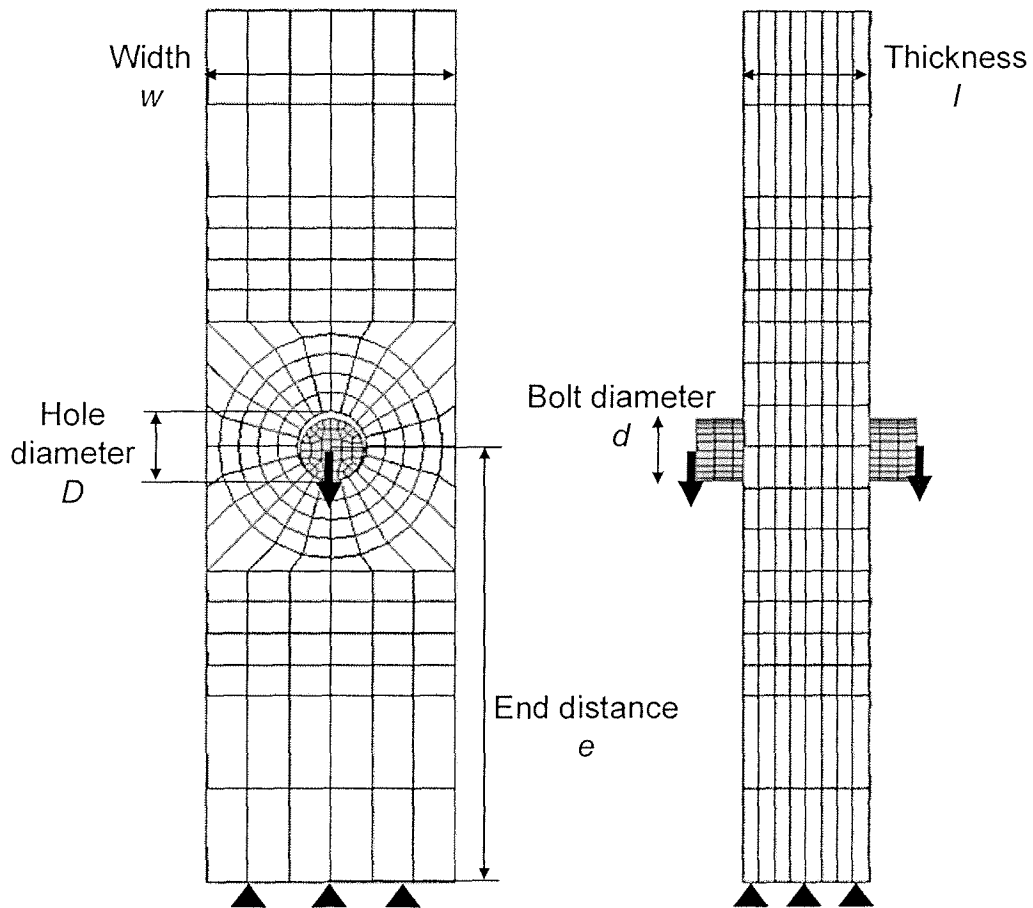


Figure 7.1 Configuration and parameters of the compression loaded bolted connection test analogous to the full-hole embedment test. The  $l/d=2$ ,  $e/d=7$  and  $w/d=4$  configuration is shown.

## 7.2 Model description

As shown in Figure 7.2, two different 3D FE models for full-hole embedment or bolted connection were created. The model without the wood foundation was the conventional model that employed only a wood material model – WOOD11 (Patton-Mallory 1996, Moses 2000, Kharouf 2001).

In order to accommodate the  $1.8 \times d$  prescribed wood foundation, the width of the wood block ( $W$ ) was set as  $4 \times d$ . This was the same width as the Pope et al. (1995) specimen. The length of the protruding bolt from the wood member was set to 9.5 mm (0.375 in.), according to the referenced models. The bolt-hole diameter was 1.6 mm (1/16 in.) larger than the bolt diameter. The displacement-controlled compression loading was applied on both end surfaces of the bolt. All nodes on the bottom end surface of the wood were fixed.

The WOOD11 material model and the wood foundation material model employed in the 12.7-mm dowel-embedment study were used. For the bolt material, an elasto-perfectly plastic model was assumed with the yield stress of 310 MPa (45 ksi) and MOE of 200 GPa ( $29 \times 10^6$  psi), as given in the referenced models. The surface-to-surface contact element was defined as the wood-to-bolt interface with the coefficient of friction of 0.3.

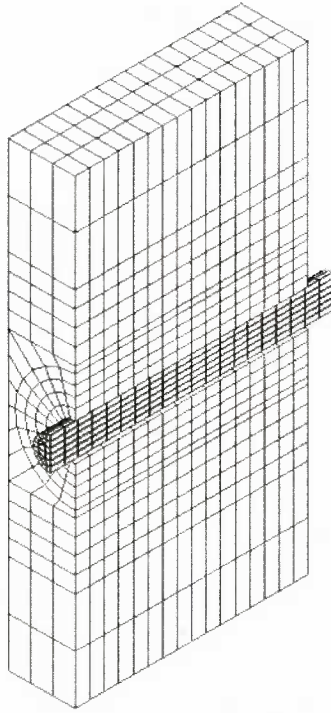
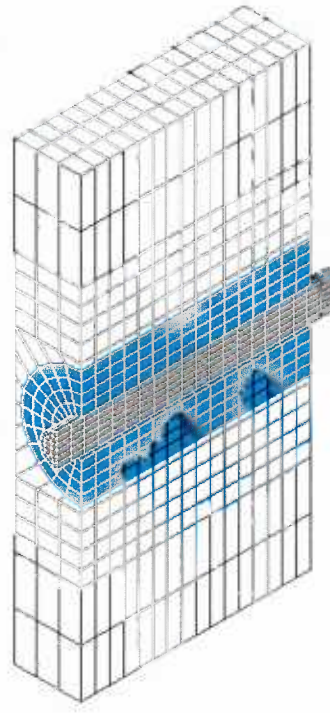
Wood material model onlyWood foundation-based model

Figure 7.2 Bi-sectioned bolted connection model with and without the wood foundation. The  $l/d=7$ ,  $e/d=7$  and  $w/d=4$  configuration is shown.

### 7.3 Simulation of the $l/d=2$ configuration: Full- vs. Half-hole embedment

According to the findings by Pope et al. (1995) and Patton-Mallory (1996), the 3D FE model for the  $l/d = 2$  and  $e/d = 7$  configuration must represent no significant plastic bend in the bolt and the similarity of load-embedment curves from the full-hole/half-hole test procedures.

Simulation of a 12.7-mm bolt half-hole embedment in a 25-mm (1 in.) thick Douglas-fir specimen gave the maximum linear embedding linear strength of 410 N/mm. Compared to 420 N/mm from the 38-mm (1.5 in.) thick average experimental linear

embedding strength (section 5.3.4.4), the simulated curve for the 25 mm-thick embedding test was assumed to be the reference curve for comparisons of the  $l/d = 2$  configurations.

### **7.3.1 The discrepancy and similarity of the full- and half-hole embedment tests**

As shown in Figure 7.3, the wood foundation-based model successfully represented the discrepancy and similarity of the full- and half-hole embedment tests. It showed that, at 2.5 mm deformation, the simulated full-hole embedding strength (11,000 N) was 8% higher than the reference half-hole embedding strength (10,200 N). A stiffer curve was also identified in the full-hole simulation. These simulated results agreed well with the behaviour observed by Pope et al. (1995) and Patton-Mallory (1996).

The conventional model (wood material model only), however, did not represent the observed behaviour. Compared to the reference curve, any simulated curves based on the conventional model could not be acceptable. More importantly, the simulated half-hole embedding strength (34,000 N at 2.5 mm) was much higher than the full-hole strength (22,000 N at 2.5 mm).

This higher stiffness of the simulated load-deformation curves has been a major problem in conducting 3D FE analysis for wood connections, as observed by Kharouf (2001) and Chen et al. (2003). The higher stiffness curves were attributed to the highly stiff foundation under the bolt. This justified the introduction of the wood foundation model. The stiff foundation of the conventional model also affected the deformation process, so that it resulted in unrealistic deformed shapes. The deformed shape of the model will be examined in the next section.

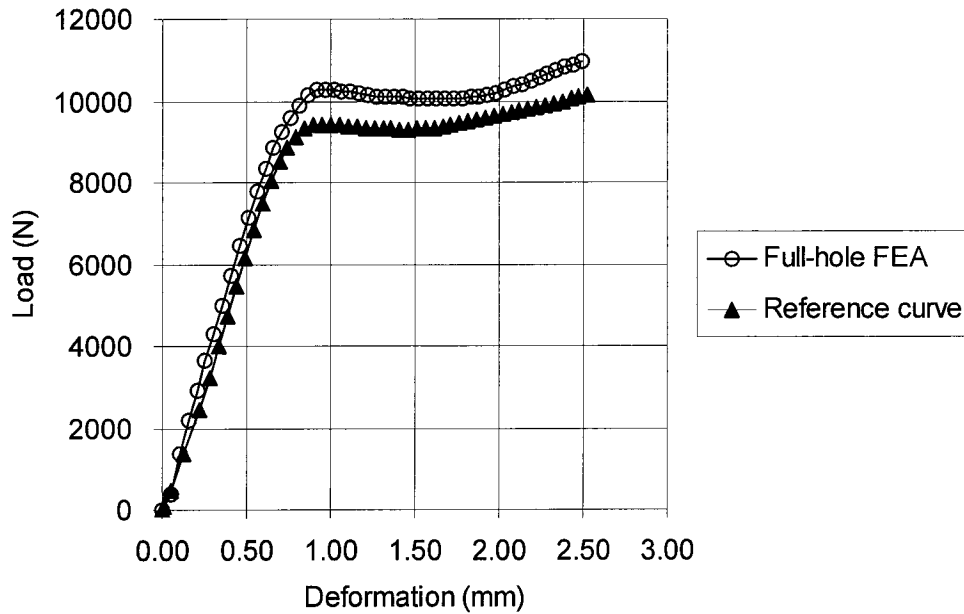


Figure 7.3 Comparison of the simulated load-embedment curves between the full-hole FEA and the half-hole FEA, using the wood foundation-based model, for the  $l/d = 2$ ,  $e/d = 7$  configuration.

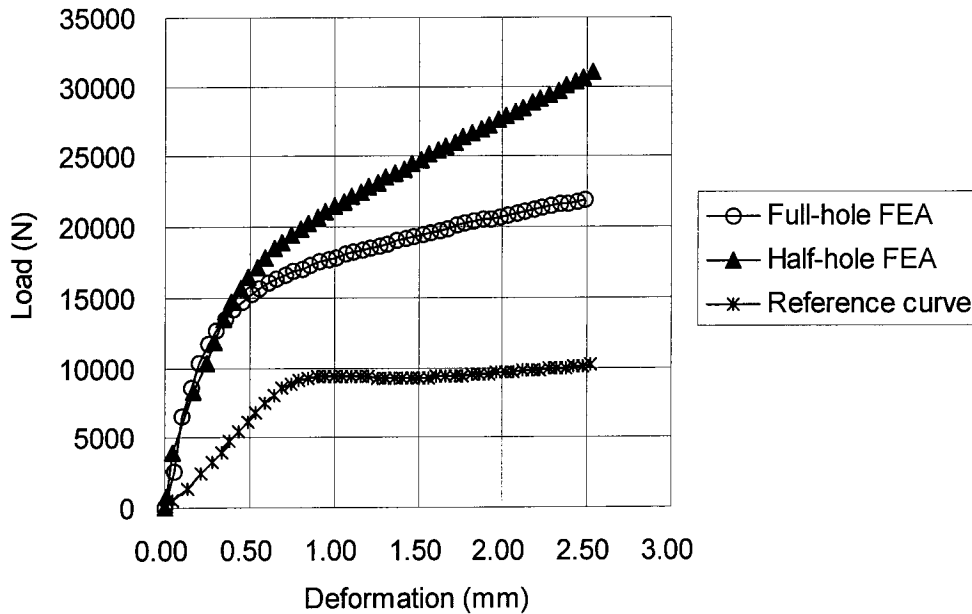


Figure 7.4 Comparison of the simulated load-embedment curves between the full-hole FEA and the half-hole FEA, using the conventional model (wood material only), for the  $l/d = 2$ ,  $e/d = 7$  configuration.

### 7.3.2 Deformed shapes of the bolt embedment model

Figure 7.5 and Figure 7.6 show the progress of permanent deformation for the full- and half-hole embedment tests, respectively. For both embedment tests, permanent bending in the bolt should not occur, since it did not happen in the experiments. For the half-hole embedment test, both models reasonably simulated the progress of the embedment behaviour without plastic deformation in the bolt (Figure 7.5).

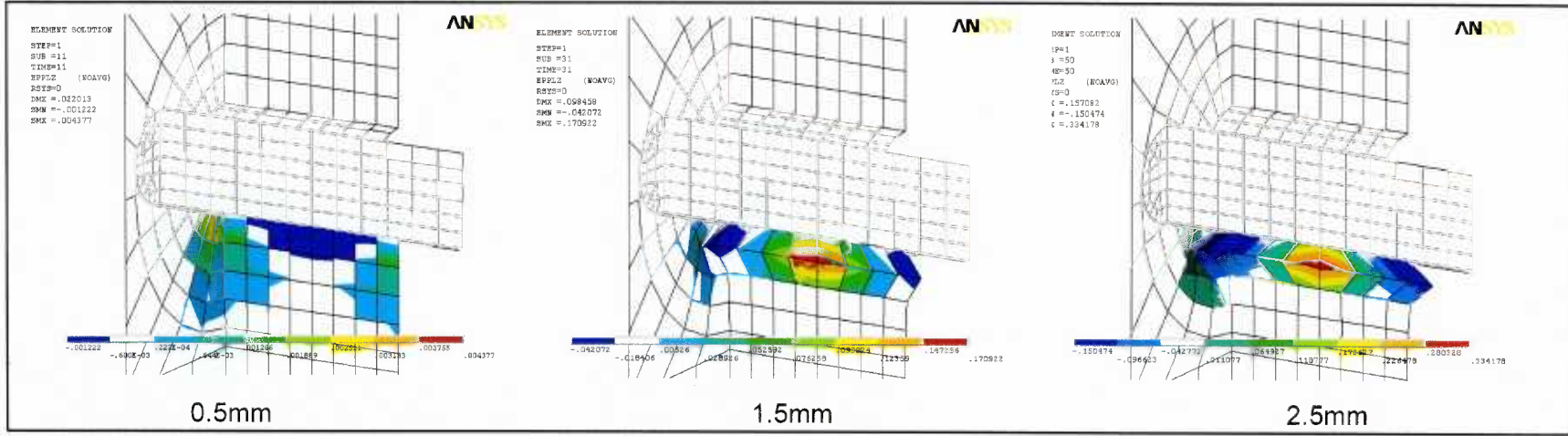
For full-hole embedment, the conventional model, however, represented unrealistic plastic bending in the bolt, while the wood foundation-based model did not produce any plastic deformation in the bolt (Figure 7.6).

It proved again that the wood compressive MOE from the standard test provided a stiffness that was too high for the wood-to-bolt contact. Accordingly, it caused significant permanent bending of the bolt. Indeed, the analysis results from the conventional model should be regarded as misleading, because it was based on the unrealistic deformation.

In three-dimensional FE analysis, special attention should be paid to the fact that, in some cases, despite unrealistic simulated deformation, the predicted and experimental load-deformation curves may show good agreement. Successful 3D FE analysis must be accompanied by verification of the deformed shape.



### Wood foundation-based model



### Wood material model only

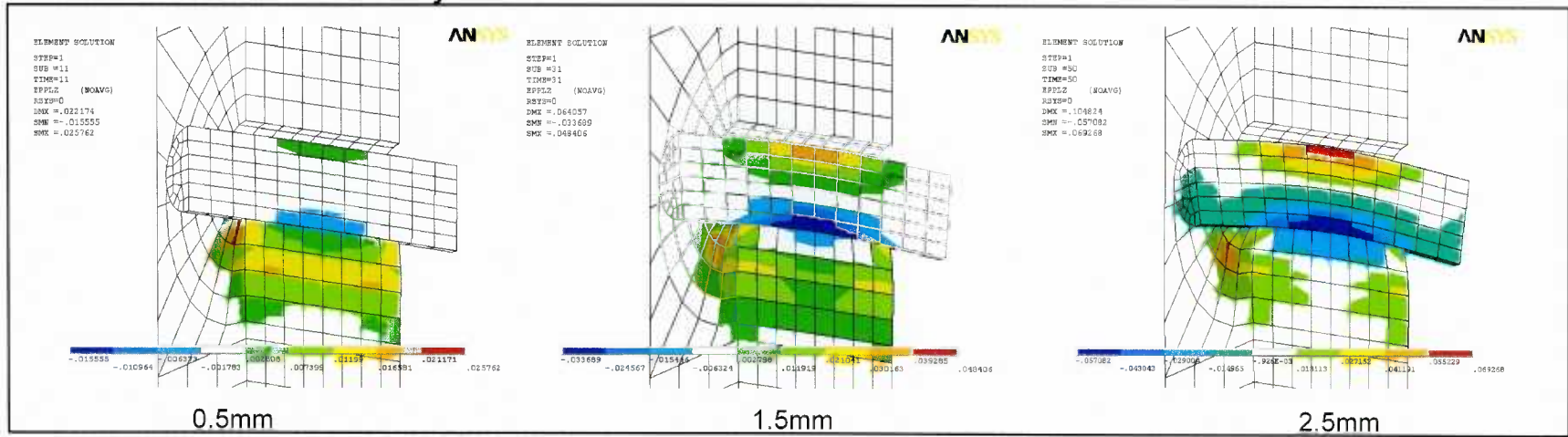


Figure 7.6 Progress of the Z-directional plastic strain contour for the  $l/d=2$ ,  $e/d=7$  full-hole embedment test: the wood foundation-based model (top) and the conventional model (bottom).

## 7.4 Simulation bolted connection: $l/d=5$ and $l/d=7$

### 7.4.1 Deformed shape of bolted connections

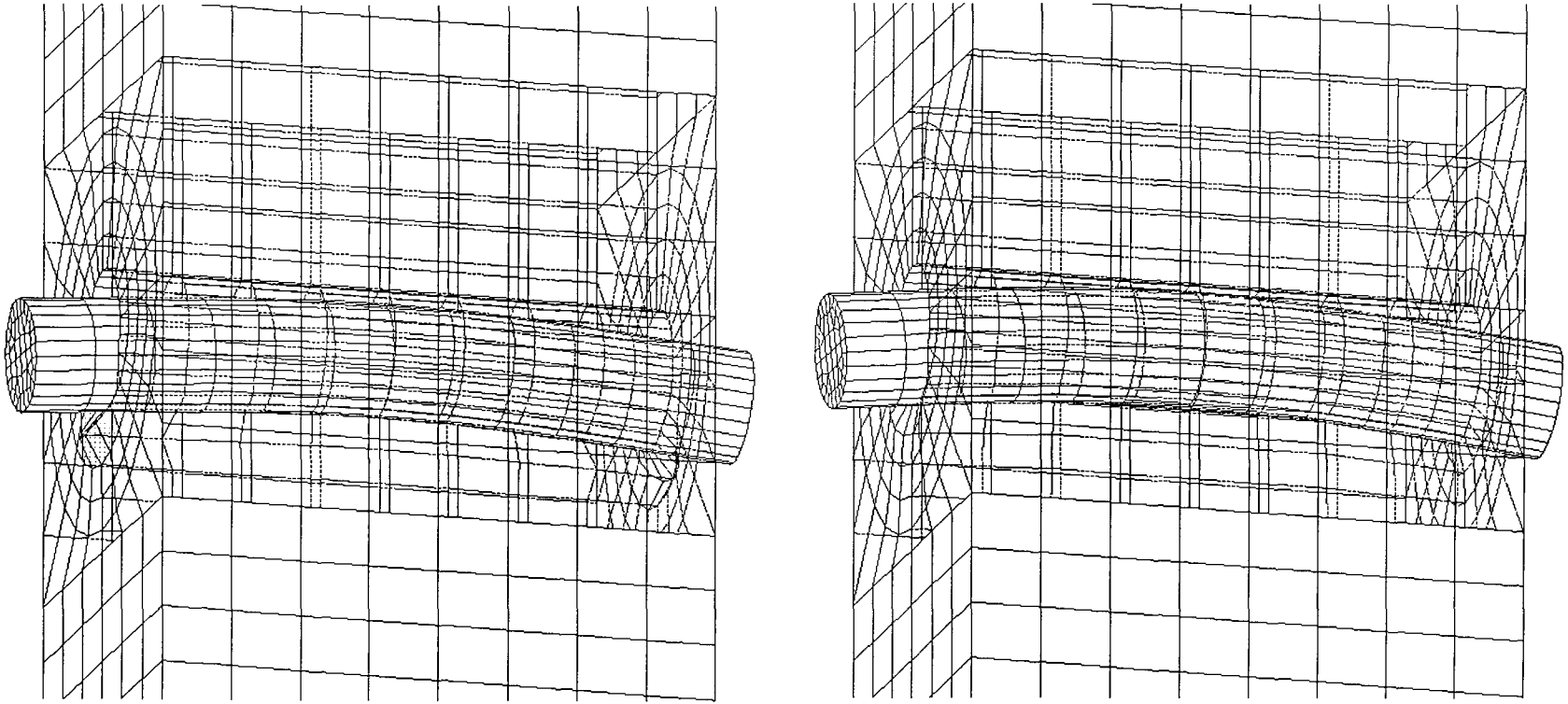
For bolted connections with  $l/d=5$  and 7, both models revealed plastic hinge formations at the centre of the bolt and plastic deformation in the wood foundation at the end supports of wood, as shown in Figure 7.8 and Figure 7.9. This deformation behaviour conforms to Patton-Mallory's experimental observations.

Although the apparent deformed shapes of the two different models looked similar, as shown in Figure 7.7, the plastic strain contour plots revealed the differences in the deformation. It was found that the conventional models produced a larger gap at the middle of the contact interface between wood and bolt, due to bolt bending. For the  $l/d = 7$  connection, the difference in the gap formation was obvious.

The difference in the gap formation was attributed to the difference in stiffness of the wood under the bolt. A bolt on a stiff wood foundation was subject to bending rather than bearing. Figure 7.10 and Figure 7.11 show comparisons of contact pressure on the wood-to-bolt contact interface. The distributions of the contact pressure revealed that the bolt on the stiff foundation in the conventional model deformed like a simply supported beam. Especially for the  $l/d=7$  connection (Figure 7.11), even at the small deformation of 0.5 mm, the conventional model showed no contact pressure in the middle region of the bolt. This means that the simulated deformation by the conventional model was governed mainly by the bolt's plastic bending.

Finally, it was concluded that the wood of the conventional model was too stiff; therefore, the plastic deformation of the bolt dominated the total deformation of the

connection, and the contribution of the wood to the total deformation was small. This conclusion is confirmed in more detail in the following sections, using comparisons of the load-deformation responses and strain energy analysis.

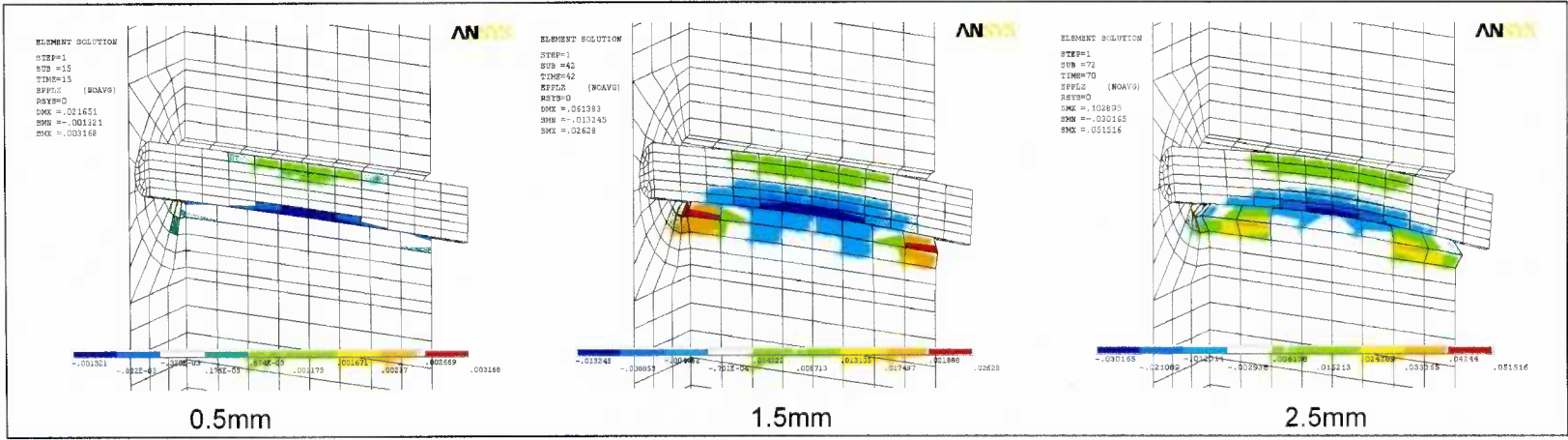


Wood foundation-based model

Wood material model only

Figure 7.7 Comparison of the apparent deformed shapes of the  $l/d=5$  bolted connection: the wood foundation-based model (left) and the wood material model only (right).

Wood foundation-based model



Wood material model only

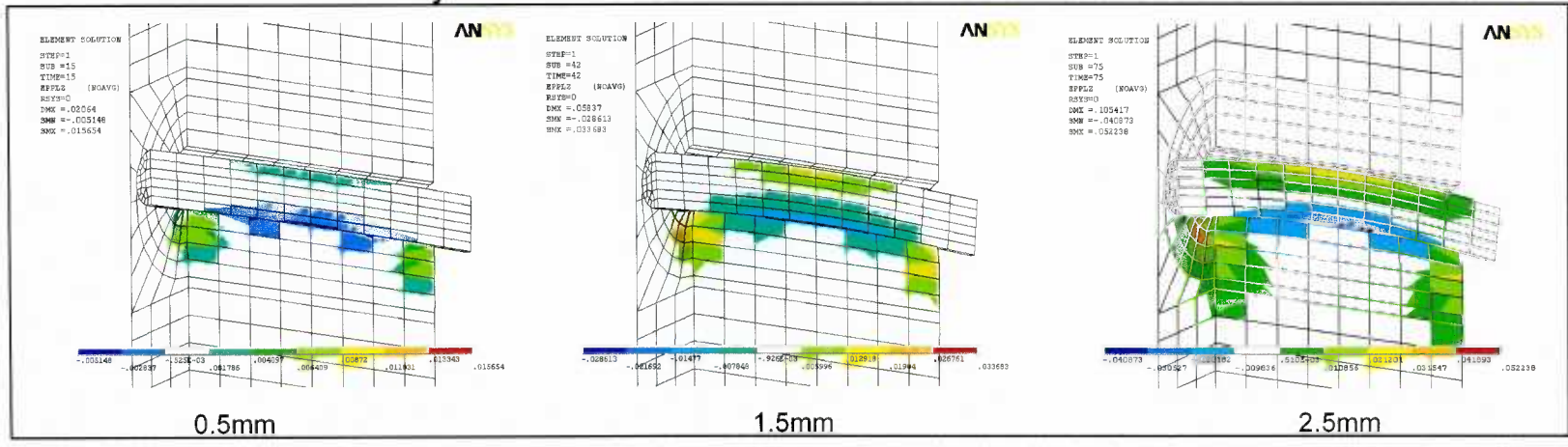
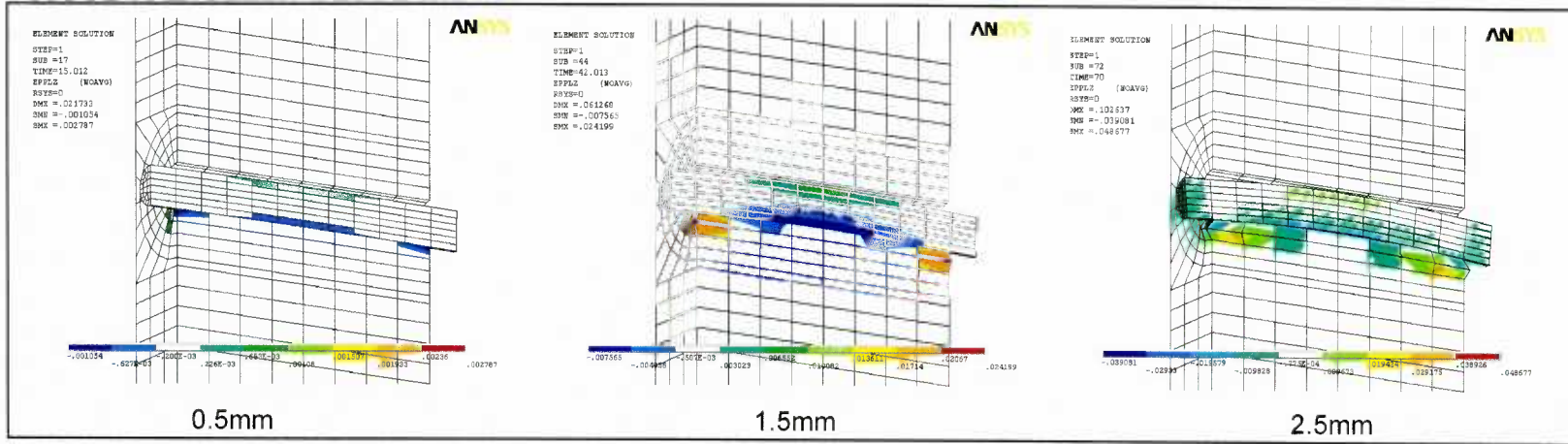


Figure 7.8 Progress of the Z-directional plastic strain contour for the  $l/d=5$ ,  $e/d=7$  bolted connection: the wood foundation-based model (top) and the conventional model (bottom).

### Wood foundation-based model



### Wood material model only

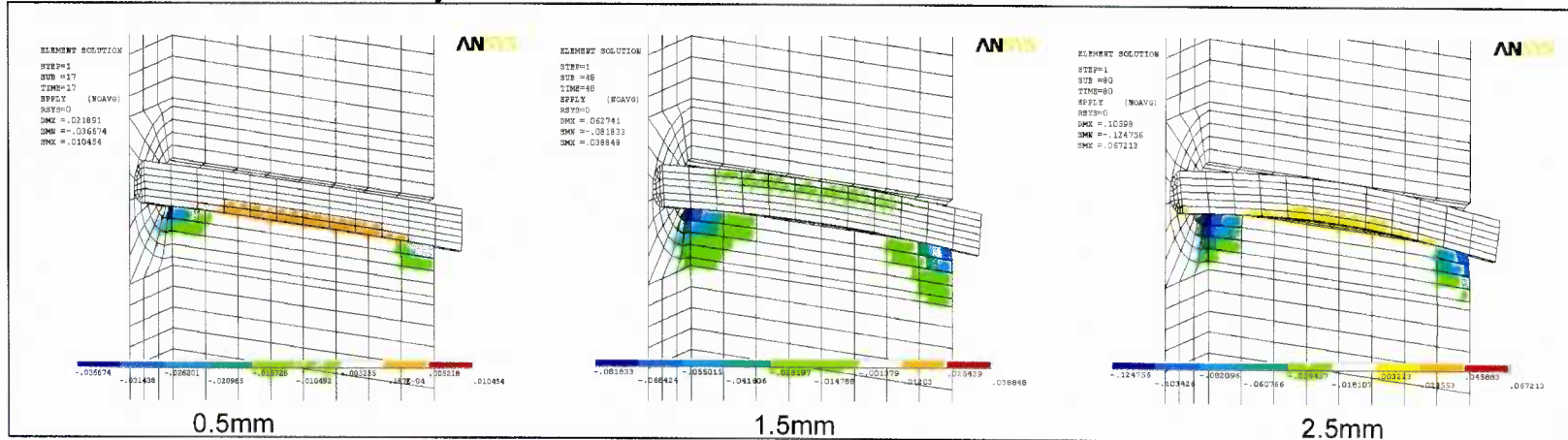


Figure 7.9 Progress of the Z-directional plastic strain contour for the  $l/d=7$ ,  $e/d=7$  bolted connection: the wood foundation-based model (top) and the conventional model (bottom).

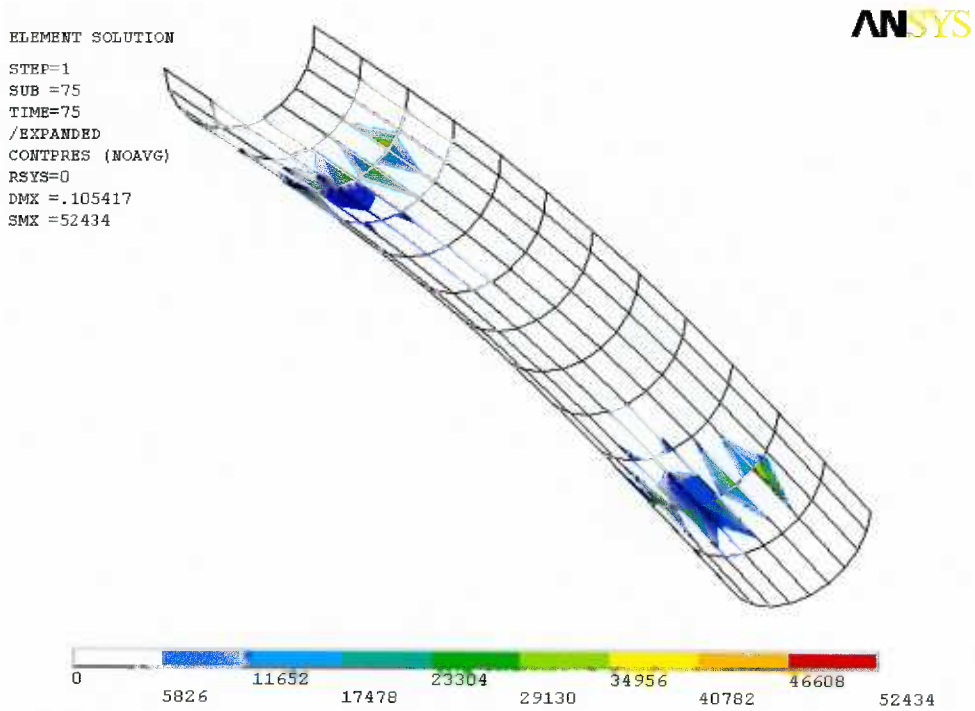
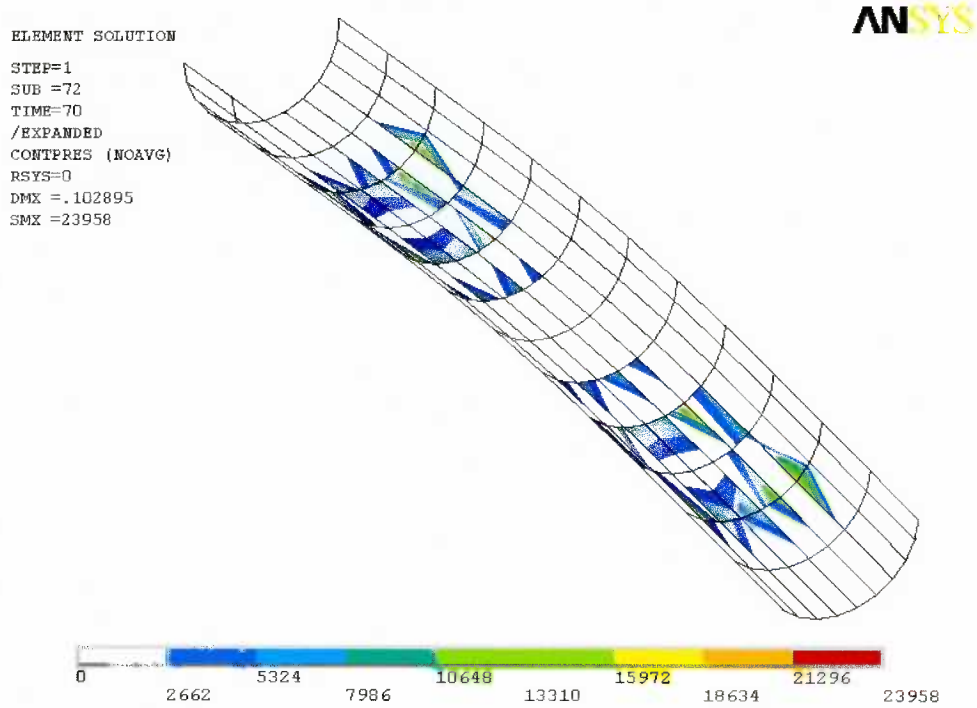
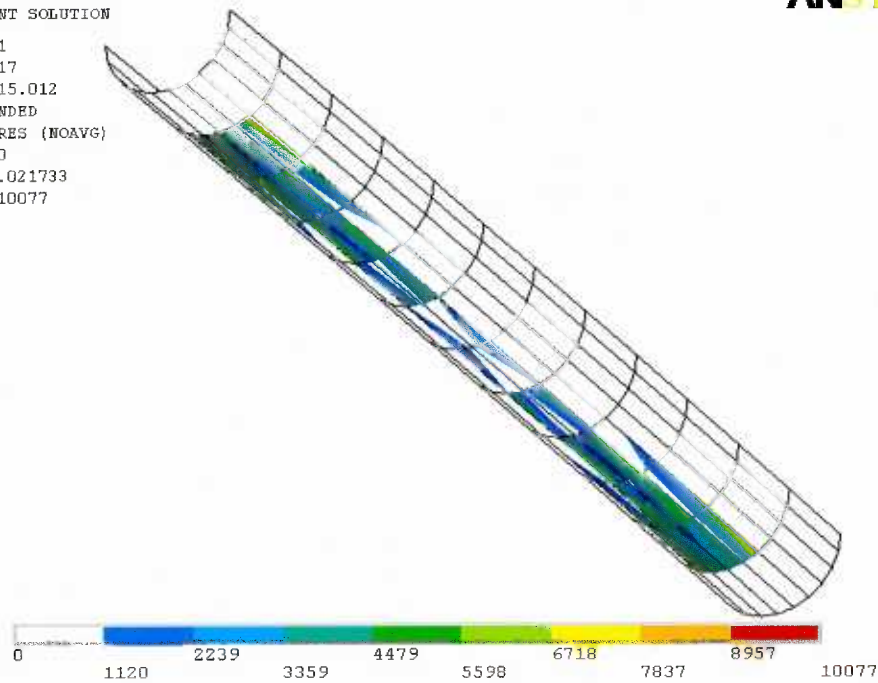


Figure 7.10 Distribution of contact pressure over the wood-to-bolt interface at a deformation of 2.5 mm for the  $l/d=5$  bolted connection: the wood foundation-based model (top) and the conventional model (bottom). Contact element-CONTA174.

ELEMENT SOLUTION  
 STEP=1  
 SUB =17  
 TIME=15.012  
 /EXPANDED  
 CONTPRES (NOAVG)  
 RSYS=0  
 DMX =.021733  
 SMX =10077



ELEMENT SOLUTION  
 STEP=1  
 SUB =17  
 TIME=17  
 /EXPANDED  
 CONTPRES (NOAVG)  
 RSYS=0  
 DMX =.021891  
 SMX =33172

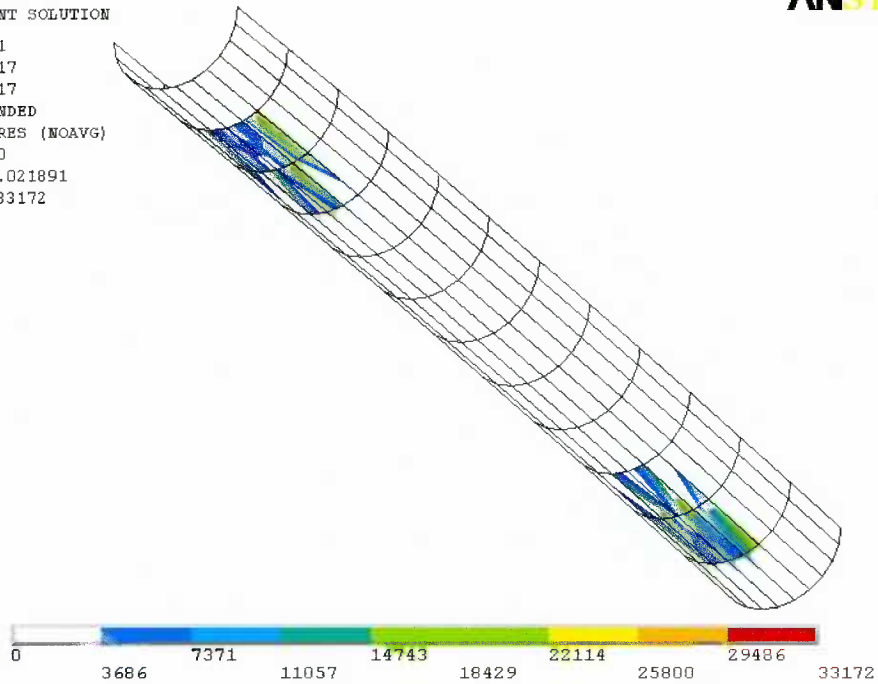


Figure 7.11 Distribution of contact pressure over the wood-to-bolt interface at a deformation of 0.5 mm for the  $l/d=7$  bolted connection: the wood foundation-based model (top) and the conventional model (bottom). Contact element-CONTA174.

### 7.4.2 Load-deformation relationship

The predicted load-deformation curves of the bolted connections with aspect ratios of  $l/d = 2, 5$  and  $7$  and the predicted half-hole embedment curve are plotted in Figure 7.12 and Figure 7.13.

The conventional model produced almost the same load-deformation curves, regardless of the aspect ratio; whereas, the wood foundation-based model gave a distinctly different load-deformation curve for the  $l/d = 2$  connection.

In terms of the European yield model (EYM), although there was no side member, under the wood foundation-based model, the yield mode of the  $l/d = 2$  connection corresponded to Mode I – yield governed by crushing of wood fibres in the main member. For the yielding in the  $l/d = 5$  and  $7$  connections, Mode IV – yield governed by formation of two plastic hinges in the bolt at each shear plane – could be assumed, because the yield model for Mode IV is not affected by member thickness. In other words, Mode IV yield occurs regardless of the aspect ratio.

The yield modes predicted by the conventional model were Mode IV for all aspect ratios. This could not be true for the  $l/d = 2$  connection or the full-hole embedment, because the plastic hinges of Mode IV should not happen in the full-hole embedment test.

It was concluded that, as employed in the conventional model, the MOE from the standard uniaxial loading test for wood should not be used as the material constant for modeling wood crushing behaviour under a dowel, because the wood stiffness under the dowel would be too high.

Owing to the success of the wood foundation model for simulating the yield by Mode I, it was recognized that, if a side member was incorporated into the model, prediction of the European yield mode may be possible. This may be a good area for further study.

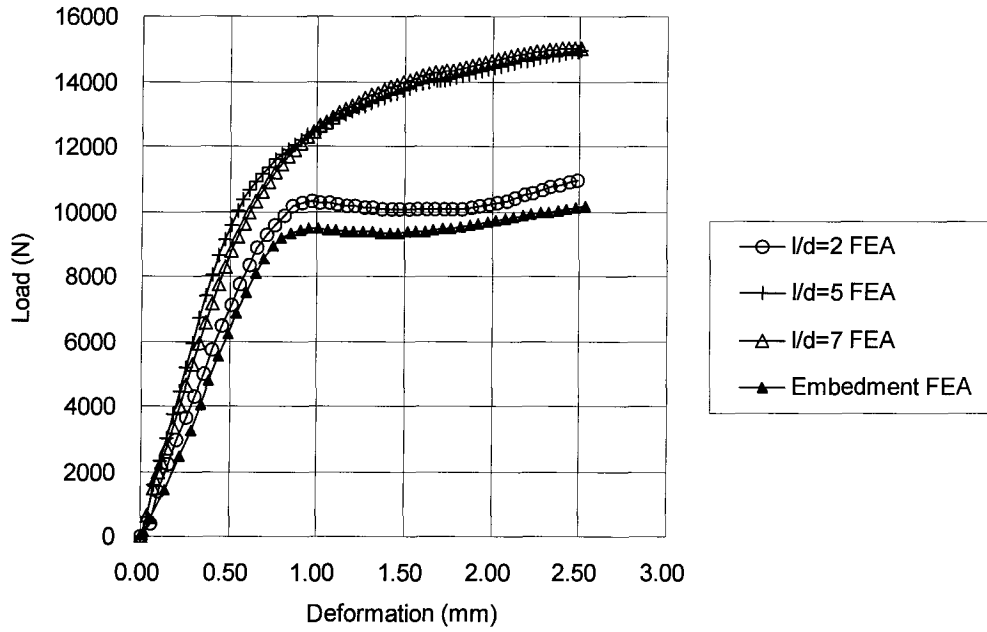


Figure 7.12 Comparison of the predicted load-deformation curves of 12.7-mm bolted connection with aspect ratios of  $l/d = 2, 5$  and  $7$ , and the predicted half-hole load-embedment curve obtained by the wood foundation-based model simulation.

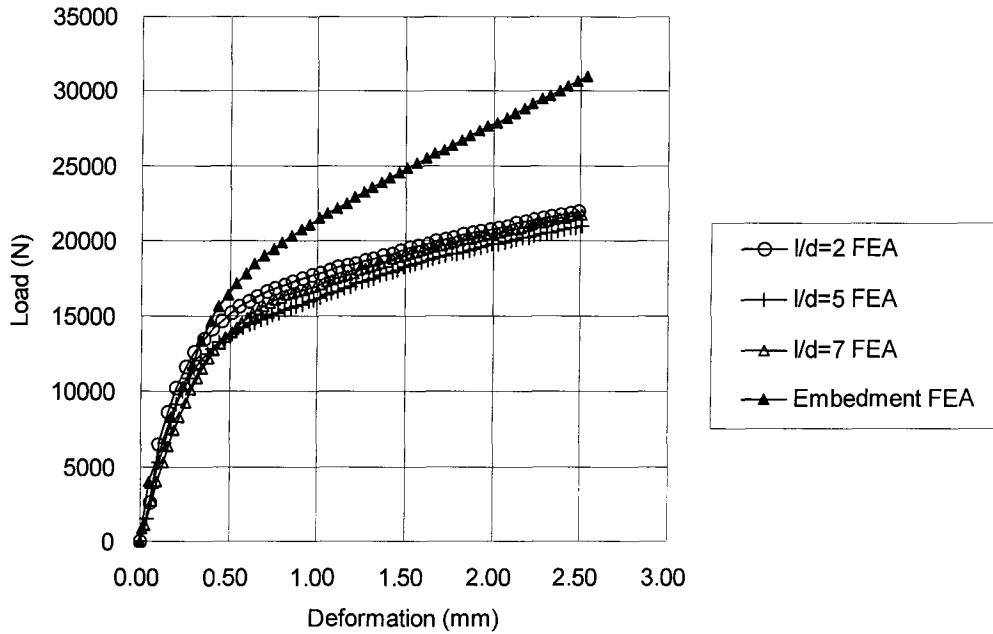


Figure 7.13 Comparison of the predicted load-deformation curves of 12.7-mm bolted connection with aspect ratios of  $l/d = 2, 5$  and  $7$ , and the predicted half-hole load-embedment curve obtained by the conventional model simulation.

### 7.4.3 Share of wood and bolt in total strain energy of the connection

As mentioned in section 7.4.1, the two different models showed quite different characteristics in load-deformation responses, although the deformed shapes appeared similar.

In order to clarify this difference, strain energy analysis was conducted, for the wood and bolt separately, at each sub-step of the solution. By investigating the changes of the respective share in total strain energy of the connections, the different characteristics were explained.

For the  $l/d = 2$  connection, the wood foundation-based model showed that the share of the wood in the total strain energy was over 90% at all the connection deformation levels (accordingly, the share of the bolt was less than 10%), as shown in Figure 7.14. This share was evident, because most of the deformation occurred by wood crushing under the bolt.

The conventional model, however, showed a different pattern. At the initial level of the deformation, the total strain energy was dominated by wood crushing. Then, the reverse occurred at the connection deformation of 0.91 mm: the bolt's share became larger than that of the wood. The final strain energy in the bolt was 65%. This indicated that bolt bending became dominant and wood deformation became small in the overall deformation of the connection. This should not happen in the  $l/d = 2$  connection.

For the  $l/d = 5$  and 7 connections, it was noted that the wood foundation-based model showed that the sharing reversed in the  $l/d = 5$  connection only, although the two different models produced almost the same load-deformation curves as assumed by Mode IV yielding (Figure 7.12 and Figure 7.13). That is, the conventional model showed

similar curves with similar sharing patterns for the  $l/d = 5$  and  $7$  connections; whereas, the wood foundation-based model produced similar curves but with different sharing patterns (Figure 7.15 and Figure 7.16).

Indeed, this kind of the strain energy share analysis is only available in 3D FE analysis. This analysis provided the mechanism of the deformation process in the connection. Thus, it was thought that the strain energy share analysis could be used to help control the ductility of the connection.

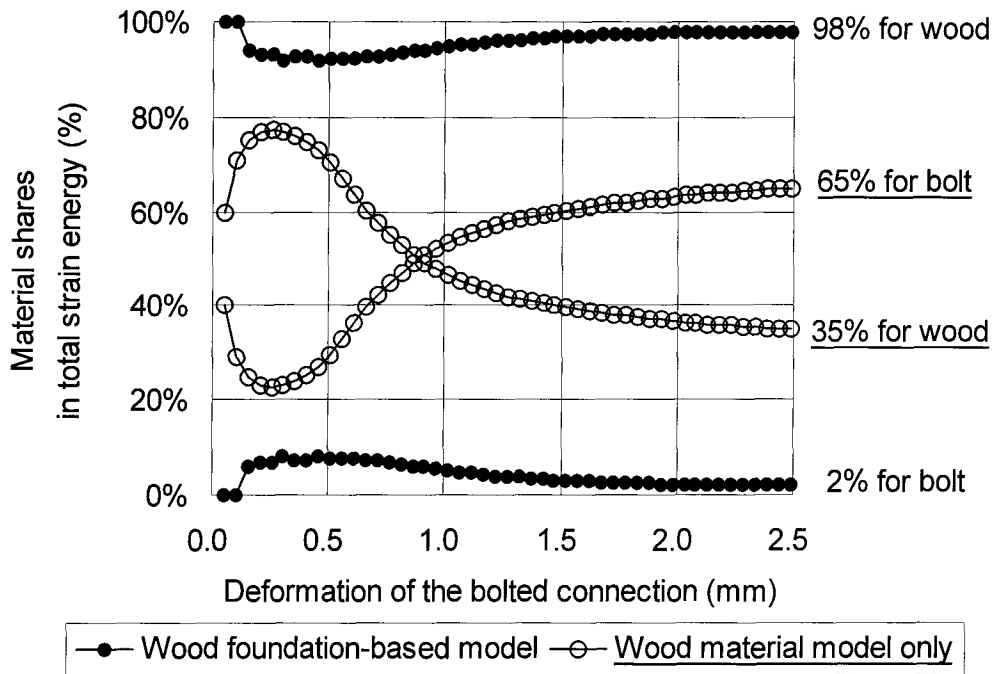


Figure 7.14 Change of material sharing in the total strain energy for the  $l/d=2$  connection.

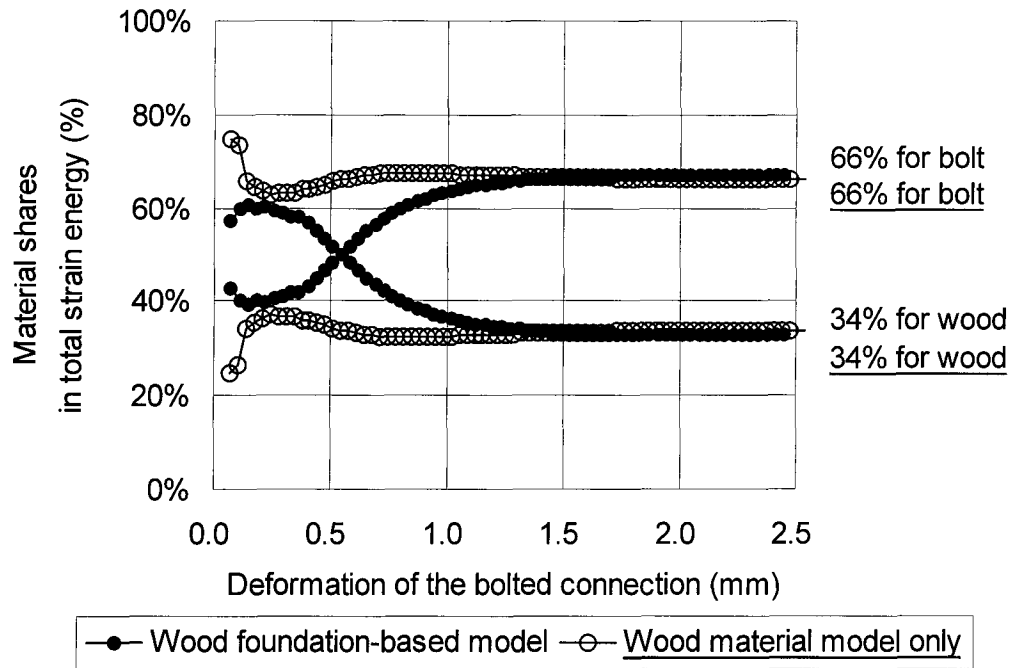


Figure 7.15 Change of material sharing in the total strain energy for the  $l/d=5$  connection.

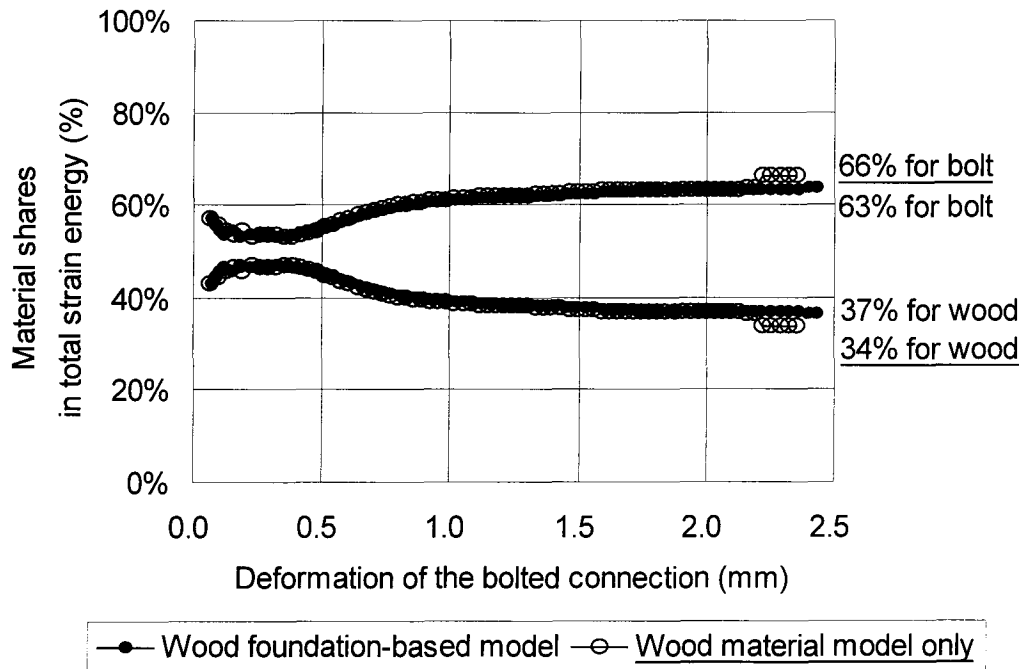


Figure 7.16 Changes of material sharing in the total strain energy for the  $l/d=7$  connection.

## **CHAPTER 8. MULTIPLE NAIL CONNECTION- JAPANESE CP-T JOINT**

This research was originally motivated by the need to develop 3D finite solid element models of Japanese post and beam connections, such as the CP-T nail connection. However, when the research project was initiated, it was found that a solid element models for nail connections had never before been studied, although many nail connection models have been developed using finite element procedures.

Having developed the 3D FE single nail connection model, development of the 3D FE models for Japanese post and beam connections was able to set out. The scope of this study, therefore, was limited to development of a pilot model for the Japanese CP-T joint, in order to investigate the applicability of the single nail connection model to a multiple connections model. For model validation, the test data, developed by Stefanescu (2000) at the University of British Columbia were used.

In this chapter, based on the findings from the pilot model study, the limitations of the plasticity-based model and recommendations for improving the CP-T connection models are discussed.

### **8.1 Japanese CP-T nail connection model**

#### **8.1.1 Experimental reference work and model description**

The Japanese CP-T connection is a standard connection for attaching a post to a beam in traditional Japanese post and beam construction. Basically, it consists of a CP-T steel

plate connector (see Figure 6.1) with ten ZN65 nails. Often, a mortise and tenon joint is combined with the CP-T plate to strengthen the joint.

Based on the single nailed connection model developed, a pilot 3D FE model for the CP-T connection with mortise and tenon joint was created. The dimensions of the connection and the boundary conditions conformed to the reference work of Stefanescu (2000).

Figure 8.1 shows the configuration of Stefanescu's CP-T connection test and the corresponding 3D FE connection model. Since it was a pilot model, any influence from loose or tight wood-to-wood contact in the mortise and tenon joint was not considered in this study.

The CP-T plate was installed on one side, which is a typical connection detail. The connection was loaded by pulling a steel pin through the post. As reported in Stefanescu's thesis, this made the connection eccentric during loading; and eventually, the connection was tilted toward the plate side, due to the twisted beam and post, as shown in Figure 8.2. This tilting behaviour was observed for all eight tests with an average tilting angle ( $\Theta$ ) of 2.8 degrees between post and beam<sup>4</sup>.

This phenomenon necessitated deliberation on the loading scheme and boundary condition for the FE model. For an initial model, the boundary condition was set with all fixed nodes on the side surfaces of the 400 mm-long beam conforming to the fixtures of bolted connections in the real test; and, for the loading scheme, an incremental displacement-controlled loading method was used at first.

---

<sup>4</sup> A measurement of angle is shown in Figure 8.2

Failure modes of the connection, which were photographed by Stefanescu (2000), are shown in Figure 8.3 and Figure 8.4. Perpendicular to grain tension splitting of the beam member, nail pull-out and plate shear were the major failure modes. However, during the process of model development, it was discovered that the most influential failure on model prediction was end-tearout of nail in the tenon. More details of end-tearout effect on the simulated results are presented in section 8.2.3.

Canadian coastal Western Hemlock was used for the post and beam, which had a 105 mm × 105 mm cross section and a range of specific gravity from 0.39 to 0.47; however, a wood foundation material model for this species was not available. Although, in order to construct an accurate foundation material model for this species, a data set of the parallel and perpendicular to grain nail-embedment tests, with the nails used, should have been prepared, the material models for Douglas-fir developed in this study were used instead. For the steel material, the elasto-perfectly plastic model with the same material constants listed in Table 6.1 was used. All volume components of the CP-T connection model are illustrated in Figure 8.5.

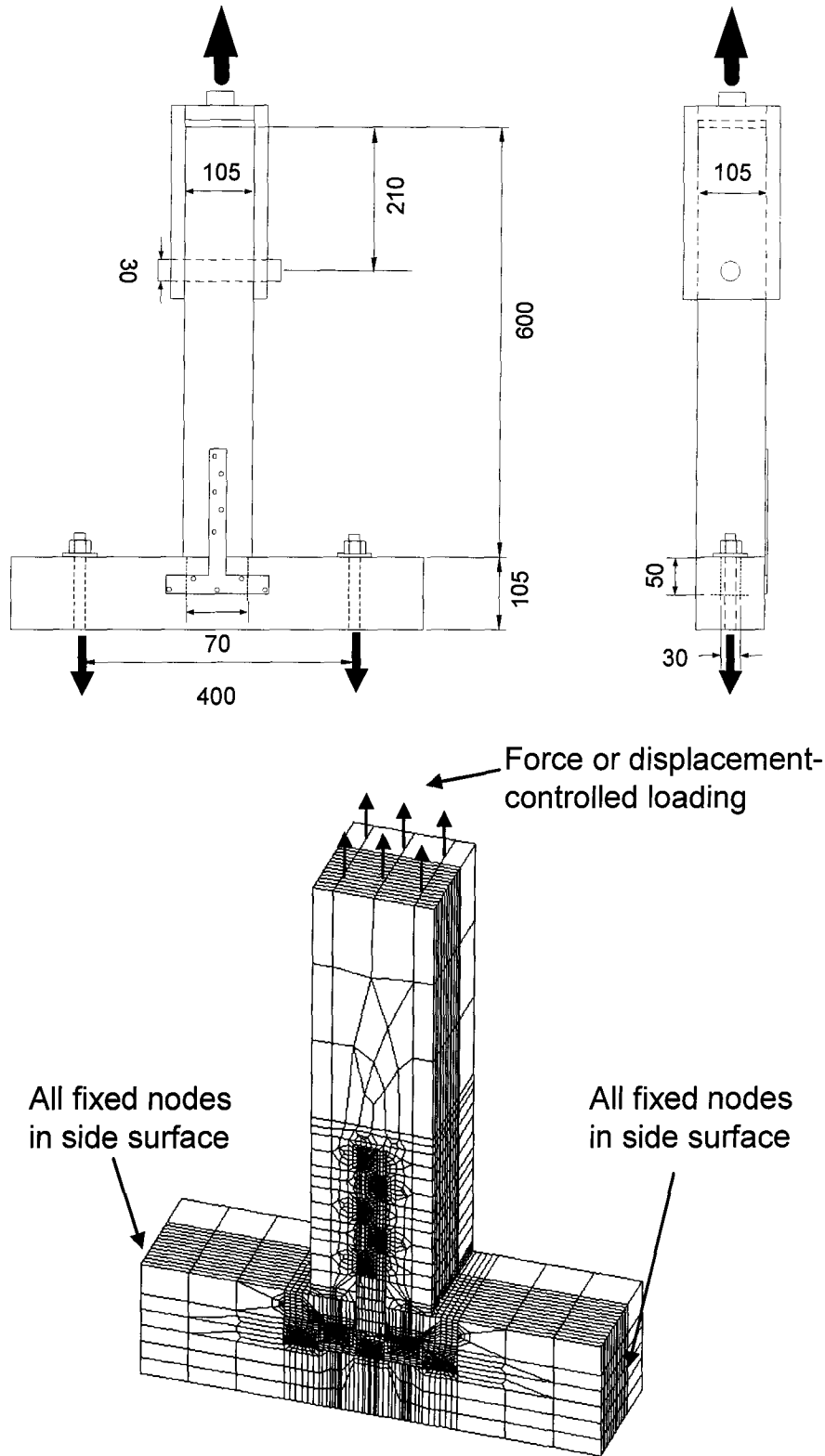


Figure 8.1 The reference test setup by Stefanescu (2000) and the corresponding 3D FE CP-T connection model (units: mm).

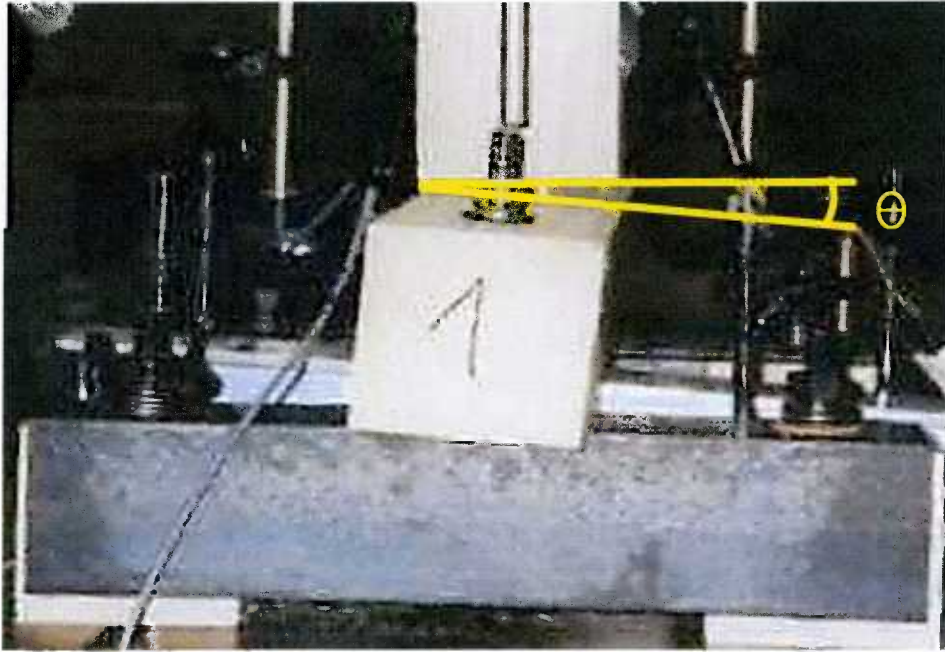


Figure 8.2 A tilted CP-T connection under loading.  $\Theta$  was the tilting angle.  
(photo by Stefanescu 2000).

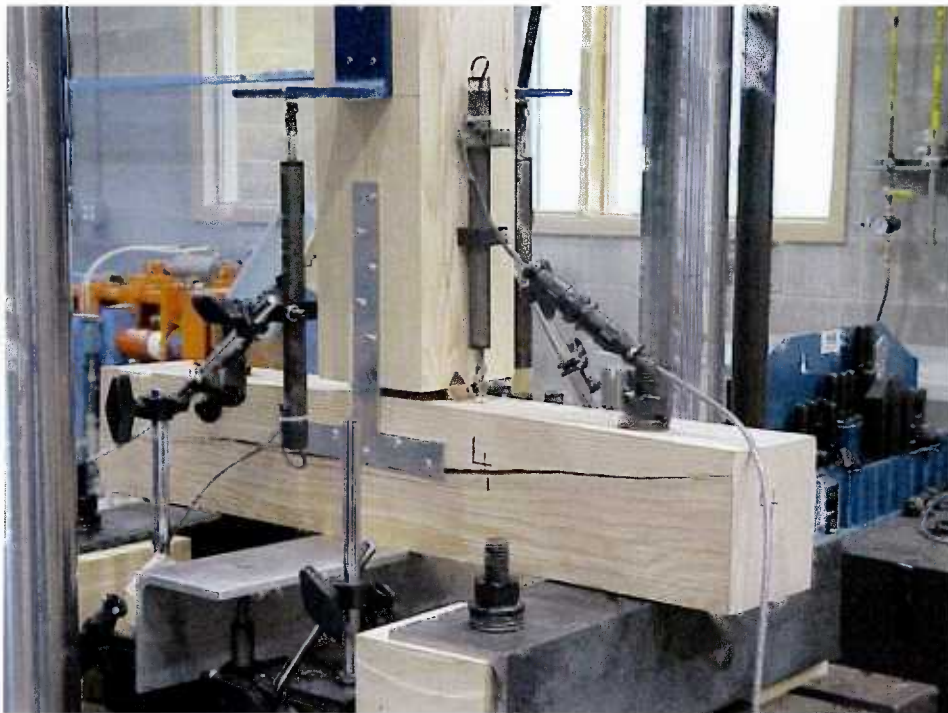


Figure 8.3 Failure mode; perpendicular to grain tension splitting  
(photo by Stefanescu 2000).

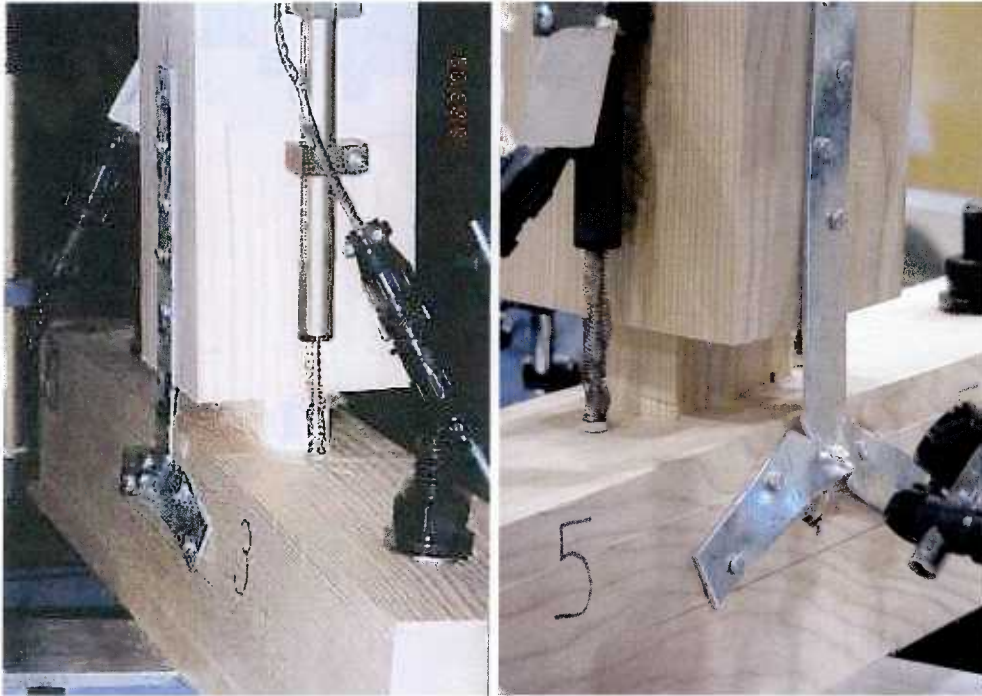


Figure 8.4 Failure modes; nail pull-out (left) and CP-T connector in shear (right) (photo by Stefanescu 2000).

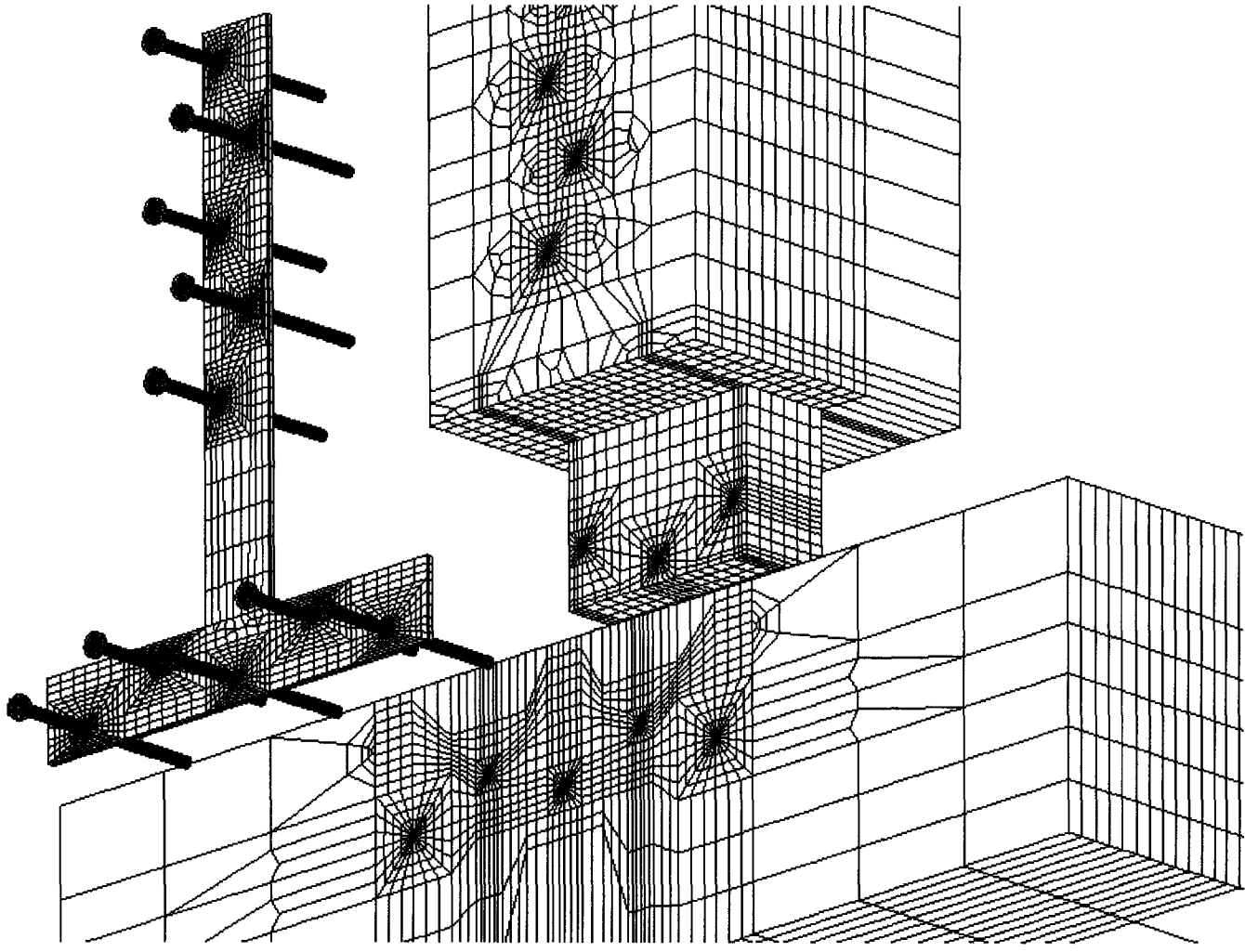


Figure 8.5 Illustration of the meshed model of the Japanese CP-T joint.

### 8.1.2 Square foundation meshing

To facilitate meshing, the wood foundation region was chosen to have a square cross section (Figure 8.6 and Figure 8.7). Since the nail spacing of the connection was too narrow to accommodate the two adjacent  $4.5 \times d$  cylindrical foundations, overlap of the foundations was inevitable. This caused difficulty in meshing the portion that was overlapped by two adjacent cylindrical foundations.

A foundation having a square cross section with the same depth of  $4.5 \times d$  was used as an alternative. Compared to the cylindrical foundation model, it produced a slightly high load-embedment curve in the parallel to grain direction, as shown in Figure 8.8. For the perpendicular to grain embedment, the square model showed a curve that was almost equivalent to that of the cylindrical model (Figure 8.9). Although the curve deviation in the parallel to grain direction could be corrected by adjusting the calibration factors, the square foundation model was assumed to be equivalent to the cylindrical foundation model.

In an initial model, the surface-to-surface contact elements were defined for every contact interface. Later, in order to consider end-tearout of nail in the tenon, the contact elements of the two side nails penetrating into the tenon were deactivated.

The coefficient of friction for the wood-to-wood contact was assumed to be 0.7. The coefficients for the wood-to-steel (0.7) and steel-to-steel (0.3) contacts were the same as those used in the single nail connection model. The contact interfaces defined with the contact element and frictional coefficients used in the initial model are summarized in Figure 8.10.

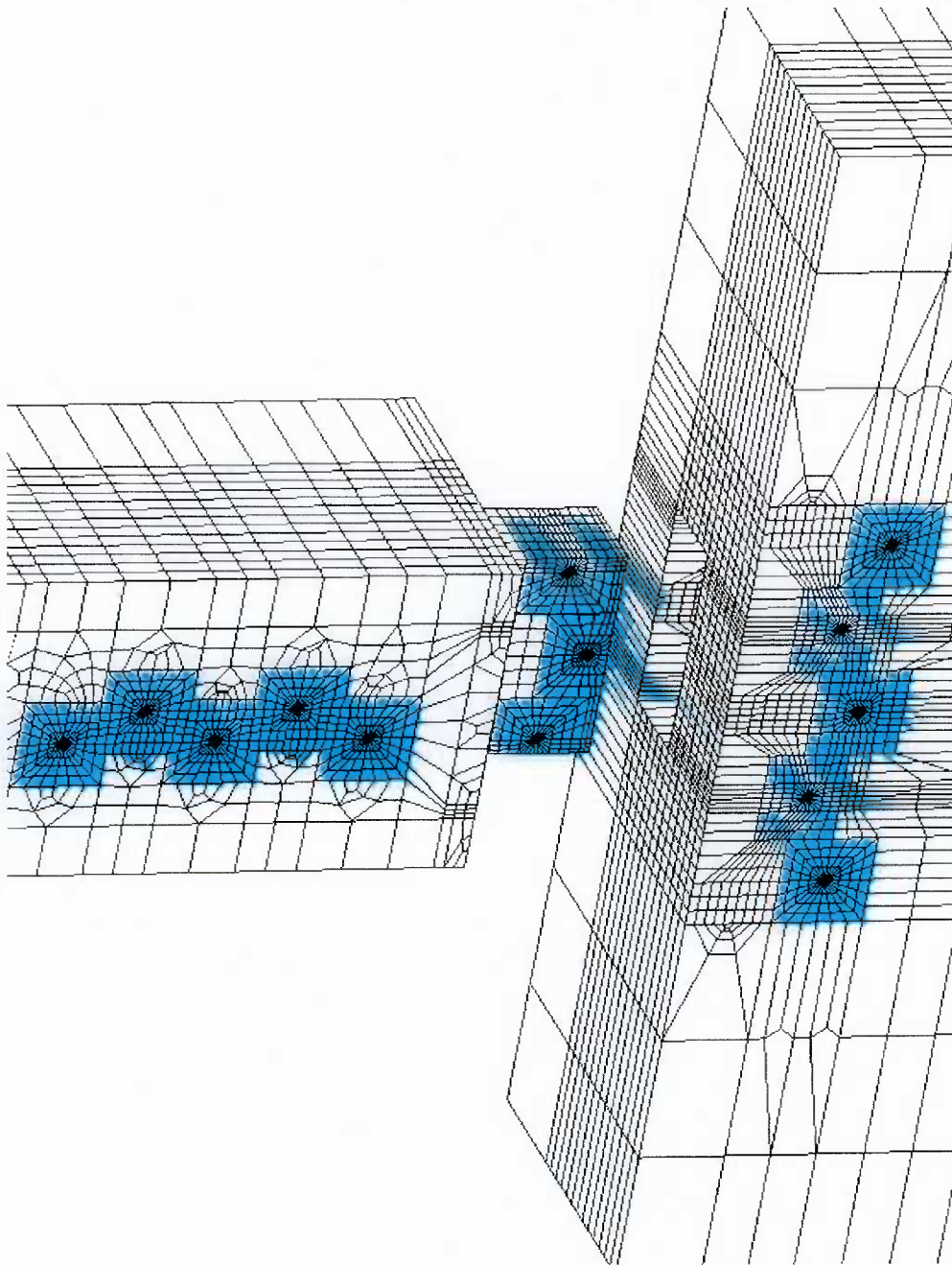


Figure 8.6 Square wood foundation model overlapped (colored portions).

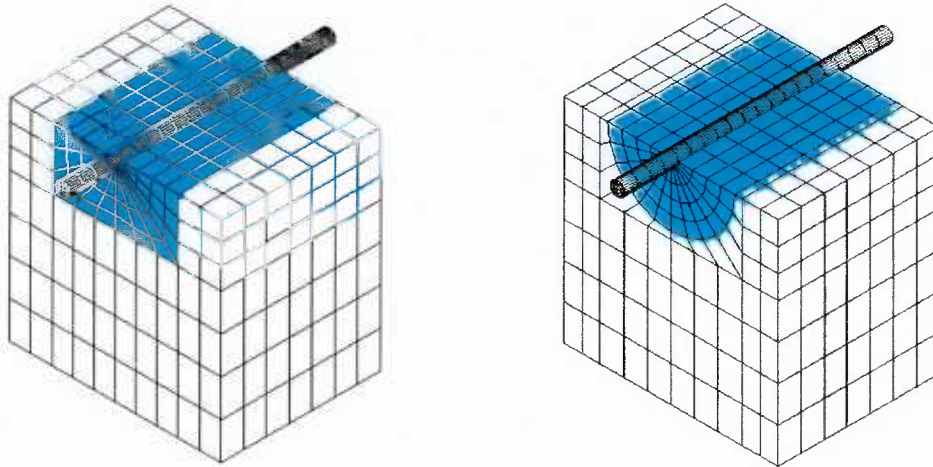


Figure 8.7 Wood foundation models: Square foundation model (left) and cylindrical foundation model (right).

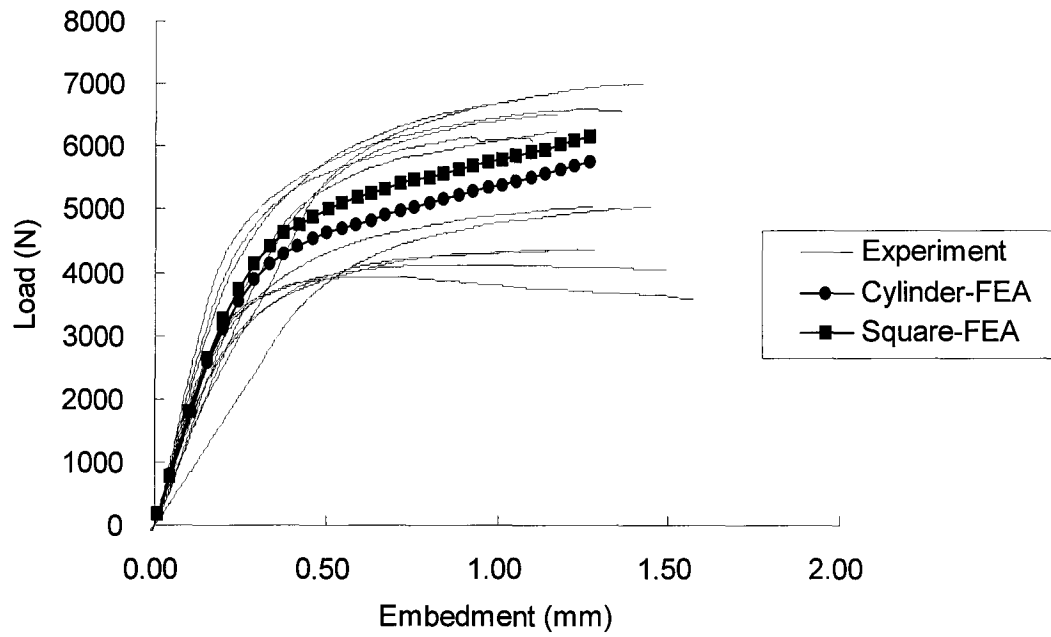


Figure 8.8 Comparison of the simulated parallel to grain load-embedment curves between the square foundation and cylindrical foundation models. 3.3-mm diameter nail in Douglas-fir.

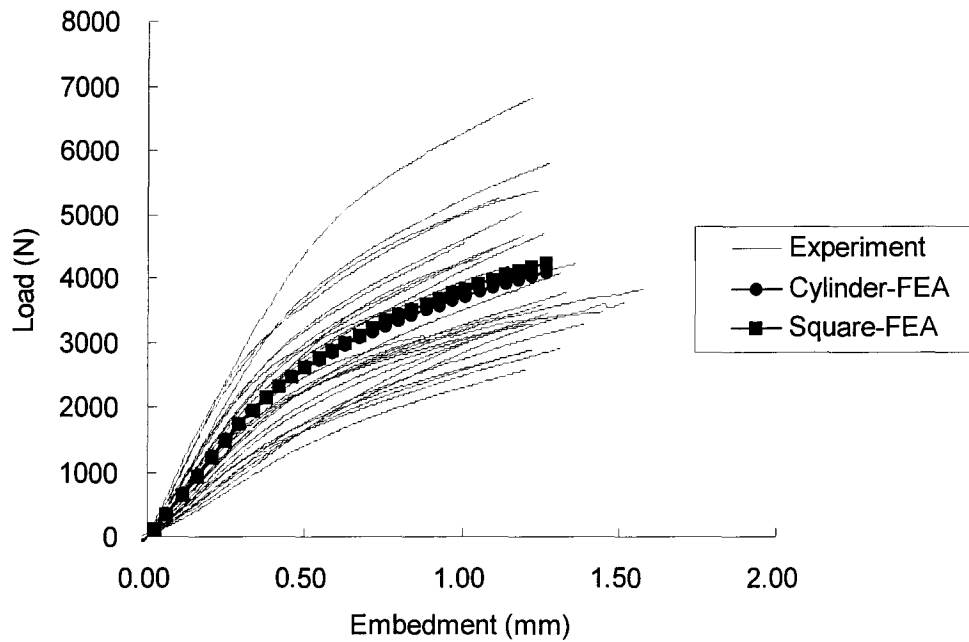


Figure 8.9 Comparison of the simulated perpendicular to grain load-embedment curves between the square foundation and cylindrical foundation models. 3.3-mm diameter nail on Douglas-fir.

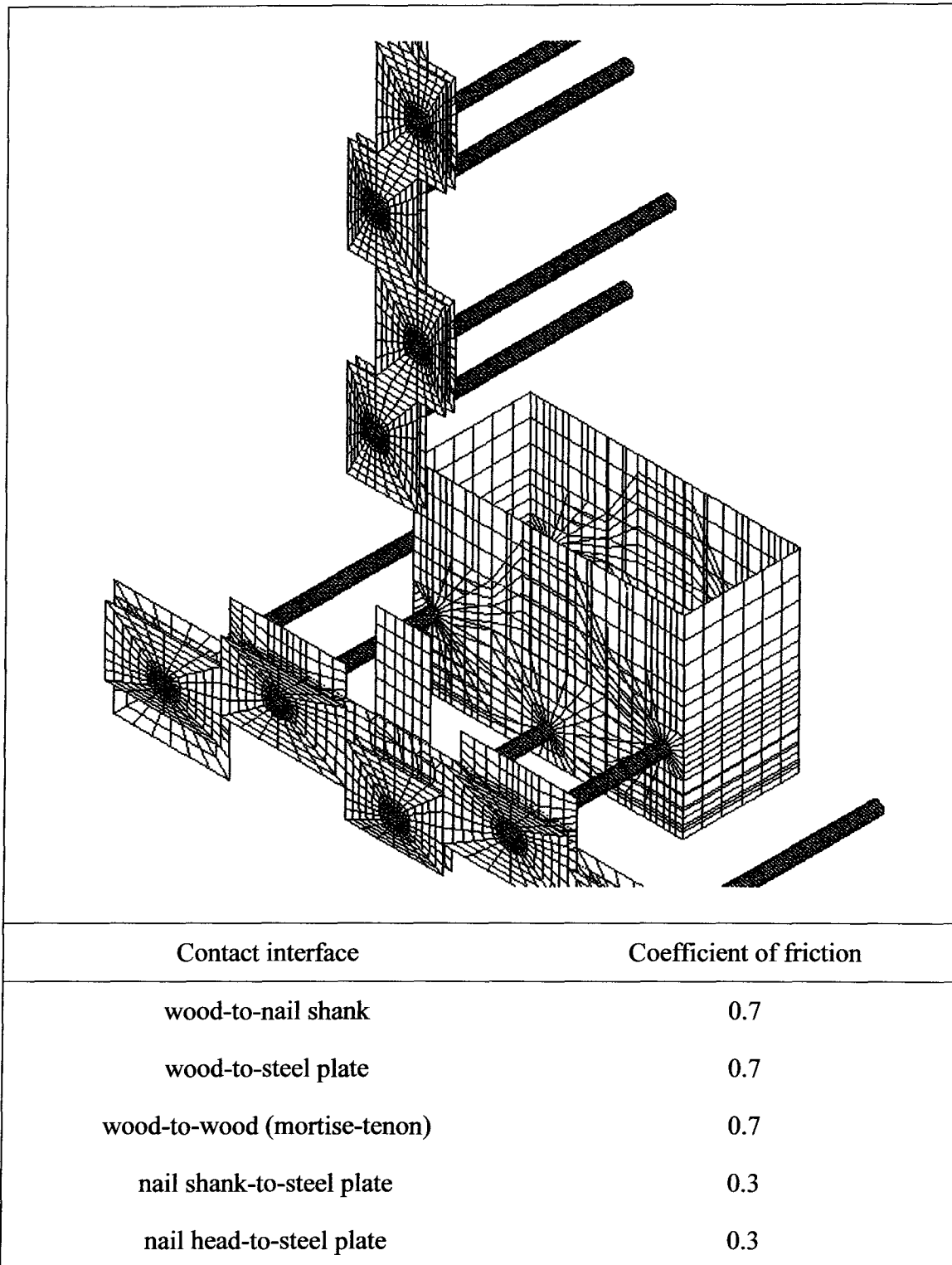


Figure 8.10 Definitions of the contact elements and the coefficients of friction.

## 8.2 Simulation results depending on the loading schemes

It was found that the model using an incremental displacement-controlled loading scheme could not simulate the tilting behaviour of the connection. It provided only a uniformly vertical translation of the post. Thus, additional simulations were conducted using a force (pressure)-controlled loading scheme. Results from two different loading methods were remarkably different. The results of both types of loading are discussed in relation to Stefanescu's experimental results.

### 8.2.1 Deformed shapes of the CP-T connection model

#### 8.2.1.1 Effect of loading method

Figure 8.11 shows the differences in the simulated deformations, depending on the loading methods. Neither method was able to accurately represent the tilting behaviour. Although the force-controlled loading method produced tilting behaviour (tilting angle  $\Theta = 5.7$  degrees), it was due to the rotation of the post only. The bottom sill was not twisted.

In fact, the boundary condition of the model provided rigid constraints. No displacement of the nodes that were assigned to zero-displacement in any degree of freedom was allowed. However, the beam fixtures of the real test consisted of two bolted connections that could allow the beam to twist. Also, the loading steel pin linking the post to the crosshead permitted swiveling of the post and deformation, due to the pin embedment on the wood post. These discrepancies between the model and the real test resulted in highly stiff predictions of the load-deformation response compared to experimental observations. Therefore, assuming that the real connection tests were conducted under ideally rigid constraints, the deformation simulated by the

displacement-controlled method was deemed reasonable. The photos on the left of Figure 8.4 seemed the case of deformation under ideally rigid constrains.

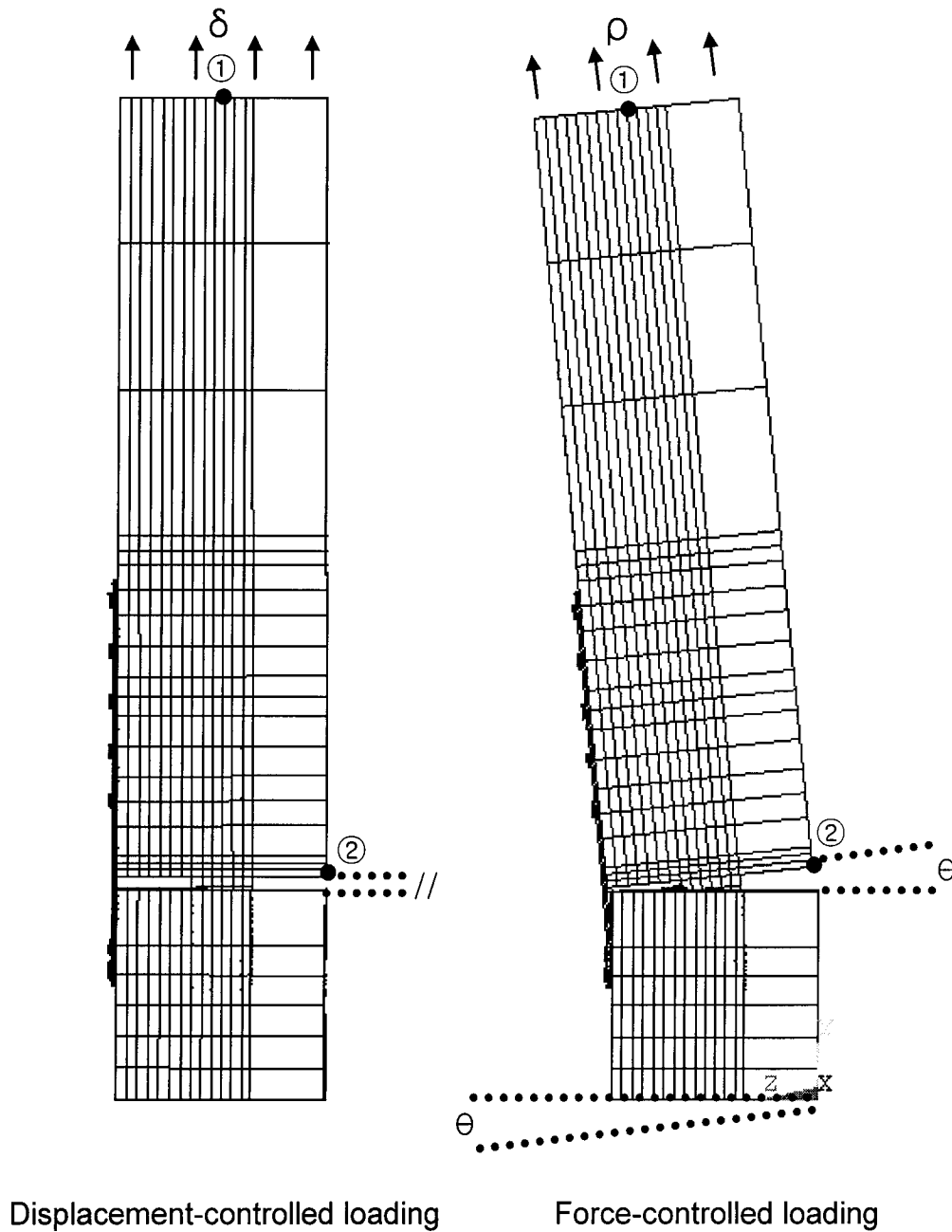


Figure 8.11 Simulated deformations by the two different loading schemes:  
 $\theta$ -tilting angle, ① and ②- points for displacement measurement.

### 8.2.1.2 Deformation of nail and CP-T connector

Figure 8.12 shows the simulated deformation of the nail. Judging from Stefanescu's test results, deformation simulated by the displacement-controlled loading method agreed more closely with the experimental observations than the force-controlled loading method. Under the displacement-controlled loading, the flexural deformation of the three nails penetrating the tenon showed a tendency for nail pull-out from the bottom sill, whereas the three nails under the force-controlled loading did not undergo plastic bending around the nail-head.

Figure 8.13 shows the difference in the Y-directional plastic strain contours in the CP-T steel plate between the two loading methods. Compared to the photo on the right of Figure 8.4, the contour from the displacement-controlled loading showed a good indication of the plate failure.

The deformation progress of the connection is shown in Figure 8.14 and Figure 8.15. The deformation under the force-controlled loading showed tilting toward the steel plate side (*Z*-direction in the figure). This invoked contact crushing of the mortise and tenon by the rotating tenon. It was reasonable to expect this crushing in the real test, due to twisting of the bottom sill. However, the simulation using displacement-controlled loading did not produce this crushing behaviour. In this respect, the results from force-controlled loading were more representative of the experimental results.

In the next section, using Stefanescu's original load-deformation plot, simulated load-deformation relationships are investigated.

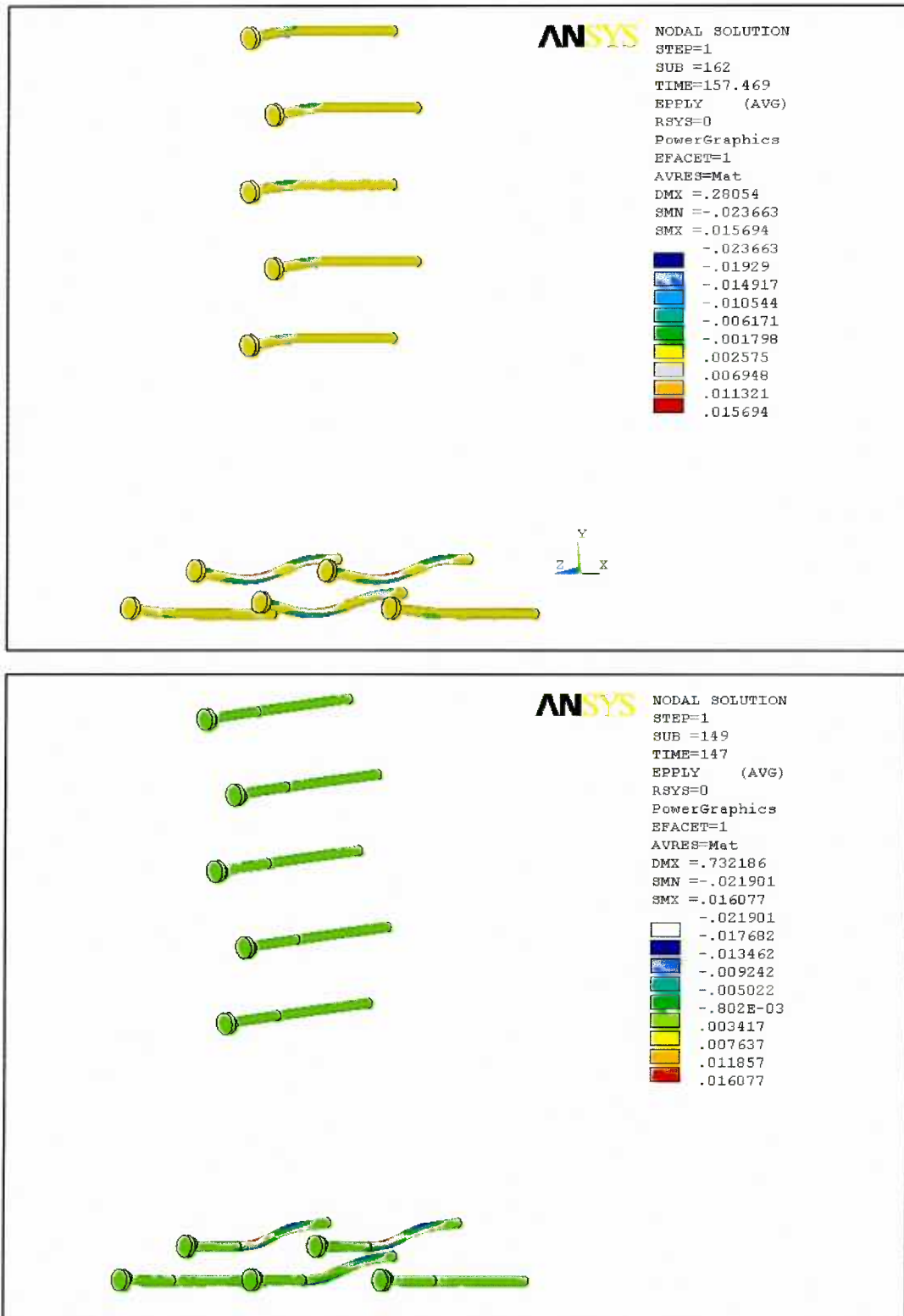


Figure 8.12 The Y-directional plastic strain contour for the nails: displacement-controlled loading (top) and force-controlled loading (bottom).

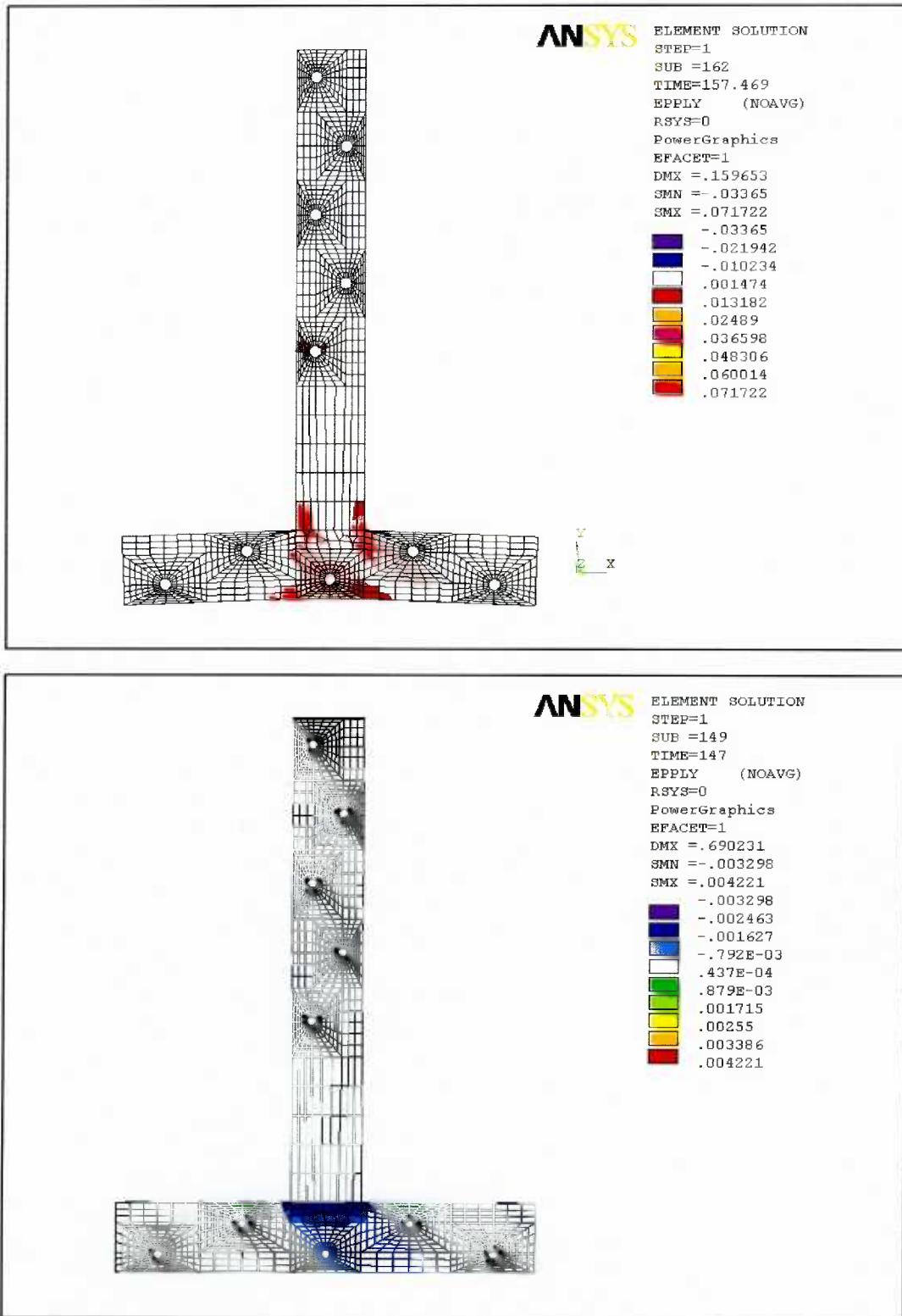


Figure 8.13 The Y-directional plastic strain contour for the CP-T connector: displacement-controlled loading (top) and force-controlled loading (bottom).

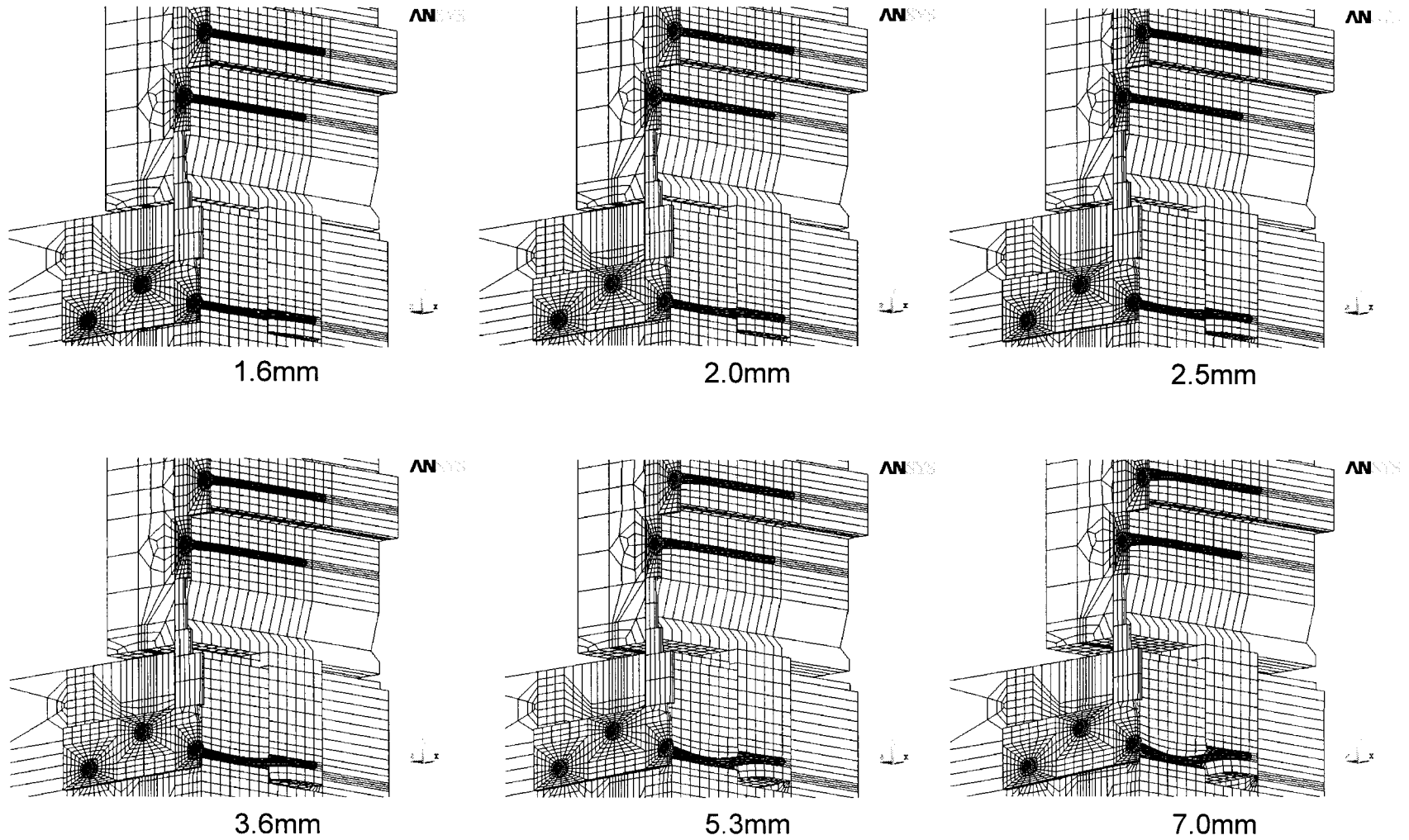


Figure 8.14 Progress of the simulated deformation by the displacement-controlled loading scheme. Sectioned views.

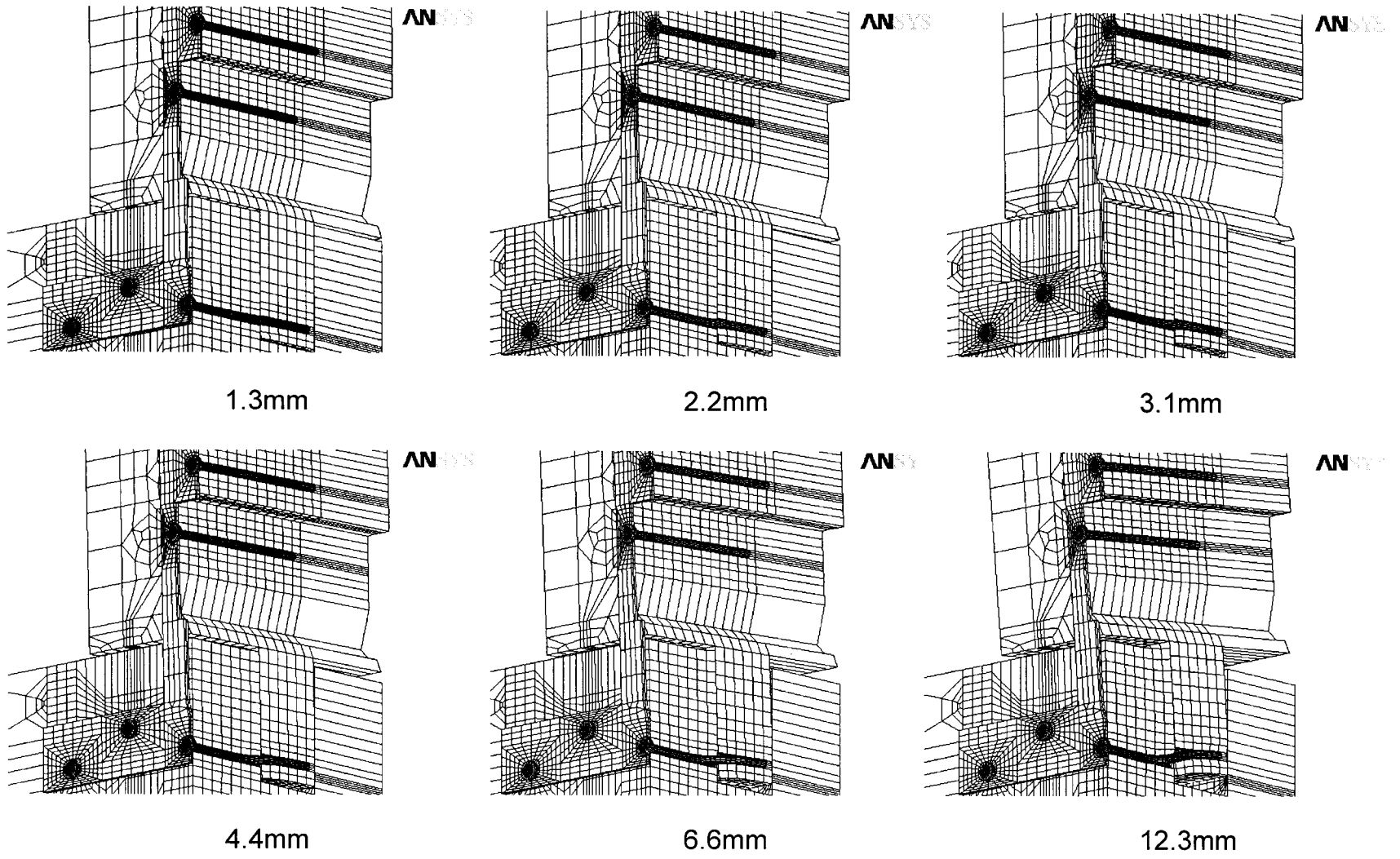


Figure 8.15 Progress of the simulated deformation by the force-controlled loading scheme. Sectioned views.

### 8.2.2 Load-deformation curve of the CP-T connection

Simulated load-deformation curves are superimposed on Stefanescu's experimental curves in Figure 8.16 and Figure 8.17. Model displacements were measured at the two reference points, as shown in Figure 8.11, conforming to the experimental displacement reading points.

All simulated curves showed high stiffness and high load-carrying capacity compared to the experimental curves. It should be noted that the wood foundation model used was based on Douglas-fir with a specific gravity of 0.54, whereas  $SG = 0.42$  for the Western Hemlock tested. For the simulated curves of the displacement-controlled loading method, no difference in deformation between the measurement points was observed. This implies that there was no twisting in the post and beam, as well as no elongation along the height of the post. Thus, this simulated curve may be regarded as an ideal load-deformation curve that was not influenced by any geometry of the deformed shape.

The simulated curves of the force-controlled loading method in Figure 8.17 show an example of the twisting effect on the load-deformation curve although the two displacement measurements of the force-controlled model may have been erroneous (see the equal angle in Figure 8.11 and the point ② curve in Figure 8.17).

It concluded, therefore, that the pilot CP-T model had constraints that were too ideal to represent the real test condition; however, the poor prediction of the load-deformation curve could not be attributed to the unrealistic constraints only. The main cause of the poor load-deformation prediction may be found in the inability of the model to predict fractures. In the next section, the influences of end-tearout of nail in the tenon on model prediction are explained.

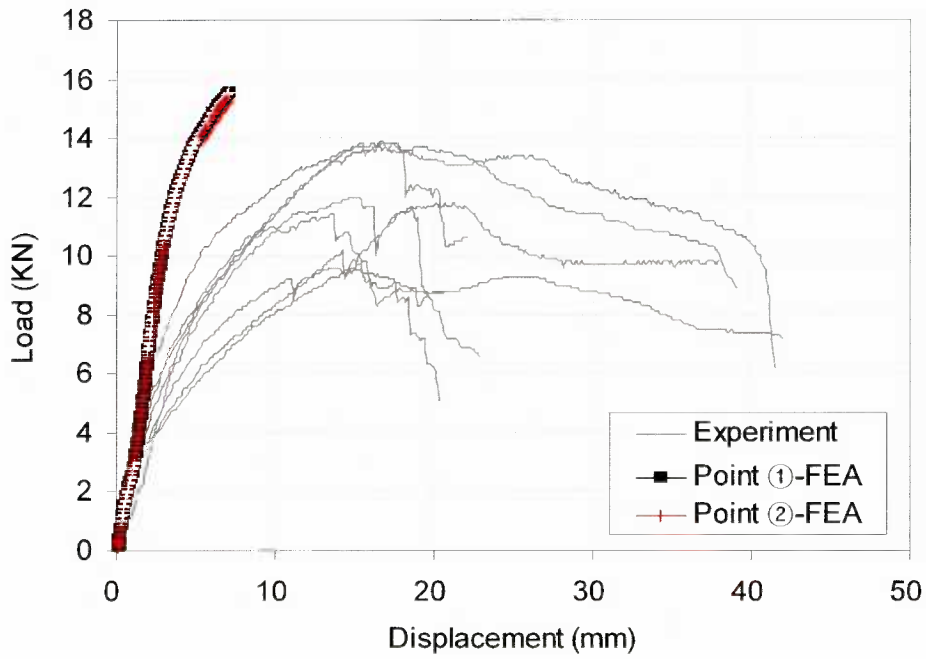


Figure 8.16 Simulated load-deformation curve of the displacement-controlled loading method, superimposed on Stefanescu's experimental curves.

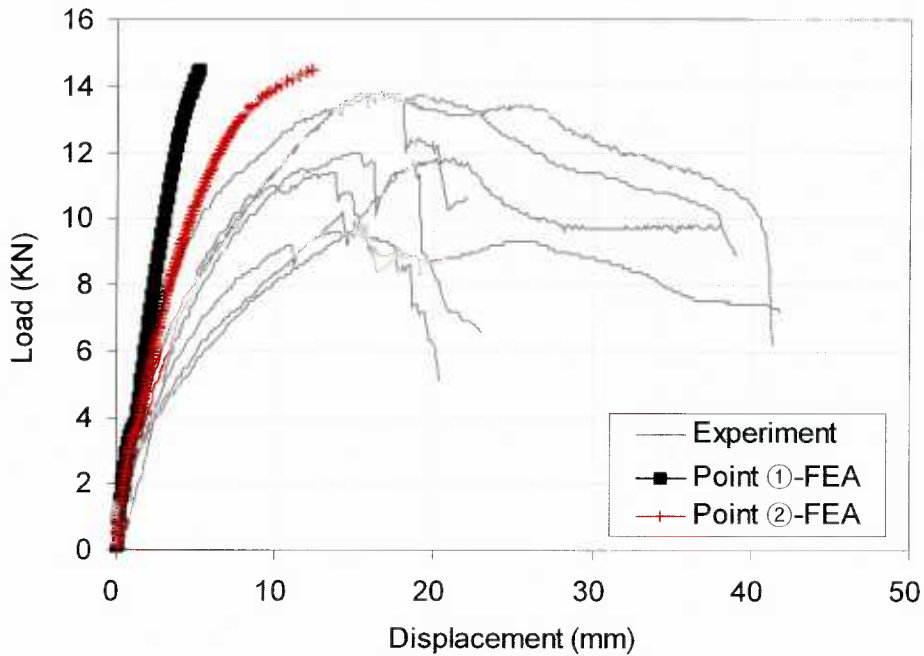


Figure 8.17 Simulated load-deformation curve of the force (pressure)-controlled loading method, superimposed on Stefanescu's experimental curves.

### **8.2.3 Influence of the end-tearout of nail in the tenon on model prediction**

In the CP-T joint, the three middle nails out of the five nails in the bottom sill penetrated into the tenon. The typical failure type of nails penetrating into the tenon is shown in Figure 8.18.

Since these connections had narrow end and edge distances in the configurations, it is most likely that the failures occurred in a brittle manner, including the edge splitting (off) in the side nail connections and the end-tearout of the centre nail in the tenon. These kinds of failures may occur at the initial deformation level or at the time when the nail was driven. Once the nail was off the tenon, the load-carrying ability of the nail connection vanished.

The model used in this study, however, could not simulate the process of the end-tearout. As shown in Figure 8.19, the wood elements surrounding the nail could not split off, unless a fracture algorithm or an intentional cleavage for allowing the end-tearout was introduced into the model. As long as the nail was surrounded by the wood elements, the load-carrying ability of the connection would remain in the model.

In order to investigate the influence of these fracture failures on model prediction, the model was modified and re-run with the assumption that the edge wood in the side nails were split in the beginning, thus eliminating the load-carrying ability of the two side nail connections.

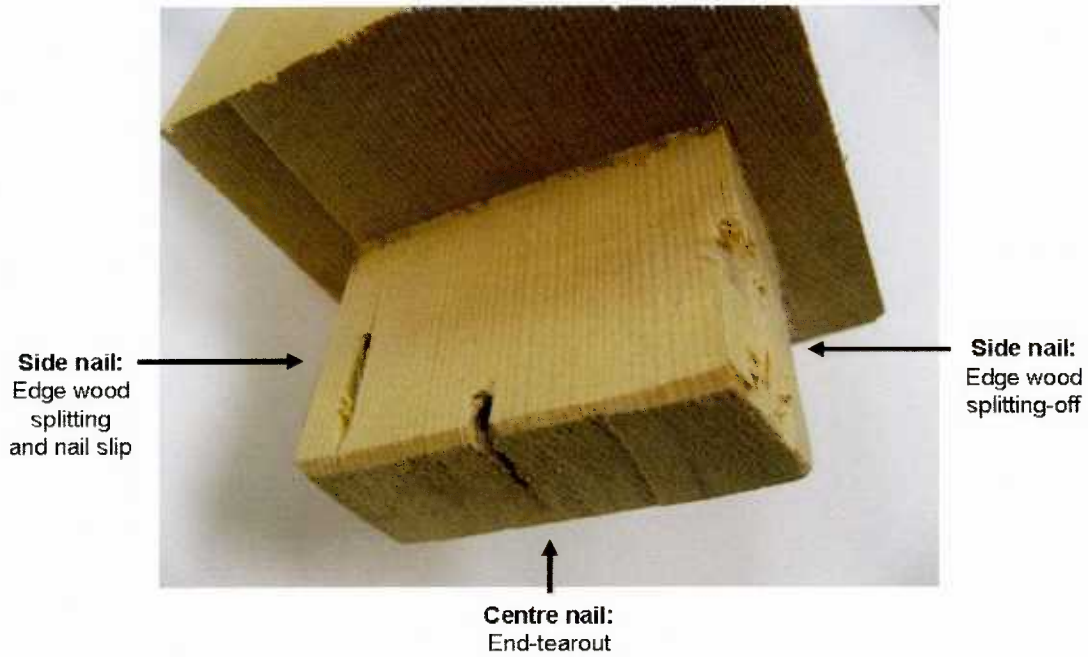


Figure 8.18 Typical failure types of the three nails penetrating the tenon: nail edge splitting (off) in the side nails and nail end-tearout in the centre nail.

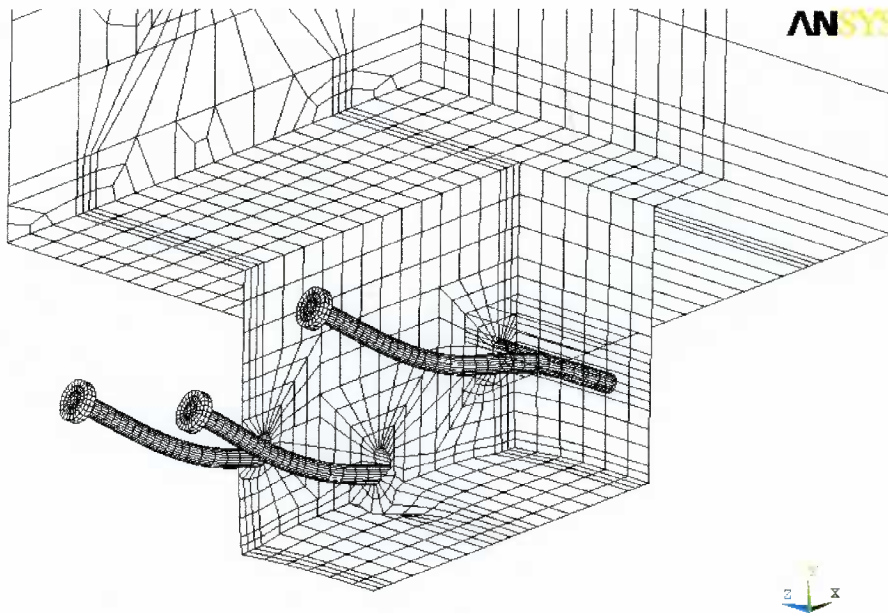


Figure 8.19 Simulated deformed shape of the three nail connections in the tenon. The model could not reproduce the edge wood splitting and the nail end-tearout.

### 8.2.3.1 Modification of the model

Assuming the initial edge split in the side nail connections, the original CP-T joint model was modified so as to remove the load-carrying ability of the side nail connections in the tenon, by eliminating the contact elements between the side nails and the tenon. The nails could then move independently, regardless of the surrounding wood elements in the tenon (Figure 8.20). The centre nail connection model remained without any modifications.

Other conditions remained the same as with the original CP-T joint model. Incremental-displacement controlled loading was applied to the modified CP-T joint model.

### 8.2.3.2 Simulation results of the modified model.

Figure 8.20 shows the deformed shape of the nail connection in the tenon with the modified CP-T joint model. As expected, the side model nails did not deform within the tenon. The goal of zero-load carrying capacity of the side nail connections, due to the edge split, was achieved.

Compared to the real failure of the centre nail connection, the bulge-out of the wood elements under the centre nail would have progressed to the nail eventually slipping off the tenon. However, the plasticity-based model could not perform this failure prediction. This shows the limitations of the model in this study. For further study, it may be useful to introduce a fracture algorithm to this kind of failure prediction.

The predicted load-deformation curve of the modified model is compared with the experimental curves in Figure 8.21. It was revealed that the influence of the nail end-tearout on model prediction was significant. Although the influences of the initial edge

split on the real connection were unknown, the model did react with sensitivity to this influence, so that the prediction of the load-deformation curve was highly improved.

If this influence was also true for the real CP-T joint, reinforcing the connections within the tenon may be useful for improving the load-carrying capacity of a traditional CP-T joint.

Based on the findings from this pilot model study, the recommendations for improving the CP-T joint models are summarized in the following section.

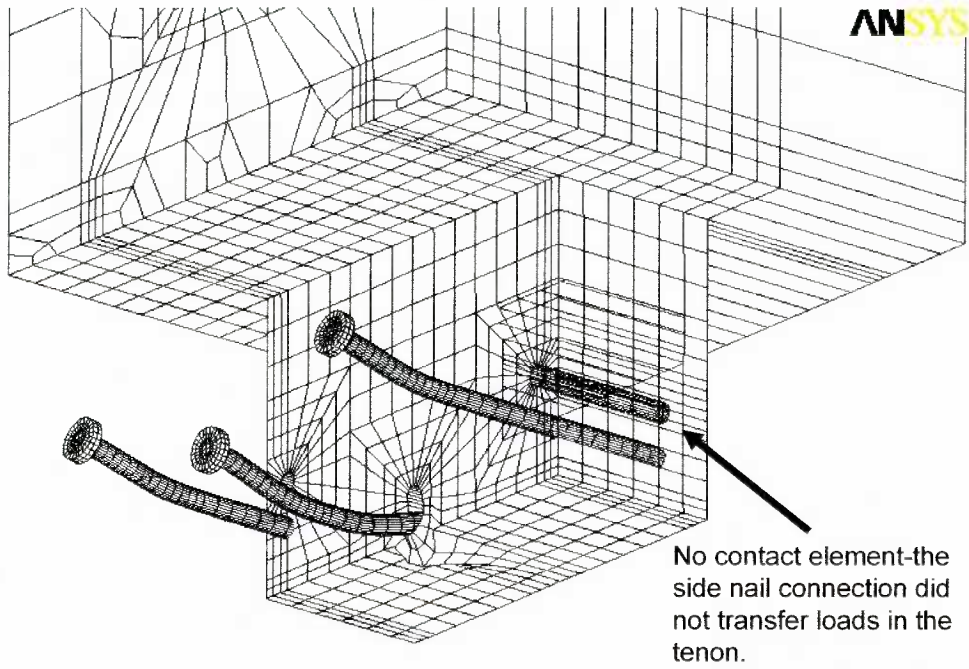


Figure 8.20 Deformed shaped of the CP-T model modified with the initial edge split of the side nail connections.

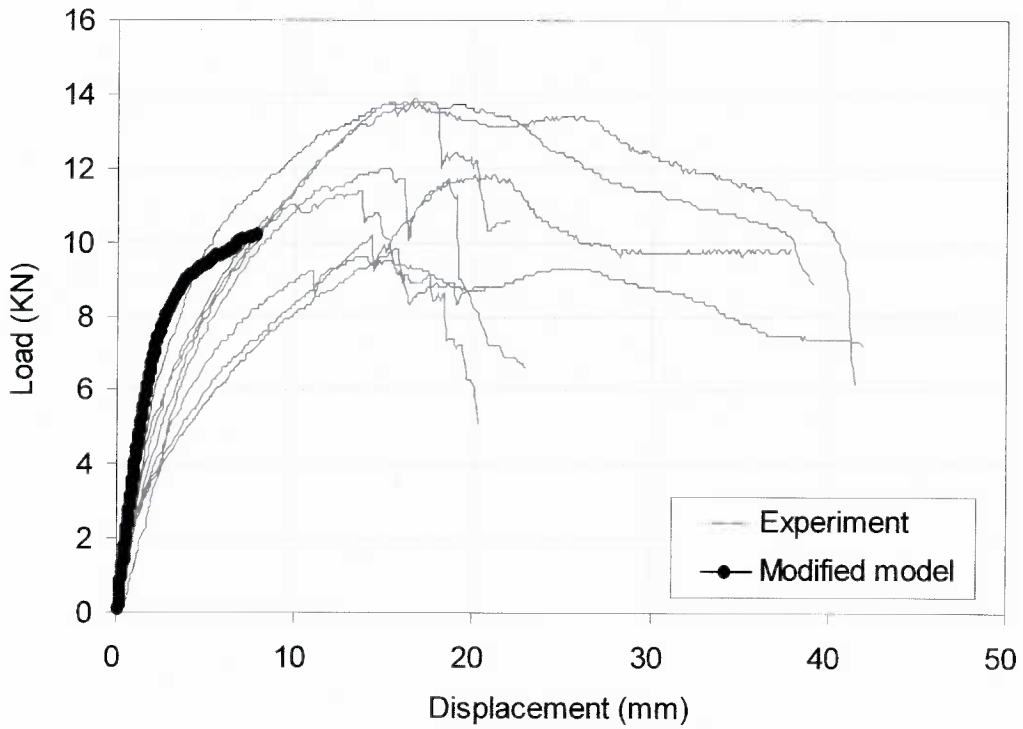


Figure 8.21 Simulated load-deformation curve of the modified CP-T model.

### **8.2.4 Recommendations for the improvement of the 3D FE CP-T joint model**

Generally, the “as-is” model is the best for 3D FE modeling. The pilot CP-T model used ideally rigid constraint conditions; thus, for the “as-is” constraint condition, it is recommended that the two bolted connections for the beam supports and the steel pin through the crosshead be modeled using the wood foundation approach, in order that the constraints would be able to represent the beam twisting effect, the crosshead steel pin embedment, and bolt embedment in the beam supports. To this end, the respective wood foundation material models with prescribed foundation zones should first be established.

Related to the failure of the end-tearout in the tenon, incorporating fracture algorithms into the model would be a solution; however, another study on the wood foundation-based fracture mechanics would be required. Otherwise, as a remedy specifically for this connection, the nail slipping off in the tenon may be modeled by making the nail-slip path open in the surrounding wood elements.

Finally, the use of a multi-processor computer is recommended for modeling multiple connections. In fact, this 3D FE model study could not have been initiated without the remarkable advancements in computer processors. However, a computer powered by the current single processor is still insufficient for the frequent runs necessary for improvement in the CP-T connection model.

## CHAPTER 9. CONCLUSIONS AND RECOMMENDATION

### 9.1 Summary of research

A plasticity-based nonlinear wood foundation model was devised to simulate the three-dimensional wood crushing behaviour under a dowel. The model contains the original concepts, including the material constant derivation process, the prescribed wood foundation and the effective foundation material constants. The model verification was conducted through experimental studies on dowel-embedment tests with a range of “dowels” from a 2.5-mm nail to a 25.4-mm bolt.

Using the wood foundation model, a three-dimensional finite element model applicable for a range of dowel-type wood connections was created. The connection model was validated by comparing it with the experimental results from single nail connections, which included the most intricate wood crushing behaviour in the dowel-type connection.

A feasibility study on the prediction of variability in the lateral resistance of a single nail connection demonstrated the applicability of the model to a statistical approach.

Limitations and shortcomings of the conventional 3D FE model for bolted connections were illustrated. It was proved that the wood material model using MOEs from the standard uniaxial loading test should not be used for modeling the wood crushing behaviour under a dowel.

Finally, as an example of the model application, a pilot model for a multiple nail connection, namely the Japanese CP-T connection, was developed. Based on the findings

about the differences between the real test and the multiple connection model, ways to improve the pilot model were discussed.

## **9.2 Scientific contribution of the research**

The main contribution of the research was to develop the wood foundation model for a 3D FE dowel-type wood connection model. Introducing the wood foundation model to general 3D FE dowel-type wood connections showed that the difficulty in simulating 3D localized wood crushing behaviour under a dowel could be overcome.

The effective foundation properties and prescribed foundation for the wood foundation model were new devices for the implementation of 3D FE analysis to timber connections. Derivation of the effective foundation properties was the key to the construction of the 3D wood foundation material model. The derivation process included a new development in the procedure to determine 3D FE material constants.

Finally, the wood foundation model was capable of predicting the behaviour of a broad range of dowel-type connections. Thus, it will make a great contribution to the utilization of the 3D FE method as a general analysis tool for dowel-type wood connections.

## **9.3 Future research**

The model developed in this study was simple, yet comprehensive for the implementation of 3D FE analysis for dowel-type wood connections. Indeed, this is the first 3D FE model that accounts for wood crushing behaviour. Thus, it will make possible the study of many unsolved problems in dowel-type wood connections, which can only

be explored with three-dimensional analysis. From this standpoint, recommendations and future research needs are discussed.

### **9.3.1 Compressive perpendicular to grain MOE**

The compressive perpendicular to grain MOE of wood has not been of much interest to timber engineers or wood scientists, whereas a great deal of attention has been given to compressive perpendicular to grain strength. However, in terms of 3D computational modeling for wood, accurate compression perpendicular to grain MOE is the critical property for the material model.

The current ASTM standard for the perpendicular to grain strength is not appropriate for determining compression perpendicular MOE because it is based on in-service condition.

A definition of the perpendicular to grain MOE and, accordingly, consensus on a standard test to evaluate the MOE appropriate for numerical modeling is required. This should also be studied for the dowel-embedment modulus.

### **9.3.2 Full bolted connection model**

Since the behaviour of the bolted connection was influenced by side member(s), more extensive study on 3D FE analysis for bolted connections that includes side member(s) is needed. From a technical point of view, a model for a bolted connection with a side member would not be much different from the single nail connection model developed in this study. Only size and the wood foundation model may be of consequence.

### **9.3.3 Failure analysis**

Although this study did not deal with failure analysis, a technique for failure analysis using Weibull's weakest link theory (Barrett et al. 1975, Foschi et al. 1975, Moses 2000) may be a good approach to predicting brittle failure of dowel-type wood connections. Also, prediction of the yield mode in the European yield model may be studied using the 3D FE model developed in this study.

For failure prediction of the dowel slipping off members, fracture mechanics need to be introduced into the 3D FE model.

### **9.3.4 Three-dimensional FE analysis for wood structure**

All 3D FE analyses presented in this study were conducted with a common personal computer (based on a single Pentium IV 2.4GHz processor or higher). Provided that a PC with multiple processors or a supercomputer is available, a wood structure consisting of dowel-type connections (for example, a wood-frame shear wall or wood-joint floor) could be analyzed using a 3D "as-is" model that incorporates the wood foundation model. A sub-modeling technique could also be utilized to reduce the model's execution time.

---

**BIBLIOGRAPHY**

- American Society for Testing and Materials (2003) "Annual Book of ASTM Standards, Section 4-Construction, Volume 04.10 Wood" ASTM international, West Conshohocken, PA.
- ANSYS, Inc. (2006) "ANSYS, Inc. Theory reference" ANSYS Release 8.0 help documentation, Swanson Analysis Systems inc. USA.
- Barrett, J. D. (1974) "Effect of size on tension perpendicular to grain strength of Douglas-fir" *Wood and Fiber Science*, 6(2):126-143.
- Barrett, J. D, Foschi, R. O, and Fox, S. P. (1975) "Perpendicular to grain strength of Douglas-Fir" *Canadian Journal of Civil Engineering*, 2(1):50-57.
- Bathe, K. J. (1996) "Finite element procedure" Prentice-Hall Inc., New Jersey, USA.
- Blass, H. J, and Görlacher, R. (2004) "Compression perpendicular to the grain" 8<sup>th</sup> World Conference on Timber Engineering, Lahti, Finland.
- Bodig, J. and Jayne, B.A. (1982) "Mechanics of wood and wood composite" Van Nostrand Reinhold Company Inc.
- Chen, C. J., Lee, T. L. and Jeng, D. S. (2003) "Finite element modeling for the mechanical behavior of dowel-type timber joints" *Computers & Structures*, 81: 2731-2738.
- Chen, W. F. (1994) "Constitutive equations for engineering materials; Vol. 2: plasticity and modeling" John Wiley & Sons, Inc.
- Chen, W. F. and Han, D. J. (1988) "Plasticity for structural engineers" Springer-Verlag New York Inc.
- Chen, W. F. and Saleeb, A. F. (1982) "Constitutive equations for engineering materials; Vol. I: elasticity and modeling" John Wiley & Sons, Inc.
- Chui, Y. H. and Ni, C. (1998) "Stress-strain relationship of common wire nails under reversed cyclic loading" *Journal of Testing and Evaluation*, 26(5): 420-425.
- Davalos-Sotelo, R. and Pellicane P. J. (1992) "Bolted connections in wood under bending/tension loading" *Journal of Structural Engineering*, 118(4): 999-1013.
- Dinwoodie, J. M. (2000) "Timber: Its nature and behaviour-second edition" E & FN Spon-The Taylor & Francis Group.

- Erki, M. A. (1991) "Modelling the load-slip behaviour of timber joints with mechanical fasteners" *Canadian Journal of Civil Engineering*, 18(4):607-616.
- Finckenstein, G. (1999) "Earthquake resistant connections for post-and-beam timber construction" The research report, Department of Wood Science, The University of British Columbia, Vancouver, BC, Canada.
- Forest Products Laboratory (1999) "Wood handbook-Wood as an engineering material" General Technical Report, FPL-GTR-113.
- Foschi, R. O. (1974) "Load-slip Characteristics of Nails" *Wood Science*, 7(1):69-76.
- Foschi, R. O. and Bonac, T. (1977) "Load-slip characteristics for connections with common nails" *Wood Science*. 9(3):118-123.
- Foschi, R. O. (1977) "Analysis of wood diaphragms and trusses, Part II: Truss-plate connections" *Canadian Journal of Civil Engineering*, 4(3):353-362.
- Foschi, R. O. and Longworth, J. (1975) "Analysis and design of griplam nailed connections" *Journal of the Structural Division, ASCE*, 7101(12):2537-2555.
- Foschi, R. O. (2000) "Modeling the hysteretic response of mechanical connections for wood structures" *Proceedings of World Conference in Timber Engineering*, Whistler, BC, Canada.
- Guan, Z. W. and Rodd, P. D. (2000) "A three-dimensional finite element model for locally reinforced timber joints made with hollow dowel fasteners" *Canadian Journal of Civil Engineering*, 27(4):785-797.
- Guan, Z. W. and Rodd, P. D. (2001) "DVW-Local reinforcement for timber joints" *Journal of Structural Engineering*, 127(8):894-900.
- He, M. (2002) "Numerical modeling of three-dimensional light wood-framed buildings" Ph.D dissertation, Department of Wood Science, The University of British Columbia, Vancouver, BC, Canada.
- Hill, R. (1983) "The Mathematical Theory of Plasticity" Oxford University Press, New York.
- Hirai, T. (1991) "Analyses of the lateral resistances of bolt joints and drift-pin joints in timber II-Numerical analyses applying the theory of a beam on an elastic foundation" *Mokuzai Gakkaishi*, 37(11):1017-1025 (in Japanese).
- Hong, J. P. and Barrett, J. D. (2006a) "Empirical wood material model for three dimensional finite element analysis of a nail joint" 9<sup>th</sup> World Conference on Timber Engineering, Portland, OR, USA.

- Hong, J. P. and Barrett, J. D. (2006b) "Three-dimensional finite element analysis of nailed connections" 9<sup>th</sup> World Conference on Timber Engineering, Portland, OR, USA.
- Kharouf, N. (2001) "Post-elastic behaviour of bolted connections in wood" Ph.D dissertation, Department of Civil Engineering and Applied Mechanics, McGill University, Montreal, QC, Canada.
- Korin, U. (1990) "Timber in compression perpendicular to grain" Proceedings of the CIB-W-18, Paper 23-6-1, Lisbon, Portugal.
- Lam, F. and Yan, H. (2004) "Comparison of "Nail power" between BC coastal species and competing species in Japan" The research report, Department of Wood Science, The University of British Columbia, Vancouver, BC, Canada.
- Leicester, R. H., Fordham, H. and Breitingner, H. (1998) "Bearing strength of timber beams" Proceedings of the CIB-W-18, Paper 31-6-5, Savonlinna, Finland.
- Lessard, L. B. and Shokprie, M. M. (1995) "Two-dimensional modeling of composite pinned-joint failure" *Journal of Composite Materials*, 29(5):671-697.
- Madsen, B. (2000) "Behavior of timber connections" Timber engineering Ltd, Alpine Court, North Vancouver, BC, Canada.
- McCarthy, C. T., McCarthy, M. A., Lawlor, V. P. and Stanley, W. F. (2005a) "Three-dimensional finite element analysis of single-bolt, single-lap composite bolted joints: Part I-model development and validation" *Composite Structures*, 71(2):140-158.
- McCarthy, C. T. and McCarthy, M. A. (2005b) "Three-dimensional finite element analysis of single-bolt, single-lap composite bolted joints: Part II-effects of bolt-hole clearance" *Composite Structures*, 71(2):159-175.
- McLain, T. E. and Thangjitham, S. (1983) "Bolted wood-joint yield model" *Journal of Structural Engineering*, 109(8):1820-1835.
- Mihailescu, T. (1998) "An investigation of the performance of mortise and tenon joints using the finite element method" Ph.D dissertation, Buckinghamshire Chilterns University.
- Mihailescu, T. and Nicholls, T. (1999) "Problems encountered in designing a finite element model of mortise and tenon joints" Conference paper, ICWSF '99, Missenden Abbey, England.
- Moses, D. M. (2000) "Constitutive and analytical models for structural composite lumber with applications to bolted connections" Ph.D dissertation, Department of Civil Engineering, The University of British Columbia, Vancouver, BC, Canada.

- Moses, D. M. and Prion, H. G. L. (2002) "Anisotropic plasticity and the notched wood shear block" *Forest Product Journal*, 52(6):43-54.
- Ni, C. (1997) "Behaviour of nailed timber joints under reversed cyclic load" Ph.D dissertation, Faculty of Forestry and Environmental, The university of New Brunswick, Fredericton, NB, Canada.
- Patton-Mallory, M., Cramer, S. M., Smith, F. W. and Pellicane, P. J. (1997a) "Nonlinear material models for analysis of bolted wood connections" *Journal of Structural Engineering*, 123(8):1063-1070.
- Patton-Mallory, M., Pellicane, P. J. and Smith, F. W. (1997b) "Modeling bolted connections in wood: Review" *Journal of Structural Engineering*, 123(8):1054-1062.
- Pope, D. J. and Hilson, B. O. (1995) "Embedment testing for bolts: A comparison of the European and American procedures" *Journal of the Institute of Wood Science* 13(6):568-571.
- Rodd, P. D. and Leijten, A. J. M. (2003) "High-performance dowel-type joints for timber structures" *Progress in structural engineering and materials*, 5(2):77-99.
- Saliklis, E. P., Urbanik, T. J. and Tokyay, B. (2003) "Bilinear modelling of cellulosic orthotropic nonlinear materials" *Journal of Pulp and Paper Science*, 29(12):407-411.
- Shih, C. F., and Lee, D. (1978) "Further developments in anisotropic plasticity", *Journal of Engineering Materials and Technology*, 100:294-302.
- Steel and tube distribution (2000) "Dimensions & properties handbook-December 2000" Steel and tube holdings limited.
- Stefanescu, M. (2000) "Lateral resistance of traditional Japanese post-and-beam frames under monotonic and cyclic loading conditions" Master thesis, Department of Wood Science, The University of British Columbia, Vancouver, BC, Canada.
- Smith, I. (1983) "Coefficient of friction value applicable to contact surfaces between mild steel connectors such as bolts and dry European white wood" *Journal of the Institute of Wood Science*, 9(5):229-234.
- Smith, I., Luke, R. J. and Barry, O. H. (1988) "An integrated approach to modeling load-slip behavior of timber joints with dowel type fasteners" *Proceedings of the 1988 International Conference on Timber Engineering*, Seattle, WA, USA.
- Soltis, L. A., Hubbard, F. K. and Wilkinson, T. L. (1986) "Bearing strength of bolted timber joints" *Journal of Structural Engineering*, 112(9):2141-2154.

- Tabiei, A. and Wu, J. (2000) "Three-dimensional nonlinear orthotropic finite element material model for wood" *Composite Structures*, 50(2):143-149.
- Tserpes, K. I, Papanikos, P. and Kermanidis, T. (2001) "A three-dimensional progressive damage model for bolted joints in composite laminates subjected to tensile loading" *Fatigue & Fracture of Engineering Materials & Structures*, 24(10):663-675.
- Tsujimoto, Y. and Wilson, D. (1986) "Elasto-plastic failure analysis of composite bolted joints" *Journal of Composite Materials*, 20(3):236-252.
- Valliappan, S., Boonlaulohr, P. and Lee, I. K. (1976) "Non-linear analysis for anisotropic materials", *International Journal for Numerical Methods in Engineering*, 10(3):597-606.
- Wriggers, P. (2002) "Computational contact mechanics" John Willey & Sons Ltd. West Sussex, England.
- Zienkiewicz, O. C. and Taylor, R. L. (1991a) "The finite element method fourth edition volume 1 Basic formulation and linear problem" McGraw-Hill Book Co.
- Zienkiewicz, O. C. and Taylor, R. L. (1991b) "The finite element method fourth edition volume 2 solid and fluid mechanics dynamics and non-linearity" McGraw-Hill Book Co.

## APPENDIX A

### Generalized Anisotropic Hill Potential Theory

The wood material model developed in this study used the generalized anisotropic Hill potential theory (ANSYS, Inc. 2006). This is a modified Hill's anisotropic plasticity theory (Hill, 1983) by Shih and Lee (1978), which accounts for differences in yield strengths in tension and compression. In this theory an associated flow rule is assumed and the yield criterion is updated by the work hardening model developed by Valliappan et al. (1976). Therefore, the yield surface forms an initially shifted cylinder in stress space as shown in Figure A-1

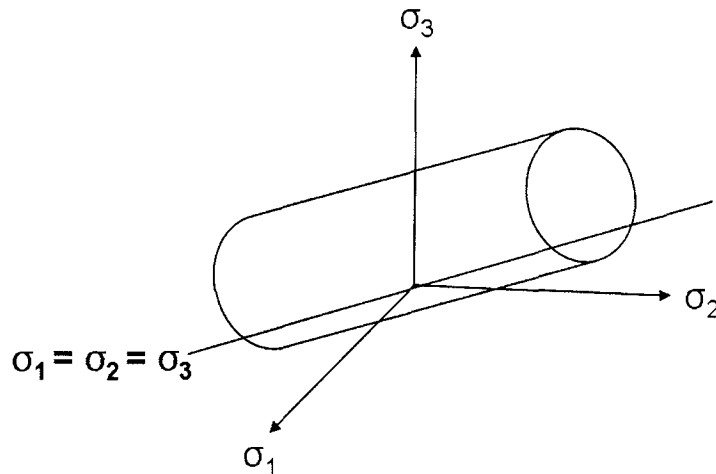


Figure A-1 Yield surface of the generalized anisotropic Hill potential theory.

The theoretical description of this plasticity-based model is as follows.

The effective stress  $\sigma_e$ , for the model is defined in Equation [A-1].

$$\sigma_e = \sqrt{\frac{1}{3}\{\sigma\}^T [A]\{\sigma\} - \frac{1}{3}\{\sigma\}^T \{\alpha\}} \quad [A-1]$$

Where,

$\{\sigma\}$  = the vector of the current stress state.

$\{\alpha\}$  = a vector that accounts for translation of the yield surface.

$[A]$  = a matrix that describes the shape of the yield surface.

Then, introducing a material parameter,  $K$ , the yield criterion,  $F$ , is derived as in Equation [A-2]. The function,  $F$ , represents that, when the effective stress is equal to  $K$ , the material is assumed to yield.

$$F = \{\sigma\}^T [A]\{\sigma\} - \{\sigma\}^T \{\alpha\} - K = 0 \quad [A-2]$$

When differences in yield strengths in tension and compression are considered,  $\{\alpha\}$  provides the initial shift of the origin of the yield surface. The change in shape of the yield surface is calculated based on the increments of plastic work throughout the history of loading.

The matrix  $[A]$  describes the shape of the yield surface and has the form as Equation [A-3].

$$[A] = \begin{bmatrix} A_{11} & A_{12} & A_{13} & 0 & 0 & 0 \\ A_{12} & A_{22} & A_{23} & 0 & 0 & 0 \\ A_{13} & A_{23} & A_{33} & 0 & 0 & 0 \\ 0 & 0 & 0 & A_{44} & 0 & 0 \\ 0 & 0 & 0 & 0 & A_{55} & 0 \\ 0 & 0 & 0 & 0 & 0 & A_{66} \end{bmatrix} \quad [A-3]$$

The diagonal terms of [A] are defined in Equation [A-4] and can be identified by evaluating the yield criterion in Equation [A-2] for all the possible uniaxial stress conditions.

$$A_{ii} = \frac{K}{\sigma_{+i}\sigma_{-i}}, \quad (i = 1 \text{ to } 6) \quad [A-4]$$

Where  $\sigma_{+i}$  and  $\sigma_{-i}$  = the tensile and compressive yield strengths in direction i (for the XYZ coordinate system, i = X, Y, Z, XY, YZ, XZ). For the shear yields,  $\sigma_{+i}$  is set equal to  $\sigma_{-i}$ . Then,

$$A_{44} = \frac{K}{\sigma_{XY}^2}, \quad A_{55} = \frac{K}{\sigma_{YZ}^2}, \quad A_{66} = \frac{K}{\sigma_{XZ}^2} \quad [A-5]$$

K is defined by normalizing [A] about  $A_{11}$ , Then,

$$K = \sigma_{+X}\sigma_{-X} \quad [A-6]$$

The vector  $\{\alpha\}$ , describing the translation of the yield surface, has the form shown in Equation [A-7].

$$\{\alpha\} = [\alpha_1 \quad \alpha_2 \quad \alpha_3 \quad 0 \quad 0 \quad 0]^T \quad [A-7]$$

$$\text{Where} \quad \alpha_i = A_{ii}(\sigma_{+i} - \sigma_{-i}) \quad (i = 1, 2, 3) \quad [A-8]$$

Assuming plastic incompressibility of the material results in Equations [A-9] and [A-10].

$$\begin{aligned}
 A_{11}+A_{12}+A_{13}&=0 \\
 A_{12}+A_{22}+A_{23}&=0 \\
 A_{13}+A_{23}+A_{33}&=0
 \end{aligned}
 \tag{A-9}$$

and

$$\alpha_1+\alpha_2+\alpha_3=0 \tag{A-10}$$

Therefore, the off-diagonal terms of [A] are given in Equation [A-11].

$$\begin{aligned}
 A_{12} &= -\frac{1}{2}(A_{11}+A_{22}-A_{33}) \\
 A_{13} &= -\frac{1}{2}(A_{11}-A_{22}+A_{33}) \\
 A_{23} &= -\frac{1}{2}(-A_{11}+A_{22}+A_{33})
 \end{aligned}
 \tag{A-11}$$

Using Equations [A-4], [A-8] and [A-10], the consistency equation is derived as shown in Equation [A-12]

$$\frac{\sigma_{+1} - \sigma_{-1}}{\sigma_{+1}\sigma_{-1}} + \frac{\sigma_{+2} - \sigma_{-2}}{\sigma_{+2}\sigma_{-2}} + \frac{\sigma_{+3} - \sigma_{-3}}{\sigma_{+3}\sigma_{-3}} = 0 \tag{A-12}$$

Due to the requirement of plastic incompressibility Equation [A-12] is a criterion that must be satisfied throughout all levels of plastic straining. Also, the yield stresses must define a closed surface. In cross section the closed surface shows as elliptical. In order to define an elliptical yield surface, the criterion of inequality [A-13] must be met.

$$A_{11}^2 + A_{22}^2 + A_{33}^2 - 2(A_{11}A_{22} + A_{22}A_{33} + A_{11}A_{33}) < 0 \tag{A-13}$$

Equations [A-12] and [A-13] imply that the yield stresses should be inter-related in order to meet the criteria. This means that all experimental data are not guaranteed for model application. Therefore, as shown in Table 3-1 the empirical procedures for determining material constants can be used for the application.

# APPENDIX B

## Procedures of Wood Foundation-based Three-dimensional Finite Element Analysis

**Wood Foundation Material Model (unit: pound and inch)**

Value in RED: Calculated, assumed or published value, DO NOT TOUCH!  
Value in BLUE: Input required

**Step 1**

Species	Douglas-Fir
Nail Shank Dia	0.188 in
Length of contact	1.5 in
Poisson's ratio $\nu_{LT}$	0.371
Poisson's ratio $\nu_{RT}$	0.363

**Step 2**

Property	Value	Unit
$E_L$	106,676	106,676
$E_T$	20,636	20,636
$E_R$	20,636	20,636
$G_{LT}$	20,126	20,126
$G_{RT}$	7,430	7,430
$\nu_{LT}$	0.071	0.071
$\nu_{RT}$	0.371	0.371
$\nu_{RT}$	0.362	0.362
$\tan \phi_{LT}$	1.687	1.687
$\tan \phi_{RT}$	2.05	2.05
$\tan \phi_{LL}$	2.01	2.01
$\tan \phi_{LR}$	2.01	2.01
$\tan \phi_{RT}$	74	74
$\sigma_{yL}$	2,323	2,323
$\epsilon_{yL}$	0.0218	0.0218
$\sigma_{yR,T}$	947	947
$\epsilon_{yR,T}$	0.0401	0.0401
$\nu_{yL}$	458	458
$\nu_{yR}$	234	234
$\nu_{yT}$	0.0233	0.0233
$\nu_{yT}$	0.0389	0.0389

**Step 3**

Material Model of Douglas Fir

ELASTIC MOE: X  
ELASTIC MOE: Y  
ELASTIC MOE: Z  
ELASTIC SHEAR MODULUS: XY  
ELASTIC SHEAR MODULUS: YZ  
ELASTIC SHEAR MODULUS: XZ  
IPOISSON'S RATIO: XY  
IPOISSON'S RATIO: YZ  
IPOISSON'S RATIO: XZ  
ISHEAR YIELD STRESS: XY,YZ,XZ  
ISHEAR TANGENT MODULI: XY,YZ,XZ

WB ANISO,1  
TBDATA,1,947,2322,947  
TBDATA,4,205,1066,205  
TBDATA,7,947,2322,947  
TBDATA,10,205,1066,205  
TBDATA,13,968,468,284  
TBDATA,16,201,201,74

WF Material properties  
Correction factor // 1.7  
Correction factor // 0.9  
Correction factor // 4.2  
Correction factor // 2.8  
WF MOE // 100676 psi  
WF MOE // 20636 psi  
Yield strain // 0.0218 psi  
Yield strain // 0.0401 psi  
Y // Inter // 2300 psi  
Y // Inter // 938 psi

stress (psi) vs strain (in/in) graph showing curves for L, R or T, and Shear RL, Shear RT.

**Step 1. Input independent variables**

For the wood material model

- Wood compressive MOE (parallel/perpendicular to grain)
- Wood yield strain (parallel/perpendicular to grain)
- Average wood Poisson's ratio (LT and RT)

**Step 2. Consistency check**

**Step 3. Copy & paste material code to ANSYS input file**

- Shape a model with 3D solid element
- Assign material attributes (wood or foundation)

# APPENDIX C

## An Example of Specimen Cutting Pattern

Cutting pattern in a piece of lumber  
(units: mm)

